

INFORMATION TO USERS

While the most advanced technology has been used to photograph and reproduce this manuscript, the quality of the reproduction is heavily dependent upon the quality of the material submitted. For example:

- Manuscript pages may have indistinct print. In such cases, the best available copy has been filmed.
- Manuscripts may not always be complete. In such cases, a note will indicate that it is not possible to obtain missing pages.
- Copyrighted material may have been removed from the manuscript. In such cases, a note will indicate the deletion.

Oversize materials (e.g., maps, drawings, and charts) are photographed by sectioning the original, beginning at the upper left-hand corner and continuing from left to right in equal sections with small overlaps. Each oversize page is also filmed as one exposure and is available, for an additional charge, as a standard 35mm slide or as a 17"x 23" black and white photographic print.

Most photographs reproduce acceptably on positive microfilm or microfiche but lack the clarity on xerographic copies made from the microfilm. For an additional charge, 35mm slides of 6"x 9" black and white photographic prints are available for any photographs or illustrations that cannot be reproduced satisfactorily by xerography.



8704773

Hung, Shi-Chang

THE UNSTEADY VISCOUS FLOW OVER A GROOVED WALL: A
COMPARISON OF TWO NUMERICAL METHODS

The University of Arizona

PH.D. 1986

University
Microfilms
International 300 N. Zeeb Road, Ann Arbor, MI 48106



PLEASE NOTE:

In all cases this material has been filmed in the best possible way from the available copy. Problems encountered with this document have been identified here with a check mark .

- 1. Glossy photographs or pages _____
- 2. Colored illustrations, paper or print _____
- 3. Photographs with dark background _____
- 4. Illustrations are poor copy _____
- 5. Pages with black marks, not original copy _____
- 6. Print shows through as there is text on both sides of page _____
- 7. Indistinct, broken or small print on several pages
- 8. Print exceeds margin requirements _____
- 9. Tightly bound copy with print lost in spine _____
- 10. Computer printout pages with indistinct print _____
- 11. Page(s) _____ lacking when material received, and not available from school or author.
- 12. Page(s) _____ seem to be missing in numbering only as text follows.
- 13. Two pages numbered _____. Text follows.
- 14. Curling and wrinkled pages _____
- 15. Dissertation contains pages with print at a slant, filmed as received _____
- 16. Other _____

University
Microfilms
International

**THE UNSTEADY VISCOUS FLOW OVER A GROOVED WALL :
A COMPARISON OF TWO NUMERICAL METHODS**

by
Shi-Chang Hung

**A Dissertation Submitted to the Faculty of the
DEPARTMENT OF AEROSPACE AND MECHANICAL ENGINEERING
In Partial Fullfillment of the Requirements
For the Degree of
DOCTOR OF PHILOSOPHY
WITH A MAJOR IN MECHANICAL ENGINEERING
In the Graduate College
The University of Arizona**

1 9 8 6

THE UNIVERSITY OF ARIZONA
GRADUATE COLLEGE

As members of the Final Examination Committee, we certify that we have read
the dissertation prepared by Shi-Chang Hung

entitled The Unsteady Viscous Flow over a Grooved Wall:
A Comparison of Two Numerical Methods.

and recommend that it be accepted as fulfilling the dissertation requirement
for the Degree of Doctor of Philosophy.

Thomas F Balsa

Nov 13/86
Date

E K Parks

Nov 13/86
Date

D C Perkins

Nov 13 '86
Date

Robert B Kuning

Nov. 13, '86
Date

Thomas Vincent

Nov 13, 1986
Date

Final approval and acceptance of this dissertation is contingent upon the
candidate's submission of the final copy of the dissertation to the Graduate
College.

I hereby certify that I have read this dissertation prepared under my
direction and recommend that it be accepted as fulfilling the dissertation
requirement.

Robert B Kuning
Dissertation Director

Nov. 13, '86
Date

STATEMENT BY AUTHOR

This dissertation has been submitted in partial fulfillment of requirements for an advanced degree at The University of Arizona and is deposited in the University Library to be made available to borrowers under rules of the Library.

Brief quotations from this dissertation are allowable without special permission, provided that accurate acknowledgment of source is made. Requests for permission for extended quotation from or reproduction of this manuscript in whole or in part may be granted by the head of the major department or the Dean of the Graduate College when in his or her judgment the proposed use of the material is in the interests of scholarship. In all other instances, however, permission must be obtained from the author.

SIGNED: _____

Shichang Hung

ACKNOWLEDGMENT

It has been my priveledge and good fortune to have received the attention of a number of outstanding individuals in the course of my study at the University of Arizona. This work is, in no small part, due to them.

I shall forever be indebted to my research director, Prof. Robert B. Kinney, whose friendship, encouragement and guidance have made this work a pleasure and a success. My sincere appreciation is extended to Prof. Henry C. Perkins, Jr. for his patient and careful review of this manuscript. I would also like to express my gratitude to the other members of my committee Prof. Thomas F. Balsa, Prof. K.Y. Fung, Prof. Edwin K. Parks and Prof. Thomas L. Vincent for their assistance. In addition, thanks are also extended to the Department of Aerospace and Mechanical Engineering at the University of Arizona for providing computer funds for this research.

To my family I owe the greatest debt of all. The courage and sacrifice shown by my parents in supporting and encouraging my studies at this wonderful country has always served as a source of personal inspiration. Most importantly, the love and continued support of my wife Sulan has brought the greatest joy to my life, and has carried me through many difficult times.

TABLE OF CONTENTS

	Page
LIST OF ILLUSTRATIONS	vi
NOMENCLATURE	xiii
ABSTRACT	xvi
1. INTRODUCTION	1
2. THEORETICAL ANALYSIS	11
Velocity Field	11
The Vorticity-Velocity Induction Method	12
The Biot-Savart Law of Induced Velocities	12
The Distribution of Bound Vorticity	18
Spatial Periodicity in the Flow Field	21
The Vorticity-Stream Function Method	30
Vorticity Dynamics	33
The Vorticity-Velocity Induction Method	36
The Vorticity-Stream Function Method	38
Drag Coefficient	39
Friction Drag Coefficient	41
Pressure Drag Coefficient	42
3. NUMERICAL ANALYSIS	43
Flow Network	43
Numerical Formulation For Vorticity Dynamics	47
Finite-Difference Form of the Vorticity Transport Equation	47
Vorticity Production at the Solid Surface	51
The Vorticity-Velocity Induction Method	51
The Vorticity-Stream Function Method	53
Numerical Formulation for the Velocity Field	57
The Vorticity-Velocity Induction Method	57
Induced Velocity due to the Free Vorticity Field	58
Induced Velocity due to the Distribution of Bound Vorticity	64
The Distribution of Bound Vorticity	68
The Vorticity-Stream Function Method	70

TABLE OF CONTENTS — Continued

Drag Coefficient	78
Friction Drag Coefficient	78
Pressure Drag Coefficient	79
Choice of the Numerical Parameters	80
Spatial Grid Increments	80
Time Increment	82
Spatial Increments for the Distribution of Bound Vorticity	84
4. RESULTS AND DISCUSSION	85
5. SUMMARY AND CONCLUDING REMARKS	142
APPENDIX A: VELOCITY INDUCED BY BOUND AND FREE VORTICITY	145
Velocity due to a Single Bound Vorticity Element	146
Velocity due to a Single Free Vorticity Element	151
APPENDIX B: INTERPOLATION METHOD FOR STREAM FUNCTION	154
APPENDIX C: INVISCID FLOW OVER A FORWARD-FACING STEP	158
Exact Solution	158
Numerical Solutions	165
Results	168
REFERENCES	175

LIST OF ILLUSTRATIONS

Figure		Page
1.1	The geometry of the periodically grooved wall.	2
2.1	Illustration of the image vortices system.	15
2.2	Graphical representation of the contribution of onset flow, the distribution of bound vorticity and the free vorticity field to the velocity at a point p in the flow field.	17
2.3	Flow geometry with the primary computational domain and the spatially repeating regions shown.	22
2.4	Representation of an infinite row of vortices.	25
2.5	Representation of an infinite row of vortices offset from X-axis.	29
3.1	Illustration of the computational domain and layout of cell elements for the flow over the grooved wall with the base geometry $a=4.0$ and $d=2.0$	45
3.2	Diagram of the node arrangement around fluid elements in the computational domain.	46
3.3	Diagram of the control volume adjacent to the horizontal surface used to determine the vorticity at the solid surface. The tangential component of velocities, V_1 , V_2 , V_3 and V_4 , are calculated at the points corresponding to 1, 2, 3 and 4, respectively.	54
3.4	Graphical representation of the distribution of bound vorticity for the element Δx_i on the horizontal surface of the step.	66
3.5	Diagram of the control volume used to obtain the finite-difference approximations for the stream function equation at a cell element adjacent to the horizontal surface of the grooved wall.	73

LIST OF ILLUSTRATIONS — Continued

Figure	Page	
3.6	Illustration of the node arrangement used in the nine-point interpolation method for the stream function.	76
4.1	Plots of the stream function contours for potential flow over the grooved wall from (a) the VVI method and (b) the VSF method.	86
4.2	Plots of the X component of velocities obtained from the VVI and VSF methods as a function of the vertical distance from the bottom wall for potential flow at $X = -0.7571$	88
4.3	Plots of the X component of velocities obtained from the VVI and VSF methods as a function of the vertical distance from the bottom wall for potential flow at $X = 0$	89
4.4	Plots of the X component of velocities obtained from the VVI and VSF methods as a function of the vertical distance from the bottom wall for potential flow at $X = 0.7571$	90
4.5	Plots of the X component of velocities obtained from the VVI and VSF methods as a function of the vertical distance from the bottom wall for potential flow at $X = 0.9911$	91
4.6	Plots of the X component of velocities obtained from the VVI and VSF methods as a function of the vertical distance from the bottom wall for potential flow at $X = 1.0689$	92
4.7	Plots of the distribution of surface pressure along the wall for potential flow obtained from the VVI (Δ) and VSF ($-$) methods.	93
4.8	Plots of the (a) stream function and (b) vorticity contours for unsteady flow over the grooved wall at $t=0.500146$ using the VVI method.	94
4.9	Plots of the (a) stream function and (b) vorticity contours for unsteady flow over the grooved wall at $t=0.500641$ using the VSF method.	95

LIST OF ILLUSTRATIONS — Continued

Figure	Page
4.10 Plots of the (a) stream function and (b) vorticity contours for unsteady flow over the grooved wall at $t=0.99921$ using the VVI method.	96
4.11 Plots of the (a) stream function and (b) vorticity contours for unsteady flow over the grooved wall at $t=0.999413$ using the VSF method.	97
4.12 Plots of the (a) stream function and (b) vorticity contours for unsteady flow over the grooved wall at $t=1.49715$ using the VVI method.	98
4.13 Plots of the (a) stream function and (b) vorticity contours for unsteady flow over the grooved wall at $t=1.49973$ using the VSF method.	99
4.14 Plots of the (a) stream function and (b) vorticity contours for unsteady flow over the grooved wall at $t=1.9998$ using the VVI method.	100
4.15 Plots of the (a) stream function and (b) vorticity contours for unsteady flow over the grooved wall at $t=2.00004$ using the VSF method.	101
4.16 Plots of the (a) stream function and (b) vorticity contours for unsteady flow over the grooved wall at $t=3.00098$ using the VVI method.	102
4.17 Plots of the (a) stream function and (b) vorticity contours for unsteady flow over the grooved wall at $t=3.00067$ using the VSF method.	103
4.18 Plots of the (a) stream function and (b) vorticity contours for unsteady flow over the grooved wall at $t=3.99888$ using the VVI method.	104
4.19 Plots of the (a) stream function and (b) vorticity contours for unsteady flow over the grooved wall at $t=3.99976$ using the VSF method.	105
4.20 Plots of the (a) stream function and (b) vorticity contours for unsteady flow over the grooved wall at $t=6.00056$ using the VVI method.	106

LIST OF ILLUSTRATIONS — Continued

Figure	Page	
4.21	Plots of the (a) stream function and (b) vorticity contours for unsteady flow over the grooved wall at $t=5.99948$ using the VSF method.	107
4.22	Plots of the X component of velocities obtained from the VVI and VSF methods as a function of the vertical distance from the bottom wall at $X = -0.7571$ and $t \cong 0.5$	110
4.23	Plots of the X component of velocities obtained from the VVI and VSF methods as a function of the vertical distance from the bottom wall at $X = 0$ and $t \cong 0.5$	111
4.24	Plots of the X component of velocities obtained from the VVI and VSF methods as a function of the vertical distance from the bottom wall at $X = 0.7571$ and $t \cong 0.5$	112
4.25	Plots of the X component of velocities obtained from the VVI and VSF methods as a function of the vertical distance from the bottom wall at $X = 0.9911$ and $t \cong 0.5$	113
4.26	Plots of the X component of velocities obtained from the VVI and VSF methods as a function of the vertical distance from the bottom wall at $X = 1.0689$ and $t \cong 0.5$	114
4.27	Plots of the X component of velocities obtained from the VVI and VSF methods as a function of the vertical distance from the bottom wall at $X = -0.7571$ and $t \cong 6.0$	115
4.28	Plots of the X component of velocities obtained from the VVI and VSF methods as a function of the vertical distance from the bottom wall at $X = 0$ and $t \cong 6.0$	116
4.29	Plots of the X component of velocities obtained from the VVI and VSF methods as a function of the vertical distance from the bottom wall at $X = 0.7571$ and $t \cong 6.0$	117

LIST OF ILLUSTRATIONS — Continued

Figure	Page	
4.30	Plots of the X component of velocities obtained from the VVI and VSF methods as a function of the vertical distance from the bottom wall at $X = 0.9911$ and $t \cong 6.0$	118
4.31	Plots of the X component of velocities obtained from the VVI and VSF methods as a function of the vertical distance from the bottom wall at $X = 1.0689$ and $t \cong 6.0$	119
4.32	Plots of the distribution of (a) shear stress and (b) pressure along the wall at $t \cong 0.5$ obtained from the VVI (Δ) and VSF (—) methods.	120
4.33	Plots of the distribution of (a) shear stress and (b) pressure along the wall at $t \cong 1.0$ obtained from the VVI (Δ) and VSF (—) methods.	121
4.34	Plots of the distribution of (a) shear stress and (b) pressure along the wall at $t \cong 1.5$ obtained from the VVI (Δ) and VSF (—) methods.	122
4.35	Plots of the distribution of (a) shear stress and (b) pressure along the wall at $t \cong 2.0$ obtained from the VVI (Δ) and VSF (—) methods.	123
4.36	Plots of the distribution of (a) shear stress and (b) pressure along the wall at $t \cong 3.0$ obtained from the VVI (Δ) and VSF (—) methods.	124
4.37	Plots of the distribution of (a) shear stress and (b) pressure along the wall at $t \cong 4.0$ obtained from the VVI (Δ) and VSF (—) methods.	125
4.38	Plots of the distribution of (a) shear stress and (b) pressure along the wall at $t \cong 6.0$ obtained from the VVI (Δ) and VSF (—) methods.	126
4.39	Plots of the time development of the drag coefficient from the VVI and VSF methods.	128

LIST OF ILLUSTRATIONS — Continued

Figure	Page	
4.40	Plots of the (a) stream function and (b) vorticity contours for unsteady flow over the grooved wall at $t=8.00074$ using the VSF method.	130
4.41	Plots of the (a) stream function and (b) vorticity contours for unsteady flow over the grooved wall at $t=10.0005$ using the VSF method.	131
4.42	Plots of the (a) stream function and (b) vorticity contours for unsteady flow over the grooved wall at $t=12.0002$ using the VSF method.	132
4.43	Plots of the (a) stream function and (b) vorticity contours for unsteady flow over the grooved wall at $t=13.9999$ using the VSF method.	133
4.44	Plots of the (a) stream function and (b) vorticity contours for unsteady flow over the grooved wall at $t=15.9996$ using the VSF method.	134
4.45	Plots of the time development of the X component of velocities from the VSF methods as a function of the vertical distance from the bottom wall at $X = -0.7571$	135
4.46	Plots of the time development of the X component of velocities from the VSF methods as a function of the vertical distance from the bottom wall at $X = 0$	136
4.47	Plots of the time development of the X component of velocities from the VSF methods as a function of the vertical distance from the bottom wall at $X = 0.7571$	137
4.48	Plots of the time development of the X component of velocities from the VSF methods as a function of the vertical distance from the bottom wall at $X = 0.9911$	138
4.49	Plots of the time development of the X component of velocities from the VSF methods as a function of the vertical distance from the bottom wall at $X = 1.0689$	139

LIST OF ILLUSTRATIONS — Continued

Figure	Page
4.50 Plots of the time development of the drag coefficient from the VSF method.	140
C.1 Irrotational flow over a forward-facing step in the physical W plane.	159
C.2 Irrotational flow due to a source at the origin in the transformed Z plane.	159
C.3 Layout of the flow network near the corner of the step.	167
C.4 Comparison between the exact (—) and numerical (Δ) solutions for the slip velocity along the surface of the step.	169
C.5 Comparison between the exact (—) and numerical (Δ) solutions for the horizontal component of the velocity at $w_r^* = -0.0689468$	170
C.6 Comparison between the exact (—) and numerical (Δ) solutions for the horizontal component of the velocity at $w_r^* = -0.0893428$	171
C.7 Comparison between the exact (—) and numerical (Δ) solutions for the horizontal component of the velocity at $w_r^* = 0$	172
C.8 Comparison between the exact (—) and numerical (Δ) solutions for the horizontal component of the velocity at $w_r^* = 0.00893428$	173
C.9 Comparison between the exact (—) and numerical (Δ) solutions for the horizontal component of the velocity at $w_r^* = 0.0689468$	174

NOMENCLATURE

C_D	total drag coefficient
C_{Df}	friction drag coefficient
C_{Dp}	pressure drag coefficient
CU	X component of the geometric coefficient
CV	Y component of the geometric coefficient
F_D	total drag force
F_{Df}	friction drag force
F_{Dp}	pressure drag force
N_b	indicates the number of bound vortex elements
NX	indicates the number of cell elements in X direction
NY	indicates the number of cell elements in Y direction
Re	Reynolds number (hU_∞/ν)
U_∞	X component of onset flow velocity, \bar{V}_∞
U_{slip}	tangential component of the velocity along the solid surface
\bar{V}	total velocity vector ($u \bar{i} + v \bar{j}$)
\tilde{V}	complex conjugate of the velocity
\bar{V}_∞	onset flow velocity
VSF	represents the Vorticity-Stream Function Method
VVI	represents the Vorticity-Velocity Induction Method
a	the periodicity length
d	the step width
\bar{e}_d	unit vector in the direction of the onset flow

NOMENCLATURE — Continued

\bar{e}_n	unit vector in the direction normal to the surface of grooved wall
\bar{e}_t	unit vector in the direction tangential to the surface of grooved wall
h	the step height
i	the complex number $(\sqrt{-1})$
\bar{i}	unit vector in the X direction
\bar{j}	unit vector in the Y direction
\bar{k}	unit vector in the Z direction
\bar{n}	unit normal vector (positive outward)
p	pressure
p_o	pressure at the surface of the grooved wall
\bar{r}	position vector
\bar{r}_{op}	position vector from point o to point p , i.e., $(\bar{r}_p - \bar{r}_o)$
u	velocity component in the X direction
v	velocity component in the Y direction
t	time
γ	bound vorticity
ω	free vorticity
τ	shear stress
τ_o	shear stress at the surface of the grooved wall
ρ	density of fluid
ν	kinematic viscosity
μ	dynamic viscosity
ϵ	infinitesimal distance

NOMENCLATURE — Continued

- ψ stream function
- \Im indicates the imaginary part of a complex argument
- \Re indicates the real part of a complex argument

Subscripts

- b indicates contribution due to the distribution of bound vorticity
- f indicates contribution due to the free vorticity field
- i position index in the X direction
- j position index in the Y direction
- o indicates position at point o
- p indicates position at point p
- q indicates position at point q on the surface of the grooved wall

Superscripts

- n indicates position at the n th spatially repeating region
- $+$ indicates the flow quantity is evaluated at time $t + \Delta t$
- $-$ indicates position in the image plane, i.e., the lower half plane.
- $*$ indicates dimensionless variable

ABSTRACT

Unsteady two-dimensional laminar flow of an incompressible viscous fluid over a periodically grooved wall is investigated by numerical simulation using two independent finite-difference methods. One is the vorticity-stream function method, and the other involves the vorticity-velocity induction law formulation. The fluid motion is initiated impulsively from rest and is assumed to be spatially periodic in the streamwise direction. The flow field, which includes the time development of the shear layer and the recirculating flow in the zone of separation, is examined in detail during the transient phase to the steady-state condition. The analytical and numerical formulations, which include the implementation of the boundary conditions, are derived in detail. The generation of vorticity at the solid surfaces is modelled differently in the two approaches. This vorticity production plays an important role in determining the surface-pressure distribution and the drag coefficient.

Characteristics of the transient solution for a moderate Reynolds number in the laminar range are presented. Included with the graphical results are the temporal development of the constant stream function contours, including the dividing contour between the zone of separation and the main flow, and the constant vorticity contours. These latter contours show the interactions of separated vortices. The flow is found to approach a steady-state condition comprising an undisturbed uniform flow, a nonuniform irrotational flow, a shear layer adjacent to the grooved wall, and a recirculating vortex flow in the groove. Results also include the time development of the surface shear stress, surface pressure,

drag coefficient and several typical velocity profiles, which characterize the flow in the recirculating region.

Comparisons of the results obtained by the two numerical methods are made during the major development of the flow. The results showing the general features of the flow development including the time development of the shear layer, free shear layer and recirculating vortex flow are in good agreement. However, a significant deviation does exist at early times for the distribution of surface pressure, which accordingly has noticeable effect on the drag coefficient. Nevertheless, the gap between the distributions of surface pressure and drag coefficients dies out gradually as time progresses. The form of the stream function and vorticity contours at the steady state agrees well with those obtained from a recent numerical investigation of the steady flow in grooved channels.

CHAPTER 1

INTRODUCTION

In the present work, an analysis is made for the unsteady flow over a grooved wall. The flow is set impulsively into motion with prescribed velocity, and its development is examined in detail through the transient phase to the steady-state condition.

The grooved wall is composed of an infinite number of periodic steps as shown in Figure 1.1. They are assumed to be infinite in extent in the spanwise (Z) direction. The dimensions of the step are described by the step height h , the step width d and the periodicity length a .

The grooves (or alternatively the steps) represent artificial roughness elements which have been machined into an otherwise smooth surface. Artificial roughness is often intentionally added to the surface in order to enhance mixing or heat and mass transfer rates. Although experimental studies have been made of some grooved surfaces to determine which geometries most economically improve heat transfer performance (Webb and Eckert, 1972; Lewis, 1975), the design of roughness elements is somewhat of an art, which relies heavily on empirical data. Applications are found in the design of coolant passages in nuclear reactors as well as a variety of process heat exchangers.

Aside from these direct practical applications, groove-flows also serve as a simple, yet rich, example of separated flows. The complex interactions of separated vortices, free shear layers, and driving wall-bounded shear flows are

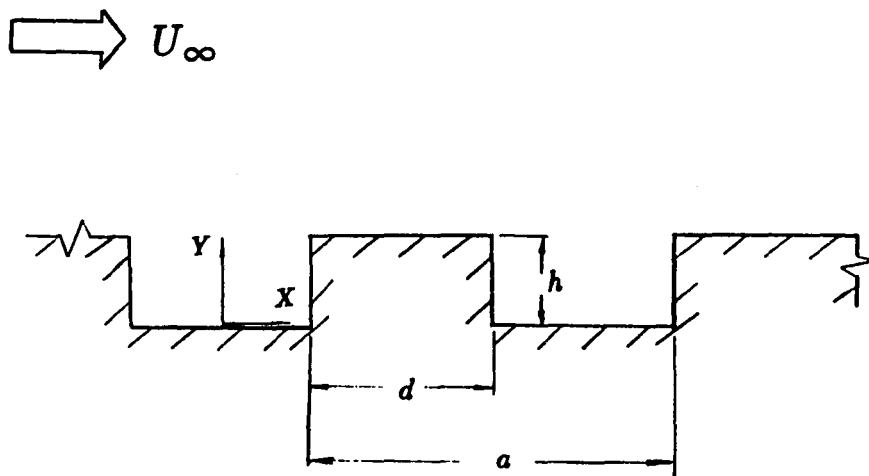


Figure 1.1 The geometry of the periodically grooved wall.

not well understood. Numerical simulation of the flow field offers one means for examining the flow development in some detail.

Since the flow is periodically disturbed at the wall by the repeated periodic steps, it is hypothesized that the solution of the velocity field can be separated into an entry-region part and a spatially periodic part. Sufficiently far downstream from the leading edge of the plate, the magnitude of the entry-region part is expected to decay to insignificance such that only the spatially periodic solution remains. As soon as this far field condition is satisfied, the flow field can be considered to be fully developed. In other words, the term "fully developed flow" will be used to mean that at any instant of time, the velocity and vorticity profiles of the flow are independent of the upstream conditions and are identical at corresponding planes between any two steps (i.e., spatially periodic flow exists).

In this study, the flow will be assumed to be fully developed in the streamwise direction, and to be independent of the spanwise co-ordinate Z . Thus, the flow is considered to be two dimensional and spatially periodic. Note that the configuration of an infinite number of periodic steps along the wall is more representative of roughness elements than, say, an isolated step. Also spatial periodicity allows minimal ambiguity in terms of boundary-condition specification. Finally, the fluid is assumed to be incompressible and to have constant kinematic viscosity ν , and the velocity of the uniform onset flow is taken to be a constant vector in the X direction (i.e., $U_\infty \bar{i}$).

In general, unsteady flow over the solid body may be analyzed through examining the development of the vorticity field around the body, because for a given movement of the body, this determines the whole flow. To fix the flow

uniquely, it requires only the boundary condition on the normal component of the velocity at the solid surface. It is shown by Rosenhead (1963) that for a given distribution of vorticity outside the surface of the solid body, there exists one and only one velocity field, except for an arbitrary additive constant tending to zero at infinity and with zero normal relative velocity at the solid surface. Thus, there is only a restricted class of vorticity distributions that corresponds to real flows satisfying also the no-slip condition on the tangential velocity.

For incompressible and viscous fluids, the vorticity, which is proportional to the instantaneous angular momentum of a fluid element, varies due to the movement of the fluid element and the tangential shear stresses exerted between fluid elements. The former variation arises from convection due to the translational component of the motion of the fluid element, and the latter variation arises from the effect due to the non-zero kinematic viscosity of the fluid and the associated spatial vorticity gradient in the flow, which is commonly interpreted as the rate of change of vorticity due to diffusion. As a result, for a step-by-step computation of the development of vorticity around the solid body, the velocity field and the value of the kinematic viscosity, which may be absorbed into a Reynolds number, are needed to progress from a given distribution of vorticity to another distribution of vorticity a short time later.

In this study, the complete analysis of the flow development is conceptually decomposed into the kinematical and dynamical parts. The kinematical part focuses on the determination of the velocity field due to a given distribution of vorticity. The dynamical part deals with the production of vorticity at solid surfaces and its transport throughout the fluid.

In this investigation, the velocity field is obtained by employing two different numerical approaches. One of them uses the integral relationship referred to here as the Biot-Savart law of induced velocities. This relates the velocity and vorticity fields directly. In the other approach, the stream function is introduced, and it is related to the vorticity through a second order partial differential equation, known as the stream function equation. Once this equation is solved and the distribution of stream function is known, components of the velocity can be determined simply by differentiating the stream function. The former approach is referred to here as the vorticity-velocity induction (VVI) method, and the latter is referred to as the vorticity-stream function (VSF) method.

As mentioned earlier, the dynamical part deals with the production and transport of vorticity. The accuracy of this part of the calculation depends strongly on the determination of the rate of vorticity production at solid surfaces. This vorticity production arises from the surface-adherence condition (i.e., the fluid velocity vanishes along stationary, impermeable boundaries) which must be satisfied at each instant of time. In the VVI method, this condition is enforced by determining the diffusive flux directly and the use of the image vortices. In the VSF method, on the other hand, the surface-adherence condition is satisfied through specifying the value of the stream function and the calculation of the vorticity exactly at the surface. This value of the wall vorticity is then used to calculate the diffusive flux of vorticity at the surface. In both methods, the vorticity produced at the solid surface enters the flow field by molecular diffusion. It is then transported and redistributed over the flow field through both convection and diffusion.

In the present work, both of the above-mentioned numerical techniques are employed. Because numerical differentiation is involved in the calculation of the velocity field in the VSF method, a lack of spatial smoothness in the stream function can be amplified in the evaluation of the fluid velocities. The effect can thus propagate throughout the flow. On the other hand, since the VVI method involves numerical integration of the vorticity field to obtain the velocity distribution, spatial irregularities will be smoothed. The different treatment of the vorticity production at the wall is also expected to have an effect on the calculations. It is not known how these numerical differences will influence a time dependent calculation.

It is our intent to examine the numerical predictions in a time-dependent flow, beginning with the same initial condition. Both methods will be applied to the same flow problem over the same computational domain and will be performed on the same computer, (i.e., Cyber 175). Therefore, any differences in the results obtained using the two methods will be due totally to differences in the numerical schemes, and not the arithmetic precision.

The concept of the vorticity-velocity induction method in conjunction with viscous flow calculation was originally suggested by Lighthill (Rosenhead, 1963). Payne (1958) was apparently the first to employ this technique to study the unsteady viscous flow past a circular cylinder. To satisfy the zero-normal component of the velocity at the solid surface, he applied the concept of image vortices. The no-slip boundary condition was then enforced by vorticity generation on the surface of the cylinder. Wu and Thompson (1971 and 1973) developed an integral-differential formulation for numerical solutions of the time-dependent Navier-Stokes equations. The integral portion dealt with the velocity

induction law. In their case, the vorticity at the solid surface was obtained from the curl of the velocity plus enforcement of the no-slip boundary condition. Paniker and Lavan (1975) investigated the unsteady flow over circular and elliptic cylinders. Although the stream function appeared in their formulation, an integral relation analogous to the Biot-Savart law was employed to determine the velocity field.

As in the above-referenced analyses, the technique employed here in the VVI method also uses the vorticity transport equation in conjunction with the Biot-Savart law of induced velocities. However, it completely avoids the calculation of the vorticity at the solid surface. A relationship for the direct evaluation of the flux of vorticity at the solid surface is deduced to make this step unnecessary. Over the past years, Kinney and co-workers have successfully applied this technique to solve a broad range of unsteady fluid flow problems. First, Kinney and Paolino (1974) pioneered the present technique in the study of unsteady flow near the leading edge of a semi-infinite flat plate at zero angle of attack. Schmall and Kinney (1974) then extended the technique to unsteady viscous flow past a flat plate at different angles of attack. Kinney and Cielak (1977) [see also Cielak and Kinney (1978)] investigated the unsteady viscous flow past a two-dimensional airfoil with finite thickness. They obtained results at angles of attack of zero and 30 degrees for a Reynolds number of 400. More recently, Taslim, Kinney and Paolino (1984) applied the technique to analyze the unsteady two-dimensional flow over elliptical bodies in arbitrary unsteady motion. The results pertain to flow over circular cylinders with constant and varying angular velocities, as well as flow over elliptical cylinders of varying aspect ratios undergoing translation and pitching oscillation. Cerutti, Kinney and Paolino (1986) also utilized this

technique to simulate the unsteady two-dimensional flow around an array of circular cylinders submerged in a uniform onset flow. Extension of the numerical technique to predict the unsteady flow and heat transfer to single cylinders at Reynolds numbers as high as 70,000 has also been made by Paolino, Kinney and Cerutti (1986).

In viewing all of these studies, it is worth noting that the various formulations have many features in common. The principal differences exist in the treatment of the solid boundary conditions and the production of vorticity there.

The conventional approach used in most two-dimensional viscous-flow analysis is based on the vorticity-stream function formulation. Giaquinta (1977) employed this technique to analyze the unsteady laminar flow of an incompressible fluid through a two-dimensional sudden expansion. It is worth noting that there exist some common features in specifying the initial condition between his work and the present study; that is, the fluid motion is initiated impulsively from rest and is examined in detail during the transient phase and ending at the steady-state condition. Atkins, Maskell and Patrick (1980) used vorticity and stream function as dependent variables to study the laminar and turbulent flows over a single backward-facing step in a two-dimensional channel. Hung (1982) also employed this approach to investigate the time-dependent incompressible flow through a two-dimensional rectangular reservoir. The vorticity at the solid surface was determined so as to eliminate the tangential component of the velocity through application of the circulation theory. The basic idea from that study is followed in the VSF method in the current investigation.

In slight contrast to the conventional stream-function approach, Kinney, Taslim and Hung (1985) used a hybrid solution method which combined the

stream function and the Biot-Savart law of induced velocities to study the break-up of a field of eddies by a flat-plate obstacle embedded in a incompressible and unsteady boundary layer. In their study, the velocity induction law was used to determine boundary velocities along the solid surfaces and on the perimeter of the computational domain. Image and bound vorticity were also used. The velocity field inside the domain was computed from the stream function. As in the VVI method, nonzero tangential velocities at solid surfaces were eliminated by the proper amount of vorticity production.

A search through the literature for numerical studies concerned with the unsteady viscous flow over a grooved wall has yielded extremely limited results. The only study found pertains to flow in a grooved channel, as reported recently by Ghaddar, Korczak, Mikic and Patera (1986). They investigated the hydrodynamic stability and self-sustained oscillations for incompressible separated flow in a two-dimensional periodically grooved channel using the spectral element method. In their study, a value of the critical Reynolds number was found. For Reynolds numbers less than the critical value, the flow was found to approach a stable steady state. In that case, for a specified flow rate, the pressure drop was found to be less than the corresponding quantity for plane Poiseuille flow (i.e., no grooves). In other words, it shows that the effect of the addition of grooves to a plane channel in laminar flow is one of drag reduction and decreased dissipation. In addition, they also verified that the single-groove calculations (i.e., using the spatially periodical boundary condition) is sufficient to simulate the flow in a muti-groove domain. No results were given for an unconfined boundary-layer flow such as that treated here.

The next chapter presents the theoretical aspects of the analysis. The numerical formulation is discussed in Chapter 3, and results from the numerical calculations using the VVI and VSF methods and the comparison between them are presented in Chapter 4.

CHAPTER 2

THEORETICAL ANALYSIS

In this chapter, the theoretical aspects on time-dependent, separated, laminar flow over a grooved wall are presented. The flow is set impulsively into motion; at that initial instant, the flow is assumed to be irrotational. The flow then starts to develop until it reaches the steady-state condition. This time development of the two-dimensional and incompressible flow is investigated with attention focused on the development of vorticity in the flow field. Initially, the vorticity is zero everywhere. Since vorticity can be neither created nor destroyed in the fluid, vorticity is physically introduced into the fluid due to the presence of the no-slip condition at solid surfaces, which are considered to be distributed surface sources and sinks of vorticity. The imposition of the no-slip condition upon the initially irrotational flow promotes the vorticity production at the solid surface. From there, the vorticity is transported into the fluid through diffusion and is then redistributed over the entire flow field through both diffusion and convection. Therefore, to complete our knowledge of the flow development, the analysis and formulation on both the velocity and vorticity fields are required.

Velocity Field

Since the knowledge of the velocity field is essential to determine the development of the vorticity field, the method employed to determine the velocity field constitutes a significant portion of the whole study. It is known that the kinematic velocity boundary condition embodies the adherence condition (i.e., no

normal and tangential components of the velocity) which must be satisfied at the solid surface in determining the velocity field. This is generally enforced in two steps. First, the normal component of the velocity is nullified, after which the tangential component is reduced to zero. In this study, the velocity field is obtained by using two different approaches. In the VVI method, the velocity field is determined through the Biot-Savart law of induced velocities and the equation of continuity. To satisfy the boundary condition of zero normal relative velocity at the solid surface, use is made of image vortices in the lower half plane and the introduction of a vortex distribution on the surface of the step. In the VSF method, on the other hand, the stream function ψ is introduced and obtained by solving the stream function equation. Once the stream function is known, the velocity field can be obtained by differentiating the stream function. The zero penetration condition is then enforced by specifying a constant value for the stream function along the surface of the grooved wall.

A second step is needed to eliminate the tangential component of the velocity at the solid surface. This is accomplished by the proper production of vorticity at the surface. The detailed procedure to achieve this step will be fully discussed in the section on vorticity dynamics in this chapter.

Since the governing equations and the procedure for the determination of the velocity field are different in the VVI and VSF methods, they are discussed separately as below.

The Vorticity-Velocity Induction Method

The Biot-Savart Law of Induced Velocities. We begin with the expression for the vorticity vector, defined by

$$\bar{\omega} = \nabla \times \bar{V} \quad (2.1)$$

which is considered to be positive if $\bar{\omega}$ is in the counter-clockwise sense. In two dimensions, the only non-zero component of the vorticity vector is in a direction perpendicular to the plane of the flow (i.e., Z -direction). In this case, $\bar{\omega}$, in Cartesian coordinates, reduces to

$$\begin{aligned}\bar{\omega} &= \omega \bar{k} \\ &= \left(\frac{\partial v}{\partial x} - \frac{\partial u}{\partial y} \right) \bar{k}\end{aligned}\quad (2.2)$$

in which \bar{k} is the unit vector in Z -axis, u and v are the scalar velocity components in the X and Y directions, respectively, and ω is the vorticity component normal to the plane of the flow. Under quite general conditions, Eqn.(2.1) can be solved to give \bar{V} in terms of $\bar{\omega}$. The resulting integral is commonly called the Biot-Savart law of induced velocities (Rosenhead, 1963; Milne-Thomson, 1968). This law requires that there be unlimited fluid in the flow field. However, if there is any physical solid body in the flow field, the result must be modified as explained below.

In two dimensions, the general form of the solution to Eqn.(2.1) is given by

$$\bar{V}(r_p, t) = \bar{V}_\infty + \frac{1}{2\pi} \iint_A \frac{\bar{\omega}_o \times \bar{r}_{op}}{|\bar{r}_{op}|^2} dA + grad\phi \quad (2.3)$$

in which the range of integration, A , is over the region of non-zero vorticity, and \bar{r}_{op} is the position vector from $\bar{\omega}_o$ at the point o inside the vorticity element dA to the point p , where the velocity is desired. On the right-hand side of Eqn.(2.3), the first term is the velocity due to the uniform onset flow which here is taken to be a constant vector given by $U_\infty \bar{i}$, where \bar{i} is the unit vector in the X direction. The second term represents the Biot-Savart law of induced velocities and is the velocity induced by the vorticity field. Physically, it means that the vorticity $\bar{\omega}_o$ in the cell element dA at the point o induces a rotation of all the fluid at a distance

$|\bar{r}_{op}|$ from $\bar{\omega}_o$ with the angular velocity $[\omega_o dA/(2\pi|\bar{r}_{op}|^2)]$ which is referred to as the angular velocity induced at p by the element at o. The third term, $grad\phi$, is a purely irrotational contribution to the velocity field and it must be included for generality and to insure that the boundary conditions of zero normal component of the velocity at the solid surfaces are satisfied. It is the modification required when physical boundaries are present.

Since the use of the Biot-Savart law excludes any rigid body, the step is then envisioned to be replaced by the fluid identical to that in the surrounding region. Furthermore, since the rigid body is considered to be stationary, the fluid replaced should remain stationary at all time. Conceptually, the replaced fluid is still referred to as the rigid body in this analysis.

To eliminate the normal component of the velocity at the solid surface, we first introduce image vortices in the lower half plane ($Y \leq 0$). This makes the bottom surface at $Y = 0$ a plane of anti-symmetry such that below it we have vorticity which is opposite in sign to that above the surface. It can be seen from Figure 2.1 that the use of image vortices has eliminated the normal component of the velocity at the surface of the bottom wall. However, zero penetration condition at the surface of the step is still not satisfied. This is accomplished by introducing a vortex distribution, denoted by the symbol $\bar{\gamma}$, on surfaces of the step. In two-dimensional flow, $\bar{\gamma}$, which is like $\bar{\omega}$, has a direction perpendicular to the flow path, and it is also assumed to be positive in a counter-clockwise sense. That is, $\bar{\gamma} = \gamma \bar{k}$. Since this vortex distribution induces a purely irrotational velocity field, it takes the place of $grad\phi$ in Eqn.(2.3). As a result, we replace surfaces of the step by a distribution of concentrated vorticity in the form of vortex sheet along its length. This vortex distribution will henceforth be called

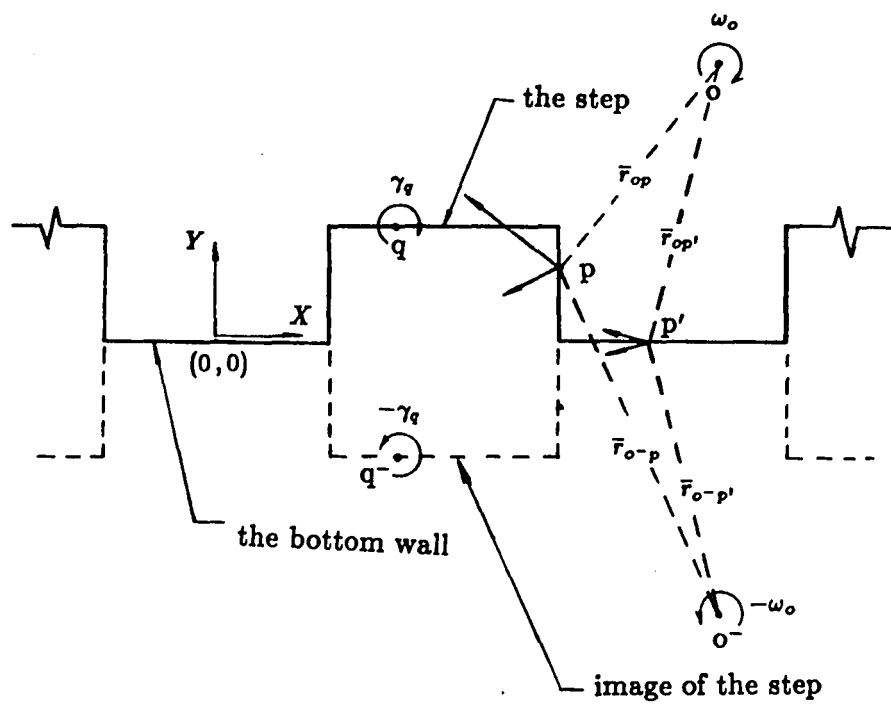


Figure 2.1 Illustration of the image vortices system.

the “bound vorticity” since its location always remains fixed to the surface of the step. Here the term “bound vorticity” is adopted to be in contrast to the term “free vorticity”, which represents $\bar{\omega}$, the vortex distribution in the flow field which is free to move along with the fluid. Therefore, we make the following substitution:

$$\text{grad}\phi = \frac{1}{2\pi} \int_{\Gamma} \frac{\bar{\gamma}_q \times \bar{r}_{qp}}{|\bar{r}_{qp}|^2} dl \quad (2.4)$$

where the range of the integration, Γ , is the line contour along the surface of the physical step and its image reflected in the lower half plane on which the bound vorticity is distributed; \bar{r}_{qp} is the position vector from $\bar{\gamma}_q$ at the point q on Γ to the point p in the fluid, and dl is the differential element of Γ .

Substitution of $\text{grad}\phi$ and the value of \bar{V}_{∞} into Eqn.(2.3), the velocity at the point p becomes

$$\bar{V}(r_p, t) = U_{\infty} \bar{i} + \frac{1}{2\pi} \iint_A \frac{\bar{\omega}_o \times \bar{r}_{op}}{|\bar{r}_{op}|^2} dA + \frac{1}{2\pi} \int_{\Gamma} \frac{\bar{\gamma}_q \times \bar{r}_{qp}}{|\bar{r}_{qp}|^2} dl. \quad (2.5)$$

A graphical representation of the velocities at a point in the fluid due to a vortex element $\Delta A_{i,j}$ and a bound vorticity element Δl_k is shown in Figure 2.2. Here,

$$\Delta \bar{V}_f = \frac{1}{2\pi} \iint_{\Delta A_{i,j}} \frac{\bar{\omega}_o \times \bar{r}_{op}}{|\bar{r}_{op}|^2} dA$$

$$\Delta \bar{V}_b = \frac{1}{2\pi} \int_{\Delta l_k} \frac{\bar{\gamma}_q \times \bar{r}_{qp}}{|\bar{r}_{qp}|^2} dl.$$

To put Eqn.(2.5) into non-dimensional form, we scale all velocities by U_{∞} and all lengths by the step height h . The following dimensionless variables are then introduced:

$$V^* = \frac{V}{U_{\infty}}$$

$$r^* = \frac{r}{h}$$

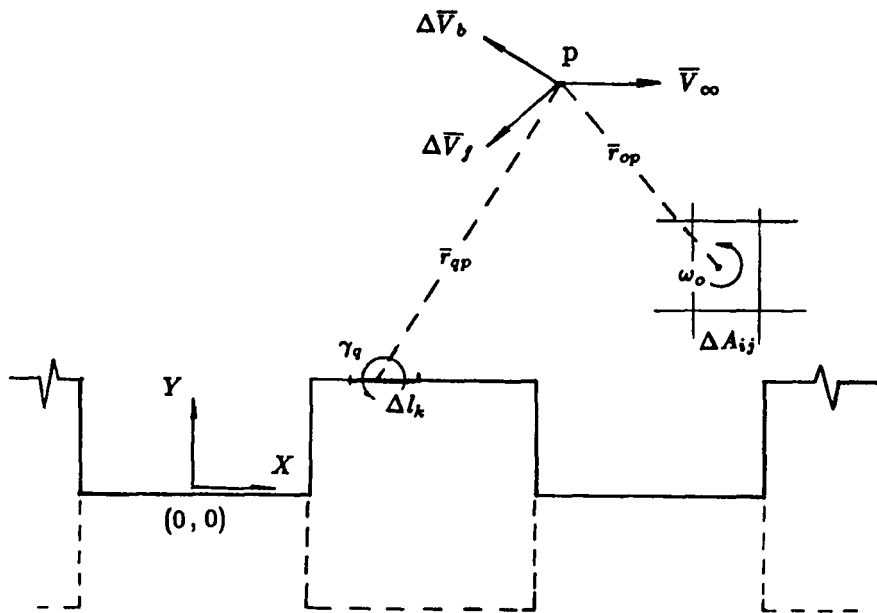


Figure 2.2 Graphical representation of the contribution of onset flow, the distribution of bound vorticity and the free vorticity field to the velocity at the point p in the flow field.

$$\begin{aligned}
dl^* &= \frac{dl}{h} \\
dA^* &= \frac{dA}{h^2} \\
\gamma^* &= \frac{\gamma}{U_\infty} \\
\omega^* &= \frac{\omega h}{U_\infty} \\
t^* &= \frac{t U_\infty}{h}
\end{aligned} \tag{2.6}$$

Substitution of the above dimensionless variables into Eqn.(2.5) yields

$$\bar{V}^*(r_p^*, t^*) = \bar{i} + \frac{1}{2\pi} \iint_A \frac{\bar{\omega}_o^* \times \bar{r}_{op}^*}{|\bar{r}_{op}^*|^2} dA^* + \frac{1}{2\pi} \int_\Gamma \frac{\bar{\gamma}_q^* \times \bar{r}_{qp}^*}{|\bar{r}_{qp}^*|^2} dl^* \tag{2.7}$$

in which the two integrals on the right-hand side represent the contributions from the free vorticity field and the distribution of bound vorticity, respectively. Since only dimensionless variables will be employed for most of the remaining analysis (unless otherwise stated), the asterisk will be omitted for convenience.

The Distribution of Bound Vorticity. As mentioned earlier, the Biot-Savart law of induced velocities requires that the fluid be unbounded. This restriction, which has been overcome by the proper specification of $grad\phi$, results in the replacement of surfaces of the step with the distribution of bound vorticity. Note that this distribution must be constituted to ensure there is no normal component of the velocity at surfaces of the step. The procedure to determine this distribution is now presented as below.

In this study, since the grooved wall is not moved relative to the flow, the replaced fluid at and inside the surface of the step must remain stationary. Referring to Figure 2.2, the velocity at the point p located at a distance ϵ (taken to be 10^{-6}) inside the surface of the step is then equal to zero. Upon rearrangement, Eqn.(2.7) becomes

$$\frac{1}{2\pi} \int_\Gamma \frac{\bar{\gamma}_q \times \bar{r}_{qp}}{|\bar{r}_{qp}|^2} dl = -\bar{i} - \frac{1}{2\pi} \iint_A \frac{\bar{\omega}_o \times \bar{r}_{op}}{|\bar{r}_{op}|^2} dA. \tag{2.8}$$

By taking the tangential component of the above equation along surfaces of the step, the integral equation for the distribution of bound vorticity is obtained,

$$\frac{1}{2\pi} \int_{\Gamma} \frac{\bar{\gamma}_q \times \bar{r}_{qp}}{|\bar{r}_{qp}|^2} dl \cdot \bar{e}_t = \left[-\bar{i} - \frac{1}{2\pi} \iint_A \frac{\bar{\omega}_o \times \bar{r}_{op}}{|\bar{r}_{op}|^2} dA \right] \cdot \bar{e}_t \quad (2.9)$$

where \bar{e}_t is a unit vector (either \bar{i} or \bar{j}) in a direction tangential to the surface of the step. Note that the term "integral equation" is used since the unknown function $\bar{\gamma}$ appears under the integral sign on the left-hand side of Eqn.(2.9). It can be shown, Hess and Smith (1967), and Wu (1976), that enforcement of the condition with vanishing tangential component of the velocity along the surface of the step as specified in Eqn.(2.9) implies that the normal component of the velocity at the corresponding location also vanishes.

As mentioned earlier in this chapter, image vortices have been introduced in the lower half plane. As a result, the vorticity field becomes anti-symmetry about X -axis. On the understanding that $\bar{\gamma}$ and $\bar{\omega}$ in the lower half plane can be expressed in terms of $-\bar{\gamma}$ and $-\bar{\omega}$ at the corresponding image point in the upper half plane, the integrand of two integrals in Eqn.(2.9) can be modified as shown in the following equation so that the range of integration, Γ and A , includes only the upper half plane.

$$\begin{aligned} & \frac{1}{2\pi} \int_{\Gamma} \left[\frac{\bar{\gamma}_q \times \bar{r}_{qp}}{|\bar{r}_{qp}|^2} + \frac{-\bar{\gamma}_q \times \bar{r}_{q-p}}{|\bar{r}_{q-p}|^2} \right] dl \cdot \bar{e}_t \\ & = \left\{ -\bar{i} - \frac{1}{2\pi} \iint_A \left[\frac{\bar{\omega}_o \times \bar{r}_{op}}{|\bar{r}_{op}|^2} + \frac{-\bar{\omega}_o \times \bar{r}_{o-p}}{|\bar{r}_{o-p}|^2} \right] dA \right\} \cdot \bar{e}_t \end{aligned} \quad (2.10)$$

where the point with the superscript "-" denotes the image of that point. In Cartesian coordinates, Eqn.(2.10) can be written as either

$$\begin{aligned} & \frac{1}{2\pi} \iint_{\Gamma} \gamma_q \left[\frac{y_p - y_q}{(x_p - x_q)^2 + (y_p - y_q)^2} - \frac{y_p + y_q}{(x_p - x_q)^2 + (y_p + y_q)^2} \right] dl \\ & = -1 - \frac{1}{2\pi} \iint_A \omega_o \left[\frac{y_p - y_o}{(x_p - x_o)^2 + (y_p - y_o)^2} - \frac{y_p + y_o}{(x_p - x_o)^2 + (y_p + y_o)^2} \right] dx_o dy_o \end{aligned} \quad (2.11a)$$

in which the point p is located at the horizontal surface of the step, i.e., $\bar{z}_i = \bar{i}$, or

$$\begin{aligned} & \frac{1}{2\pi} \iint_{\Gamma} \gamma_q \left[\frac{x_p - x_q}{(x_p - x_q)^2 + (y_p - y_q)^2} - \frac{x_p - x_q}{(x_p - x_q)^2 + (y_p + y_q)^2} \right] dl \\ &= -\frac{1}{2\pi} \iint_A \omega_o \left[\frac{x_p - x_o}{(x_p - x_o)^2 + (y_p - y_o)^2} - \frac{x_p - x_o}{(x_p - x_o)^2 + (y_p + y_o)^2} \right] dx_o dy_o \quad (2.11b) \end{aligned}$$

in which the point p is located at the vertical surface of the step, i.e., $\bar{z}_i = \bar{j}$, and dl is defined by

$$dl = \begin{cases} dx, & \text{if } \gamma_q \text{ is located at the horizontal surface of the step;} \\ dy, & \text{if } \gamma_q \text{ is located at the vertical surface of the step.} \end{cases}$$

Upon rearrangement, Eqns.(2.11a, b) can be expressed in the following form:

$$\gamma(S) - \int_{\Gamma} K(S, T) \gamma(T) dT = f(S) \quad (2.12)$$

where S and T are real variables along Γ , the nonhomogeneous term f and the kernel K are known while γ is to be determined. Since the range of the integration, Γ is finite, Eqn.(2.12) is then classified as the linear Fredholm integral equation of the second kind. Since the integral equation, Eqn.(2.12), cannot be solved in closed form, a recourse has to be taken to approximate methods. In this way, Eqn.(2.12) can be considered to be approximated as the limiting case of a system of linear algebraic equations. According to Fredholm's theorem, whether the solution to this system of equations is unique or has an infinite number of solutions depends on the determinant of the coefficient matrix of this system of equations. Since the derivation of this coefficient matrix involves the numerical coordinate system, the further discussion of the solution to this system will be resumed in the section on numerical formulation for the velocity field in Chapter 3. An analysis of these types of equations may be found in several books (Lovitt, 1950; Mikhlin, 1960; Kanwal, 1971; Greenberg, 1978).

In summary, the distribution of bound vorticity from Eqn.(2.10) and the given free vorticity field is substituted into Eqn.(2.7) to find \bar{V} . The resulting velocity field satisfies all the requirements of the problem, except the no-slip condition on the solid surface. Thus, it can be concluded that for a given distribution of the free vorticity outside the surface of the step, there exists a distribution of bound vorticity on the surface of the step such that their combined flow field will prevent the fluid from penetrating the solid surface.

Spatial Periodicity in the Flow Field Now, we consider the streamwise spatial periodicity in the fully developed flow, and follow a scheme similar to that developed by Cerrutti (1984). Under this condition, the flow leaving at the point c is considered to reenter the primary computational domain at the point b (referring to Figure 2.3). In this way, the flow boundary conditions are spatially periodic. It is recognized that by enforcing this spatial periodicity in the flow field, it is impossible for random perturbations to occur in only one or several parts of the flow region. However, this enables the computations to be carried out for the entire unbounded flow domain in terms of the flow quantities only in a smaller domain (e.g., the primary computational domain), and it is also felt that the consequent reduction in the size of the flow region was necessary to make the computation costs manageable.

In view of Eqn.(2.7), the range of the integration A in the first integral is limited to the region of non-zero vorticity; nevertheless, it still covers a flow field of infinite extent in the streamwise direction. The line contour Γ on which the bound vorticity is distributed also includes surfaces of an infinite number of steps. However, because the flow field is considered to be spatially periodic, the

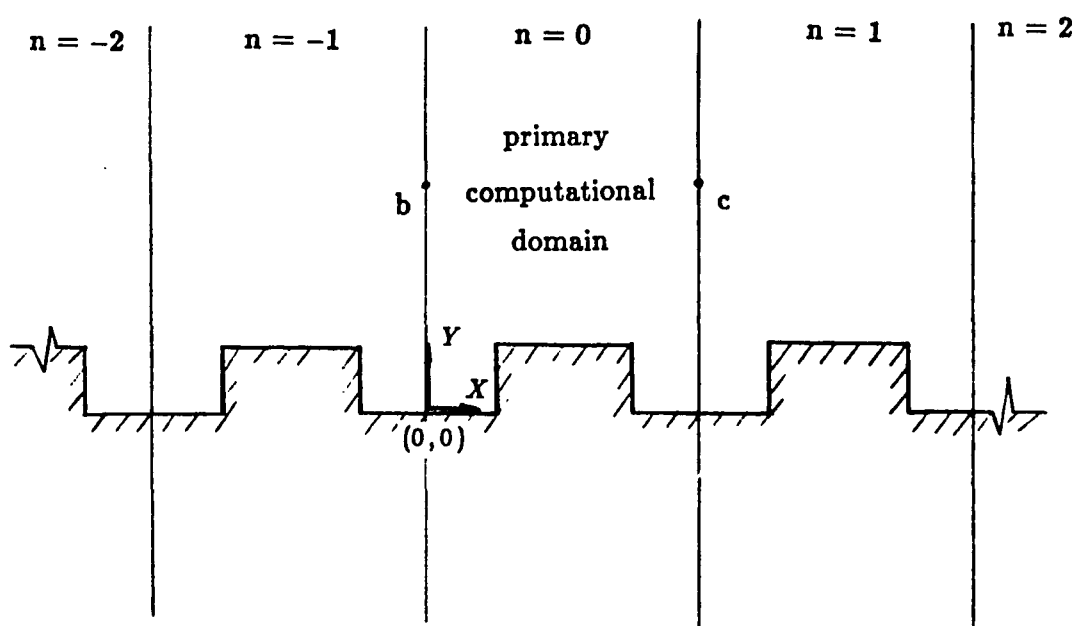


Figure 2.3 Flow geometry with the primary computational domain and the spatially repeating regions shown.

integrals in Eqn.(2.7) may be recast into an infinite series of single integrals as follows:

$$\bar{V}(r_p, t) = \bar{i} + \frac{1}{2\pi} \sum_{n=-\infty}^{\infty} \iint_{A^n} \frac{\bar{\omega}_o^n \times \bar{r}_{op}^n}{|\bar{r}_{op}^n|^2} dA + \frac{1}{2\pi} \sum_{n=-\infty}^{\infty} \int_{\Gamma^n} \frac{\bar{\gamma}_q^n \times \bar{r}_{qp}^n}{|\bar{r}_{qp}^n|^2} dl \quad (2.13)$$

where “n” denotes the nth spatially repeating region as shown in Figure 2.3. Note that the two summation signs, which are in front of the integrals in the above equation, result from the spatial periodicity in the flow field and the presence of an infinite number of periodic steps. For the spatially periodic flow field, the following conditions are obtained:

$$\bar{\omega} = \bar{\omega}^n \quad (2.14a)$$

$$\bar{\gamma} = \bar{\gamma}^n \quad (2.14b)$$

where $n = 0, \pm 1, \pm 2, \dots, \pm \infty$, and $\bar{\omega}$ and $\bar{\gamma}$ are calculated in the region with the index 0, which is denoted as the primary computational domain. Substitution of Eqns.(2.14a, b) into Eqn.(2.13) yields

$$\bar{V}(r_p, t) = \bar{i} + \frac{1}{2\pi} \sum_{n=-\infty}^{\infty} \iint_{A^n} \frac{\bar{\omega}_o \times \bar{r}_{op}^n}{|\bar{r}_{op}^n|^2} dA + \frac{1}{2\pi} \sum_{n=-\infty}^{\infty} \int_{\Gamma^n} \frac{\bar{\gamma}_q \times \bar{r}_{qp}^n}{|\bar{r}_{qp}^n|^2} dl. \quad (2.15)$$

Note that the point p where the velocity is desired is always considered located in the primary computational domain. For convenience, the following definitions are made:

$$\bar{V}_b(r_p, t) \equiv \frac{1}{2\pi} \sum_{n=-\infty}^{\infty} \int_{\Gamma^n} \frac{\bar{\gamma}_q \times \bar{r}_{qp}^n}{|\bar{r}_{qp}^n|^2} dl \quad (2.16a)$$

$$\bar{V}_f(r_p, t) \equiv \frac{1}{2\pi} \sum_{n=-\infty}^{\infty} \iint_{A^n} \frac{\bar{\omega}_o \times \bar{r}_{op}^n}{|\bar{r}_{op}^n|^2} dA \quad (2.16b)$$

in which the subscripts “*b*” and “*f*” indicate the contribution due to the distribution of bound vorticity and the free vorticity field, respectively. Using the notation defined by the above expressions, Eqn.(2.15) becomes

$$\bar{V}(r_p, t) = \bar{i} + \bar{V}_f(r_p, t) + \bar{V}_b(r_p, t). \quad (2.17)$$

By interchanging orders of summation and integration in Eqn.(2.15), we obtain

$$\bar{V}(r_p, t) = \bar{i} + \frac{1}{2\pi} \iint_A \sum_{n=-\infty}^{\infty} \frac{\bar{\omega}_o \times \bar{r}_{op}^n}{|\bar{r}_{op}^n|^2} dA + \frac{1}{2\pi} \int_{\Gamma} \sum_{n=-\infty}^{\infty} \frac{\bar{\gamma}_q \times \bar{r}_{qp}^n}{|\bar{r}_{qp}^n|^2} dl. \quad (2.18)$$

Note that the range of integration A^n and Γ^n has been changed to A and Γ , which is now confined only in the primary computational domain. However, the calculation of position vector \bar{r} , which still involves inter-spatially-repeating regions, should be appropriately accounted for.

Furthermore, Eqn.(2.18) can be expressed as

$$\bar{V}(r_p, t) = \bar{i} + \frac{1}{2\pi} \iint_A \omega_o \left[\sum_{n=-\infty}^{\infty} \frac{\bar{k} \times \bar{r}_{op}^n}{|\bar{r}_{op}^n|^2} \right] dA + \frac{1}{2\pi} \int_{\Gamma} \gamma_q \left[\sum_{n=-\infty}^{\infty} \frac{\bar{k} \times \bar{r}_{qp}^n}{|\bar{r}_{qp}^n|^2} \right] dl. \quad (2.19)$$

It can be seen that the terms inside the brackets in the above equation are in the same form. Physically, they represent the flow field induced by an infinite array of row vortices with unit strength and the periodicity length a as shown in Figure 2.4.

Now, we consider the term in the first bracket in Eqn.(2.19) and note that in the Cartesian coordinate system, the position vector \bar{r} corresponding to each spatially repeating region can be written as

$$\begin{aligned} \bar{r}_{op}^{[0]} &= x_p \bar{i} + y_p \bar{j} \\ \bar{r}_{op}^{[1]} &= (x_p - a) \bar{i} + y_p \bar{j} \\ \bar{r}_{op}^{[-1]} &= (x_p + a) \bar{i} + y_p \bar{j} \\ &\vdots \end{aligned}$$

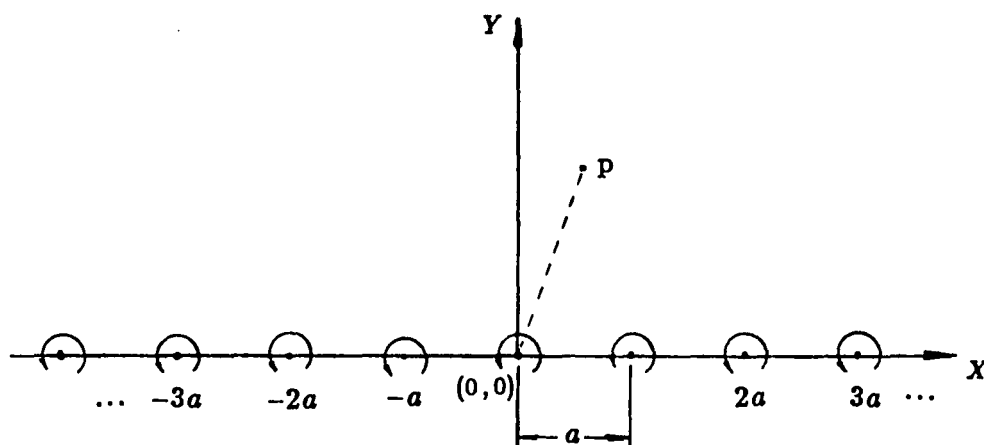


Figure 2.4 Representation of an infinite row of vortices.

In view of the above expressions, the following results are easily derived.

$$\begin{aligned} |\bar{r}_{op}^{[0]}|^2 &= x_p^2 + y_p^2 \\ |\bar{r}_{op}^{[1]}|^2 &= (x_p - a)^2 + y_p^2 \\ |\bar{r}_{op}^{[-1]}|^2 &= (x_p + a)^2 + y_p^2 \\ &\vdots \end{aligned}$$

and

$$\begin{aligned} \frac{\bar{k} \times \bar{r}_{op}^{[0]}}{|\bar{r}_{op}^{[0]}|^2} &= \frac{x_p \bar{j} - y_p \bar{i}}{x_p^2 + y_p^2} \\ \frac{\bar{k} \times \bar{r}_{op}^{[1]}}{|\bar{r}_{op}^{[1]}|^2} &= \frac{(x_p - a) \bar{j} - y_p \bar{i}}{(x_p - a)^2 + y_p^2} \\ \frac{\bar{k} \times \bar{r}_{op}^{[-1]}}{|\bar{r}_{op}^{[-1]}|^2} &= \frac{(x_p + a) \bar{j} - y_p \bar{i}}{(x_p + a)^2 + y_p^2} \\ &\vdots \end{aligned}$$

Finally, the quantity in the bracket in Eqn.(2.19) becomes

$$\begin{aligned} \sum_{n=-\infty}^{n=\infty} \frac{\bar{k} \times \bar{r}_{op}^n}{|\bar{r}_{op}^n|^2} &= \left[-\frac{y_p}{x_p^2 + y_p^2} - \frac{y_p}{(x_p - a)^2 + y_p^2} - \frac{y_p}{(x_p + a)^2 + y_p^2} - \dots \right] \bar{i} \\ &\quad + \left[\frac{x_p}{x_p^2 + y_p^2} + \frac{x_p - a}{(x_p - a)^2 + y_p^2} + \frac{x_p + a}{(x_p + a)^2 + y_p^2} + \dots \right] \bar{j} \\ &= - \left\{ \frac{y_p}{y_p^2 + x_p^2} + \sum_{n=1}^{\infty} \left[\frac{y_p}{y_p^2 + (x_p - na)^2} + \frac{y_p}{y_p^2 + (x_p + na)^2} \right] \right\} \bar{i} \\ &\quad + \left\{ \frac{x_p}{y_p^2 + x_p^2} + \sum_{n=1}^{\infty} \left[\frac{x_p - na}{y_p^2 + (x_p - na)^2} + \frac{x_p + na}{y_p^2 + (x_p + na)^2} \right] \right\} \bar{j}. \quad (2.20) \end{aligned}$$

To simply further, we introduce the following expressions for the complex variable z :

$$z = x + iy, \quad z + na = (x + na) + iy \quad \text{and} \quad z - na = (x - na) + iy$$

where $\mathfrak{t} = \sqrt{-1}$. Substitution of the above expressions into Eqn.(2.20), the equation can be expressed in terms of z as

$$\begin{aligned} \sum_{n=-\infty}^{n=\infty} \frac{\bar{k} \times \bar{r}_{op}^n}{|\bar{r}_{op}^n|^2} &= \Im \left\{ \frac{1}{z_p} + \sum_{n=1}^{\infty} \left(\frac{1}{z_p - na} + \frac{1}{z_p + na} \right) \right\} \bar{\mathfrak{i}} \\ &+ \Re \left\{ \frac{1}{z_p} + \sum_{n=1}^{\infty} \left(\frac{1}{z_p - na} + \frac{1}{z_p + na} \right) \right\} \bar{\mathfrak{j}} \end{aligned} \quad (2.21)$$

where “ \Im ” and “ \Re ” denote the imaginary and real parts of the argument in two curly brackets. Furthermore, the argument can be simplified as follows:

$$\begin{aligned} &\frac{1}{z_p} + \sum_{n=1}^{\infty} \left(\frac{1}{z_p - na} + \frac{1}{z_p + na} \right) \\ &= \frac{1}{z_p} + \sum_{n=1}^{\infty} \frac{2z_p}{z_p^2 - n^2 a^2} \\ &= \frac{d}{dz_p} \left[\ln z_p + \sum_{n=1}^{\infty} \ln(z_p^2 - n^2 a^2) \right] \\ &= \frac{d}{dz_p} \left\{ \ln \left[z_p(z_p^2 - a^2)(z_p^2 - 2^2 a^2) \dots (z_p^2 - n^2 a^2) \dots \right] \right\} \\ &= \frac{d}{dz_p} \left\{ \ln \left[\frac{\pi z_p}{a} \left(1 - \frac{z_p^2}{a^2}\right) \left(1 - \frac{z_p^2}{2^2 a^2}\right) \dots \left(1 - \frac{z_p^2}{n^2 a^2}\right) \dots \right] \right. \\ &\quad \left. + \ln \left[\frac{a}{\pi} \cdot a^2 \cdot 2^2 a^2 \dots n^2 a^2 \dots \right] \right\} \\ &= \frac{d}{dz_p} \left\{ \ln \left[\frac{\pi z_p}{a} \left(1 - \frac{z_p^2}{a^2}\right) \left(1 - \frac{z_p^2}{2^2 a^2}\right) \dots \left(1 - \frac{z_p^2}{n^2 a^2}\right) \dots \right] \right\} \end{aligned} \quad (2.22)$$

since the derivative of second term, which is a constant, is zero.

As shown by Hobson (1918), for a complex variable z' , $\sin z'$ can be expressed as an infinite product in the following form,

$$\sin z' = z' \left(1 - \frac{z'^2}{\pi^2}\right) \left(1 - \frac{z'^2}{2^2 \pi^2}\right) \dots \left(1 - \frac{z'^2}{n^2 \pi^2}\right) \dots$$

By letting $z' = \pi z_p/a$, the infinite series in the above equation can be written as

$$\sin \frac{\pi z_p}{a} = \frac{\pi z_p}{a} \left(1 - \frac{z_p^2}{a^2}\right) \left(1 - \frac{z_p^2}{2^2 a^2}\right) \dots \left(1 - \frac{z_p^2}{n^2 a^2}\right) \dots$$

Substitution of the above equation into Eqn.(2.22) yields

$$\begin{aligned} \frac{1}{z_p} + \sum_{n=1}^{\infty} \left(\frac{1}{z_p - na} + \frac{1}{z_p + na} \right) &= \frac{d}{dz_p} \left[\ln \left(\sin \frac{\pi z_p}{a} \right) \right] \\ &= \frac{\pi \cos \frac{\pi z_p}{a}}{a \sin \frac{\pi z_p}{a}} \\ &= \frac{\pi}{a} \cot \frac{\pi z_p}{a}. \end{aligned}$$

In terms of the real and imaginary parts, the above equation is expressed as

$$\begin{aligned} \frac{1}{z_p} + \sum_{n=1}^{\infty} \left(\frac{1}{z_p - na} + \frac{1}{z_p + na} \right) \\ = \left[\frac{\pi}{a} \frac{\sin \frac{2\pi x_p}{a}}{\cosh \frac{2\pi y_p}{a} - \cos \frac{2\pi x_p}{a}} \right] - \left[\frac{\pi}{a} \frac{\sinh \frac{2\pi y_p}{a}}{\cosh \frac{2\pi y_p}{a} - \cos \frac{2\pi x_p}{a}} \right] \hat{i}. \end{aligned} \quad (2.23)$$

In view of Eqn.(2.21), it follows that

$$\begin{aligned} \sum_{n=-\infty}^{n=\infty} \frac{\bar{k} \times \bar{r}_{op}^n}{|\bar{r}_{op}^n|^2} &= - \left[\frac{\pi}{a} \frac{\sinh \frac{2\pi y_p}{a}}{\cosh \frac{2\pi y_p}{a} - \cos \frac{2\pi x_p}{a}} \right] \bar{i} \\ &+ \left[\frac{\pi}{a} \frac{\sin \frac{2\pi x_p}{a}}{\cosh \frac{2\pi y_p}{a} - \cos \frac{2\pi x_p}{a}} \right] \bar{j}. \end{aligned} \quad (2.24)$$

Note that Eqn.(2.24) is derived based on the case where the row of vortices lies on the X -axis and one of the vortices is located at the origin, as shown in Figure 2.4.

To apply this to our model, we need to consider the case of row vortices arranged as shown in Figure 2.5. For this purpose, the expression on the right-hand side of Eqn.(2.24) need to be modified and this can be done by simply replacing x_p

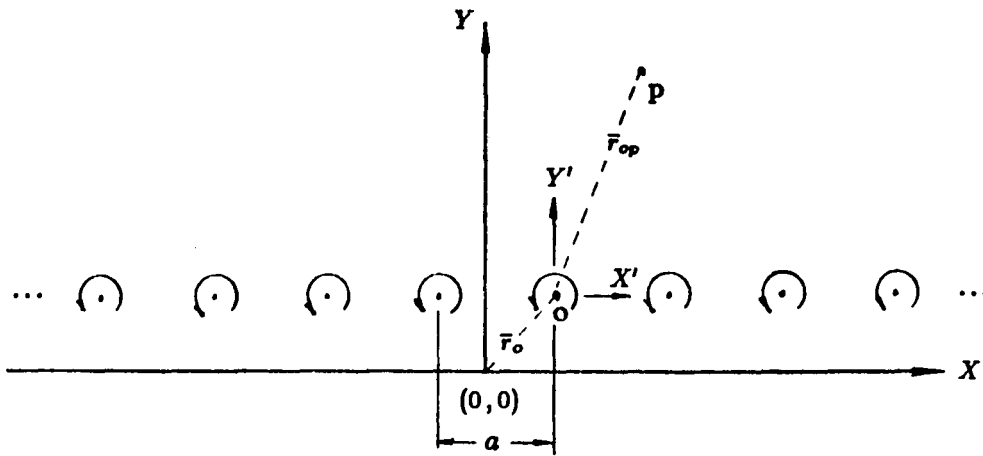


Figure 2.5 Representation of an infinite row of vortices offset from X axis.

and y_p in Eqn.(2.24) with $x_p - x_o$ and $y_p - y_o$. The result is

$$\sum_{n=-\infty}^{n=\infty} \frac{\vec{k} \times \vec{r}_{op}^n}{|\vec{r}_{op}^n|^2} = - \left[\frac{\pi}{a} \frac{\sinh \frac{2\pi(y_p - y_o)}{a}}{\cosh \frac{2\pi(y_p - y_o)}{a} - \cos \frac{2\pi(x_p - x_o)}{a}} \right] \vec{i} + \left[\frac{\pi}{a} \frac{\sin \frac{2\pi(x_p - x_o)}{a}}{\cosh \frac{2\pi(y_p - y_o)}{a} - \cos \frac{2\pi(x_p - x_o)}{a}} \right] \vec{j} \quad (2.25)$$

According to Eqns.(2.16b), (2.19) and (2.25), the velocity at the point p due to the free vorticity field can be expressed in terms of two scalar velocity components u_f and v_f as

$$\vec{V}_f(r_p, t) = u_f \vec{i} + v_f \vec{j} \quad (2.26)$$

in which \vec{j} is the unit vector in the Y direction, and u_f and v_f are given as

$$u_f = -\frac{1}{2a} \iint_A \left[\frac{\omega_o \sinh \frac{2\pi(y_p - y_o)}{a}}{\cosh \frac{2\pi(y_p - y_o)}{a} - \cos \frac{2\pi(x_p - x_o)}{a}} \right] dx_o dy_o \quad (2.26a)$$

$$v_f = \frac{1}{2a} \iint_A \left[\frac{\omega_o \sin \frac{2\pi(x_p - x_o)}{a}}{\cosh \frac{2\pi(y_p - y_o)}{a} - \cos \frac{2\pi(x_p - x_o)}{a}} \right] dx_o dy_o. \quad (2.26b)$$

In like manner, a similar set of expressions may be obtained for the velocity due to the distribution of bound vorticity. The result is

$$\vec{V}_b(r_p, t) = u_b \vec{i} + v_b \vec{j} \quad (2.27)$$

in which

$$u_b = -\frac{1}{2a} \int_{\Gamma} \left[\frac{\gamma_q \sinh \frac{2\pi(y_p - y_q)}{a}}{\cosh \frac{2\pi(y_p - y_q)}{a} - \cos \frac{2\pi(x_p - x_q)}{a}} \right] dl \quad (2.27a)$$

$$v_b = \frac{1}{2a} \int_{\Gamma} \left[\frac{\gamma_q \sin \frac{2\pi(x_p - x_q)}{a}}{\cosh \frac{2\pi(y_p - y_q)}{a} - \cos \frac{2\pi(x_p - x_q)}{a}} \right] dl. \quad (2.27b)$$

The Vorticity-Stream Function Method

In this method, we introduce the so-called stream function ψ , defined so as to satisfy the law of conservation of mass flow, i.e., the equation of continuity. In incompressible flow, the equation of continuity, in vector form, is

$$\nabla \cdot \bar{V} = 0 \quad (2.28)$$

In two dimensions and using the Cartesian coordinate system, the above equation becomes

$$\frac{\partial u}{\partial x} + \frac{\partial v}{\partial y} = 0 \quad (2.29)$$

For two-dimensional flow of an incompressible fluid, the stream function has a comparatively simple relation to the velocity components. By introducing the non-dimensional variable for the stream function defined as

$$\psi^* = \frac{\psi}{hU_\infty} \quad (2.30)$$

and the use of Eqn.(2.6), the dimensionless stream function $\psi^*(x, y)$ is related to the velocity components by

$$u = \frac{\partial \psi}{\partial y} \quad \text{and} \quad v = -\frac{\partial \psi}{\partial x} \quad (2.31)$$

in which the asterisk "*" representing non-dimensionalized variable has been omitted. It is easy to show that the velocity components from the above equation satisfy the equation of continuity, Eqn.(2.29).

Since a given distribution of vorticity outside the surface of the solid body determines a unique velocity field with zero normal relative velocity at the solid surface, it is anticipated that values of the stream function at any instant of time could be determined based on the distribution of vorticity at the corresponding instant. To establish the relationship between ψ and ω , Eqn.(2.31) is

substituted into Eqn.(2.2) which results in a second order elliptic partial differential equation,

$$\frac{\partial^2 \psi}{\partial x^2} + \frac{\partial^2 \psi}{\partial y^2} = -\omega. \quad (2.32)$$

This equation is referred to as the stream function equation, which is the kinematic relationship between the distribution of the stream function and the vorticity. Note that Eqn.(2.32) represents the boundary value problem with the prescribed boundary conditions as follows:

$$\psi|_{\omega \neq 0} = 0 \quad (2.33a)$$

$$\frac{\partial \psi}{\partial y} \Big|_{y \rightarrow \infty} = 1 \quad (2.33b)$$

$$\psi(x + na, y) = \psi(x, y) \quad (2.33c)$$

in which n is an integer. To determine the velocity field, Eqn.(2.32) with the above prescribed boundary conditions is solved first. Note that since the solution of the velocity field involves solving an equation of Poisson's type for the stream function, this requires that the computation be performed in the whole disturbed flow field, which includes rotational and irrotational zones, instead of in the region of non-zero vorticity. Once the value of the stream function is known, X and Y components of the velocity can be calculated according to Eqn.(2.31).

Up to this point, the analytical development has been purely kinematical. That is, the analysis has been confined only to the motions in a flow field without regard to the forces producing them. To complete our knowledge on the flow field evolving with respect to time, we must understand dynamical relations describing the motion of fluid particles with the response to external influences. In addition, it is also instructive to understand the role that the viscosity of the fluid plays in preventing the slippage of the fluid over the solid surface and in the

diffusion of vorticity into the flow field. These topics are covered in the following sections.

Vorticity Dynamics

The motion of viscous flows of an incompressible isotropic Newtonian fluid with constant ν is governed by the equation of motion, known as the Navier-Stokes equations, and the equation of continuity. The vector form of the Navier-Stokes equations, in dimensional form, is

$$\frac{\partial \bar{V}}{\partial t} + (\bar{V} \cdot \nabla) \bar{V} = -\frac{1}{\rho} \nabla p + \nu \nabla^2 \bar{V} \quad (2.34)$$

in which p is the pressure, t is the time, and ρ and ν are the mass density and kinematic viscosity of the fluid, respectively. This equation equates the rate of change of momentum of a selected element of fluid and the sum of all forces acting on that element of fluid.

Eliminating pressure by taking the curl ($\nabla \times$) of Eqn.(2.34) and with the aid of the expression, Eqn.(2.1), the Navier-Stokes equations becomes

$$\frac{\partial \bar{\omega}}{\partial t} + (\bar{V} \cdot \nabla) \bar{\omega} - (\bar{\omega} \cdot \nabla) \bar{V} = \nu \nabla^2 \bar{\omega}.$$

In two dimensions, the third term in the above equation is identically zero and the equation is then reduced to one component about the Z -axis (i.e., $\bar{\omega} = \omega \bar{k}$).

Thus,

$$\frac{\partial \omega}{\partial t} + (\bar{V} \cdot \nabla) \omega = \nu \nabla^2 \omega \quad (2.35a)$$

or in shorthand form,

$$\frac{D\omega}{Dt} = \nu \nabla^2 \omega. \quad (2.35b)$$

Equation (2.35a) or (2.35b) is referred to as the vorticity transport equation. It states that the substantive variation of vorticity, which consists of the local and

convective terms is equal to the rate of diffusion of vorticity, which results from tangential shear stresses due to the fluid viscosity. Note that this equation is nonlinear in the convective term, since \bar{V} is functions of the dependent variable, ω .

By vector algebra, the convective term, $(\bar{V} \cdot \nabla)\omega$, in Eqn.(2.35a) can be expressed as

$$\begin{aligned}\nabla \cdot (\bar{V} \omega) &= (\bar{V} \cdot \nabla) \omega + \omega (\nabla \cdot \bar{V}) \\ &= (\bar{V} \cdot \nabla) \omega.\end{aligned}$$

The continuity equation has been used in the second quantity. Thus, we may replace $(\bar{V} \cdot \nabla)\omega$ with $\nabla \cdot (\bar{V} \omega)$ in Eqn.(2.35a) to obtain the conservative form of the vorticity transport equation, that is

$$\frac{\partial \omega}{\partial t} + \nabla \cdot (\bar{V} \omega) = \nu \nabla^2 \omega \quad (2.36)$$

Using the dimensionless variables defined in Eqn.(2.6) and the following definition for the Reynolds number:

$$Re = \frac{U_\infty h}{\nu}, \quad (2.37)$$

Eqn.(2.36) is then written in terms of dimensionless variables as follows:

$$\frac{\partial \omega}{\partial t} + \nabla \cdot (\bar{V} \omega) = \frac{1}{Re} \nabla^2 \omega. \quad (2.38)$$

In Cartesian coordinates, the above equation becomes

$$\frac{\partial \omega}{\partial t} + \frac{\partial u \omega}{\partial x} + \frac{\partial v \omega}{\partial y} = \frac{1}{Re} \left(\frac{\partial^2 \omega}{\partial x^2} + \frac{\partial^2 \omega}{\partial y^2} \right). \quad (2.39)$$

An equation is said to possess the conservative property if it preserves the integral conservative relations of the continuum equation (Roache, 1973). To

illustrate this, we integrate Eqn.(2.38) over some space region R . With the aid of the Gauss divergence theorem, we obtain

$$\frac{\partial}{\partial t} \int_R \omega \, dR = - \int_{\partial R} (\bar{V}\omega) \cdot \bar{n} \, ds + \frac{1}{Re} \int_{\partial R} (\nabla\omega) \cdot \bar{n} \, ds \quad (2.40)$$

where ∂R is the boundary of R , \bar{n} is the unit normal vector (positive outward) and ds is the differential element of the boundary ∂R . The above equation states that the rate of accumulation of ω in R is identically equal to the net flux of ω across ∂R into R by convection and diffusion. Therefore, Eqn.(2.38) or (2.39) satisfies the above integral relation identically over any finite region of space and not simply at points in the fluid, as implied by Eqn.(2.35a). This point will be recalled when the numerical formulation is presented in Chapter 3.

Initially, the entire flow field is at rest and vorticity is zero everywhere. At $t = 0^+$, a uniform onset flow with constant velocity, $U_\infty \bar{i}$, is impulsively started. At this instant of time, the fluid slips tangentially along the solid surface as though it lacks viscosity. Therefore, at time $t = 0^+$, the velocity field can be determined through the use of the potential flow theory, or from the previously developed expressions with $\omega = 0$. This tangential component of the velocity along the solid surface violates the surface-adherence condition for viscous flows, and it should not be allowed to persist in time. In this case, we deduce that exactly enough vorticity must have been created at the solid surface during the sufficiently small time interval, Δt , so that the velocity field due to that vorticity combines with that previously determined to give zero slip. This vorticity first enter the fluid by diffusion, which dominates over convection near to the solid surface, and tends to spread the vorticity created at any instant of time over the cell element adjacent to the solid surface. From there, the vorticity is transported and redistributed over surrounding cell elements through convection and diffusion.

in accordance with Eqn.(2.39). Note that vorticity is neither created nor destroyed in the flow field, and that convection and diffusion provide a mechanism leading to a redistribution of the vorticity field which no longer corresponds to zero slip at the solid surface. This requires the generation of new vorticity, which may be in a different direction from that originally created. This in turn is convected downstream, a redistribution of which leads to still further vorticity production at the surface. Since the treatment of vorticity production at the solid surface is different in the VVI and the VSF methods, we shall discuss them separately as below.

The Vorticity-Velocity Induction Method

As pointed out by Lighthill (Rosenhead,1963), the gradient of vorticity along the normal to the solid surface times the fluid viscosity, $\nu \partial \omega / \partial n$, integrated over a small time increment is equal to the vorticity produced at the solid surface. Since the tangential slip velocity, \bar{U}_{slip} , determines the vorticity production, we can write in dimensional form as

$$\nu \int_t^{t+\Delta t} \left. \frac{\partial \omega}{\partial n} \right|_{wall} dt' = \pm \bar{U}_{slip}(t) \cdot \bar{e}_t \quad (2.41)$$

where \bar{e}_t , as defined earlier, is the unit vector (either \bar{i} or \bar{j}) in a direction tangential to the surface of the grooved wall. The ambiguous sign will be discussed shortly. For convenience, the following definition is made,

$$U_{slip} = \bar{U}_{slip}(t) \cdot \bar{e}_t \quad (2.42)$$

Using the dimensionless variables defined in Eqns.(2.6), (2.37) and the above expression, Eqn.(2.41), in dimensionless form, becomes

$$\frac{1}{Re} \int_{t^*}^{t^*+\Delta t^*} \left. \frac{\partial \omega^*}{\partial n^*} \right|_{wall} dt^{*'} = \pm U_{slip}^* \quad (2.43)$$

This important result points out that the local slip velocity at any instant of time t determines the amount of new free vorticity per unit area of the surface which enters the fluid in the subsequent time increment Δt . The only restriction is that Δt be sufficiently small that this new vorticity is confined to a very thin layer adjacent to the surface. As a result, Eqn.(2.43) becomes an essential boundary condition in the solution of Eqn.(2.39) using the VVI method.

In applying Eqn.(2.43), the sign convention adopted here is important to keep in mind. For a positive slip velocity on the upper surface of the bottom wall and the exterior side of the horizontal and left-hand vertical surfaces of the step, negative (clockwise) free vorticity is generated, and the positive sign is used. On the other hand, a positive (i.e., upward directed) slip velocity on the exterior side of the right-hand vertical surface of the step generates positive free vorticity, and the negative sign is used. The sign of the slip velocity is thus important in determining which portions of the surface act as vorticity sources and which act as vorticity sinks.

Along the surface of the step, the magnitude of \bar{U}_{slip} is equal to the strength of the bound vorticity at its corresponding location. However, the sign, as explained above, will depend on the surface at which the bound vorticity is located. On the horizontal and left-hand vertical surfaces of the step, negative (clockwise) bound vorticity corresponds to positive slip velocity (i.e., $U_{slip} = -\gamma$), and negative free vorticity is produced there. On the right-hand vertical surface, positive bound vorticity produces positive slip velocity (i.e., $U_{slip} = \gamma$) and thus positive free vorticity. On the other hand, since no bound vorticity is distributed on the surface of the bottom wall, \bar{U}_{slip} at this surface is determined directly from

Eqn.(2.7). A positive slip velocity there produces negative free vorticity, just as it does on the horizontal surface of the step.

To summarize, at each instant of time, the distribution of bound vorticity, $\bar{\gamma}$, is determined from Eqn.(2.10). This gives \bar{U}_{slip} on the surface of the step. On the bottom wall, \bar{U}_{slip} is obtained from Eqn.(2.7) directly for $Y = 0$. If \bar{U}_{slip} is nonzero, new free vorticity departs from the surface into the fluid over the next time increment, Δt , according to Eqn.(2.43). If the remaining free vorticity of the fluid were frozen in time, the wall slip velocity would be reduced to zero. Since free vorticity actually changes throughout the fluid in the time interval Δt , \bar{U}_{slip} must be computed at the next higher time level, and so on and so forth.

The Vorticity-Stream Function Method

In this method, the vorticity production along the solid surface is determined through the calculation of the wall vorticity exactly at the surface. For this purpose, the Stokes theorem is employed, which is expressed by

$$\oint_C \bar{V} \cdot d\bar{l} = \iint_A (\nabla \times \bar{V}) \cdot d\bar{A} \quad (2.44)$$

where $d\bar{A} = dA\bar{k}$. The above equation states that the surface integral of the normal component of the curl of the velocity vector taken over any surface, A , is equal to the line integral of the tangential component of the velocity around the periphery of the surface, C . The term on the left-hand side of Eqn.(2.44) is defined as the "circulation", and the integrand of the integral on the right-hand side of the equation is the component of the vorticity normal to the flow field. Using the notation of the vorticity vector, Eqn.(2.1), Eqn.(2.44) is rewritten as

$$\iint_A \omega dA = \oint_C \bar{V} \cdot d\bar{l}. \quad (2.45)$$

At each instant of time, the value of wall vorticity is determined according to Eqn.(2.45). If the value of the wall vorticity is different from the value a small distance above the wall, new free vorticity enters the flow field by diffusion over the next time increment. Consequently, Eqn.(2.45) becomes an essential boundary condition in solving Eqn.(2.39) using the VSF method.

Finally, the vorticity transport equation, Eqn.(2.39), subjected to the initial condition that the vorticity field be identically zero and the boundary conditions described above, is solved to determine the vorticity field. Once the vorticity field is known, the velocity field can be determined following the procedures discussed in the preceding section. This cyclic procedure is then repeated for each time step to obtain the complete features of the flow field.

Drag Coefficient

When a solid body is immersed in a fluid flow, experience tell us that the flowing fluid exerts a force on the surface of the immersed body. The component of force parallel to the direction of the fluid motion and acting against the fluid movement is called drag F_D . In general, drag is the sum of friction (shear) drag F_{Df} due to the boundary layer flow on the surface and the form (pressure) drag F_{Dp} due to pressure differences, and the magnitude of this depends on the form of the submerged object. Thus, to find F_D , it is necessary to calculate the pressure p_o and the viscous shear stress τ_o on every element at the surface and then to integrate them over the entire surface. In dimensional form, this is represented by

$$F_D = F_{Df} + F_{Dp} \quad (2.46)$$

in which F_{Df} and F_{Dp} are determined as

$$F_{Df} = \int_S \tau_o (\bar{e}_t \cdot \bar{e}_d) dl \quad (2.46a)$$

$$F_{Dp} = \int_S p_o (\bar{e}_n \cdot \bar{e}_d) dl \quad (2.46b)$$

where the range of integration, S , is the line contour along the surface of the grooved wall, \bar{e}_t and \bar{e}_n are the unit vectors in the direction tangential and normal to S , respectively, and \bar{e}_d is the unit vector in the direction of the onset flow. Note that a unit depth is taken in the spanwise direction.

In practice, drag is customarily expressed in the non-dimensional form. For this purposes, the following dimensionless variables are introduced:

$$r^* = \frac{\tau}{\frac{1}{2} \rho U_\infty^2} \quad (2.47a)$$

$$p^* = \frac{p}{\frac{1}{2} \rho U_\infty^2} \quad (2.47b)$$

With the aid of the above expressions and Eqn.(2.6), Eqns.(2.46a, b) are then written in dimensionless form as follows:

$$C_D = C_{Df} + C_{Dp} \quad (2.48)$$

in which C_D , C_{Df} and C_{Dp} are referred to as the total drag, friction drag and pressure drag coefficients, respectively, and they are defined as

$$C_D = \frac{F_D}{\frac{1}{2} \rho h U_\infty^2} \quad (2.48a)$$

$$\begin{aligned} C_{Df} &= \frac{F_{Df}}{\frac{1}{2} \rho h U_\infty^2} \\ &= \int_S r_o^* (\bar{e}_t \cdot \bar{e}_d) dl^* \end{aligned} \quad (2.48b)$$

$$\begin{aligned} C_{Dp} &= \frac{F_{Dp}}{\frac{1}{2} \rho h U_\infty^2} \\ &= \int_S p_o^* (\bar{e}_n \cdot \bar{e}_d) dl^* \end{aligned} \quad (2.48c)$$

Friction Drag Coefficient

The viscous shear stress at the solid surface may be evaluated through Newton's law of friction, that is

$$\tau_o = \mu \left. \frac{\partial u}{\partial n} \right|_w \quad (2.49)$$

where \bar{n} is the unit vector normal to the surface, and μ is defined as the dynamic viscosity, which is related to kinematic viscosity ν by $\nu = \mu/\rho$. Recall from Eqn.(2.2) that, vorticity, in the Cartesian coordinates, is given by

$$\omega = \frac{\partial v}{\partial x} - \frac{\partial u}{\partial y}$$

Along the horizontal surface, $\partial v/\partial x = 0$ and $\partial/\partial n = \partial/\partial y$, thus

$$\omega = -\left. \frac{\partial u}{\partial y} \right|_w \quad \text{and} \quad \tau_o = \mu \left. \frac{\partial u}{\partial y} \right|_w \quad (2.50)$$

Consequently, a relationship between τ_o and ω can be deduced which is

$$\tau_o = -\mu\omega \quad (2.51)$$

Using the dimensionless variables defined in Eqns.(2.6), (2.37) and (2.47a), the above equation in dimensionless form is found to be

$$\tau_o^* = -\frac{2}{Re} \omega^* \quad (2.52)$$

Note that the same expression as Eqn.(2.52) is found when the analysis is performed along the left-hand vertical surface of the step. However, the above expression with a different sign is obtained when the analysis is made along the right-hand vertical surface of the step. Since ω^* is either known directly from the solution or can be expressed in terms of the known quantities such as velocity

and vorticity, τ_o^* , therefore, can be determined. Once the distribution of τ_o^* is known, C_{Df} can be determined according to Eqns.(2.48b)

Pressure Drag Coefficient

The pressure distribution along the surface can be obtained directly from the Navier-Stokes equations, Eqn.(2.34). Using the Cartesian notation, the X component of Eqn.(2.34) can be written as

$$\frac{\partial u}{\partial t} + u \frac{\partial u}{\partial x} + v \frac{\partial u}{\partial y} = -\frac{1}{\rho} \frac{\partial p}{\partial x} + \nu \left(\frac{\partial^2 u}{\partial x^2} + \frac{\partial^2 u}{\partial y^2} \right). \quad (2.53)$$

Along the surface, $u = v = 0$, therefore, we obtain

$$\frac{1}{\rho} \frac{\partial p_o}{\partial x} = \nu \frac{\partial^2 u}{\partial y^2} \Big|_w. \quad (2.54)$$

In view of Eqn.(2.50), the above equation can be written as

$$\frac{1}{\rho} \frac{\partial p_o}{\partial x} = -\nu \frac{\partial \omega}{\partial y} \Big|_w. \quad (2.55)$$

Recalling from Eqns.(2.6) and (2.47b), the above equation in dimensionless form becomes

$$\frac{\partial p_o^*}{\partial x^*} = -\frac{2}{Re} \frac{\partial \omega^*}{\partial y^*} \Big|_w. \quad (2.56)$$

In like manner, a similar expression may be obtained when the analysis is performed along the vertical surface of the step using the Y component of the Navier-Stokes equations. The result is

$$\frac{\partial p_o^*}{\partial y^*} = \frac{2}{Re} \frac{\partial \omega^*}{\partial x^*} \Big|_w. \quad (2.57)$$

On the right-hand side of Eqns.(2.56) and (2.57), the diffusive vorticity flux at the surface, $\partial \omega^* / \partial y^*$ or $\partial \omega^* / \partial x^*$, can be expressed in terms of known quantities, such as U_{slip} and/or ω . Therefore, the distribution of pressure along the surface of the grooved wall can be determined. Once p_o^* is known, C_{Dp} can be evaluated according to Eqn.(2.48c)

CHAPTER 3

NUMERICAL ANALYSIS

The fundamental principles underlying the formulation of the velocity field and the equations governing the generation and transport of vorticity were discussed in Chapter 2. This chapter is devoted to the development of the numerical formulations and the computational procedure used to determine the velocity and vorticity fields of the flow. The discussion starts with the layout of the flow network, which is required in performing the numerical computation. The development of numerical formulations for vorticity dynamics is followed wherein the vorticity transport equation (VTE), in finite difference form, is derived and the treatment of vorticity production at the solid surface is discussed. Next, the development of the numerical formulation and computational procedure for the determination of the velocity field is presented. This is followed by the numerical evaluation of the drag coefficient. The chapter is concluded with the specification of the numerical parameters, such as the spatial and time increments.

Flow Network

For purposes of numerical computation, a flow network is chosen to be 44 by 62 nodes in the horizontal and vertical directions, respectively. The base geometry used in this study corresponds to the choice of the periodicity length a and the step width d equal to 4.0 and 2.0, respectively. Note that the above length parameters have been non-dimensionalized with respect to the step height h . As shown in Figure 2.3, the flow field consists of an infinite number of

spatially repeating regions corresponding to $n=0, \pm 1, \pm 2$, etc.. In the present study, the region with index $n=0$ is taken as the primary computational domain in which the numerical simulation of the flow development is analyzed. Note that the computational domain includes only one groove, and the height of the domain is taken as 5.0 dimensionless units. The layout of cell elements in the primary computational domain is shown in Figure 3.1. Details of the grid design will be given in the last section.

Referring to the preliminary study for irrotational flow over a single forward-facing step discussed in Appendix C, it indicates that the potential velocity field of the flow may have singular values at the two upper corners of each step. This is expected to be the region of large vorticity and velocity gradients. The grid size in this region is thus refined to improve numerical accuracy. The technique of grid generation near the corners is based on the Schwarz-Christoffel transformation, as explained later.

A typical cell element, denoted as $\Delta A_{i,j}$, in the primary computational domain is shown in Figure 3.2. The subscripts i and j indicate the number of the cell element at the horizontal X and vertical Y axes, respectively. As shown in the figure, values of the vorticity $\omega_{i,j}$ and the stream function $\psi_{i,j}$ are calculated at the node point (i,j) with the coordinate (x_i, y_j) , which is the centroid of the cell element. The horizontal component of the velocities $u_{i-1/2,j}$ and $u_{i+1/2,j}$ are calculated at $(x_{i-1/2}, y_j)$ and $(x_{i+1/2}, y_j)$ which denote the middle of the left and the right vertical faces of the cell element (lines of constant x), respectively. The vertical component of the velocities $v_{i,j-1/2}$ and $v_{i,j+1/2}$ are calculated at $(x_i, y_{j-1/2})$ and $(x_i, y_{j+1/2})$, which denote the middle of the bottom and the top horizontal

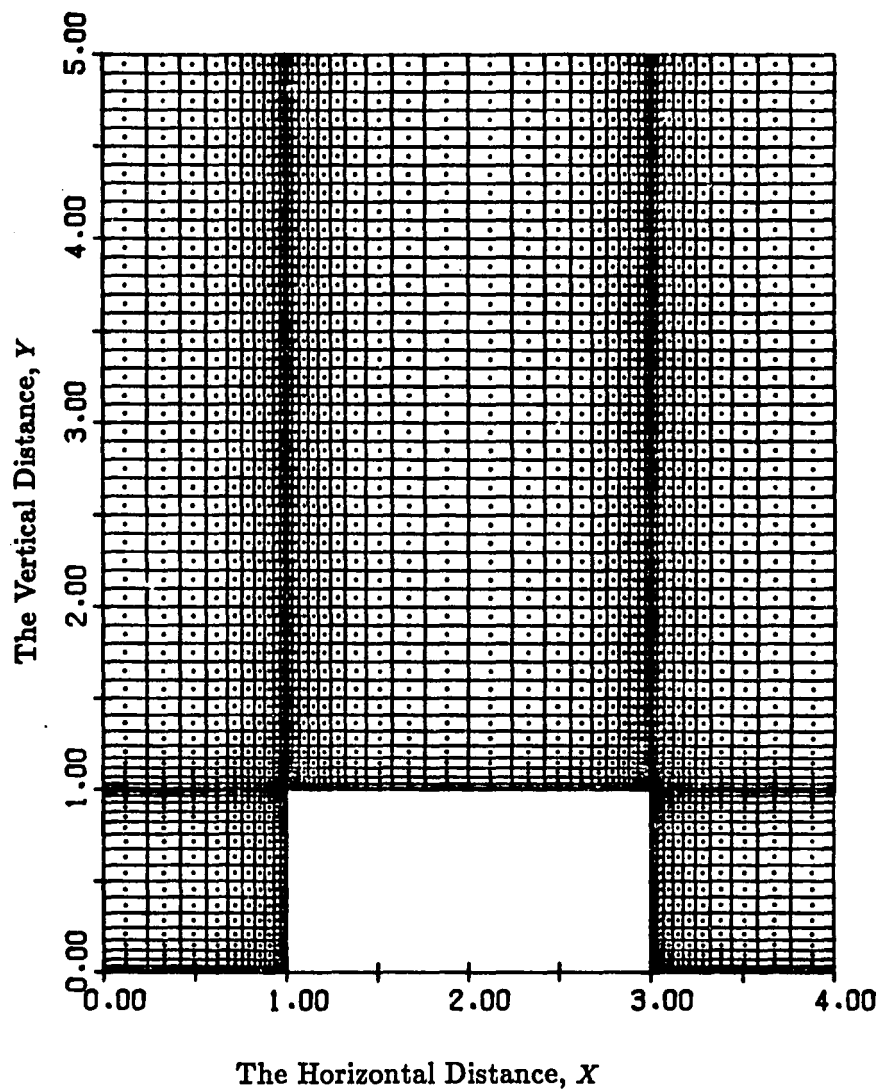


Figure 3.1 Illustration of the computational domain and layout of cell elements for the flow over the grooved wall with the base geometry $a=4.0$ and $d=2.0$.

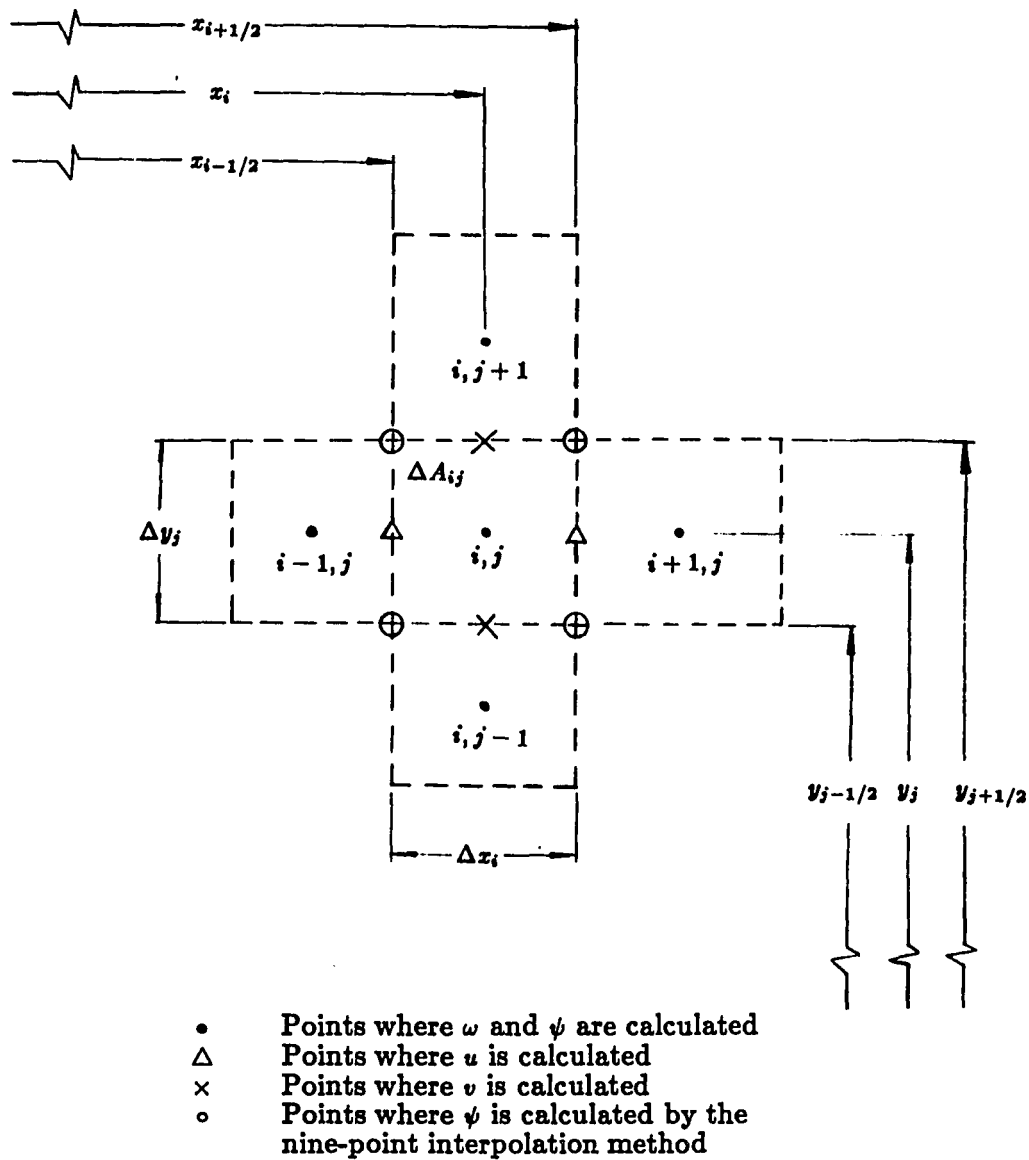


Figure 3.2 Diagram of the node arrangement around fluid elements in the computational domain.

faces of the cell element (lines of constant y), respectively. These components of the velocity are needed in solving the vorticity transport equation.

Numerical Formulation for Vorticity Dynamics

The vorticity transport equation, in conservative form, is restated here as

$$\frac{\partial \omega}{\partial t} + \frac{\partial u \omega}{\partial x} + \frac{\partial v \omega}{\partial y} = \frac{1}{Re} \left(\frac{\partial^2 \omega}{\partial x^2} + \frac{\partial^2 \omega}{\partial y^2} \right) \quad (3.1)$$

The solution is advanced in time from some given initial condition. This section is concerned with the development of the numerical formulation to solve the above equation over the computational domain as shown in Figure 3.1. Initially, values of u and v for the fluid particles and the vorticity production at the solid surface are determined from the potential flow with the value of the free vorticity identically equal to zero.

Finite-Difference Form of the Vorticity Transport Equation

For purposes of numerical computation, Eqn.(3.1) is expressed in finite difference form. To proceed, the terms in Eqn.(3.1) are multiplied by the area $\Delta A_{i,j} = (\Delta x_i \Delta y_j)$ of the cell element. We obtain

$$\frac{\partial \omega}{\partial t} \Delta x_i \Delta y_j + \Delta x_i \Delta y_j \left(\frac{\partial u \omega}{\partial x} + \frac{\partial v \omega}{\partial y} \right) = \frac{\Delta x_i \Delta y_j}{Re} \left(\frac{\partial^2 \omega}{\partial x^2} + \frac{\partial^2 \omega}{\partial y^2} \right) \quad (3.2)$$

The first term in Eqn.(3.2), i.e., the rate of vorticity storage in the cell element, is approximated by employing a forward-difference formula. The result is

$$\frac{\partial \omega}{\partial t} \Delta x_i \Delta y_j = \Delta x_i \Delta y_j \frac{\omega_{i,j}^+ - \omega_{i,j}}{\Delta t}, \quad (3.3)$$

where ω with the superscript “+” in the finite-difference expression is evaluated at time $t + \Delta t$; otherwise, it is evaluated at time t .

The net efflux of the vorticity across the cell faces by convection is given by the second term of Eqn.(3.2). This term is approximated using the upwind differences, which results in

$$\begin{aligned}
& \Delta x_i \Delta y_j \left(\frac{\partial u \omega}{\partial x} + \frac{\partial v \omega}{\partial y} \right) \\
&= \Delta y_j \left\{ [f_2 u_{i+\frac{1}{2},j} \omega_{i,j} + (1-f_2) u_{i+\frac{1}{2},j} \omega_{i+1,j}] \right. \\
&\quad \left. - [f_1 u_{i-\frac{1}{2},j} \omega_{i-1,j} + (1-f_1) u_{i-\frac{1}{2},j} \omega_{i,j}] \right\} \\
&\quad + \Delta x_i \left\{ [f_4 v_{i,j+\frac{1}{2}} \omega_{i,j} + (1-f_4) v_{i,j+\frac{1}{2}} \omega_{i,j+1}] \right. \\
&\quad \left. - [f_3 v_{i,j-\frac{1}{2}} \omega_{i,j-1} + (1-f_3) v_{i,j-\frac{1}{2}} \omega_{i,j}] \right\} \tag{3.4}
\end{aligned}$$

where the weighting factors f_1 , f_2 , f_3 and f_4 are associated with vorticities at nodes $(i-1, j)$, $(i+1, j)$, $(i, j-1)$ and $(i, j+1)$, respectively. These factors have values of zero or unity, depending on the sign of the normal component of the velocities at their corresponding cell faces. They are used to determine in which direction, from their corresponding cell faces, the vorticity is convected. The values of these factors are defined as below

$$f_1 \equiv .5[1 + \text{sign}(u_{i-\frac{1}{2},j})]$$

$$f_2 \equiv .5[1 + \text{sign}(u_{i+\frac{1}{2},j})]$$

$$f_3 \equiv .5[1 + \text{sign}(v_{i,j-\frac{1}{2}})]$$

$$f_4 \equiv .5[1 + \text{sign}(v_{i,j+\frac{1}{2}})]$$

where

$$\text{sign}(w) = \begin{cases} 1, & \text{if } w \geq 0; \\ -1, & \text{otherwise.} \end{cases}$$

For example, if $u_{i-1/2,j}$ is positive, then $f_1 = 1$. Thus, vorticity will be convected into the cell element across the left vertical cell face. This is given by

$u_{i-1/2,j}\omega_{i-1,j}\Delta y_j$. However, if $u_{i-1/2,j}$ is negative, then $f_1 = 0$. Therefore, vorticity will be convected out of the cell element across the left vertical cell face, according to the expression $u_{i-1/2,j}\omega_{i,j}\Delta y_j$.

It is worth noting that the spatial derivatives in the convective terms may alternatively be replaced by the central-difference formula. However, it is known that the central-difference approximation of the convective terms may give rise to instabilities, which can be eliminated by employing one-sided differences. This assures that the flow of numerical information is consistent with the physical flow. Roache and Mueller (1970) incorporated this idea in their definition of the "transportive property" which states that "A finite difference formulation of a flow equation possesses the Transportive Property if the effect of a perturbation in a transport property is advected only in the direction of the velocity." The finite-difference expressions for the convective terms, which satisfy this property, are called upwind differences and depend upon the direction of the velocity components at each point. In the present study, upwind differences are employed in the explicit formulation to take advantage of the improved stability and to preserve the transportive property.

It remains to approximate the diffusion term, as given by the right-hand side of Eqn.(3.2). This term represents the net influx of the vorticity across the cell faces due to viscous diffusion. The finite-difference expression for this term is

$$\begin{aligned}
& \frac{\Delta x_i \Delta y_j}{Re} \left(\frac{\partial^2 \omega}{\partial x^2} + \frac{\partial^2 \omega}{\partial y^2} \right) \\
&= \frac{\Delta x_i \Delta y_j}{Re} \left[\frac{\frac{\partial \omega}{\partial x} \Big|_{x+\Delta x_i/2} - \frac{\partial \omega}{\partial x} \Big|_{x_i - \Delta x_i/2}}{\Delta x_i} + \frac{\frac{\partial \omega}{\partial y} \Big|_{y+\Delta y_j/2} - \frac{\partial \omega}{\partial y} \Big|_{y_j - \Delta y_j/2}}{\Delta y_j} \right] \\
&= \frac{\Delta y_j}{Re} \left[\frac{\omega_{i+1,j} - \omega_{i,j}}{H_r} - \frac{\omega_{i,j} - \omega_{i-1,j}}{H_l} \right] + \frac{\Delta x_i}{Re} \left[\frac{\omega_{i,j+1} - \omega_{i,j}}{H_b} - \frac{\omega_{i,j} - \omega_{i,j-1}}{H_t} \right] \quad (3.5)
\end{aligned}$$

where

$$\begin{aligned} H_r &= \frac{\Delta x_i + \Delta x_{i+1}}{2} & H_l &= \frac{\Delta x_i + \Delta x_{i-1}}{2} \\ H_t &= \frac{\Delta y_j + \Delta y_{j+1}}{2} & H_b &= \frac{\Delta y_j + \Delta y_{j-1}}{2}. \end{aligned}$$

After substitution of Eqns. (3.3), (3.4) and (3.5) into Eqn.(3.2) and expressing $\omega_{i,j}^+$ in terms of quantities at a previous time level, we obtain the finite-difference approximation of Eqn.(3.1) as follows:

$$\begin{aligned} \omega_{i,j}^+ &= \omega_{i,j} \left\{ 1 + \frac{\Delta t}{\Delta x_i \Delta y_j} \left\{ \Delta y_j [(1-f_1)u_{i-\frac{1}{2},j} - f_2 u_{i+\frac{1}{2},j}] \right. \right. \\ &\quad \left. \left. + \Delta x_i [(1-f_3)v_{i,j-\frac{1}{2}} - f_4 v_{i,j+\frac{1}{2}}] - \frac{1}{Re} \left[\frac{\Delta x_i}{H_t} + \frac{\Delta x_i}{H_b} + \frac{\Delta y_j}{H_r} + \frac{\Delta y_j}{H_l} \right] \right\} \right\} \\ &\quad + \frac{\Delta t}{\Delta x_i \Delta y_j} \left\{ \omega_{i-1,j} [f_1 \Delta y_j u_{i-\frac{1}{2},j} + \frac{1}{Re} \frac{\Delta y_j}{H_l}] \right. \\ &\quad \left. + \omega_{i+1,j} [-(1-f_2) \Delta y_j u_{i+\frac{1}{2},j} + \frac{1}{Re} \frac{\Delta y_j}{H_r}] + \omega_{i,j-1} [f_3 \Delta x_i v_{i,j-\frac{1}{2}} + \frac{1}{Re} \frac{\Delta x_i}{H_b}] \right. \\ &\quad \left. + \omega_{i,j+1} [-(1-f_4) \Delta x_i v_{i,j+\frac{1}{2}} + \frac{1}{Re} \frac{\Delta x_i}{H_t}] \right\}. \end{aligned} \quad (3.6)$$

The above equation, as does Eqn.(2.39), also preserves the integral conservation relations of the continuum equation. As a result, the difference algorithm will not allow excessive accumulation of errors in the fluxes of the conserved quantities. As discussed in Roache (1973), the experience of many researchers indicates that conservative systems do generally give more accurate results, and the use of this system is therefore highly recommended. Based on the above argument, the conservative systems is employed in the present study. Note that Eqn.(3.6) is valid only to determine the vorticity field at cell elements which are not adjacent to the solid surface. The finite-difference expressions dealing with cell elements adjacent to the solid surface are discussed below.

Vorticity Production at the Solid Surface

It was discussed in Chapter 2 that when a flow passes a solid surface, this solid surface acts as either a distributed source or a sink of vorticity. Therefore, for those cell elements adjacent to the solid surface, a production term of vorticity at the surface must be accounted for. Due to the surface-adherence condition, vorticity created at the surface can only be imparted to the fluid through viscous diffusion. Consequently, the diffusion term in Eqn (3.5) must be modified to allow the vorticity created at the surface to enter the flow field. Since the treatment of the vorticity production at the solid surface is different for the VVI and VSF methods, the derivation of the finite-difference equations corresponding to each method shall be presented separately in this section.

The Vorticity-Velocity Induction Method. In the VVI method, the vorticity production is specified by the vorticity gradient along the normal to the surface which is related to the slip velocity (U_{slip}) at the surface. The relationship is given by Eqn.(2.43), which is rewritten as

$$\frac{1}{Re} \int_t^{t+\Delta t} \left. \frac{\partial \omega}{\partial n} \right|_{wall} dt' = \pm U_{slip}. \quad (3.7)$$

Assuming $(\partial \omega / \partial n)|_{wall}$ is constant during the small time interval Δt , Eqn.(3.7) is then approximated by

$$\left. \frac{\partial \omega}{\partial n} \right|_{wall} \cong \pm \frac{U_{slip} Re}{\Delta t}. \quad (3.8)$$

To incorporate the vorticity production into the development of the vorticity field, the diffusion terms in Eqn.(3.5) need to be modified for cell elements adjacent to the solid surfaces. For horizontal surfaces, Eqn.(3.5) is first written in the following form:

$$\begin{aligned} & \frac{\Delta x_i \Delta y_j}{Re} \left(\frac{\partial^2 \omega}{\partial x^2} + \frac{\partial^2 \omega}{\partial y^2} \right) \\ &= \frac{\Delta y_j}{Re} \left[\frac{\omega_{i+1,j} - \omega_{i,j}}{H_r} - \frac{\omega_{i,j} - \omega_{i-1,j}}{H_t} \right] + \frac{\Delta x_i}{Re} \left[\frac{\omega_{i,j+1} - \omega_{i,j}}{H_t} - \frac{\partial \omega}{\partial y} \Big|_{wall} \right]. \end{aligned} \quad (3.9)$$

Next, we substitute Eqn.(3.8) into the above equation and note that the normal to the surface is in the Y direction. The resulting equation, along with Eqns.(3.3) and (3.4) are then substituted into Eqn.(3.2). Upon rearrangement, we obtain

$$\begin{aligned} \omega_{i,j}^+ &= \omega_{i,j} \left\{ 1 + \frac{\Delta t}{\Delta x_i \Delta y_j} \left\{ \Delta y_j [(1-f_1)u_{i-\frac{1}{2},j} - f_2 u_{i+\frac{1}{2},j}] \right. \right. \\ &\quad \left. \left. - \Delta x_i f_4 v_{i,j+\frac{1}{2}} - \frac{1}{Re} \left[\frac{\Delta x_i}{H_t} + \frac{\Delta y_j}{H_r} + \frac{\Delta y_j}{H_t} \right] \right\} \right\} \\ &\quad + \frac{\Delta t}{\Delta x_i \Delta y_j} \left\{ \omega_{i-1,j} [f_1 \Delta y_j u_{i-\frac{1}{2},j} + \frac{1}{Re} \frac{\Delta y_j}{H_t}] \right. \\ &\quad \left. + \omega_{i+1,j} [-(1-f_2) \Delta y_j u_{i+\frac{1}{2},j} + \frac{1}{Re} \frac{\Delta y_j}{H_r}] \right. \\ &\quad \left. + \omega_{i,j+1} [-(1-f_4) \Delta x_i v_{i,j+\frac{1}{2}} + \frac{1}{Re} \frac{\Delta x_i}{H_t}] \right\} - \frac{U_{slip}}{\Delta y_j}. \end{aligned} \quad (3.10)$$

Note that the above equation is applicable only to the cell element adjacent to the horizontal solid surface. In like manner, the difference equations for the cell element adjacent to the left and right vertical surfaces of the step can be derived. The final expressions are given here for completeness. For a cell element adjacent to the left vertical surface of the step, the result is

$$\begin{aligned} \omega_{i,j}^+ &= \omega_{i,j} \left\{ 1 + \frac{\Delta t}{\Delta x_i \Delta y_j} \left\{ \Delta y_j (1-f_1)u_{i-\frac{1}{2},j} + \Delta x_i [(1-f_3)v_{i,j-\frac{1}{2}} - f_4 v_{i,j+\frac{1}{2}}] \right. \right. \\ &\quad \left. \left. - \frac{1}{Re} \left[\frac{\Delta x_i}{H_t} + \frac{\Delta x_i}{H_b} + \frac{\Delta y_j}{H_t} \right] \right\} \right\} + \frac{\Delta t}{\Delta x_i \Delta y_j} \left\{ \omega_{i-1,j} [f_1 \Delta y_j u_{i-\frac{1}{2},j} + \frac{1}{Re} \frac{\Delta y_j}{H_t}] \right. \\ &\quad \left. + \omega_{i,j-1} [f_3 \Delta x_i v_{i,j-\frac{1}{2}} + \frac{1}{Re} \frac{\Delta x_i}{H_b}] \right. \\ &\quad \left. + \omega_{i,j+1} [-(1-f_4) \Delta x_i v_{i,j+\frac{1}{2}} + \frac{1}{Re} \frac{\Delta x_i}{H_t}] \right\} - \frac{U_{slip}}{\Delta x_i}. \end{aligned} \quad (3.11)$$

For a cell element adjacent to the right vertical surface of the step, the result is

$$\begin{aligned}
\omega_{i,j}^+ = \omega_{i,j} & \left\{ 1 + \frac{\Delta t}{\Delta x_i \Delta y_j} \left\{ -\Delta y_j f_2 u_{i+\frac{1}{2},j} \right. \right. \\
& + \Delta x_i [(1-f_3)v_{i,j-\frac{1}{2}} - f_4 v_{i,j+\frac{1}{2}}] - \frac{1}{Re} \left[\frac{\Delta x_i}{H_t} + \frac{\Delta x_i}{H_b} + \frac{\Delta y_j}{H_r} \right] \left. \right\} \\
& + \frac{\Delta t}{\Delta x_i \Delta y_j} \left\{ \omega_{i+1,j} [-(1-f_2)\Delta y_j u_{i+\frac{1}{2},j} + \frac{1}{Re} \frac{\Delta y_j}{H_r}] \right. \\
& + \omega_{i,j-1} [f_3 \Delta x_i v_{i,j-\frac{1}{2}} + \frac{1}{Re} \frac{\Delta x_i}{H_b}] \\
& \left. + \omega_{i,j+1} [-(1-f_4)\Delta x_i v_{i,j+\frac{1}{2}} + \frac{1}{Re} \frac{\Delta x_i}{H_t}] \right\} + \frac{U_{slip}}{\Delta x_i}. \tag{3.12}
\end{aligned}$$

The Vorticity-Stream Function Method. In the VSF method, the vorticity production is specified by the value of the vorticity exactly at the solid surface, which can be determined by applying the circulation theory to the control volume ΔA_w adjacent to the solid surface. The relationship is given by Eqn.(2.45), which is

$$\iint_{\Delta A_w} \omega \, dA = \oint_c \bar{V} \cdot d\bar{l}. \tag{3.13}$$

Considering the case for ΔA_w adjacent to the horizontal surface shown in Figure 3.3 and with the assumption that ω , denoted as $\omega_{i,j}|_{wall}$, is constant and uniformly distributed over ΔA_w , Eqn.(3.13) can then be approximated by

$$\omega_{i,j}|_{wall} \Delta x_i \Delta l_j \cong V_1 \Delta l_j + V_2 \Delta x_i - V_3 \Delta l_j - V_4 \Delta x_i \tag{3.14}$$

where $\Delta l_j = \Delta y_j/4$ and V_1, V_2, V_3 and V_4 are the components of the velocities tangential to the corresponding cell faces. Due to the surface-adherence condition (i.e., $V_4 = 0$), the above equation becomes

$$\omega_{i,j}|_{wall} = \frac{V_1 \Delta l_j + V_2 \Delta x_i - V_3 \Delta l_j}{\Delta x_i \Delta l_j}. \tag{3.15}$$

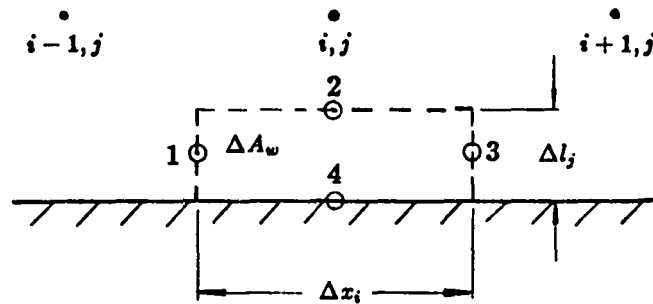


Figure 3.3 Diagram of the control volume adjacent to the horizontal surface used to determine the vorticity at the solid surface. The tangential component of velocities, V_1 , V_2 , V_3 and V_4 are calculated at the points corresponding to 1, 2, 3 and 4, respectively.

The evaluation of V_1 , V_2 and V_3 is explained in a later section. To account for the vorticity production at the solid surface, the diffusion term in Eqn.(3.5) for a cell element adjacent to the horizontal surface is modified as follows:

$$\begin{aligned} & \frac{\Delta x_i \Delta y_j}{Re} \left(\frac{\partial^2 \omega}{\partial x^2} + \frac{\partial^2 \omega}{\partial y^2} \right) \\ &= \frac{\Delta y_j}{Re} \left[\frac{\omega_{i+1,j} - \omega_{i,j}}{H_r} - \frac{\omega_{i,j} - \omega_{i-1,j}}{H_l} \right] + \frac{\Delta x_i}{Re} \left[\frac{\omega_{i,j+1} - \omega_{i,j}}{H_t} - \frac{\omega_{i,j} - \omega_{i,j}|_{wall}}{H'_b} \right] \end{aligned} \quad (3.16)$$

where $H'_b = \Delta y_j/2$. Combining Eqns.(3.16), (3.3), (3.4) and (3.2), we obtain

$$\begin{aligned} \omega_{i,j}^+ &= \omega_{i,j} \left\{ 1 + \frac{\Delta t}{\Delta x_i \Delta y_j} \left\{ \Delta y_j [(1-f_1)u_{i-\frac{1}{2},j} - f_2 u_{i+\frac{1}{2},j}] \right. \right. \\ &\quad \left. \left. - \Delta x_i f_4 v_{i,j+\frac{1}{2}} - \frac{1}{Re} \left[\frac{\Delta x_i}{H_t} + \frac{\Delta x_i}{H'_b} + \frac{\Delta y_j}{H_r} + \frac{\Delta y_j}{H_l} \right] \right\} \right\} \\ &\quad + \frac{\Delta t}{\Delta x_i \Delta y_j} \left\{ \omega_{i-1,j} [f_1 \Delta y_j u_{i-\frac{1}{2},j} + \frac{1}{Re} \frac{\Delta y_j}{H_l}] \right. \\ &\quad \left. + \omega_{i+1,j} [-(1-f_2) \Delta y_j u_{i+\frac{1}{2},j} + \frac{1}{Re} \frac{\Delta y_j}{H_r}] + \omega_{i,j}|_{wall} \left[\frac{1}{Re} \frac{\Delta x_i}{H'_b} \right] \right. \\ &\quad \left. + \omega_{i,j+1} [-(1-f_4) \Delta x_i v_{i,j+\frac{1}{2}} + \frac{1}{Re} \frac{\Delta x_i}{H_t}] \right\}. \end{aligned} \quad (3.17)$$

For a cell element adjacent to the left vertical surface of the step, the result is

$$\begin{aligned} \omega_{i,j}^+ &= \omega_{i,j} \left\{ 1 + \frac{\Delta t}{\Delta x_i \Delta y_j} \left\{ \Delta y_j (1-f_1) u_{i-\frac{1}{2},j} \right. \right. \\ &\quad \left. \left. + \Delta x_i [(1-f_3) v_{i,j-\frac{1}{2}} - f_4 v_{i,j+\frac{1}{2}}] - \frac{1}{Re} \left[\frac{\Delta x_i}{H_t} + \frac{\Delta x_i}{H'_b} + \frac{\Delta y_j}{H'_r} + \frac{\Delta y_j}{H_l} \right] \right\} \right\} \\ &\quad + \frac{\Delta t}{\Delta x_i \Delta y_j} \left\{ \omega_{i-1,j} [f_1 \Delta y_j u_{i-\frac{1}{2},j} + \frac{1}{Re} \frac{\Delta y_j}{H_l}] \right. \\ &\quad \left. + \omega_{i,j}|_{wall} \left[\frac{1}{Re} \frac{\Delta y_j}{H'_r} \right] + \omega_{i,j-1} [f_3 \Delta x_i v_{i,j-\frac{1}{2}} + \frac{1}{Re} \frac{\Delta x_i}{H_b}] \right. \\ &\quad \left. + \omega_{i,j+1} [-(1-f_4) \Delta x_i v_{i,j+\frac{1}{2}} + \frac{1}{Re} \frac{\Delta x_i}{H_t}] \right\}. \end{aligned} \quad (3.18)$$

For a cell element adjacent to the right vertical surface of the step, the result is

$$\begin{aligned}
\omega_{i,j}^+ = \omega_{i,j} & \left\{ 1 + \frac{\Delta t}{\Delta x_i \Delta y_j} \left\{ \Delta y_j f_2 u_{i+\frac{1}{2},j} \right. \right. \\
& + \Delta x_i [(1-f_3)v_{i,j-\frac{1}{2}} - f_4 v_{i,j+\frac{1}{2}}] - \frac{1}{Re} \left[\frac{\Delta x_i}{H_i} + \frac{\Delta x_i}{H_b} + \frac{\Delta y_j}{H_r} + \frac{\Delta y_j}{H'_i} \right] \left. \right\} \\
& + \frac{\Delta t}{\Delta x_i \Delta y_j} \left\{ \omega_{i,j} |_{wall} \left[\frac{1}{Re} \frac{\Delta y_j}{H'_i} \right] \right. \\
& + \omega_{i+1,j} [-(1-f_2)\Delta y_j u_{i+\frac{1}{2},j} + \frac{1}{Re} \frac{\Delta y_j}{H_r}] + \omega_{i,j-1} [f_3 \Delta x_i v_{i,j-\frac{1}{2}} + \frac{1}{Re} \frac{\Delta x_i}{H_b}] \\
& \left. + \omega_{i,j+1} [-(1-f_4)\Delta x_i v_{i,j+\frac{1}{2}} + \frac{1}{Re} \frac{\Delta x_i}{H_i}] \right\} \quad (3.19)
\end{aligned}$$

where $H'_r = H'_i = \Delta x_i/2$.

At the initial time ($t = 0$), the flow is initiated impulsively, and at this moment the flow is considered to be potential flow (i.e., vorticity is everywhere zero and the fluid slips at the solid surface). Thus, all terms vanish on the right-hand side of Eqns.(3.10), (3.11), (3.12), (3.17), (3.18) and (3.19) except the terms which include U_{slip} or $\omega_{i,j}|_{wall}$. These are present in order to satisfy the surface-adherence condition, and they are referred to as the vorticity production terms at the solid surface. Therefore, after the first time step, the vorticity only diffuses into the cell elements adjacent to the surface. For those cell elements, the value of the vorticity using the VVI method is

$$\omega_{i,j}^+ = \frac{U_{slip}^{0+}}{C}$$

where the value of C is $-\Delta y_j$ in Eqn.(3.10), $-\Delta x_i$ in Eqn.(3.11) and Δx_i in Eqn.(3.12), and the value of the vorticity using the VSF method is

$$\omega_{i,j}^+ = \frac{C'}{Re} \frac{\Delta t}{\Delta x_i \Delta y_j} \omega_{i,j}^{0+} |_{wall}$$

where the value of C' is $\Delta x_i/H'_b$ in Eqn.(3.17), $\Delta y_j/H'_r$ in Eqn.(3.18), $\Delta y_j/H'_i$ in Eqn.(3.19). In the above equations, U_{slip}^{0+} , $\omega_{i,j}^{0+} |_{wall}$ are the slip velocity and the

wall vorticity at the solid surface immediately following the impulsive motion of the fluid, corresponding to the solution for the potential flow. This shows that the vorticity generated at the solid surface chosen to eliminate the tangential component of the velocity at the solid surface, has diffused into those cell elements during the first time step. For subsequent time steps, the vorticity in the flow field is redistributed through both convection and diffusion, and new vorticity enters the flow field whenever the values of slip velocity is nonzero, or the value of wall vorticity is different from the value of the free vorticity at the node point adjacent to it. The evaluation of U_{slip} and components of the velocity needed in evaluating wall vorticity is covered in the next section.

Numerical Formulation for the Velocity Field

As discussed in Chapter 2, the velocity field of the flow is determined by two approaches corresponding to the VVI and VSF methods, respectively. In this section, the numerical formulation and the computational procedure for these two approaches are presented. The discussion is divided into two parts dealing with each of the approaches separately.

The Vorticity-Velocity Induction Method

In the VVI method, the velocity field is determined through a combination of the Biot-Savart law of induced velocities and the equation of continuity. A preliminary calculation of the velocity field of the irrotational flow over a forward-facing step using the Biot-Savart law of induced velocities is presented in Appendix C. This test case was chosen because there is a known exact solution. It is observed that for all the selected velocity profiles near the corner of the step, where the flow is expected to change rapidly, there is exceptionally

good agreement between the numerical and corresponding exact velocity profiles. Based on this observation, we conclude that our numerical scheme is sufficiently accurate to handle the singular condition near the corner, and we believe that an accurate numerical solution to this irrotational flow is a minimum requirement for any numerical scheme purporting to simulate the full viscous flow over a grooved wall.

The velocity at the point p using the Biot-Savart law of induced velocities is given by Eqn.(2.17), which is rewritten as

$$\bar{V}(r_p, t) = \bar{i} + \bar{V}_f(r_p, t) + \bar{V}_b(r_p, t), \quad (3.20)$$

and $\bar{V}_f(r_p, t)$ and $\bar{V}_b(r_p, t)$ are given as

$$\bar{V}_f(r_p, t) = \frac{1}{2\pi} \sum_{n=-\infty}^{\infty} \iint_{A^n} \frac{\bar{\omega}_o \times \bar{r}_{op}^n}{|\bar{r}_{op}^n|^2} dA \quad (3.20a)$$

$$\bar{V}_b(r_p, t) = \frac{1}{2\pi} \sum_{n=-\infty}^{\infty} \int_{\Gamma^n} \frac{\bar{\gamma}_q \times \bar{r}_{qp}^n}{|\bar{r}_{qp}^n|^2} dl. \quad (3.20b)$$

Induced Velocity due to the Free Vorticity Field. The evaluation of $\bar{V}_f(r_p, t)$ involving the free vorticity is a very time consuming operation performed during each time step. If NX and NY denote the numbers of cell elements with non-zero vorticity in the horizontal and vertical directions, respectively, there are $N = NX \cdot NY$ non-zero vortex cell elements in the primary computational domain and each spatially repeating region. The contribution of these cell elements in the flow field must be summed for each point p at which the velocity is desired. This is expressed as follows:

$$\bar{V}_f(r_p, t) = \sum_{i=1}^{NX} \sum_{j=1}^{NY} \left[\frac{1}{2\pi} \sum_{n=-\infty}^{\infty} \iint_{\Delta A_{i,j}^n} \frac{\bar{\omega}_o \times \bar{r}_{op}^n}{|\bar{r}_{op}^n|^2} dA \right]. \quad (3.21)$$

In this calculation, the vorticity $\bar{\omega}$ is assumed to be a constant and uniformly distributed throughout the cell element $\Delta A_{i,j}^n$. Therefore, $\bar{\omega}$ in $\Delta A_{i,j}^n$ is the same as $\bar{\omega}_{i,j}^n$, and note that $\bar{\omega}_{i,j}^n = \bar{\omega}_{i,j}$, which is evaluated at the node point (i,j) in the primary computational domain. This approximation allows $\bar{\omega}_{i,j}$ to be taken out of the integral sign, such that,

$$\bar{V}_f(r_p, t) \cong \sum_{i=1}^{NX} \sum_{j=1}^{NY} \left[\frac{1}{2\pi} \sum_{n=-\infty}^{\infty} \bar{\omega}_{i,j} \times \iint_{\Delta A_{i,j}^n} \frac{\bar{r}_{op}^n}{|\bar{r}_{op}^n|^2} dA \right]. \quad (3.22)$$

In Cartesian coordinates, the velocity vector \bar{V}_f can be written as

$$\bar{V}_f(r_p, t) = u_f \bar{i} + v_f \bar{j} \quad (3.23)$$

where u_f and v_f are the X and Y components of the velocity due to the free vorticity field, respectively, and they are given as

$$u_f = \sum_{i=1}^{NX} \sum_{j=1}^{NY} \Delta u_{f,ij} \quad (3.23a)$$

$$v_f = \sum_{i=1}^{NX} \sum_{j=1}^{NY} \Delta v_{f,ij}. \quad (3.23b)$$

The terms, $\Delta u_{f,ij}$ and $\Delta v_{f,ij}$, shown in the above equations are the velocity components induced by the free vorticity in the cell element $\Delta A_{i,j}$ in the primary computational domain and its corresponding cell elements in the spatially repeating regions. They can be expressed as

$$\begin{aligned} \Delta u_{f,ij} &= \sum_{n=-\infty}^{\infty} \Delta u_{f,ij}^n \\ &= \omega_{i,j} \left\{ -\frac{1}{2\pi} \sum_{n=-\infty}^{\infty} \iint_{\Delta A_{i,j}^n} \left[\frac{y_p - y_o}{(x_p - x_o)^2 + (y_p - y_o)^2} \right] dx_o dy_o \right\} \quad (3.23c) \\ &= \omega_{i,j} \left\{ -\frac{1}{2\pi} \iint_{\Delta A_{i,j}} \left[\frac{y_p - y_o}{(x_p - x_o)^2 + (y_p - y_o)^2} \right] \right. \end{aligned}$$

$$\begin{aligned}
& + \sum_{n=1}^{\infty} \left[\frac{y_p - y_o}{[(x_p - x_o) + na]^2 + (y_p - y_o)^2} \right. \\
& \left. + \frac{y_p - y_o}{[(x_p - x_o) - na]^2 + (y_p - y_o)^2} \right] dx_o dy_o \} \quad (3.23d)
\end{aligned}$$

$$\begin{aligned}
\Delta v_{f,ij} &= \sum_{n=-\infty}^{\infty} \Delta v_{f,i,j}^n \\
&= \omega_{i,j} \left\{ \frac{1}{2\pi} \sum_{n=-\infty}^{\infty} \iint_{\Delta A_{i,j}^n} \left[\frac{x_p - x_o^n}{(x_p - x_o^n)^2 + (y_p - y_o)^2} \right] dx_o dy_o \right\} \quad (3.23e)
\end{aligned}$$

$$\begin{aligned}
&= \omega_{i,j} \left\{ \frac{1}{2\pi} \iint_{\Delta A_{i,j}} \left[\frac{x_p - x_o}{(x_p - x_o)^2 + (y_p - y_o)^2} \right. \right. \\
& \quad + \sum_{n=1}^{\infty} \left[\frac{x_p - x_o}{[(x_p - x_o) + na]^2 + (y_p - y_o)^2} \right. \\
& \quad \left. \left. + \frac{x_p - x_o}{[(x_p - x_o) - na]^2 + (y_p - y_o)^2} \right] \right] dx_o dy_o \} \quad (3.23f)
\end{aligned}$$

Note that $x_o^n = x_o + na$, $y_o^n = y_o$, $dx_o^n = dx_o$ and $dy_o^n = dy_o$, where $n = 0, \pm 1, \pm 2$, etc.. The terms inside the curve brackets in Eqns.(3.23d, f) involve only the geometry, and they are referred to as the X and Y components of the geometric coefficients for the cell element $\Delta A_{i,j}$ with respect to the point p . Since the geometric coefficients remain invariant for the entire calculation, they are evaluated in advance and stored for future calculations. For example, if the X component of the velocity at the point p due to the free vorticity field is desired, then N values of the free vorticity $\omega_{i,j}$ at the cell element $\Delta A_{i,j}$ are multiplied by their corresponding X component geometric coefficients appropriate to that point, and the products are summed together. The procedure employed to evaluate these geometric coefficients is explained below.

As shown in Chapter 2, each of the two series of the integrals inside the curve brackets in Eqns.(3.23d, f) can be reduced to a single integral, individually. That is,

$$\begin{aligned}
CU_{f,ij} &\equiv -\frac{1}{2\pi} \iint_{\Delta A_{i,j}} \left\{ \frac{y_p - y_o}{(x_p - x_o)^2 + (y_p - y_o)^2} \right. \\
&\quad + \sum_{n=1}^{\infty} \left[\frac{y_p - y_o}{[(x_p - x_o) + na]^2 + (y_p - y_o)^2} \right. \\
&\quad \left. \left. + \frac{y_p - y_o}{[(x_p - x_o) - na]^2 + (y_p - y_o)^2} \right] \right\} dx_o dy_o \\
&= -\frac{1}{2a} \iint_{\Delta A_{i,j}} \left[\frac{\sinh \frac{2\pi(y_p - y_o)}{a}}{\cosh \frac{2\pi(y_p - y_o)}{a} - \cos \frac{2\pi(x_p - x_o)}{a}} \right] dx_o dy_o \quad (3.24a)
\end{aligned}$$

$$\begin{aligned}
CV_{f,ij} &\equiv \frac{1}{2\pi} \iint_{\Delta A_{i,j}} \left\{ \frac{x_p - x_o}{(x_p - x_o)^2 + (y_p - y_o)^2} \right. \\
&\quad + \sum_{n=1}^{\infty} \left[\frac{x_p - x_o}{[(x_p - x_o) + na]^2 + (y_p - y_o)^2} \right. \\
&\quad \left. \left. + \frac{x_p - x_o}{[(x_p - x_o) - na]^2 + (y_p - y_o)^2} \right] \right\} dx_o dy_o \\
&= \frac{1}{2a} \iint_{\Delta A_{i,j}} \left[\frac{\sin \frac{2\pi(x_p - x_o)}{a}}{\cosh \frac{2\pi(y_p - y_o)}{a} - \cos \frac{2\pi(x_p - x_o)}{a}} \right] dx_o dy_o. \quad (3.24b)
\end{aligned}$$

Trial calculations showed that for $|\bar{r}_{o,p}|$, the distance between the point p and the node point o' which has coordinates (x_i^o, y_j) and is located at the centroid of the cell element $\Delta A_{i,j}^o$, and l , the diagonal length of the $\Delta A_{i,j}^o$ (i.e., $l = \sqrt{\Delta x_i^2 + \Delta y_j^2}$), if the ratio R_l , defined by $|\bar{r}_{o,p}|/l$, is greater than 10, the integrand in Eqns.(3.24a, b) can be treated approximately as a constant. Therefore, Eqns.(3.24a, b) can be expressed approximately as

$$CTU_{f,ij} \cong -\frac{1}{2a} \left[\frac{\sinh \frac{2\pi(y_p - y_j)}{a}}{\cosh \frac{2\pi(y_p - y_j)}{a} - \cos \frac{2\pi(x_p - x_i)}{a}} \right] \Delta x_i \Delta y_j \quad (3.25a)$$

$$CTV_{f,ij} \cong \frac{1}{2a} \left[\frac{\sin \frac{2\pi(x_p - x_i)}{a}}{\cosh \frac{2\pi(y_p - y_j)}{a} - \cos \frac{2\pi(x_p - x_i)}{a}} \right] \Delta x_i \Delta y_j. \quad (3.25b)$$

The coefficients, $CTU_{f,ij}$ and $CTV_{f,ij}$, obtained from the above equations are here referred to as the X and Y components of the approximate geometric coefficient for the cell element $\Delta A_{i,j}$, respectively. However, when the point o' is close to the point p (i.e., $R_i \leq 10$), the accuracy of the above expression is no longer acceptable. In this case, the following procedure is taken.

Note that each single integral in Eqns.(3.23c,e) can be integrated analytically. The results are derived in the Appendix A, and they are given as follows:

$$\begin{aligned}
CEU_{f,ij} &\equiv -\frac{1}{2\pi} \iint_{\Delta A_{i,j}^n} \frac{y_p - y_o}{(x_p - x_o^n)^2 + (y_p - y_o)^2} dx_o dy_o \\
&= \frac{1}{4\pi} \left\{ \left(x_{pi}^n - \frac{\Delta x_i}{2} \right) \ln \frac{\left(y_{pj} + \frac{\Delta y_j}{2} \right)^2 + \left(x_{pi}^n - \frac{\Delta x_i}{2} \right)^2}{\left(y_{pj} - \frac{\Delta y_j}{2} \right)^2 + \left(x_{pi}^n - \frac{\Delta x_i}{2} \right)^2} \right. \\
&\quad - \left(x_{pi}^n + \frac{\Delta x_i}{2} \right) \ln \frac{\left(y_{pj} + \frac{\Delta y_j}{2} \right)^2 + \left(x_{pi}^n + \frac{\Delta x_i}{2} \right)^2}{\left(y_{pj} - \frac{\Delta y_j}{2} \right)^2 + \left(x_{pi}^n + \frac{\Delta x_i}{2} \right)^2} \\
&\quad + 2 \left(y_{pj} + \frac{\Delta y_j}{2} \right) \left[\arctan \frac{x_{pi}^n - \frac{\Delta x_i}{2}}{y_{pj} + \frac{\Delta y_j}{2}} - \arctan \frac{x_{pi}^n + \frac{\Delta x_i}{2}}{y_{pj} + \frac{\Delta y_j}{2}} \right] \\
&\quad \left. - 2 \left(y_{pj} - \frac{\Delta y_j}{2} \right) \left[\arctan \frac{x_{pi}^n - \frac{\Delta x_i}{2}}{y_{pj} - \frac{\Delta y_j}{2}} - \arctan \frac{x_{pi}^n + \frac{\Delta x_i}{2}}{y_{pj} - \frac{\Delta y_j}{2}} \right] \right\} \quad (3.26a)
\end{aligned}$$

$$\begin{aligned}
CEV_{f,ij} &\equiv \frac{1}{2\pi} \iint_{\Delta A_{i,j}^n} \frac{x_p - x_o^n}{(x_p - x_o^n)^2 + (y_p - y_o)^2} dx_o dy_o \\
&= \frac{1}{4\pi} \left\{ \left(y_{pj} - \frac{\Delta y_j}{2} \right) \ln \frac{\left(x_{pi}^n - \frac{\Delta x_i}{2} \right)^2 + \left(y_{pj} - \frac{\Delta y_j}{2} \right)^2}{\left(x_{pi}^n - \frac{\Delta x_i}{2} \right)^2 + \left(y_{pj} - \frac{\Delta y_j}{2} \right)^2} \right. \\
&\quad - \left(y_{pj} + \frac{\Delta y_j}{2} \right) \ln \frac{\left(y_{pj} + \frac{\Delta y_j}{2} \right)^2 + \left(x_{pi}^n - \frac{\Delta x_i}{2} \right)^2}{\left(y_{pj} + \frac{\Delta y_j}{2} \right)^2 + \left(x_{pi}^n + \frac{\Delta x_i}{2} \right)^2} \\
&\quad \left. - \left(y_{pj} - \frac{\Delta y_j}{2} \right) \ln \frac{\left(y_{pj} + \frac{\Delta y_j}{2} \right)^2 + \left(x_{pi}^n - \frac{\Delta x_i}{2} \right)^2}{\left(y_{pj} + \frac{\Delta y_j}{2} \right)^2 + \left(x_{pi}^n + \frac{\Delta x_i}{2} \right)^2} \right\}
\end{aligned}$$

$$\begin{aligned}
& + 2\left(x_{pi}^n - \frac{\Delta x_i}{2}\right) \left[\arctan \frac{y_{pj} - \frac{\Delta y_j}{2}}{x_{pi}^n - \frac{\Delta x_i}{2}} - \arctan \frac{y_{pj} + \frac{\Delta y_j}{2}}{x_{pi}^n - \frac{\Delta x_i}{2}} \right] \\
& - 2\left(x_{pi}^n - \frac{\Delta x_i}{2}\right) \left[\arctan \frac{y_{pj} - \frac{\Delta y_j}{2}}{x_{pi}^n + \frac{\Delta x_i}{2}} - \arctan \frac{y_{pj} + \frac{\Delta y_j}{2}}{x_{pi}^n + \frac{\Delta x_i}{2}} \right] \} \quad (3.26b)
\end{aligned}$$

where $x_{pi}^n = x_p - x_i^n$ and $y_{pj} = y_j^n = y_p - y_j^n$, and the coefficients, $CEU_{f,ij}$ and $CEV_{f,ij}$, are referred to as the X and Y components of the exact cell geometric coefficient for the single cell element $\Delta A_{i,j}^n$, respectively.

On the other hand, the X and Y components of the approximate cell geometric coefficients for $\Delta A_{i,j}^n$, obtained by treating the integrand in Eqns.(3.26a, b) as a constant are given as

$$\begin{aligned}
CAU_{f,ij} & \equiv -\frac{1}{2\pi} \iint_{\Delta A_{i,j}^n} \frac{y_p - y_o}{(x_p - x_o^n)^2 + (y_p - y_o)^2} dx_o dy_o \\
& \cong -\frac{1}{2\pi} \frac{y_p - y_j}{(x_p - x_i^n)^2 + (y_p - y_j)^2} \Delta x_i \Delta y_j \quad (3.27a)
\end{aligned}$$

$$\begin{aligned}
CAV_{f,ij} & \equiv \frac{1}{2\pi} \iint_{\Delta A_{i,j}^n} \frac{x_p - x_o^n}{(x_p - x_o^n)^2 + (y_p - y_o)^2} dx_o dy_o \\
& \cong \frac{1}{2\pi} \frac{x_p - x_i^n}{(x_p - x_i^n)^2 + (y_p - y_j)^2} \Delta x_i \Delta y_j \quad (3.27b)
\end{aligned}$$

First, the geometric coefficients at the point p due to all spatially repeating periodic cell elements $\Delta A_{i,j}^n$ are calculated according to Eqns.(3.25a, b). However, if there is a cell element in any spatially repeating region with R_i less than 100, then the exact cell geometric coefficient due to this cell element is calculated according to Eqns.(3.26a, b). In this case, the corresponding component of the approximate cell geometric coefficient from Eqn.(3.27a, b) must be subtracted from the exact cell geometric coefficient of the same cell element to the point p , and it is then added to the corresponding component of the total approximate

geometric coefficients from Eqns.(3.25a,b). In summary, both components of the geometric coefficient at the point p due to the cell element $\Delta A_{i,j}$ in the primary computational domain and its corresponding cell elements in all spatially repeating regions are determined by

$$CU_{f,ij} = CTU_{f,ij} + \sum_m (CEU_{f,ij} - CAU_{f,ij})_m \quad (3.28a)$$

$$CV_{f,ij} = CTV_{f,ij} + \sum_m (CEV_{f,ij} - CAV_{f,ij})_m \quad (3.28b)$$

where m is the number of cell elements with R_l less than 100 in all computational regions.

Once both components of the geometric coefficients are obtained from Eqns.(3.28a,b), u_f and v_f can be determined according to Eqns.(3.23a,b), which are expressed as

$$u_f = \sum_{i=1}^{NX} \sum_{j=1}^{NY} \omega_{i,j} \cdot CU_{f,ij} \quad (3.29a)$$

$$v_f = \sum_{i=1}^{NX} \sum_{j=1}^{NY} \omega_{i,j} \cdot CV_{f,ij} \quad (3.29b)$$

It is worth noting that in the calculation, the computational domain in the Y direction is allowed to grow as time progresses. Initially, the value of NY is set equal to 25, which corresponds to $Y \cong 1.2$. At $t = 6.0$, however, the value of NY is found to be 39, which corresponds to $Y \cong 2.5$.

Induced Velocity due to the Distribution of Bound Vorticity. In like manner, $\bar{V}_b(r_p, t)$, the induced velocity due to the distribution of bound vorticity, can be obtained in a form similar to Eqns.(3.29a,b). The result is

$$\bar{V}_b(r_p, t) = u_b \bar{i} + v_b \bar{j} \quad (3.30)$$

where u_b and v_b are given by

$$u_b = \sum_{k=1}^{N_b} \gamma_k \cdot CU_{b,k} \quad (3.30a)$$

$$v_b = \sum_{k=1}^{N_b} \gamma_k \cdot CV_{b,k} \quad (3.30b)$$

in which N_b is the total number of bound vorticity elements distributed along the horizontal and vertical surfaces of the step. A node point is positioned at the center of each bound vorticity element, the size of which is either Δx_i or Δy_j , depending on whether the element is at the horizontal or the vertical surface. According to the flow network discussed at the end of this chapter, the value of N_b is found to be 58. In Eqns.(3.30a, b), $CU_{b,k}$ and $CV_{b,k}$ are calculated by following the same procedure as described in determining $CU_{f,ij}$ and $CV_{f,ij}$ in Eqns.(3.29a, b) and the results derived in Appendix A. However, it needs to be pointed out that in the calculation, γ is assumed to be a linear function of its distributed length. A graphical representation of the distribution of bound vorticity for a element Δx_i on the horizontal surface of the step is shown in Figure 3.4, in which γ_i , γ_{i-1} and γ_{i+1} are the strengths of the bound vorticity at the coordinates of $(x_i, 1.0)$, $(x_{i-1}, 1.0)$ and $(x_{i+1}, 1.0)$. Referring to the figure, the strength of the bound vorticity distributed on the element Δx_i is given by

$$\gamma(x, t) = \begin{cases} \frac{2(\gamma_i - \gamma_{i-1})}{\Delta x_{i-1} + \Delta x_i} (x - x_i) + \gamma_i & \text{if } x_i - \frac{\Delta x_i}{2} \leq x \leq x_i; \\ \frac{2(\gamma_{i+1} - \gamma_i)}{\Delta x_i + \Delta x_{i+1}} (x - x_i) + \gamma_i & \text{if } x_i \leq x \leq x_i + \frac{\Delta x_i}{2}. \end{cases} \quad (3.31)$$

A similar distribution is given for the bound vorticity on Δy_j at the vertical surface of the step.

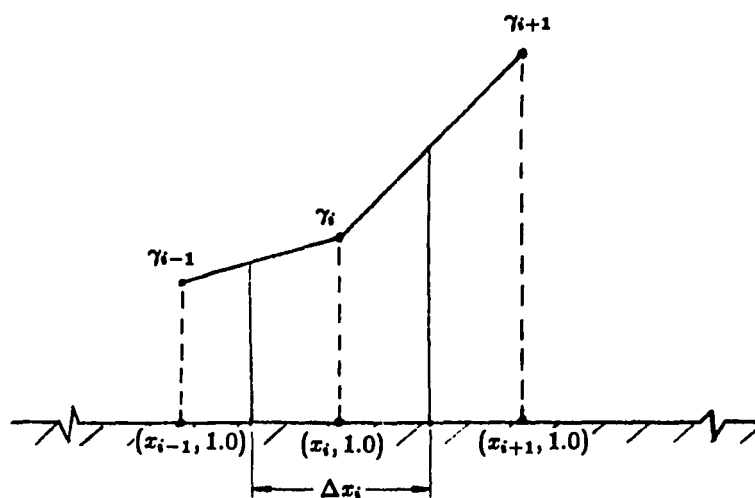


Figure 3.4 Graphical representation of the distribution of bound vorticity for the element Δx_i on the horizontal surface of the step.

Using the notations defined by Eqns.(3.23) and (3.30), Eqn.(3.20) can be rewritten in terms of two scalar velocity components, u and v , as

$$\vec{V}(r_p, t) = u\vec{i} + v\vec{j} \quad (3.32)$$

where

$$u = u_f + u_b \quad (3.32a)$$

$$v = v_f + v_b \quad (3.32b)$$

From the above analysis, it can be seen that both components of velocity, u and v , can be determined by employing the Biot-Savart law of induced velocities. However, as mentioned earlier, the calculation using the induction law is a time consuming operation. Thus, it is more expedient to obtain the Y -component of the velocity v from the equation of continuity, once the X -component of the velocity u due to the onset flow, the free vorticity field and the distribution of bound vorticity is found.

To obtain the finite-difference approximation to the equation of continuity, the spatial derivatives in Eqn.(2.29) are replaced by the central-difference formula. Referring to Figure 3.2, we obtain

$$\frac{u_{i+\frac{1}{2},j} - u_{i-\frac{1}{2},j}}{\Delta x_i} + \frac{v_{i,j+\frac{1}{2}} - v_{i,j-\frac{1}{2}}}{\Delta y_j} = 0. \quad (3.33)$$

Upon rearrangement, the above equation is expressed as either

$$v_{i,j+\frac{1}{2}} = v_{i,j-\frac{1}{2}} - \frac{\Delta y_j}{\Delta x_i} (u_{i+\frac{1}{2},j} - u_{i-\frac{1}{2},j}) \quad (3.34)$$

or

$$v_{i,j-\frac{1}{2}} = v_{i,j+\frac{1}{2}} + \frac{\Delta y_j}{\Delta x_i} (u_{i+\frac{1}{2},j} - u_{i-\frac{1}{2},j}). \quad (3.35)$$

The Y -component of the velocity is then obtained by marching Eqn.(3.34) from the bottom boundary upward and Eqn.(3.35) from the top boundary downward. Both operations stop when they reach the specified cell element in each vertical column of elements. In this study, this cell element is chosen to be the one at which the X -component of the velocity u reaches the maximum. This two-direction summation procedure was found to be necessary in order to eliminate the accumulation of small errors. It was found that the factor $\Delta y_j/\Delta x_i$ in Eqns.(3.34) and (3.35) can be as large as 10 or greater. Thus even small changes in u can cause large changes in v , sometimes forcing v to become negative. It is worth noting that v at the bottom boundary needed in Eqn.(3.34) is identically zero, according to the surface-adherence condition, and v at the top boundary needed in Eqn.(3.35) is obtained from Eqn.(3.32b) using the Biot-Savart law of induced velocities. It is noted that this approach does ensure that mass is conserved and results in sharply reduced computational cost.

The Distribution of Bound Vorticity. As shown in Eqn.(3.20), $\bar{V}(r_p, t)$ consists of three components, i.e., the velocity due to the onset flow, the free vorticity field and the distribution of bound vorticity. The velocity of the onset flow is a given constant vector, $U_\infty \bar{i}$, and the second term which involves evaluation of the free vorticity field and its contribution to the velocity field were discussed earlier in this chapter. To complete the determination for the velocity field, it remains to evaluate the distribution of bound vorticity. Once the distribution of bound vorticity is known, the induced velocity due to this distribution can be determined as described in the preceding section.

The governing equation for determining the distribution of bound vorticity was given by Eqns.(2.11a, b) which are the Fredholm integral equation of

the second kind, and they can be expressed in the form of Eqn.(2.12). As mentioned in Chapter 2, the integral equation, in our case, does not have a known analytical solution; consequently, an approximate method is employed in which the integral equation (2.12) is approximated as the limiting case of a system of linear algebraic equations. Furthermore, this approximate method enables us to get explicit formulas for the solution of the bound vorticity in term of certain determinants. In view of the coordinate system shown in Figure 3.1, thereby, we have the approximate formula

$$\int_{\Gamma} K(S, T)\gamma(T)dT \cong \sum_{j=1}^n K(S, S_j)\gamma(S_j)\Delta S_j$$

in which $n = N_b$. Eqn.(2.12) then takes the form

$$\gamma(S) \cong f(S) + \sum_{j=1}^n K(S, S_j)\gamma(S_j)\Delta S_j \quad (3.36)$$

which must hold for all values of S along the range of the integration Γ . In particular, this equation is also satisfied at n node points of division $S_i, i = 1, \dots, n$ on Γ . This leads to the system of equations

$$\gamma(S_i) = f(S_i) + \sum_{j=1}^n K(S_i, S_j)\gamma(S_j)\Delta S_j, \quad i = 1, \dots, n. \quad (3.37)$$

writing

$$f(S_i) = f_i, \quad \gamma(S_i) = \gamma_i, \quad K(S_i, S_j) = K_{ij}, \quad (3.38)$$

Eqn.(3.37) yields an approximation for Eqn.(2.12) in terms of the system of n linear equations

$$\gamma_i - \sum_{j=1}^n K_{ij}\gamma_j\Delta S_j = f_i \quad (3.39)$$

in n unknown quantities $\gamma_1, \dots, \gamma_n$. The discrete values of γ obtained by solving this algebraic system are approximate solutions to the integral equation at the points S_1, S_2, \dots, S_n . In matrix form, Eqn.(3.39) can be written as

$$[A] [\gamma] = [B] \quad (3.40)$$

The resolvent coefficient matrix of the algebraic system A is

$$A = \begin{pmatrix} 1 - K_{11}\Delta S_1 & -K_{12}\Delta S_2 & \dots & -K_{1n}\Delta S_n \\ -K_{21}\Delta S_1 & 1 - K_{22}\Delta S_2 & \dots & -K_{2n}\Delta S_n \\ \vdots & \vdots & \ddots & \vdots \\ -K_{n1}\Delta S_1 & -K_{n2}\Delta S_2 & \dots & 1 - K_{nn}\Delta S_n \end{pmatrix}. \quad (3.41)$$

Since the determinant of the above matrix A is non-zero in our case, the inhomogeneous Fredholm equation has a unique solution according to the Fredholm's First Theorem. Also, the solution corresponding to the homogeneous equation, i.e., Eqn.(3.39) with $f_i \equiv 0$, is found to be zero as expected. This is not surprising since the image vorticity has been introduced in deriving Eqn.(3.40). Thus the velocity induced by the bound vorticity is symmetrical about $Y = 0$. However, if the determinant of A turns out to be zero, Eqn.(3.40) either is insoluble or has an infinite number of solutions, depending on the condition which is described by the Fredholm's Third Theorem (Kanwal, 1971). In case there are an infinite number of solutions, the uniqueness of the problem can be obtained by enforcement of a global conservation principle, which requires the total vorticity be conserved for all the instants of time. A case for which this occurs is treated by Cerutti (1984).

To obtain the distribution of bound vorticity, the above system of equations, Eqn.(3.40), is solved by using the Gaussian elimination technique. Once the

distribution of bound vorticity is known, the slip velocity along the surface of the step is determined by

$$\vec{U}_{slip,q} = \begin{cases} -\gamma_q \vec{i}, & \text{if the point } q \text{ is at the horizontal surface;} \\ -\gamma_q \vec{j}, & \text{if the point } q \text{ is at the left vertical surface;} \\ \gamma_q \vec{j}, & \text{if the point } q \text{ is at the right vertical surface.} \end{cases} \quad (3.42)$$

The Vorticity-Stream Function Method

If we apply the circulation theorem to a cell element $\Delta A_{i,j}$ in the fluid (referring to Figure 3.2), the numerical analog of Eqn.(2.32) is obtained as follows:

$$\begin{aligned} -\omega_{i,j} \Delta x_i \Delta y_j = & \frac{\psi_{i,j+1} - \psi_{i,j}}{.5(\Delta y_j + \Delta y_{j+1})} \Delta x_i - \frac{\psi_{i,j} - \psi_{i+1,j}}{.5(\Delta x_i + \Delta x_{i+1})} \Delta y_j \\ & - \frac{\psi_{i,j} - \psi_{i,j-1}}{.5(\Delta y_{j-1} + \Delta y_j)} \Delta x_i + \frac{\psi_{i-1,j} - \psi_{i,j}}{.5(\Delta x_{i-1} + \Delta x_i)} \Delta y_j \end{aligned} \quad (3.43)$$

where it is important to remember that the velocities that make up the right-hand side of Eqn.(3.43) are tangential to the surfaces of the cell element. Upon simplification, one has the final equation

$$\psi_{i,j-1} = B \omega_{i,j} + C \psi_{i,j} + D \psi_{i,j+1} + E \psi_{i+1,j} + F \psi_{i-1,j} \quad (3.44)$$

where

$$B = -\frac{\Delta y_j (\Delta y_{j-1} + \Delta y_j)}{2} \quad (3.44a)$$

$$\begin{aligned} C = 1 + & \frac{\Delta y_j (\Delta y_{j-1} + \Delta y_j)}{\Delta x_i (\Delta x_i + \Delta x_{i+1})} + \frac{\Delta y_j (\Delta y_{j-1} + \Delta y_j)}{\Delta x_i (\Delta x_i + \Delta x_{i-1})} \\ & + \frac{(\Delta y_{j-1} + \Delta y_j)}{(\Delta y_j + \Delta y_{j+1})} \end{aligned} \quad (3.44b)$$

$$D = -\frac{(\Delta y_{j-1} + \Delta y_j)}{(\Delta y_j + \Delta y_{j+1})} \quad (3.44c)$$

$$E = -\frac{\Delta y_j (\Delta y_{j-1} + \Delta y_j)}{\Delta x_i (\Delta x_i + \Delta x_{i+1})} \quad (3.44d)$$

$$F = -\frac{\Delta y_j (\Delta y_{j-1} + \Delta y_j)}{\Delta x_i (\Delta x_i + \Delta x_{i-1})} \quad (3.44e)$$

Recall that the boundary conditions are given by Eqns.(2.33a, b, c). To satisfy the top boundary condition, ideally, the location of the upper boundary must approach infinity as specified in Eqn.(2.33b). However, since the numerical computation requires that the computational domain be finite, the condition is henceforth assumed to be satisfied when $y \geq 4.9h$. In this way and if the central-difference formula is employed to approximate Eqn.(2.33b), one obtains $\psi_{i,N}$, the stream function for the top row of nodes, as follows:

$$\psi_{i,N} = \psi_{i,N-1} + \frac{\Delta y_N + \Delta y_{N-1}}{2}. \quad (3.45)$$

On the other hand, if ψ at the interior node point along the left and right vertical boundaries is denoted as $\psi_{1,j}$ and $\psi_{M,j}$, respectively, the periodic boundary condition specified by Eqn.(2.33c) then becomes

$$\psi_{1,j} = \psi_{M,j} \quad (3.46a)$$

$$\psi_{M+1,j} = \psi_{2,j} \quad (3.46b)$$

Finally, we consider the treatment of boundary condition at the bottom solid surface. Along this surface, ψ is zero as specified by Eqn.(2.33a). However, the numerical scheme used to obtain the stream function in the VSF method requires the calculation of ψ at this surface. As a result, the given condition specified by Eqn.(2.33a) becomes the controlling criterion in the determination of ψ for the entire field. To obtain the finite-difference expression for $\psi_{i,w}$, we consider a typical control volume surrounding the point (i, w) at the horizontal surface as shown in Figure 3.5. The height of this control volume is $.75\Delta y_j$, and the lower control face is midway between the wall and node (i, j) . Using the same procedure

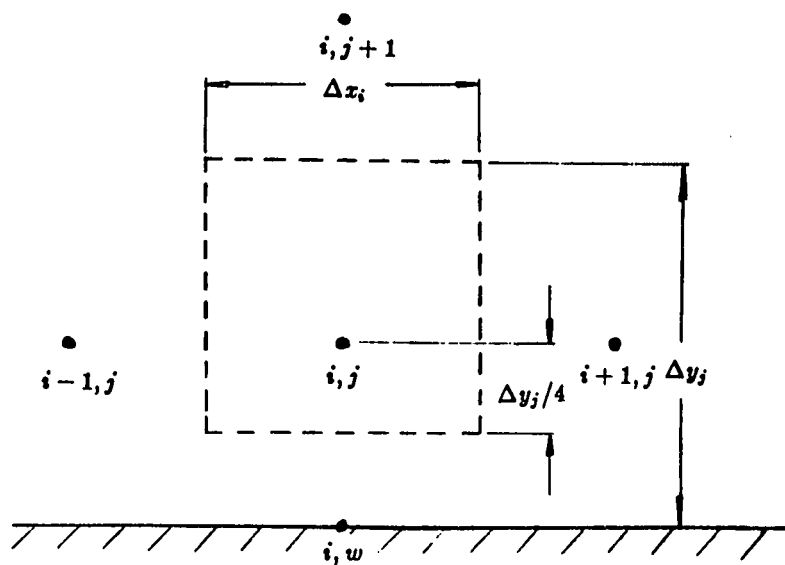


Figure 3.5 Diagram of the control volume used to obtain the finite-difference approximations for the stream function equation at a cell element adjacent to the horizontal surface of the grooved wall.

as used to derive Eqn.(3.43), that is, using the circulation theorem applied to the control volume, we obtain

$$\begin{aligned} \psi_{i,w} = & -(.375\Delta y_j^2)\omega_{i,j} + \left\{ 1 + \frac{\Delta y_j}{\Delta y_j + \Delta y_{j+1}} + .75\Delta y_j^2 \left[\frac{1}{\Delta x_i(\Delta x_i + \Delta x_{i+1})} \right. \right. \\ & \left. \left. + \frac{1}{\Delta x_i(\Delta x_i + \Delta x_{i-1})} \right] \right\} \psi_{i,j} - \left[\frac{.75\Delta y_j^2}{\Delta x_i(\Delta x_i + \Delta x_{i+1})} \right] \psi_{i+1,j} \\ & - \left[\frac{.75\Delta y_j^2}{\Delta x_i(\Delta x_i + \Delta x_{i-1})} \right] \psi_{i-1,j} - \left(\frac{\Delta y_j}{\Delta y_j + \Delta y_{j+1}} \right) \psi_{i,j+1}. \end{aligned} \quad (3.47)$$

The solution algorithm used to calculate ψ is based on the Stabilized Error Vector Propagation (SEVP) method as described by Madala and McDonald, 1981. It is a direct (i.e., non-iterative) method and is an extension of the Error Vector Propagation (EVP) method described by Roache, 1972. The procedure for this algorithm is briefly summarized below.

In the calculation, we begin at the second row from the top (i.e., $j = N - 1$) of the computational domain. If values for the stream function along this row of nodes are assigned arbitrarily, the value of ψ for the nodes at the top boundary (i.e., $j = N$), the left boundary (i.e., $i = 1$) and the right boundary (i.e., $i = M + 1$) can then be obtained using Eqns.(3.45) and (3.46a, b). Following this, Eqn.(3.44) can be used to obtain ψ at the next lower row of nodes (i.e. $j = N - 2$). The result is an expression for $\psi_{i,N-2}$ in terms of $\psi_{i-1,N-1}$, $\psi_{i,N-1}$, $\psi_{i+1,N-1}$, $\psi_{i,N}$, where $i = 2, 3, \dots, M$, and other known quantities. This procedure is repeated for the next lower row of nodes (i.e., $j = N - 3, N - 4, \dots$) until the nodes are reached at the bottom wall and the stream function there is calculated by Eqn.(3.47). Had the initial distribution for ψ along $j = N - 1$ been correctly given, then $\psi_{i,w}$ would be zero as specified by the boundary condition, Eqn.(2.33a). The departure of $\psi_{i,w}$ from zero is a measure of the error, and one can correct the guess for ψ along the second from the top row of nodes according to a systematic procedure

(Madala and McDonald, 1981; Kinney, Taslim and Hung, 1985). In this way, the correct distribution at $j = N - 1$ can be deduced, and the true values for the stream function over the entire field can be determined. As stated earlier, this is a direct solution method which avoids iteration.

This method fails when the number of computational cell elements in the marching direction (i.e., the downward vertical direction) is large. This is because the error introduced at the second top row of nodes will eventually grow until the solution is meaningless. Therefore, the solution has to be stabilized by subdividing the vertical extent of the domain into subregions or blocks. A direct measure of the error can be obtained, and so subdivisions proceed until the error is acceptable. In this work, twenty blocks were used. The maximum error occurs at locations on the block boundaries and is $O(E-8)$; however, most are $O(E-12)$.

Having obtained the stream function, it remains to determine the X and Y components of the velocity. Referring to Figure 3.2, since ψ is computed at node points, the usual expression given by $(\psi_{i,j+1} - \psi_{i,j}) / .5(\Delta y_j + \Delta y_{j+1})$ gives the component of the velocity tangential to the top face of the cell element $\Delta A_{i,j}$. However, the component of the velocity desired is perpendicular to the face of the cell element. These can be found if the values of ψ are known at the intersection points where the vertical and horizontal cell faces are crossed. For this purpose, a biquadratic formula was used to obtain ψ at the desired locations by interpolating the calculated stream function between nine adjacent node points. To illustrate the procedure, consider the nine node points shown in Figure 3.6. Note that there is variable horizontal and vertical spacing. Also the local origin of the x and y coordinates is at node $(i - 1, j - 1)$. In this way, ψ within the nine-point

region can be interpolated by

$$\begin{aligned} \psi = & \left[\psi_1 N_1(x) + \psi_2 N_2(x) + \psi_3 N_3(x) \right] N_1(y) \\ & + \left[\psi_4 N_1(x) + \psi_5 N_2(x) + \psi_6 N_3(x) \right] N_2(y) \\ & + \left[\psi_7 N_1(x) + \psi_8 N_2(x) + \psi_9 N_3(x) \right] N_3(y) \end{aligned} \quad (3.48)$$

where

$$\begin{aligned} N_1(x) &= \frac{(x - h_1)(x - h_1 - h_2)}{h_1(h_1 + h_2)} \\ N_2(x) &= \frac{-x(x - h_1 - h_2)}{h_1 h_2} \\ N_3(x) &= \frac{x(x - h_1)}{h_2(h_1 + h_2)} \end{aligned}$$

and similarly for $N_1(y)$, $N_2(y)$, and $N_3(y)$. Upon rearrangement, Eqn.(3.48) becomes

$$\psi = A + Bx + Cy + Dxy + Ex^2 + Fy^2 + Gx^2y + Hxy^2 + Ix^2y^2. \quad (3.49)$$

The nine unknown coefficients (A, B, \dots, I) are found in terms of the nine values of ψ at the node points $(i-1, j-1)$, $(i, j-1)$, $(i+1, j-1)$, \dots , $(i+1, j+1)$. The values of ψ at the four intersection points are then found from the above equation with the coordinate of (x, y) equal to $(x_{i-1/2}, y_{j-1/2})$, $(x_{i-1/2}, y_{j+1/2})$, $(x_{i+1/2}, y_{j-1/2})$ and $(x_{i+1/2}, y_{j+1/2})$. Since the coefficients A, B, \dots , etc. are not given by simple expressions when the node spacing is nonuniform they are summarized in Appendix B.

It is worth noting, however, that choices do exist when specifying the nine node points used in the interpolation procedure. For example, to interpolate ψ at the point, $(x_{i+1/2}, y_{j+1/2})$, there are up to four possible groups of nine node points which can be formed, and all of them include that point. Since each choice yields a slightly different result, the actual value used in the calculations of the velocity field is taken to be the average of the values from all possible

groups. This ensures that the outflow velocity from one cell element exactly equals the inflow velocity to the cell element immediately downstream from it. Thus the conservative property is preserved. Once the stream function is known at the intersection points of the entire field, components of the velocity normal to the faces of each cell element can be found by applying the central-difference approximations to Eqn.(2.31).

Drag Coefficient

Friction Drag Coefficient

Recalling from Eqn.(2.52), the non-dimensional form of the viscous shear stress is given by

$$\tau_o = -\frac{2}{Re} \omega_o.$$

In the VSF method, the distribution of ω_o is known directly from the numerical solutions; therefore, τ_o can be calculated accordingly. However, in the VVI method, ω_o is not available; instead, it can be evaluated from the diffusive vorticity flux at the surface given by Eqn.(3.8). Along the horizontal surface of grooved wall, Eqn.(3.8) becomes

$$\left. \frac{\partial \omega}{\partial y} \right|_w = \frac{Re}{\Delta t} U_{slip}. \quad (3.50)$$

If the derivative term on the left-hand side of the above equation is approximated by the forward-difference formula and upon rearrangement, Eqn.(3.50) becomes

$$\omega_o = \omega_1 - \frac{Re \Delta l}{\Delta t} U_{slip} \quad (3.51)$$

in which ω_1 is the vorticity at the node point in the vicinity of the surface and Δl is the distance between the points 0 and 1. Substitution of Eqn.(3.51) into

Eqn.(2.52) yields

$$\tau_o = -\frac{2}{Re} \left(\omega_1 - \frac{Re \Delta l}{\Delta t} U_{slip} \right). \quad (3.52)$$

To determine the friction drag coefficient C_{Df} , we need to integrate τ_o over the entire surface as given by Eqn.(2.48b). Note that

$$\bar{e}_t \cdot \bar{e}_d = \begin{cases} 0, & \text{if } dl \text{ is on the vertical surface;} \\ 1, & \text{if } dl \text{ is on the horizontal surface.} \end{cases}$$

Thus, Eqn.(2.48b) reduces to

$$C_{Df} = \int_S \tau_o dl \quad (3.53)$$

where S includes only the horizontal surfaces of the grooved wall. Since τ_o is evaluated at discrete nodal points, the integral in the above equation needs to be carried out numerically. In this calculation, it is determined by employing the simple trapezoidal rule.

Pressure Drag Coefficient

Recalling from Eqn.(2.56), the pressure gradient along the horizontal surface is given as

$$\frac{\partial p_o}{\partial x} = -\frac{2}{Re} \frac{\partial \omega}{\partial y} \Big|_w.$$

By integrating this equation, we obtain

$$p_o(\xi) = p_o(0) - \frac{2}{Re} \int_0^\xi \frac{\partial \omega}{\partial y} \Big|_w dx \quad (3.54)$$

in which ξ is the variable tangential to the horizontal surface. Note that the integration in the above equation can begin at any point on the surface. However, a reference pressure $p_o(0)$ needs to be assigned at an initial point (taken at the origin (0,0) here) before the distribution of surface pressure can be obtained. In the VVI method, the diffusive vorticity flux is obtained directly from Eqn.(3.50).

In the VSF method, on the other hand, $(\partial\omega/\partial y)|_w$ can be determined through the expression in terms of ω at discrete node points using the forward-difference approximation. The result is

$$\frac{\partial\omega}{\partial y}\Big|_w = \frac{\omega_1 - \omega_0}{\Delta l}. \quad (3.55)$$

Since the distribution of surface pressure along the entire surface of the grooved wall is desired, the vorticity diffusive flux at the left and right vertical surfaces of the step must be determined. These can be obtained by following the procedure similar to that used in obtaining Eqn.(3.55). Once the distribution of the vorticity diffusive flux at the entire surface is known, it is then substituted into the corresponding governing equation (either Eqn.(2.56) or (2.57)). The integration is carried out numerically by employing the trapezoidal rule which gives the distribution of pressure at the surface of the grooved wall.

To obtain the pressure drag coefficient C_{Dp} , the integral in Eqn.(2.48c) needs to be carried out along the entire surface of grooved wall. However, since

$$\bar{e}_n \cdot \bar{e}_d = \begin{cases} 1, & \text{if } dl \text{ is on the vertical surface;} \\ 0, & \text{if } dl \text{ is on the horizontal surface,} \end{cases}$$

Eqn.(2.48c) becomes

$$C_{Dp} = \int_S p_o dl \quad (3.56)$$

where S includes only the left and right vertical surfaces of the step. To obtain C_{Dp} , the integration is also carried out numerically using the trapzoidal rule. Finally, the total drag coefficient C_D is evaluated according to Eqn.(2.48).

Choice of the Numerical Parameters

In this section, the choice of the spatial grid increments is presented first. It is then followed by the discussion of the time increment. Finally, the

specification of the spatial increment for the evaluation of the distribution of the bound vorticity concludes this section.

Spatial Grid Increments

In the present study, the grid network near the corners of the step in the primary computational domain, Figure 3.1, is generated using an algorithm based on the Schwarz-Christoffel transformation applied to the flow over a forward-facing step which is infinitely long. As discussed in Appendix C, the physical boundary (i.e., the forward-facing step) is transformed into a straight line of infinite extent in the transformed plane. To obtain the grid distribution, we first divide the height of the step in the transformed plane into 10 uniform spatial increments. The corresponding spatial increments for the step height in the physical plane can then be obtained. It is observed that this transformation results in a higher density of cell elements in the region near the corner of the step. As mentioned earlier, this is desirable because in the region of large vorticity and velocity gradients, the grid size generally needs to be refined in order to improve the numerical accuracy. Finally, the refined grid increments near the corner of the step are employed to construct the grid coordinates for the present calculation. The procedure to obtain this grid coordinates is described as below.

To start, the first seven increments near the corner of the step, which correspond to 0.00893428, 0.0223357, 0.0376768, 0.0498574, 0.0553687, 0.0687468 and 0.0800158, respectively, are chosen as the base increments. Note that the total length of these base increments obtained by summing them up is 0.3229355. To construct the vertical spatial increments (i.e., Δy_j), the grid distribution along the length from $Y = 0.5$ to 1.0 is obtained first by employing the base increments

and two additional increments with a constant value of 0.0885323, which are obtained by equally dividing the difference between the length of 0.5 and 0.3229355. This grid distribution is then reflected to the region from $Y = 0$ to .5 and from $Y = 1.0$ to 1.5. Finally, a constant value of 0.1 is chosen for the grid increments for the coordinates $Y \geq 1.5$.

To construct the horizontal spatial increments (i.e., Δx_i), the base increments plus four additional increments corresponding to 0.114167, 0.144114, 0.179479 and 0.239305, respectively, are first used along the length from $X = 0$ to 1.0. This distribution of grid increments is again reflected to the region from $X = 1.0$ to 2.0, $X = 2.0$ to 3.0 and $X = 3.0$ to 4.0. In this manner, there are totally 62 and 44 spatial increments in the vertical (Y) and the horizontal (X) direction, respectively. It is clear that the grid coordinates are symmetric with respect to the center of the step (i.e., $X = 2.0$), and the center of the groove (i.e., $X = 0$). The symmetric behavior can also be easily seen in the regions of $Y = 0$ to $Y = 0.5$, $Y = 0.5$ to $Y = 1.0$ and $Y = 1.0$ to $Y = 1.5$.

Time Increment

The time-explicit finite difference equation, Eqn.(3.6), used to generate the vorticity at the new time level, implies a limit on the time interval, Δt . The relation governing the determination of Δt can be obtained by requiring that the magnitude of errors introduced into the vorticity field do not grow in time. This leads to the stability criterion for the solution of Eqn.(3.6).

In order to select a suitable time step, the stability analysis with the above stability criterion is performed on Eqn.(3.6). Examples of this analysis can be found in Hung (1982); Torrance and Rockett (1969). The result is summarized below.

First write the finite-difference equation in the following form.

$$\begin{aligned}
\omega_{i,j}^+ = & F \omega_{i,j} + \frac{\Delta t}{\Delta x_i \Delta y_j} \left\{ \omega_{i-1,j} \left[f_1 \Delta y_j u_{i-\frac{1}{2},j} + \frac{1}{Re} \frac{\Delta y_j}{H_i} \right] \right. \\
& + \omega_{i+1,j} \left[-(1-f_2) \Delta y_j u_{i+\frac{1}{2},j} + \frac{1}{Re} \frac{\Delta y_j}{H_r} \right] \\
& + \omega_{i,j-1} \left[f_3 \Delta x_i v_{i,j-\frac{1}{2}} + \frac{1}{Re} \frac{\Delta x_i}{H_b} \right] \\
& \left. + \omega_{i,j+1} \left[-(1-f_4) \Delta x_i v_{i,j+\frac{1}{2}} + \frac{1}{Re} \frac{\Delta x_i}{H_t} \right] \right\} \quad (3.57)
\end{aligned}$$

where

$$\begin{aligned}
F = & 1 + \frac{\Delta t}{\Delta x_i \Delta y_j} \left\{ \Delta y_j \left[(1-f_1) u_{i-\frac{1}{2},j} - f_2 u_{i+\frac{1}{2},j} \right] \right. \\
& + \Delta x_i \left[(1-f_3) v_{i,j-\frac{1}{2}} - f_4 v_{i,j+\frac{1}{2}} \right] \\
& \left. - \frac{1}{Re} \left[\frac{\Delta x_i}{H_t} + \frac{\Delta x_i}{H_b} + \frac{\Delta y_j}{H_r} + \frac{\Delta y_j}{H_i} \right] \right\}. \quad (3.58)
\end{aligned}$$

The stability of Eqn.(3.57) requires that the coefficient F , defined by Eqn.(3.58), be greater than or equal to zero at each fluid element for every instant of time. It is observed that this condition relates the time step to the grid increments and the Reynolds number. The grid coordinates were discussed in the preceding section, and the Reynolds number is chosen to be 100 in the present study. The base geometry of the grooved wall is selected to be $a=4.0$ and $d=2.0$. The procedure then becomes one of selecting a time step Δt which insures that the coefficient F in Eqn.(3.58) is greater than zero. Note that near the surface of the grooved wall, the velocities are very small and diffusive transport predominates. It is apparent from Eqn.(3.58) that a stable Δt implies that vorticity diffused from the surface does not penetrate beyond the first layer of fluid cells. On the other hand, in the region where the convective transport predominates, a stable Δt requires that a particle of fluid should not enter and exit any cell element during a single time

step. In general, both of the above restrictions are met when the effect of both diffusive and convective transport are of equal importance. Since the velocity is not known a priori at each time level, a stable time increment must be selected as the solution proceeds. This is done before the vorticity is obtained at each new time level.

Spatial Increments for the Distribution of Bound Vorticity

Because the distribution of bound vorticity is required to determine the production of vorticity at the solid surface in the VVI method, the solution of the Fredholm integral equation is performed at every time step, accordingly. As discussed earlier in this chapter, the numerical evaluation of this equation involves a system of N_b linear algebraic equations in N_b unknown, where N_b is the number of bound vortex elements distributed on the surface of the step. Practically, N_b should be large in order to approximate the integral equation with sufficient accuracy, and in principal, it can be chosen independently without relating it to the cell elements in the computational domain shown in Figure 3.1. In the present study, $N_b=198$ is chosen initially to obtain the potential-flow solution, which corresponds to the initial flow field for the calculations. This is all that is needed to advance the solution of the vorticity transport equation for one increment of time interval. After that instant, N_b is set equal to 58 which is equal to the number of cell elements along the surface of the step in the computational domain. Trial cases indicate that this number is sufficient, since the large gradient of the velocity near the two upper corners of the step found in the potential flow is reduced significantly after the viscous effect enters the calculation during the first time interval. In addition, it is noticed that the reduction of the number of bound vorticity elements results in a small savings in the computational cost.

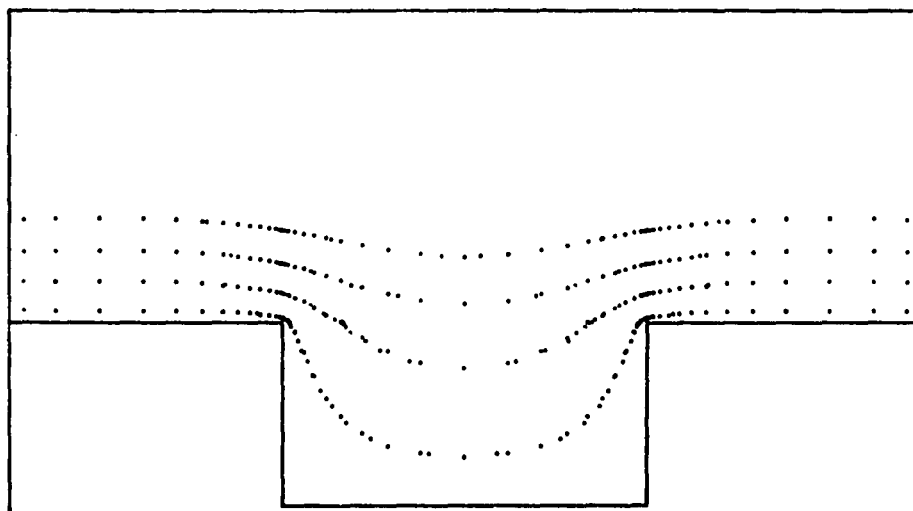
CHAPTER 4

RESULTS AND DISCUSSION

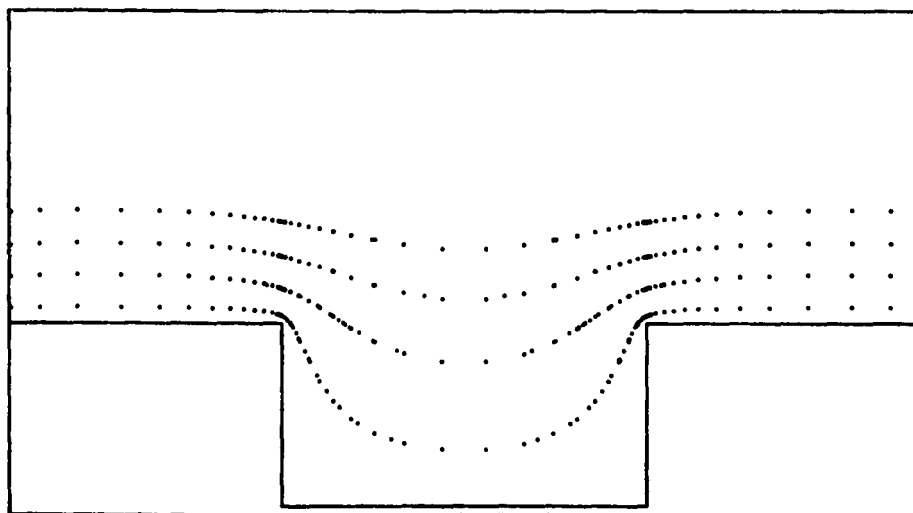
In this chapter, the results of the computations for the flow over a grooved wall are presented and discussed. First, the discussion and comparison of the numerical results obtained from the VVI and VSF methods for a dimensionless time period of 6 units are presented. The flow is then investigated by using only the VSF method from that instant up to the time of 16 units. At the final instant of time, the flow is believed to be very close to a steady state.

The comparisons are made by presenting three groups of pictures. The first are the pictures showing the general behavior of the flow described in the form of stream function and vorticity contours. The second are the pictures showing the velocity profiles versus the distance in the vertical direction, i.e., in the Y direction. Finally, the plots showing the distribution of shear stress and pressure along the solid surface and the time development of the drag coefficient conclude this part of the discussion.

It is worth noting that in the present study, the computations using the VVI and VSF methods are performed over the same computational domain as shown in Figure 3.1, with the same Reynolds number, i.e., $Re = 100$, and with the same initial state, which is taken to be the potential flow with the vorticity field identical zero. The contours of the stream function for potential flow obtained using the VVI and VSF methods are shown in Figures 4.1(a), and (b), respectively. It is noticed that the symmetry of the stream function contours about the



(a)



(b)

Figure 4.1 Plots of the stream function contours for the potential flow over the grooved wall from (a) the VVI method and (b) the VSF method.

center of the groove, i.e., the Y -axis, in each picture is observed, which is consistent with the potential flow theory. The velocity profiles for the X -component of velocity versus the distance in the vertical direction at $X = -0.7571, 0, 0.7571, 0.9911$ and 1.0689 are given in Figures 4.2 through 4.6, and the distribution of pressure along the solid surface is given in Figure 4.7. Note that the symmetry of the flow can again be justified since the same velocity profiles are obtained at $X = 0.7571$ and -0.7571 , which locations are placed symmetrically with respect to the center of groove. This is also confirmed by the distribution of pressure along the wall. In general, good agreement between the stream function contours, velocity profiles and pressure distributions is observed, which ensures that both methods have almost the same initial state. It is worth noting, however, that the negative spikes in the pressure distribution are more pronounced for the VVI method than for the VSF method.

The viscous-flow results in the form of stream function and vorticity contours are plotted for a single groove in Figures 4.8 through 4.21. Results at 7 different instants of time are presented. The first series corresponds approximately to a dimensionless time of 0.5 units, with the remaining series corresponding to approximately 1.0, 1.5, 2.0, 3.0, 4.0 and 6.0 units of time, respectively. Each series consists of two figures with each of them corresponding to the results from either the VVI or the VSF methods. In each figure, there are two pictures showing the contours of constant stream function and vorticity, respectively. The values of the constants chosen in the stream function contours are 0.7, 0.5, 0.3, 0.1, 0., -0.01, -0.02, -0.04, -0.06, -0.08, and the values of the constants chosen in the vorticity contours are -0.1, -0.5, -1.0, -2.0, -5.0, 0.2, 1.0.

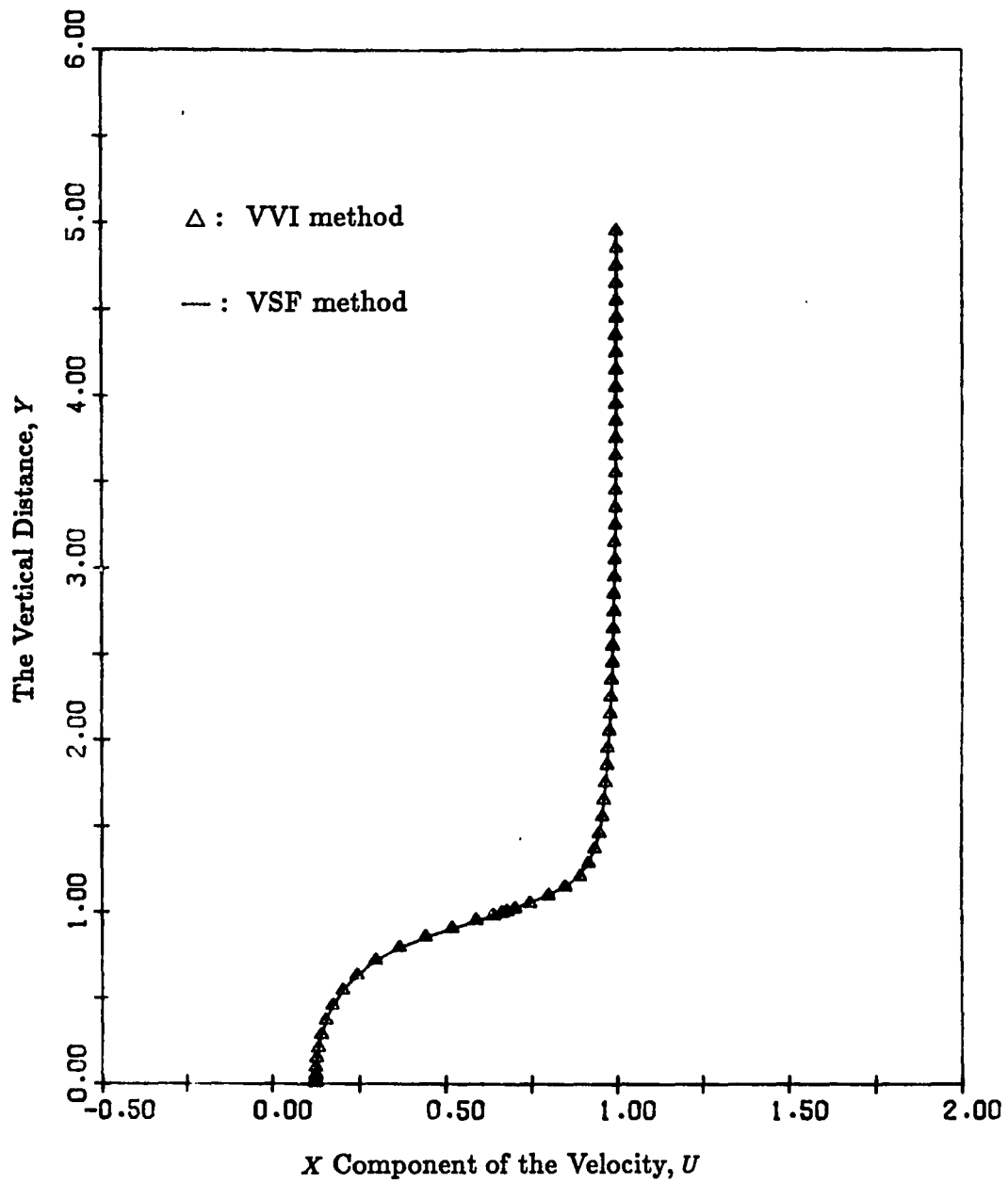


Figure 4.2 Plots of the X component of velocities obtained from the VVI and VSF methods as a function of the vertical distance from the bottom wall for potential flow at $X = -0.7571$.

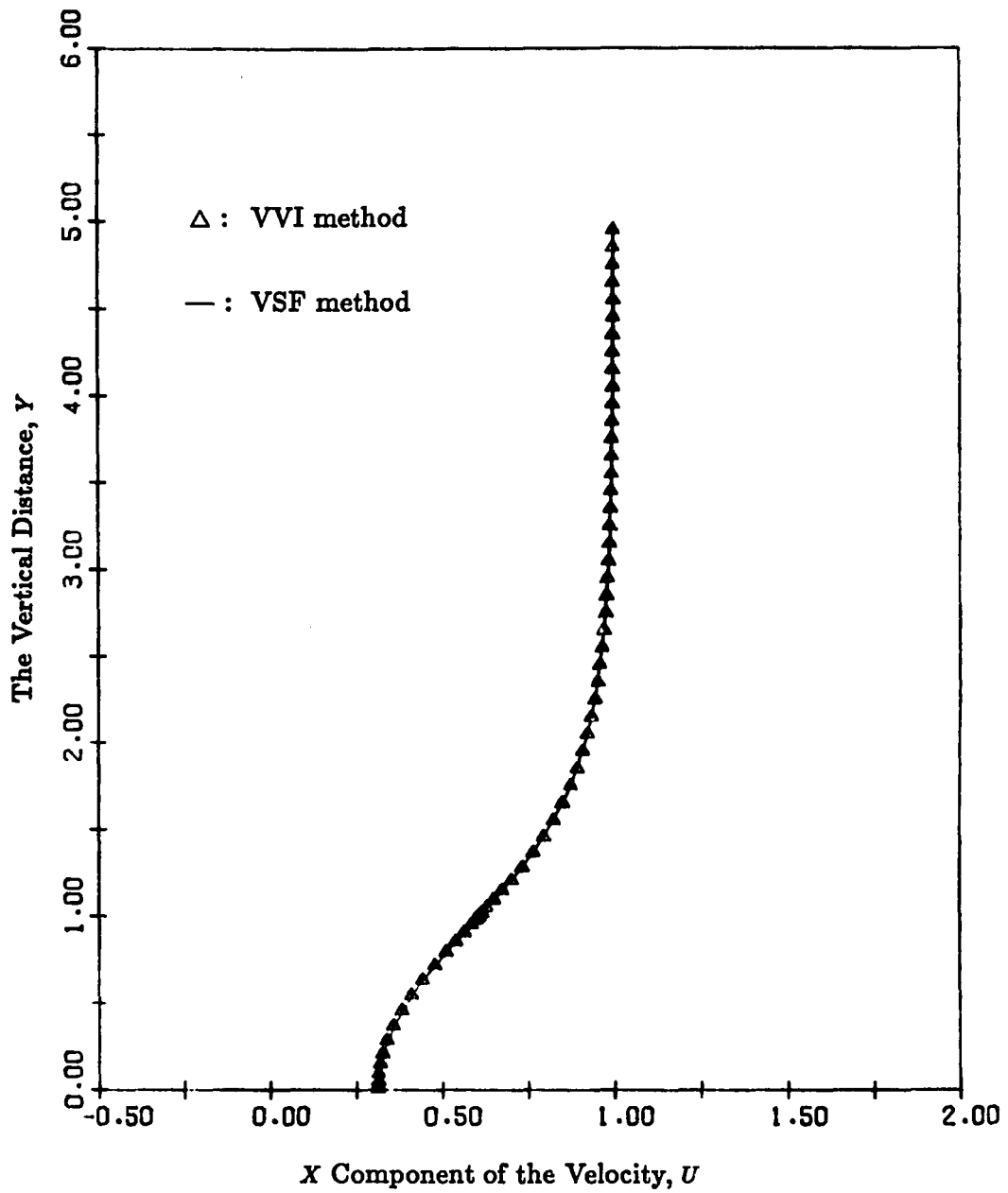


Figure 4.3 Plots of the X component of velocities obtained from the VVI and VSF methods as a function of the vertical distance from the bottom wall for potential flow at $X = 0$.

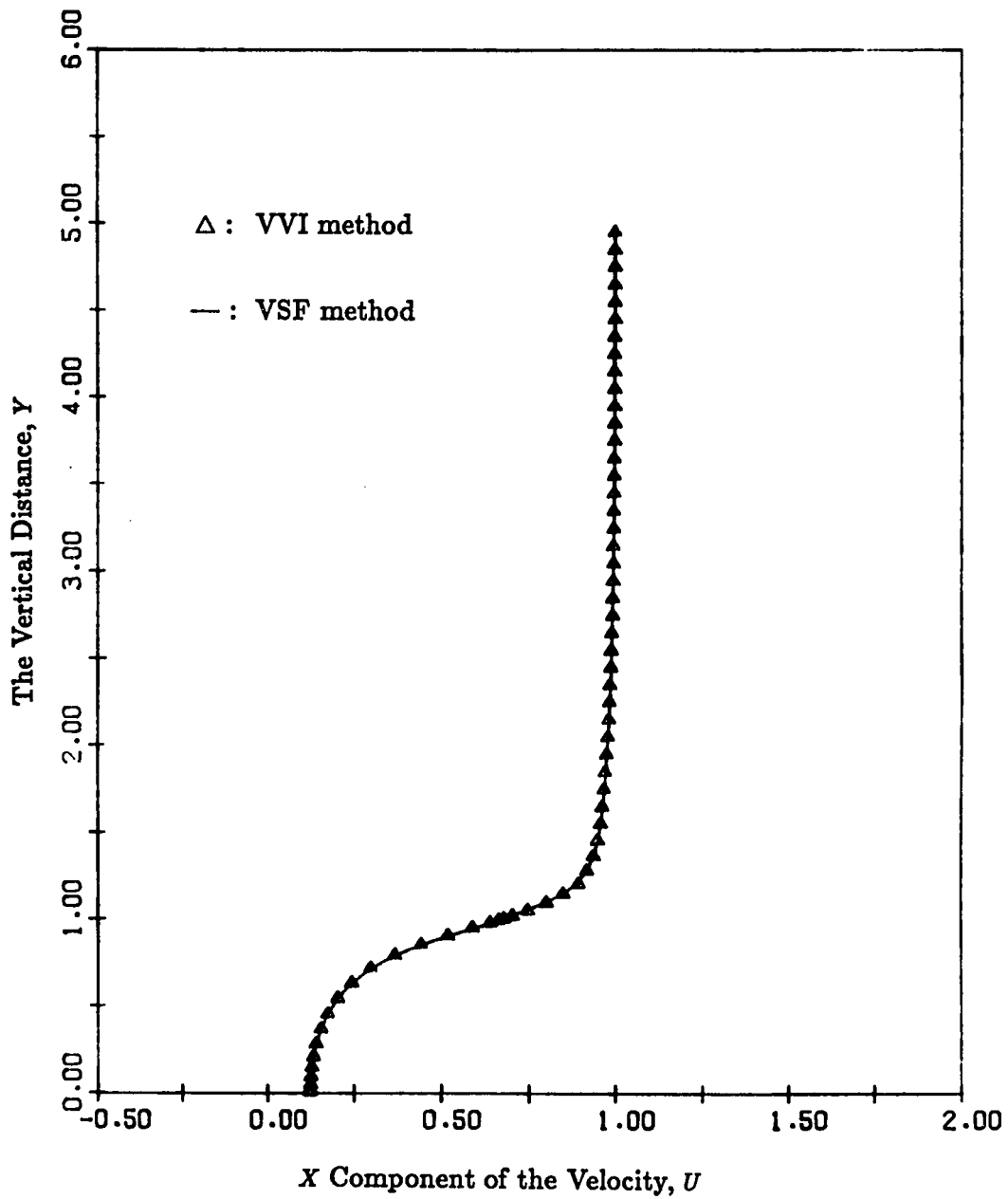


Figure 4.4 Plots of the X component of velocities obtained from the VVI and VSF methods as a function of the vertical distance from the bottom wall for potential flow at $X = 0.7571$.

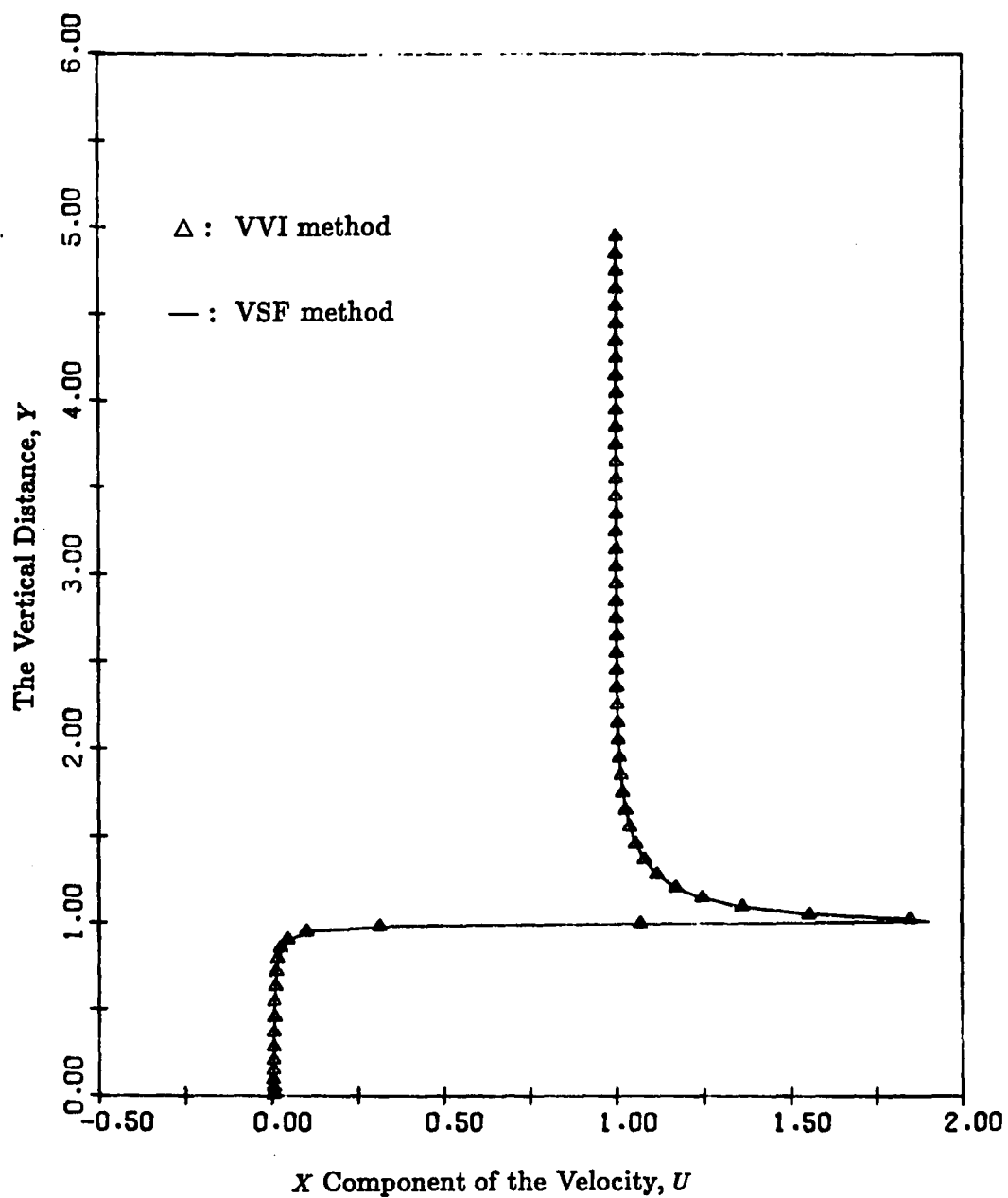


Figure 4.5 Plots of the X component of velocities obtained from the VVI and VSF methods as a function of the vertical distance from the bottom wall for potential flow at $X = 0.9911$.

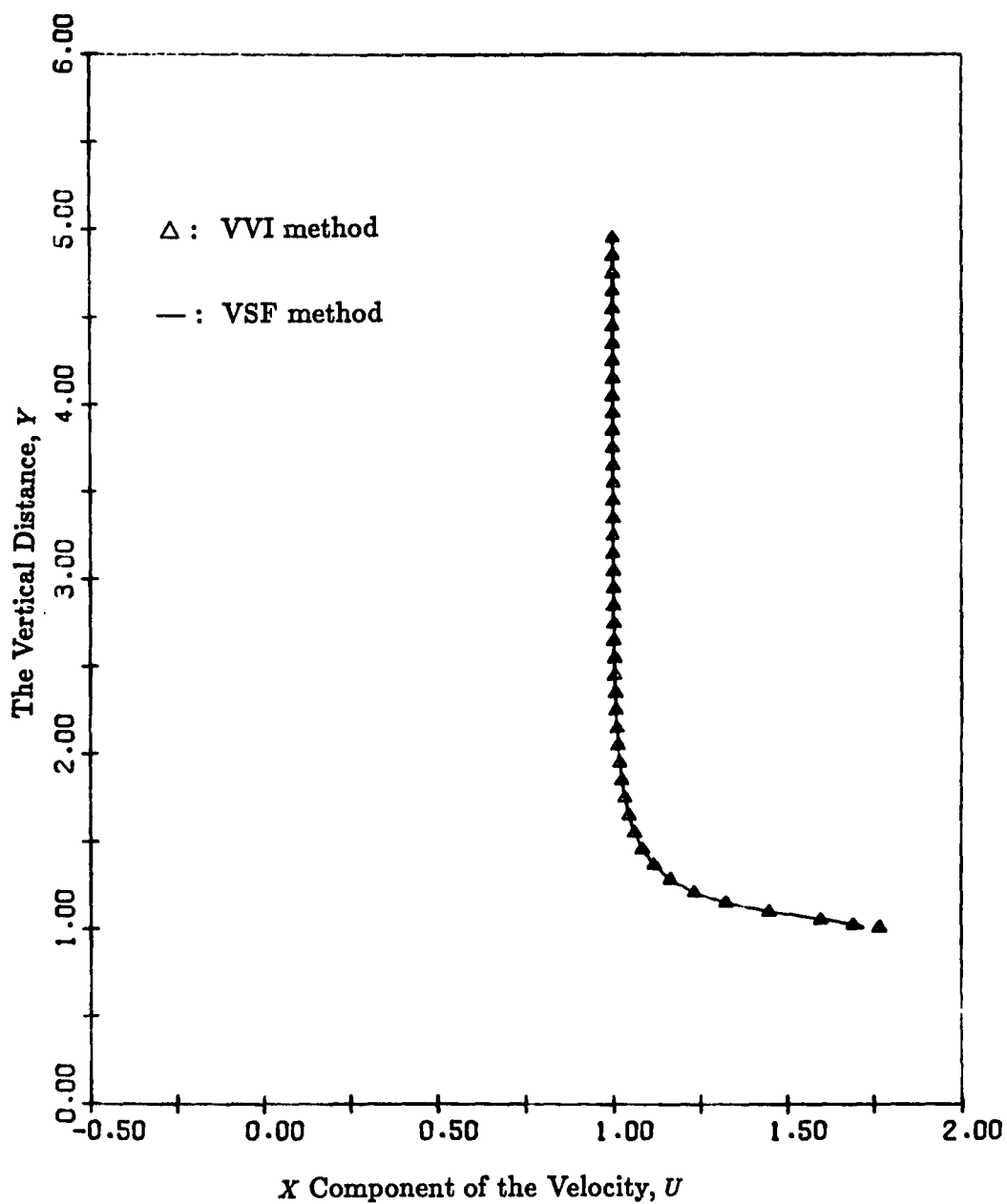


Figure 4.6 Plots of the X component of velocities obtained from the VVI and VSF methods as a function of the vertical distance from the bottom wall for potential flow at $X = 1.0689$.

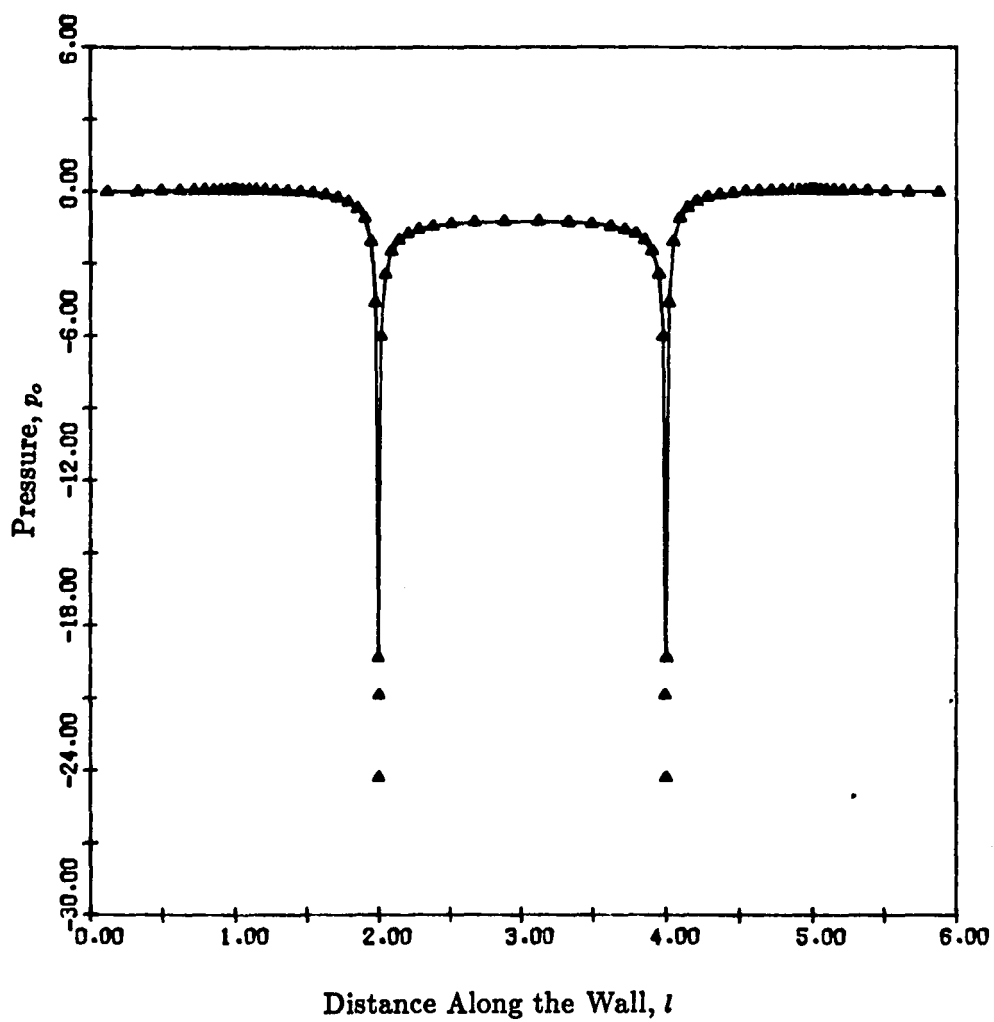
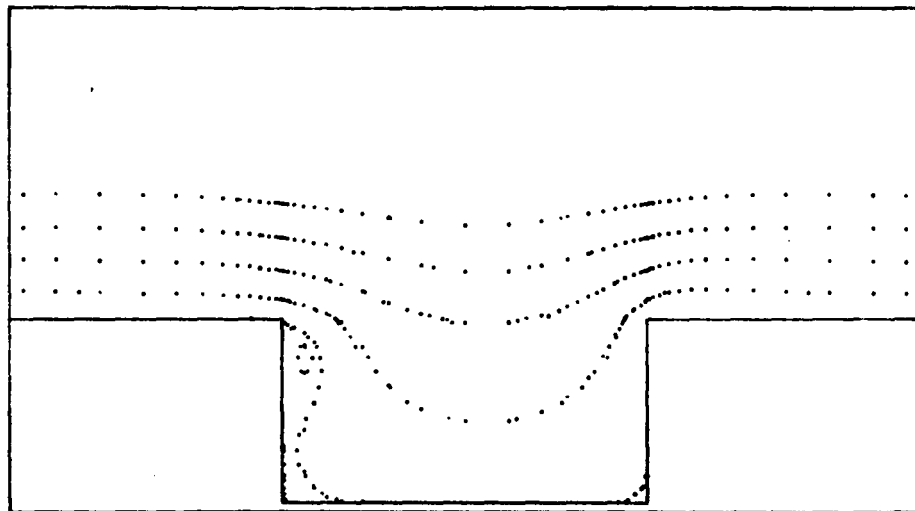
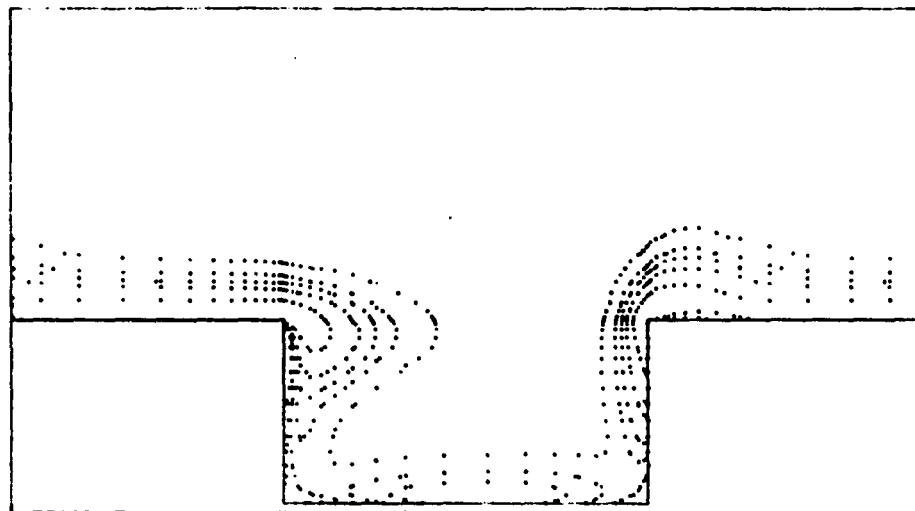


Figure 4.7 Plots of the distribution of surface pressure along the wall for potential flow obtained from the VVI (Δ) and VSF ($-$) methods.

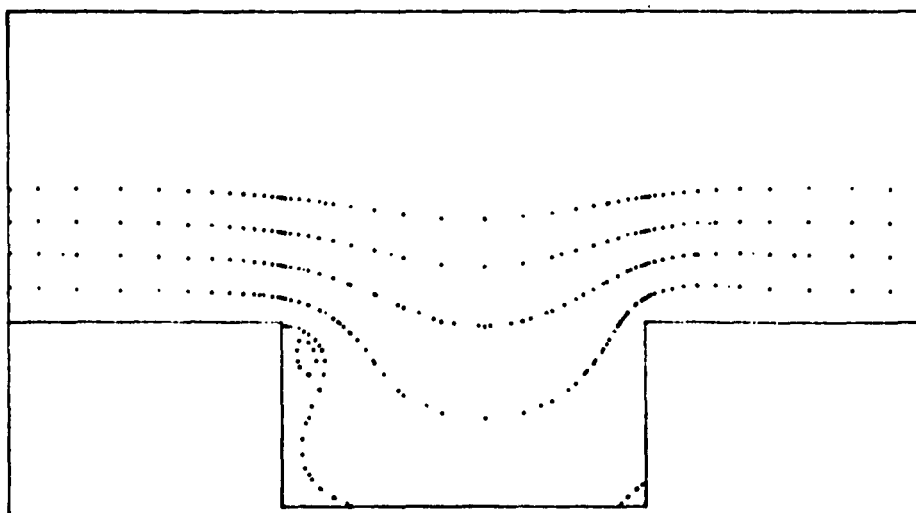


(a)

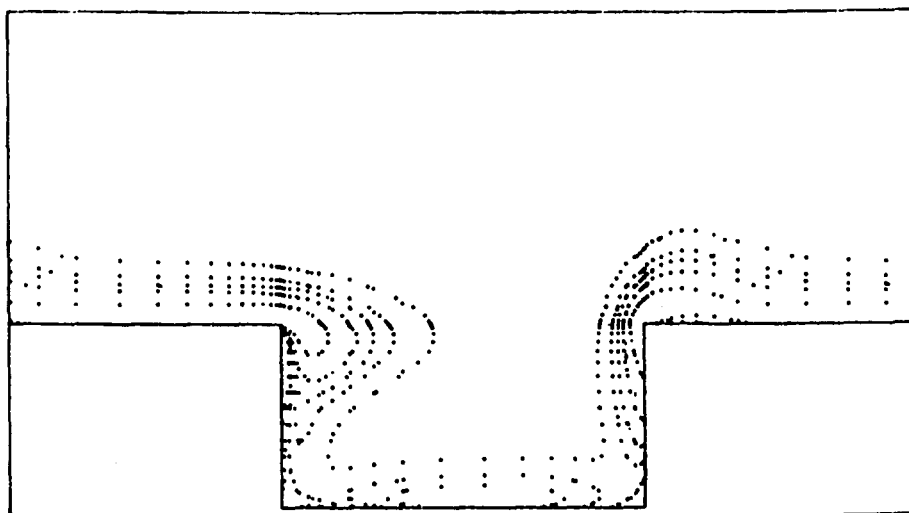


(b)

Figure 4.8 Plots of the (a) stream function and (b) vorticity contours for unsteady flow over the grooved wall at $t=0.500146$ using the VVI method.

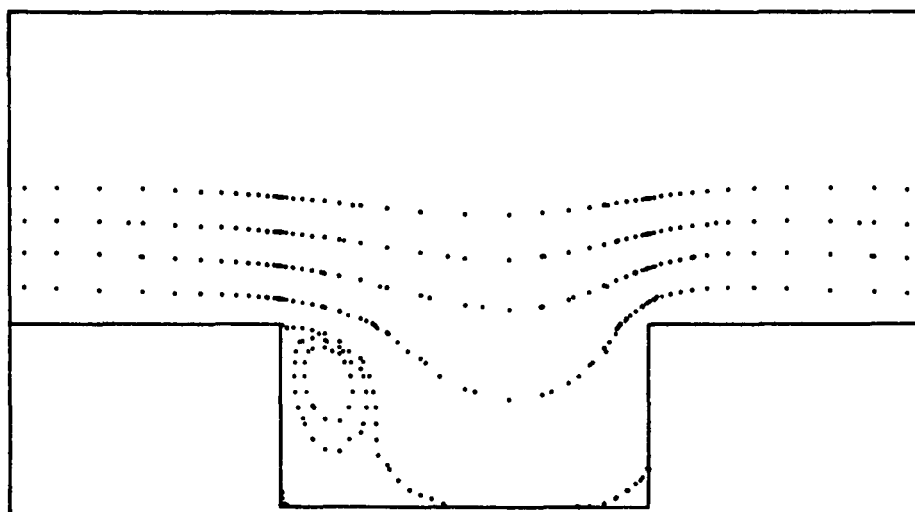


(a)

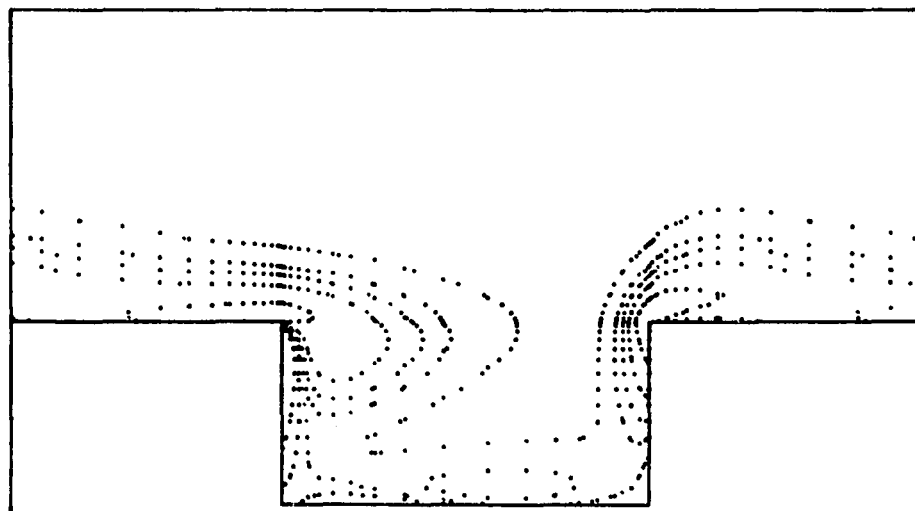


(b)

Figure 4.9 Plots of the (a) stream function and (b) vorticity contours for unsteady flow over the grooved wall at $t=0.500641$ using the VSF method.

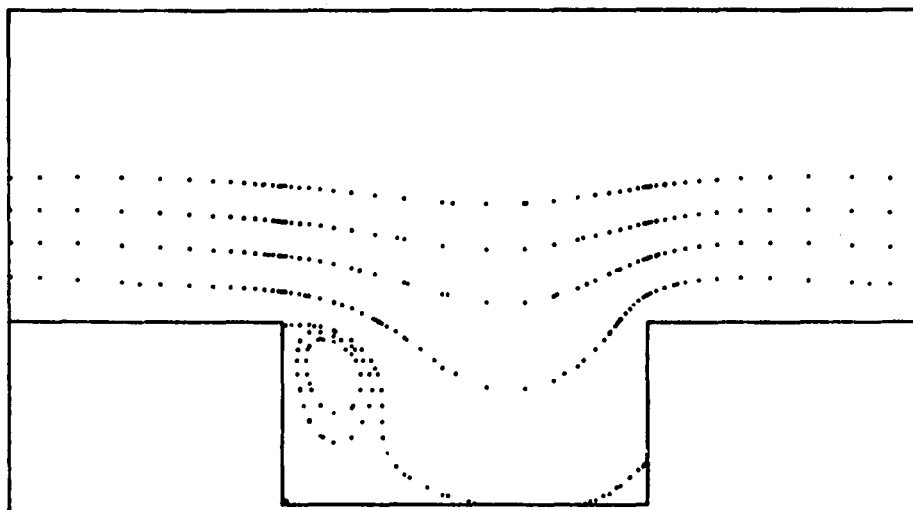


(a)

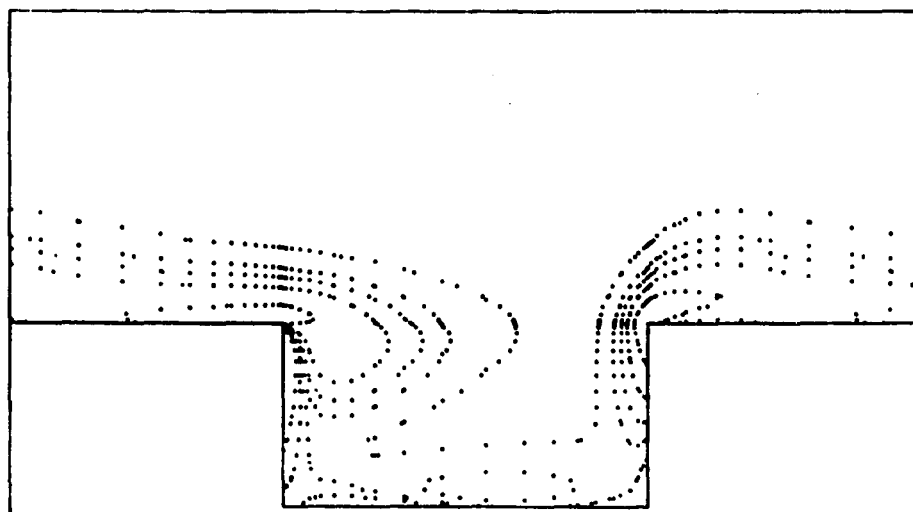


(b)

Figure 4.10 Plots of the (a) stream function and (b) vorticity contours for unsteady flow over the grooved wall at $t=0.99921$ using the VVI method.

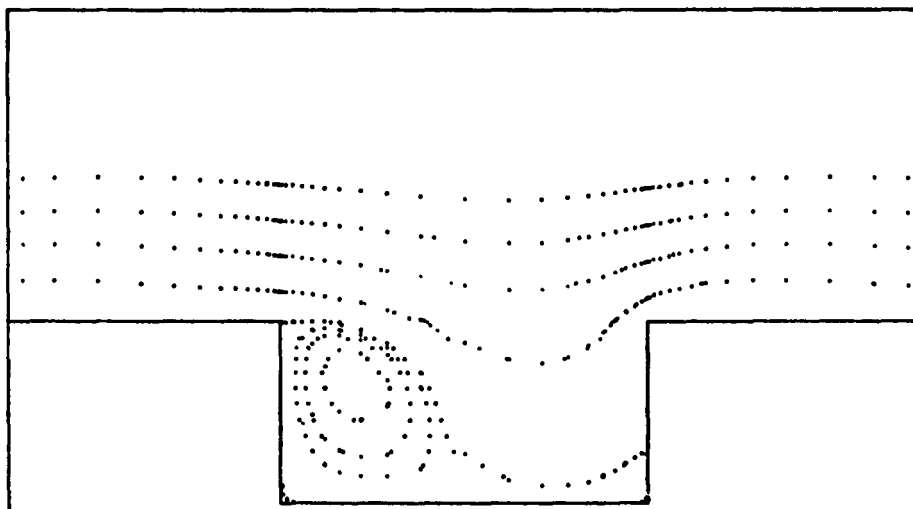


(a)

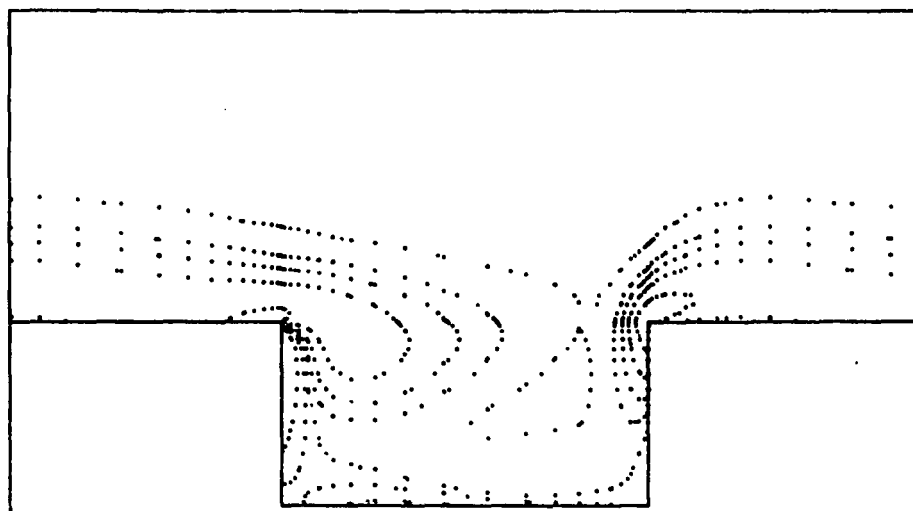


(b)

Figure 4.11 Plots of the (a) stream function and (b) vorticity contours for unsteady flow over the grooved wall at $t=0.999413$ using the VSF method.

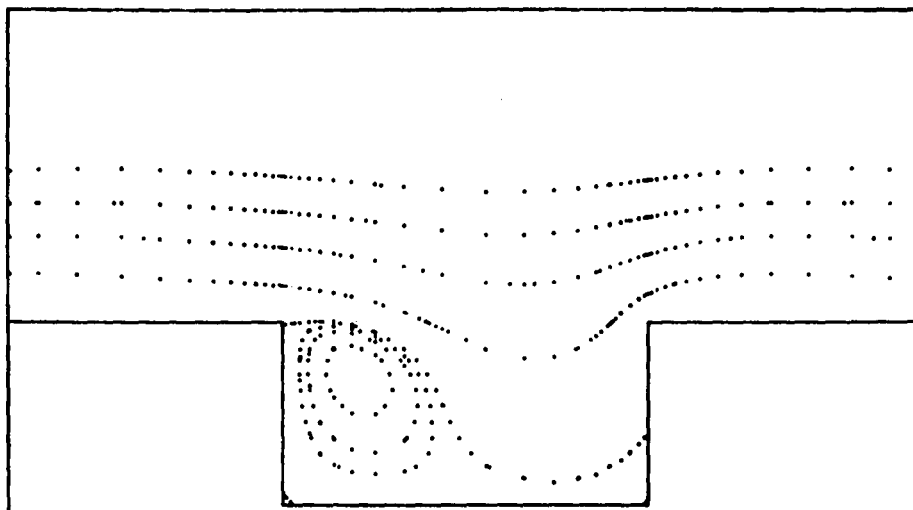


(a)

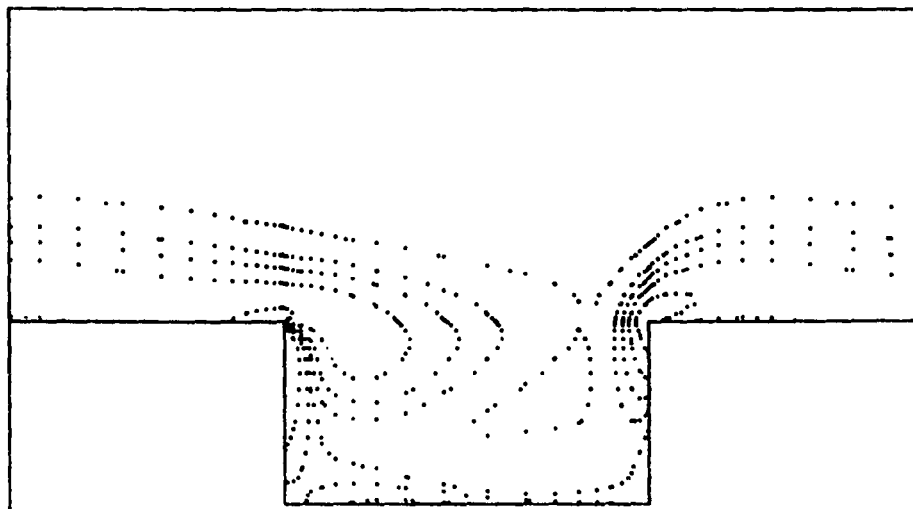


(b)

Figure 4.12 Plots of the (a) stream function and (b) vorticity contours for unsteady flow over the grooved wall at $t=1.49715$ using the VVI method.

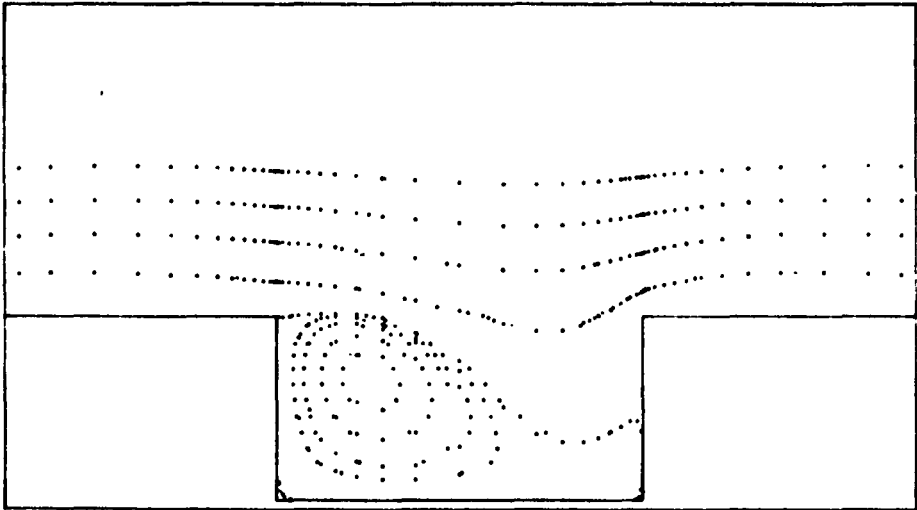


(a)

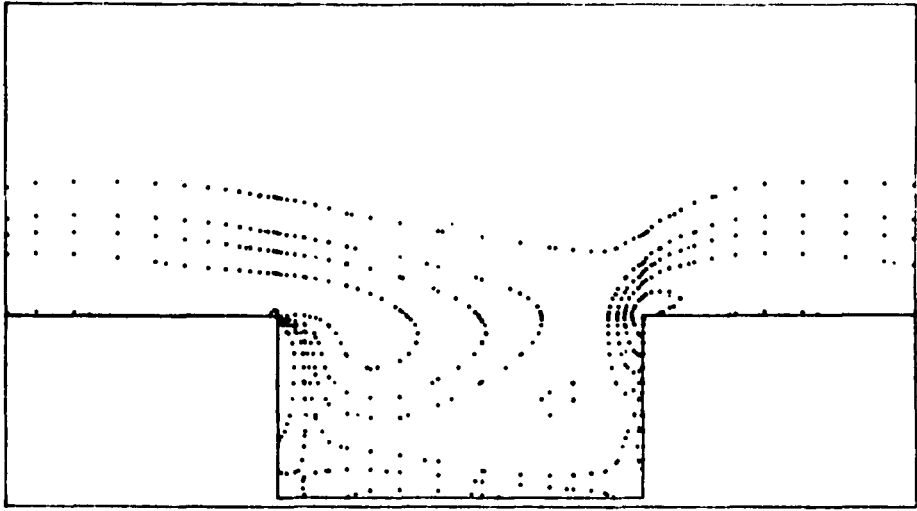


(b)

Figure 4.13 Plots of the (a) stream function and (b) vorticity contours for unsteady flow over the grooved wall at $t=1.49973$ using the VSF method.

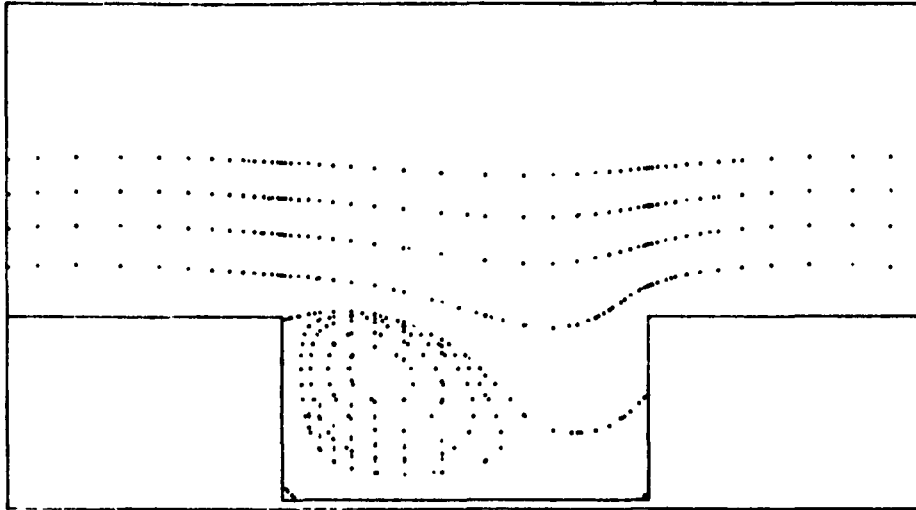


(a)

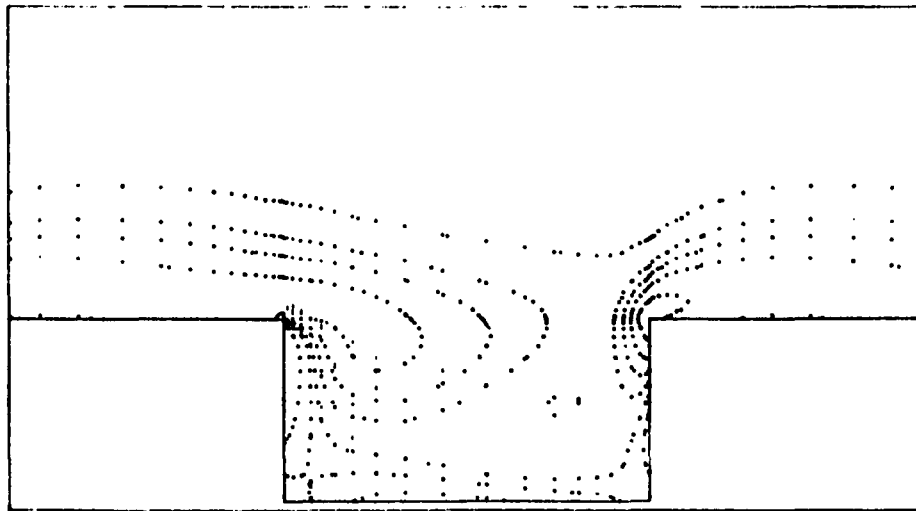


(b)

Figure 4.14 Plots of the (a) stream function and (b) vorticity contours for unsteady flow over the grooved wall at $t=1.9998$ using the VVI method.

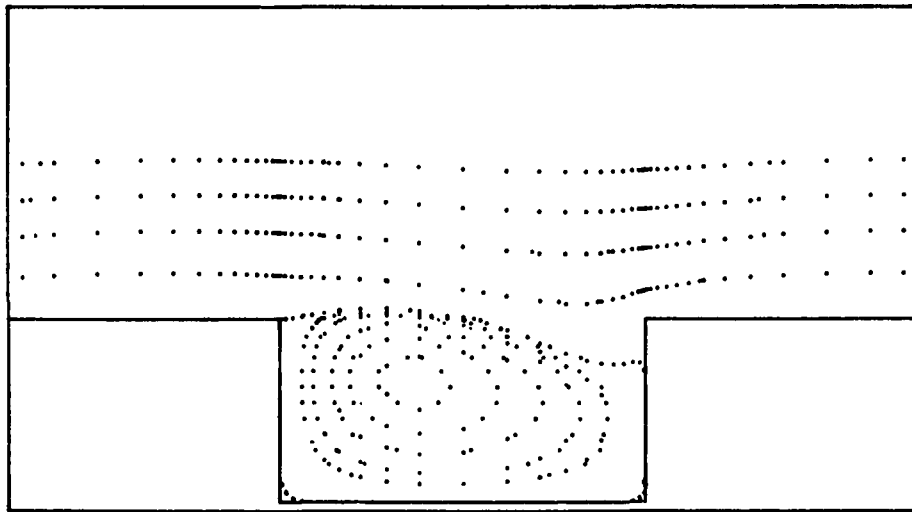


(a)

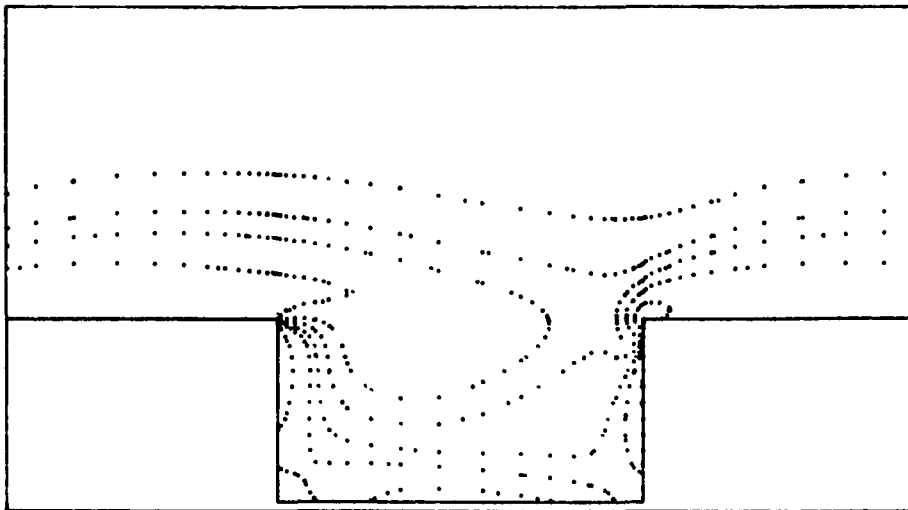


(b)

Figure 4.15 Plots of the (a) stream function and (b) vorticity contours for unsteady flow over the grooved wall at $t=2.00004$ using the VSF method.

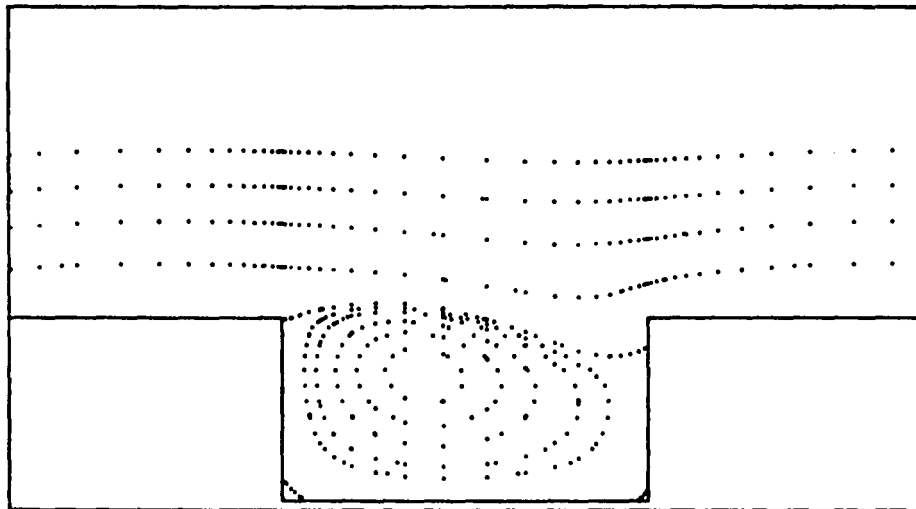


(a)

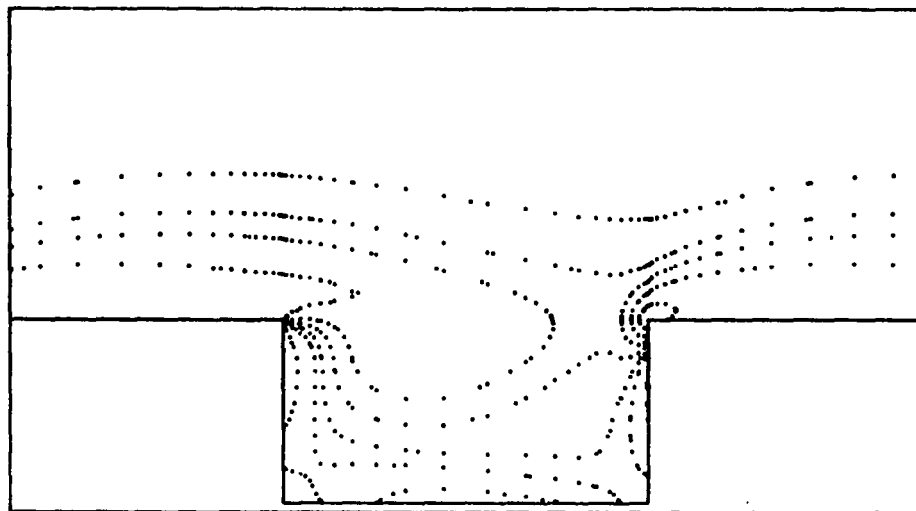


(b)

Figure 4.16 Plots of the (a) stream function and (b) vorticity contours for unsteady flow over the grooved wall at $t=3.00098$ using the VVI method.

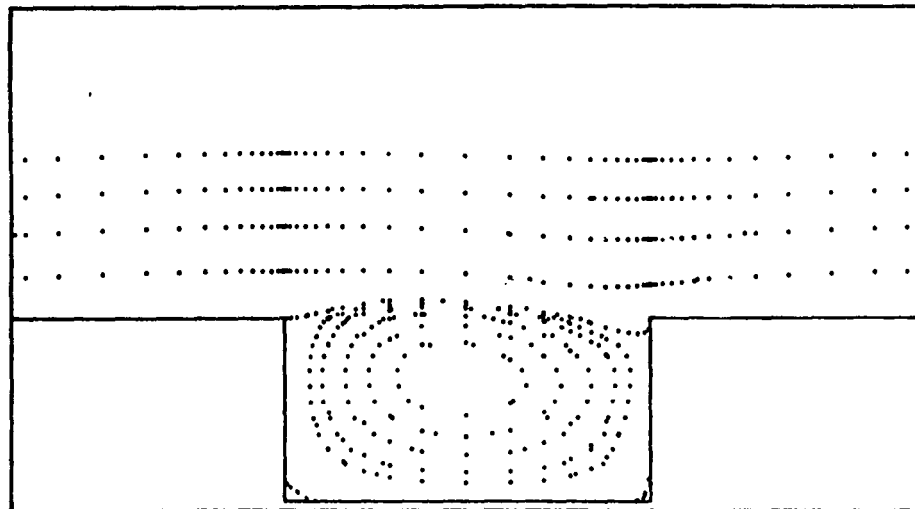


(a)

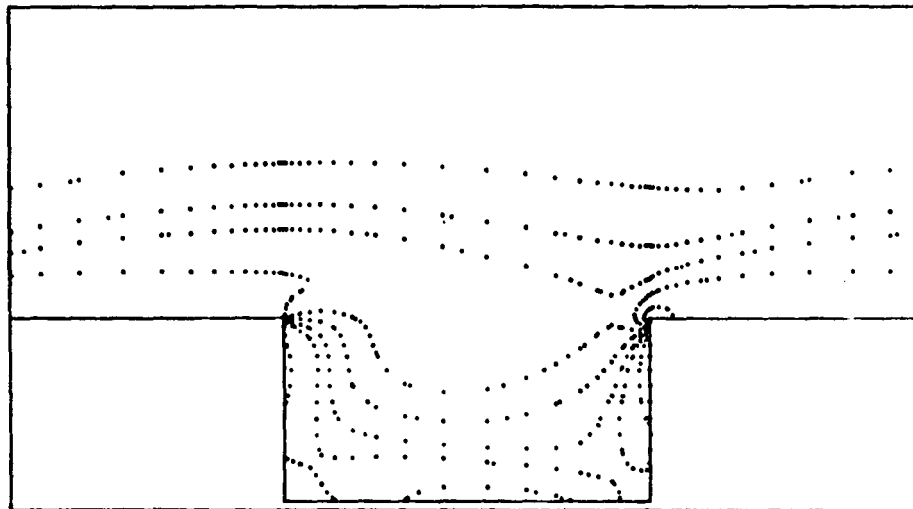


(b)

Figure 4.17 Plots of the (a) stream function and (b) vorticity contours for unsteady flow over the grooved wall at $t=3.00067$ using the VSF method.

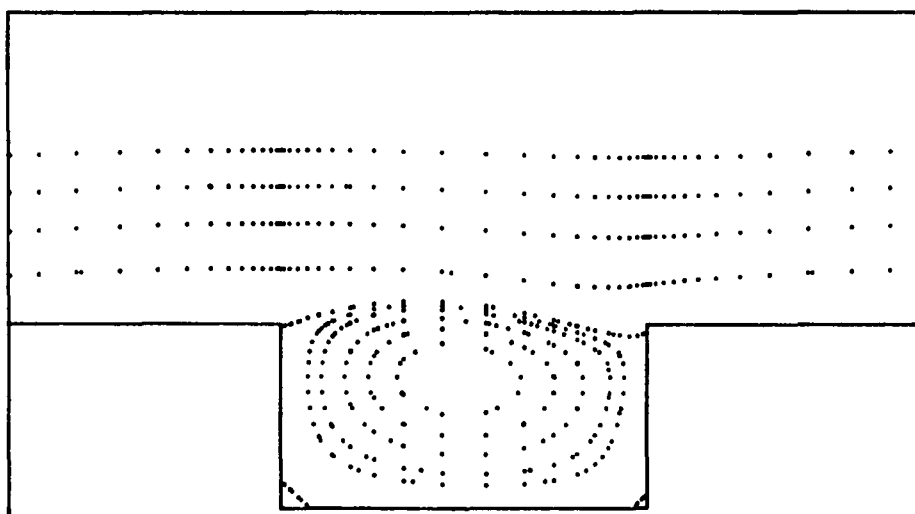


(a)

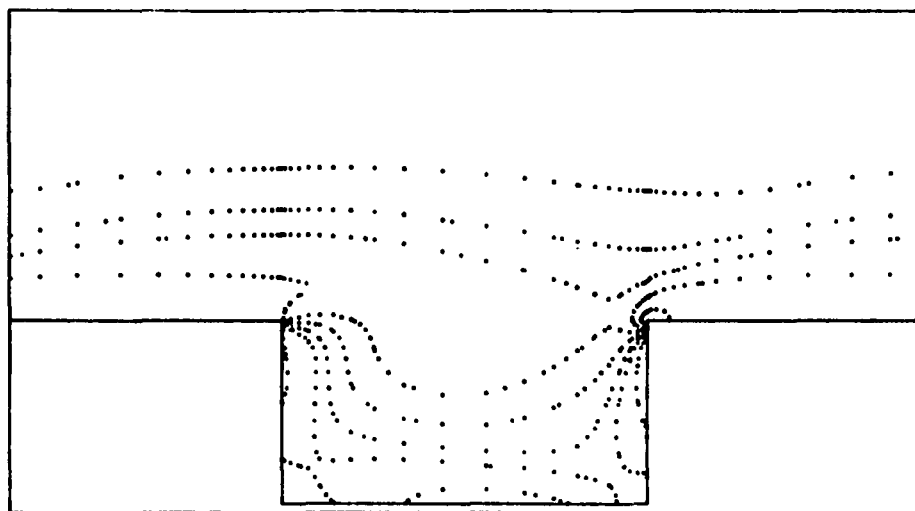


(b)

Figure 4.18 Plots of the (a) stream function and (b) vorticity contours for unsteady flow over the grooved wall at $t=3.99888$ using the VVI method.

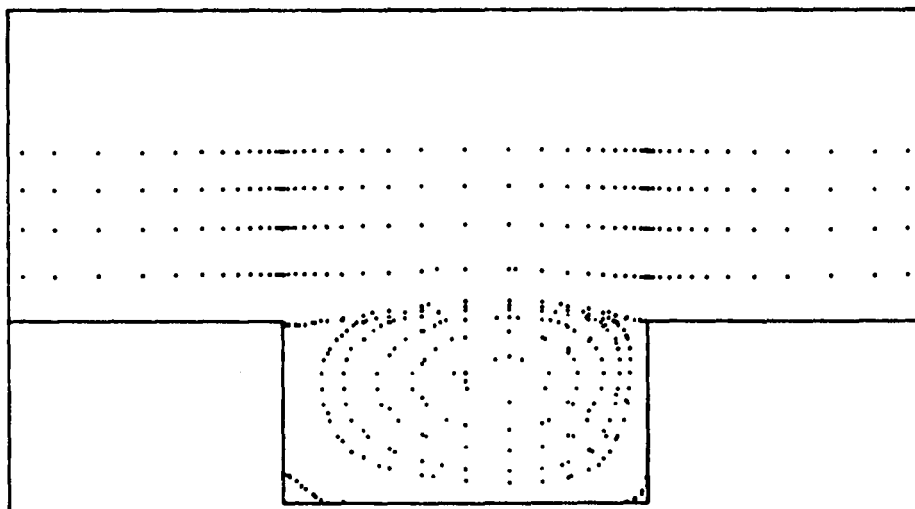


(a)

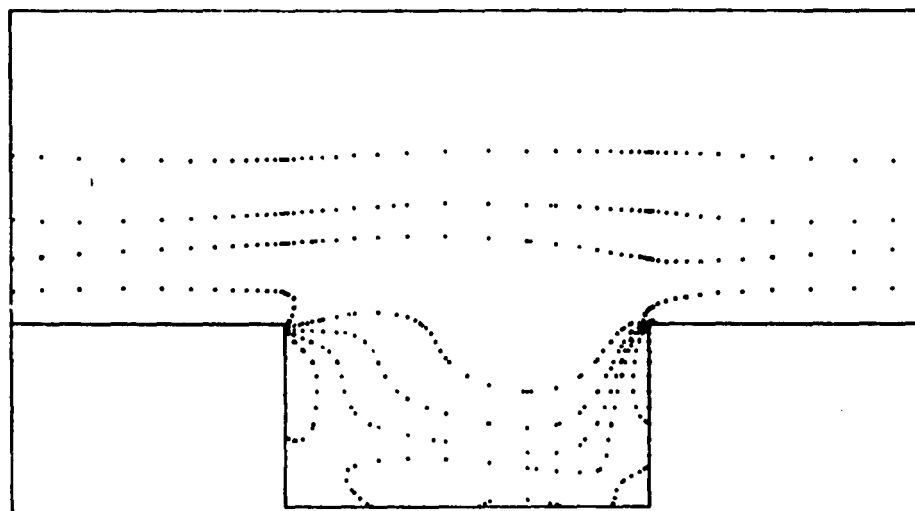


(b)

Figure 4.19 Plots of the (a) stream function and (b) vorticity contours for unsteady flow over the grooved wall at $t=3.99976$ using the VSF method.

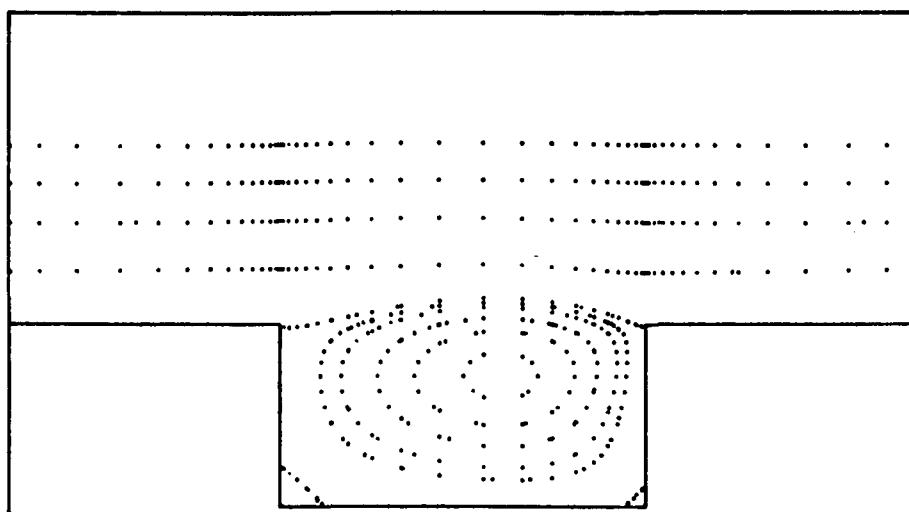


(a)

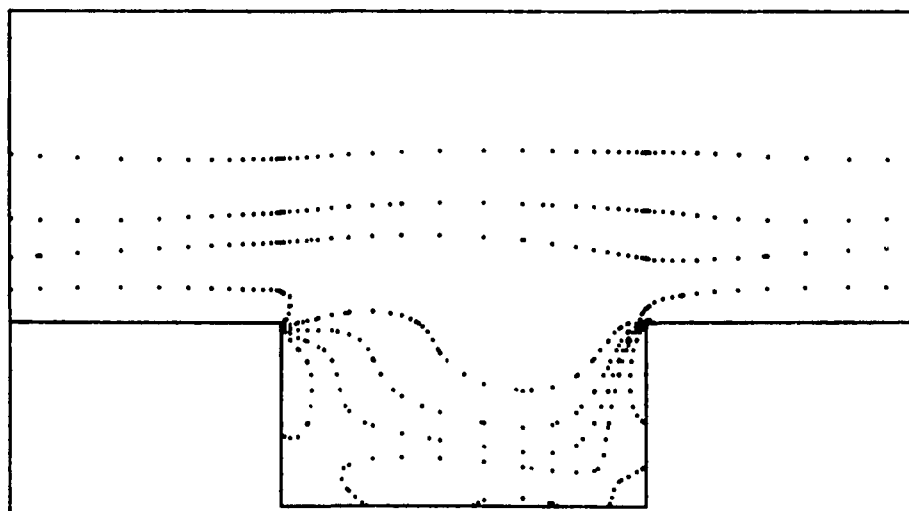


(b)

Figure 4.20 Plots of the (a) stream function and (b) vorticity contours for unsteady flow over the grooved wall at $t=6.00056$ using the VVI method.



(a)



(b)

Figure 4.21 Plots of the (a) stream function and (b) vorticity contours for unsteady flow over the grooved wall at $t=5.99948$ using the VSF method.

It is clear from the pictures that the contours of stream function or vorticity corresponding to the both methods are qualitatively the same. All vorticity contours are seen to end at the solid surface, to form closed contours or extend periodically to infinity. At $t \cong 0.5$, a shear layer can be seen being developed along the surface of the grooved wall. At this instant, the shear layer is found to be deflected sideways from a point near the upper corner on the left vertical surface of the groove. It separates from it, moving into the main stream and then reattaching at the bottom wall. This leads to the formation of recirculating flow in a closed region, in which the fluid elements recirculate and are separated from the main flow. The point on the wall at which the flow is deflected is the separation point. This is also the point at which the velocity gradient normal to the wall vanishes. It is also seen that a second reversal of the flow is developing in the right lower corner of the groove. At this early instant of time, the vorticity generated due to the presence of the solid surface is confined relatively near the surface. As time progresses, the outward diffusion of free vorticity generated at the solid surface can be easily ascertained from the increasing distance between the outer contour and the solid surface. One can see that the vorticity bubbles on the bottom wall of the groove at $t \cong 0.5$ have moved upward and the inner vorticity bubble disappears at $t \cong 1.0$. It is noticed that at the latter instant, positive vortices start to develop along the bottom wall which indicates that the reverse flow is present, and there is an unfavorable (positive) pressure gradient at the surface. At $t \cong 1.5$, the two recirculating flows are seen to be merging together, and they become a single recirculating flow. By comparing these pictures with those at previous instants, it is seen that the separation point now has moved relatively closer to the upper corner, and the

shear layer reattaches at the right vertical surface of the groove. It is seen that vortices in the upstream start to interact with the vortices in the downstream. As flow develops, the recirculating zone grows and the vortices interact continuously. By referring to the contours of the stream function at $t \cong 6.0$, the recirculating flow is seen to have filled the whole groove. At this instant, the separation points are almost coinciding with the left upper corner of the groove, and the point at which the shear layer reattaches has moved very close to the right upper corner of the groove. To conclude this part of discussion, it is worth remarking that the intersection points between the contours of zero vorticity and the solid surface represent the points of vanishing shear stress. Therefore, they are either the separation or the reattached points of the flow.

Next, the profiles of the X -component of velocities versus the distance in the vertical direction obtained from the VVI and VSF methods at $X = -0.7571, 0, 0.7571, 0.9911, \text{ and } 1.0689$ for dimensionless times of 0.5 and 6.0 units are shown in Figure 4.22 through 4.31. At $t \cong 0.5$, the profile at $X = -0.7571$ shows reversed flow, which is consistent with the flow pattern for the recirculating flow at the corresponding location in Figures 4.8 and 4.9, and at this instant, the shear layer is confined to a small region adjacent to the wall. At $t \cong 6.0$, the shear layer has extended to about $Y = 2.0$ along the entire surface of the grooved wall, and back-flow can be found at most locations inside the groove. Clearly, the velocity profiles from the both methods are nearly congruent.

Finally, Figures 4.32 through 4.38 compare the shear stress and the pressure along the solid surface obtained from the VVI and VSF methods at dimensionless time of 0.5, 1.0, 1.5, 2.0, 3.0, 4.0 and 6.0 units. Note that there are two sharp peaks which appear in each of the shear stress and pressure curves.

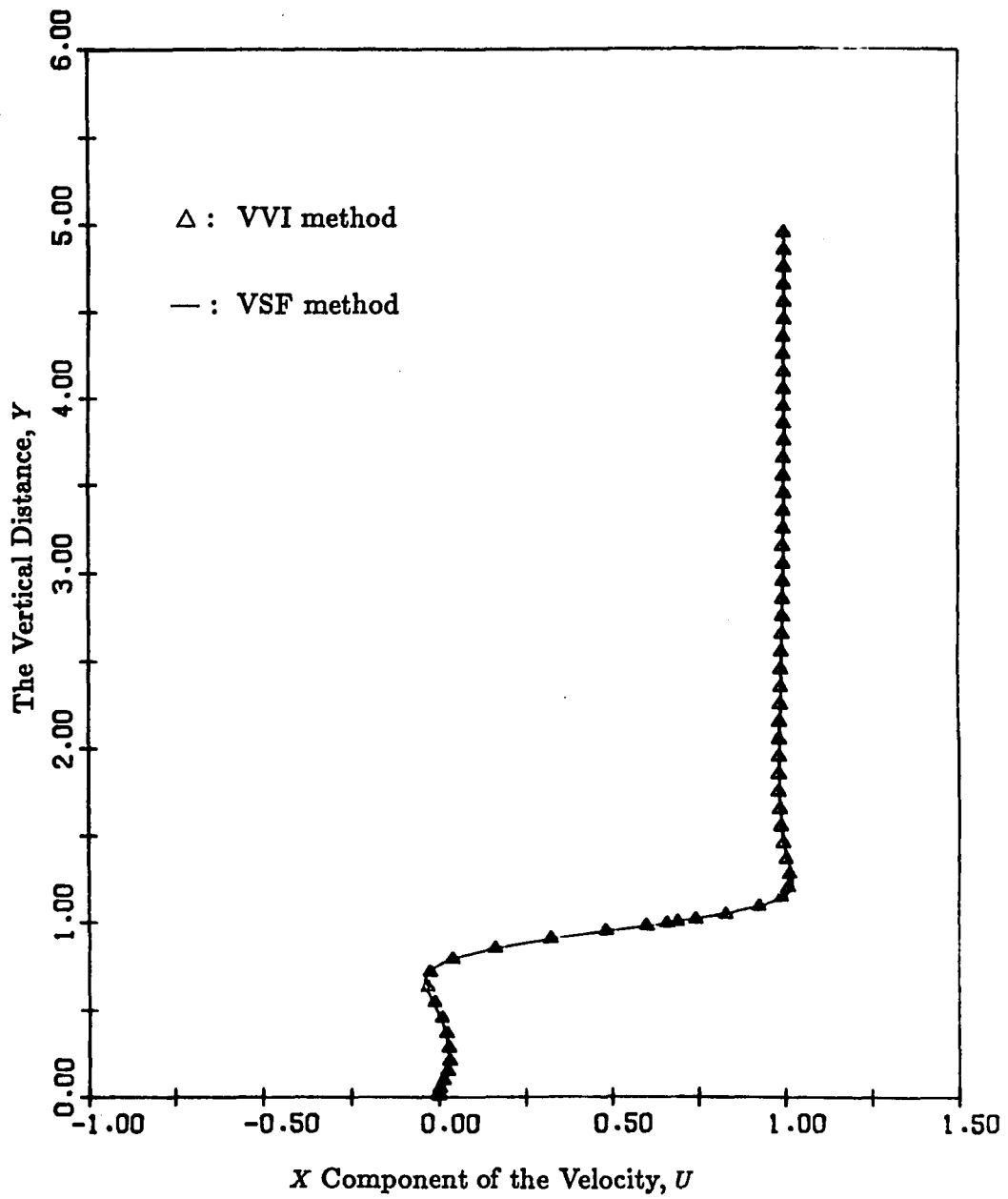


Figure 4.22 Plots of the X component of velocities obtained from the VVI and VSF methods as a function of the vertical distance from the bottom wall at $X = -0.7571$ and $t \cong 0.5$.

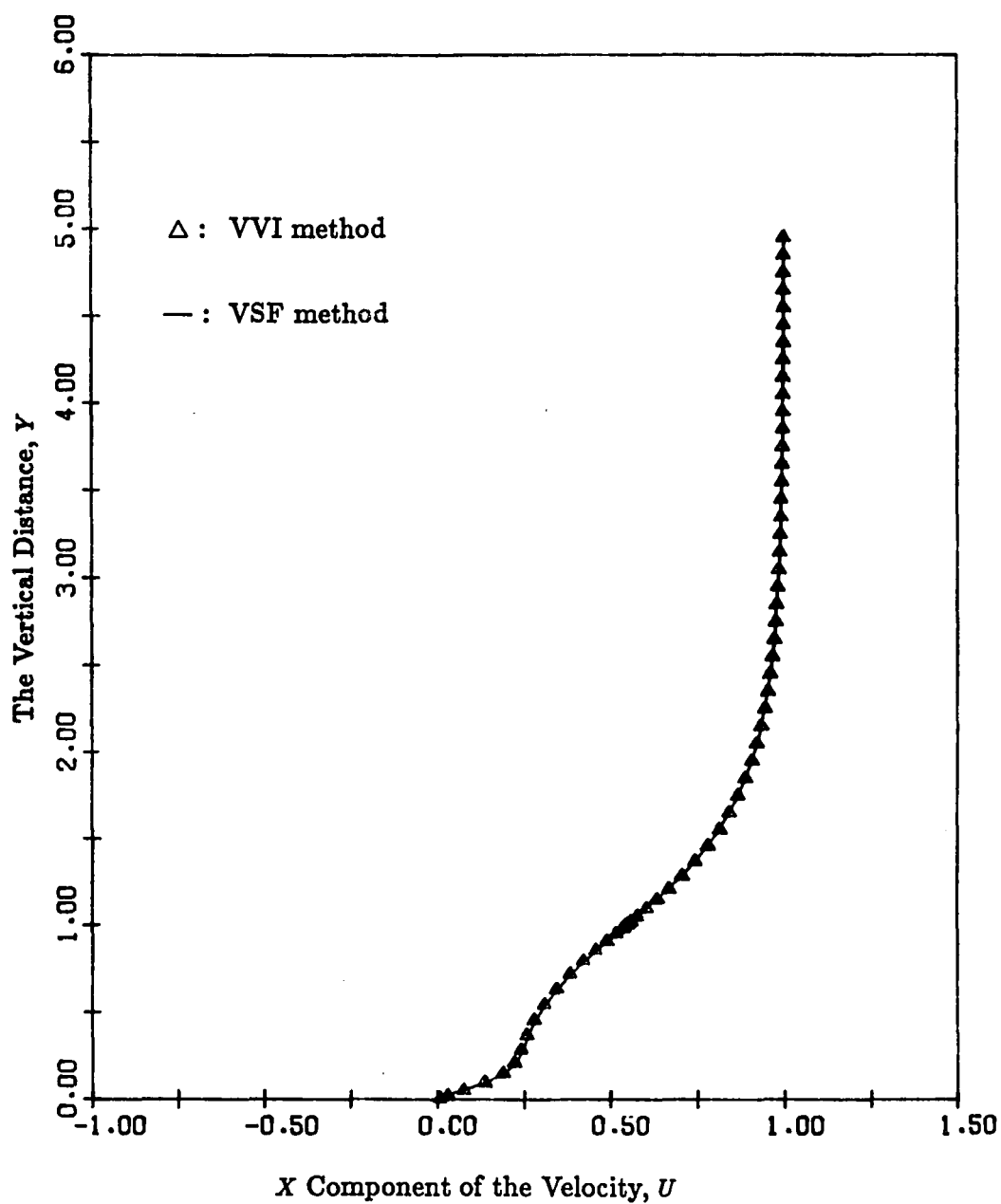


Figure 4.23 Plots of the X component of velocities obtained from the VVI and VSF methods as a function of the vertical distance from the bottom wall at $X = 0$ and $t \approx 0.5$.

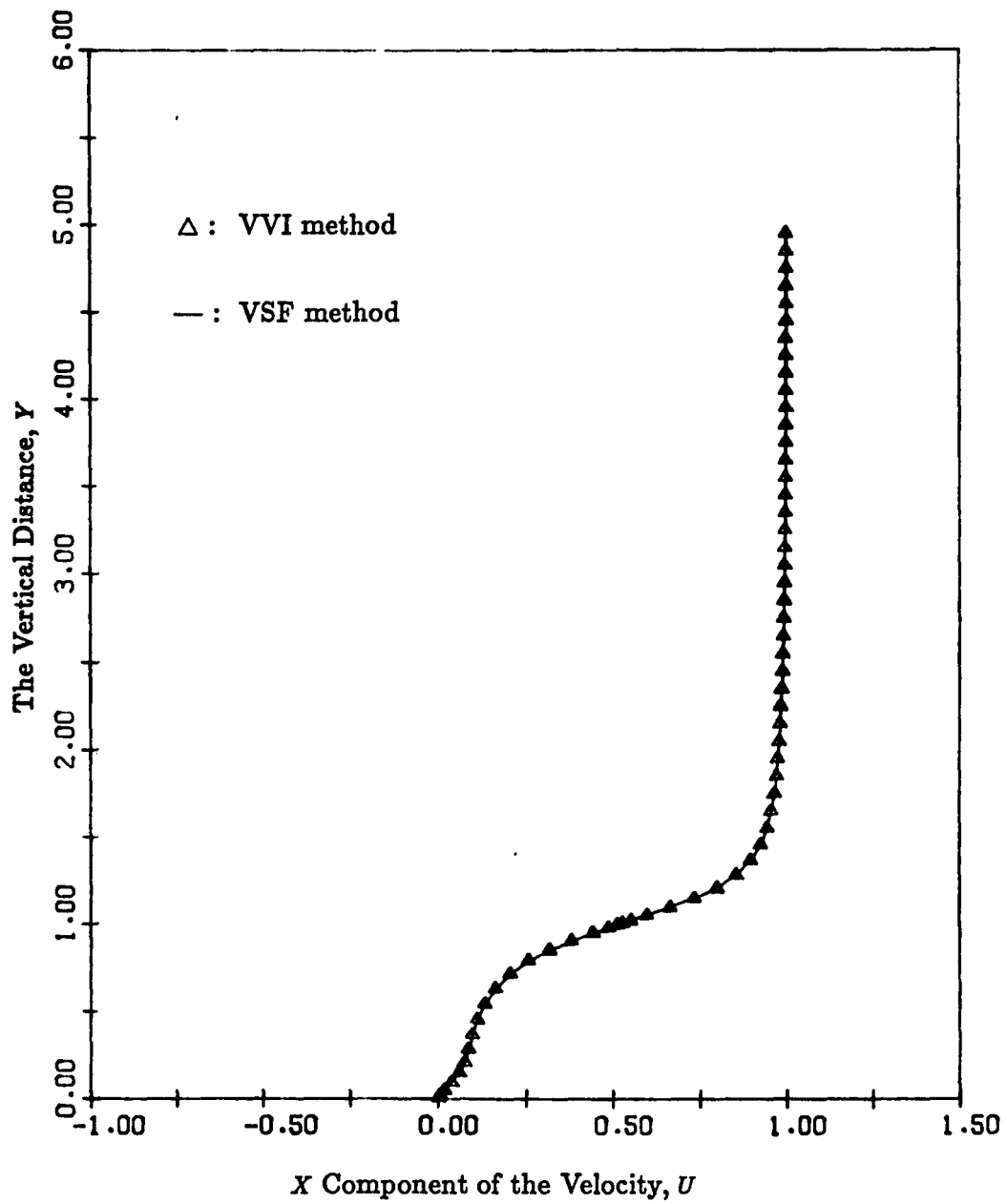


Figure 4.24 Plots of the X component of velocities obtained from the VVI and VSF methods as a function of the vertical distance from the bottom wall at $X = 0.7571$ and $t \cong 0.5$.

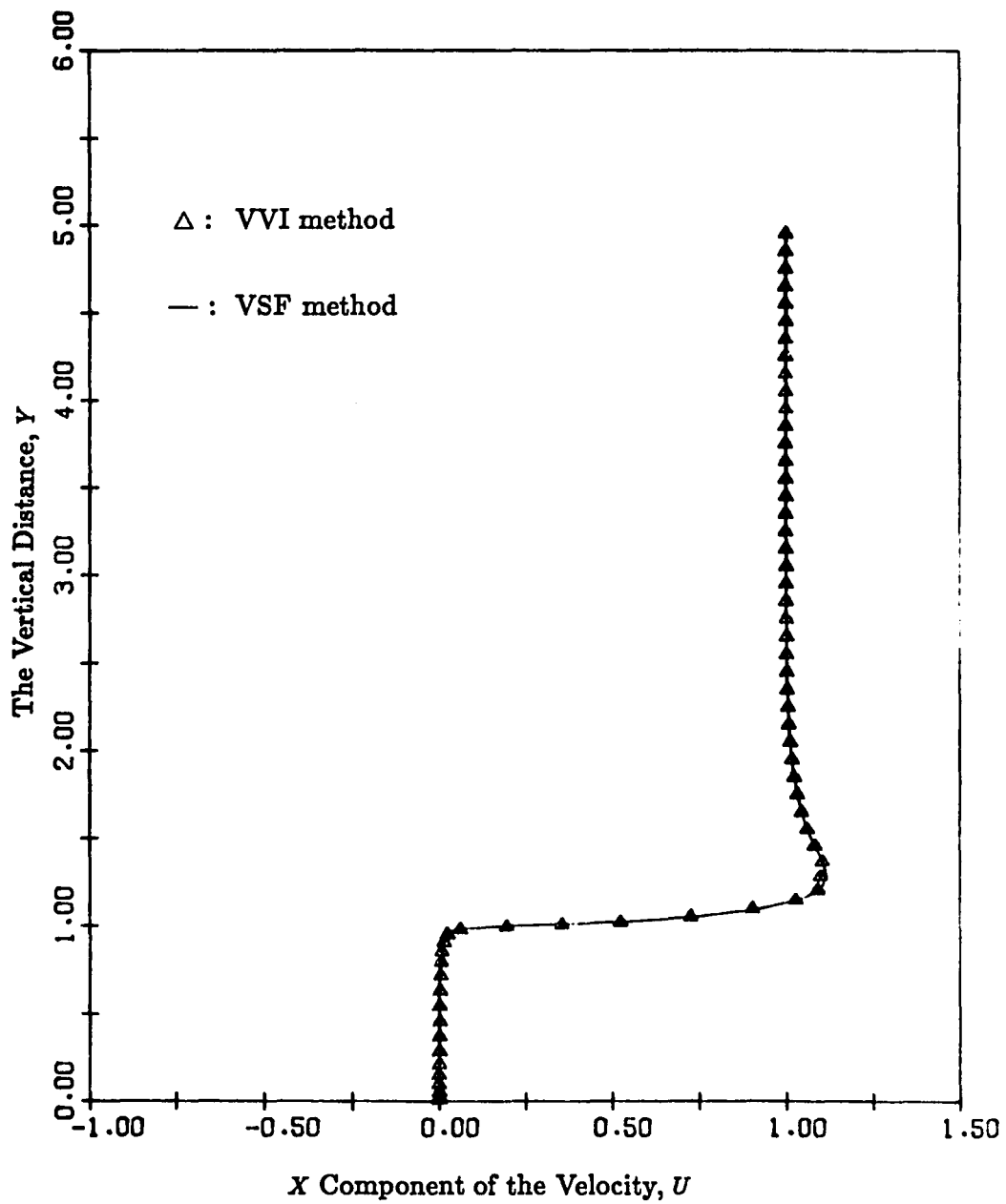


Figure 4.25 Plots of the X component of velocities obtained from the VVI and VSF methods as a function of the vertical distance from the bottom wall at $X = 0.9911$ and $t \approx 0.5$.

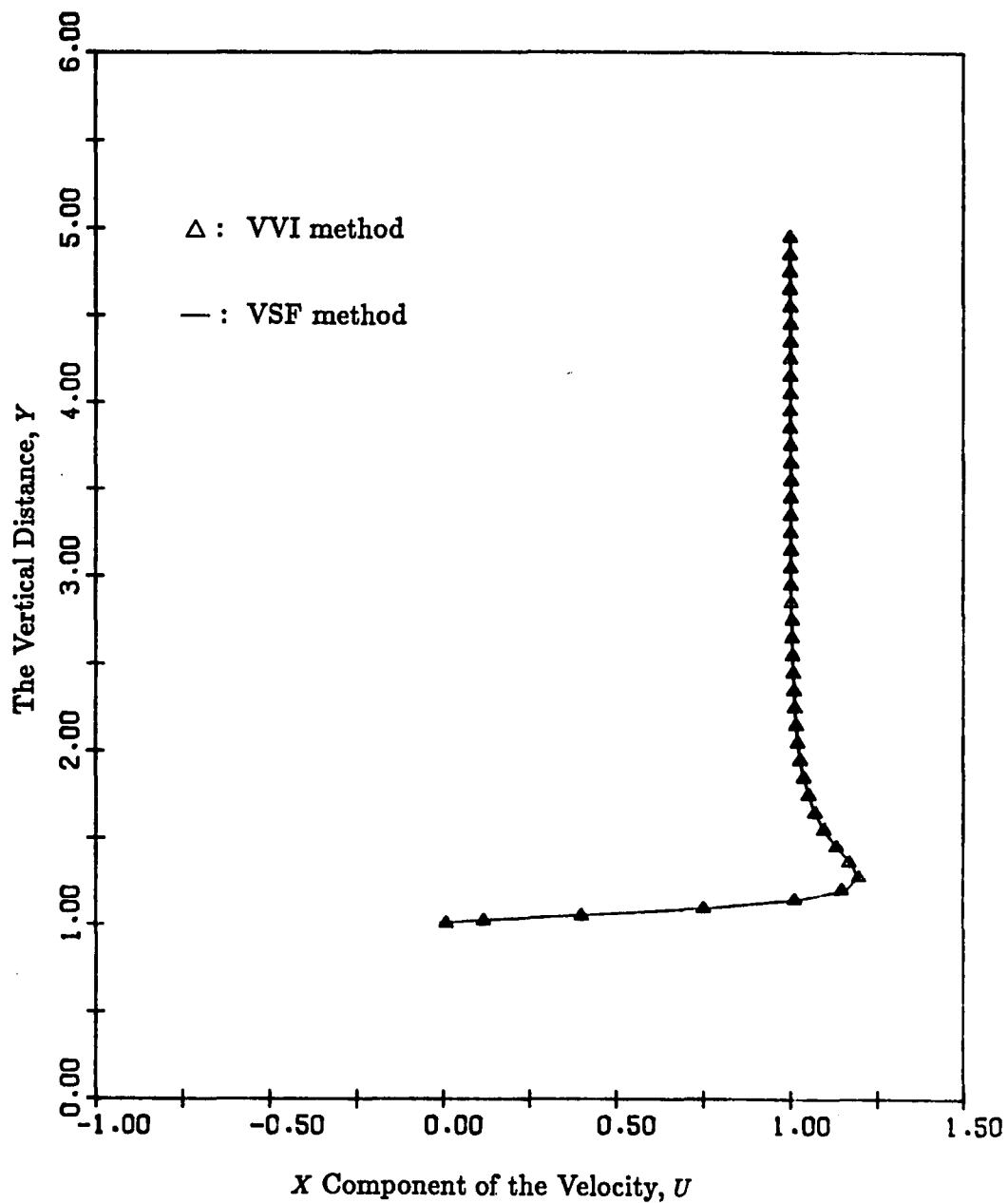


Figure 4.26 Plots of the X component of velocities obtained from the VVI and VSF methods as a function of the vertical distance from the bottom wall at $X = 1.0689$ and $t \approx 0.5$.

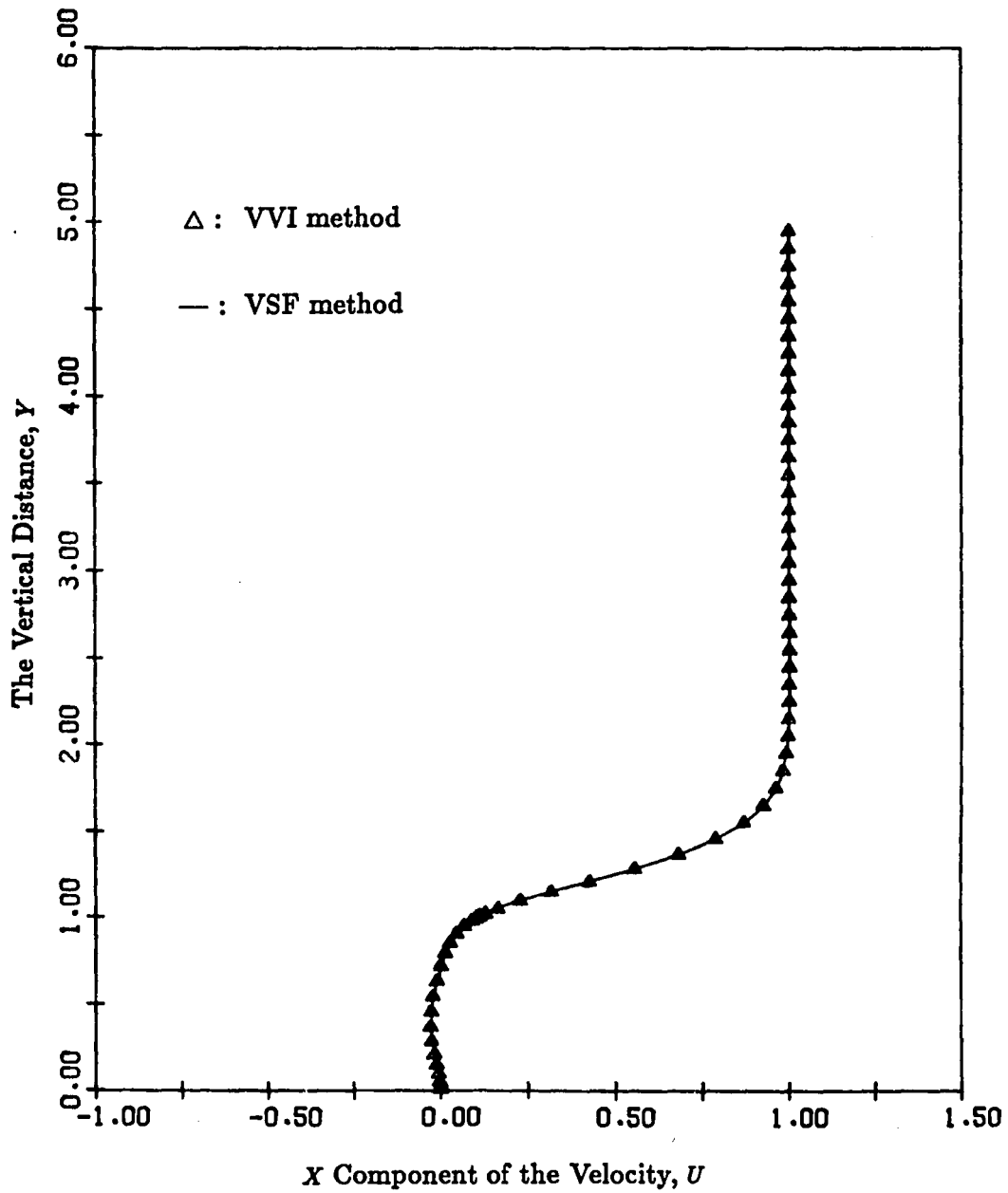


Figure 4.27 Plots of the X component of velocities obtained from the VVI and VSF methods as a function of the vertical distance from the bottom wall at $X = -0.7571$ and $t \cong 6.0$.

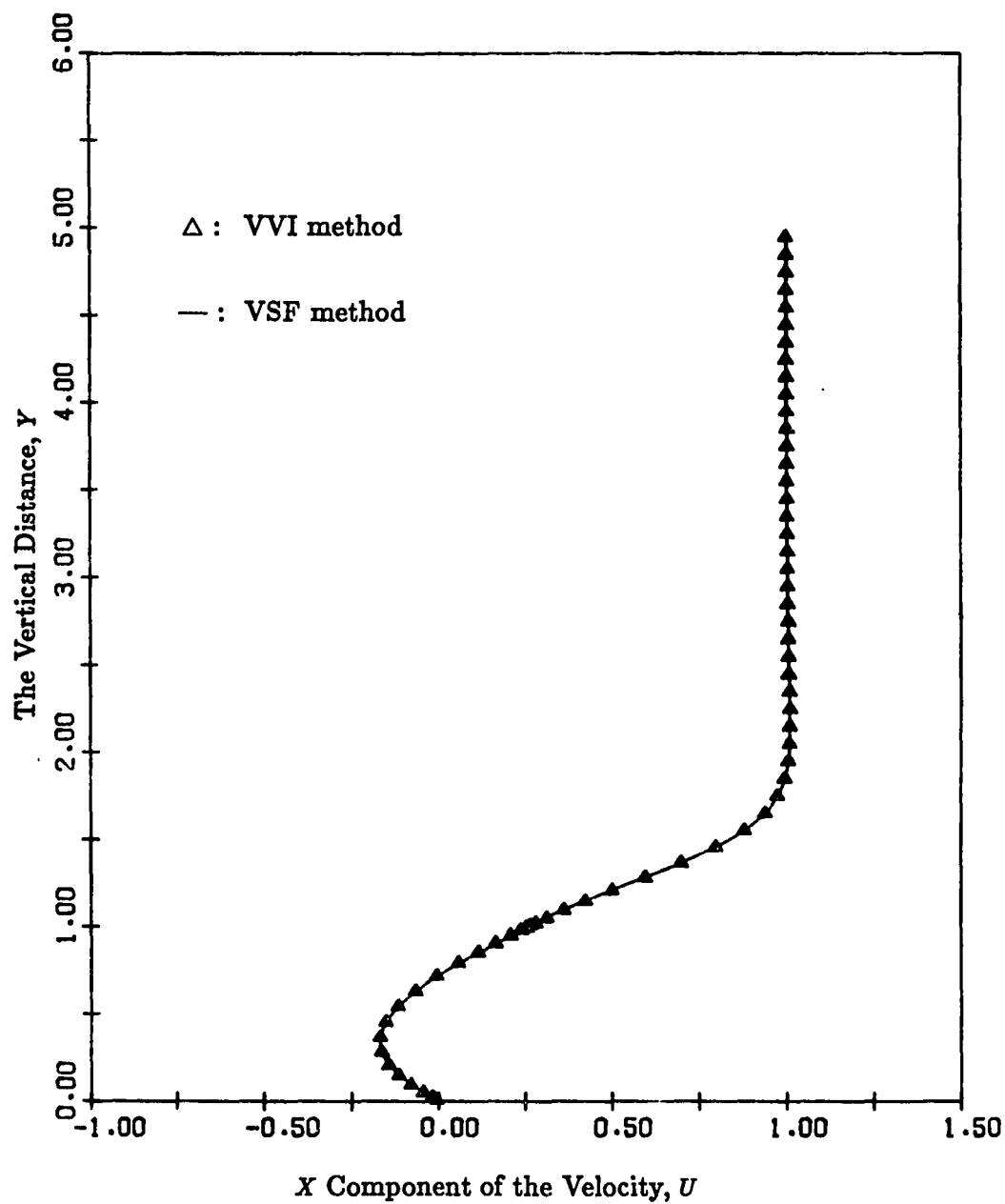


Figure 4.28 Plots of the X component of velocities obtained from the VVI and VSF methods as a function of the vertical distance from the bottom wall at $X = 0$ and $t \cong 6.0$.

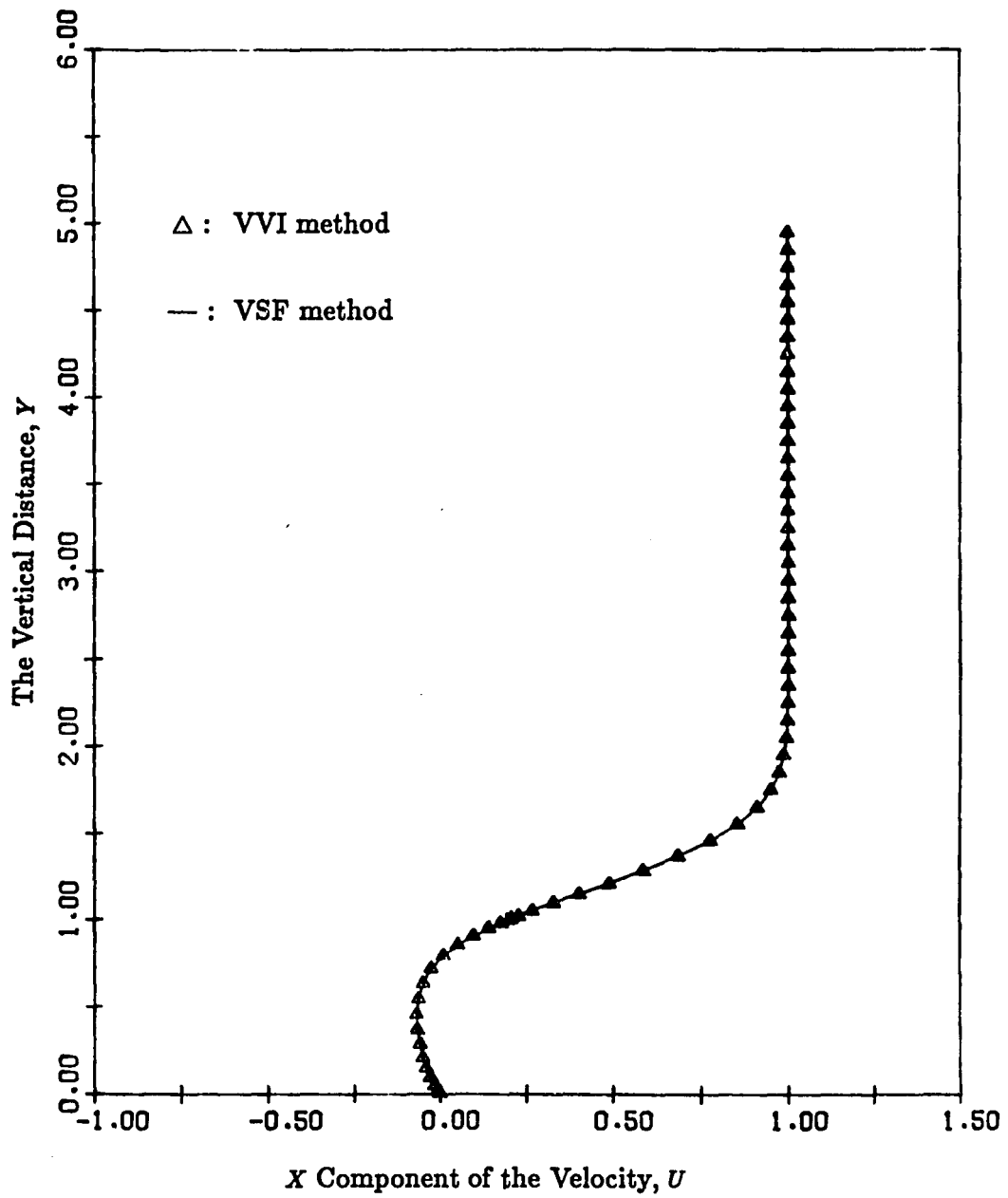


Figure 4.29 Plots of the X component of velocities obtained from the VVI and VSF methods as a function of the vertical distance from the bottom wall at $X = 0.7571$ and $t \approx 6.0$.

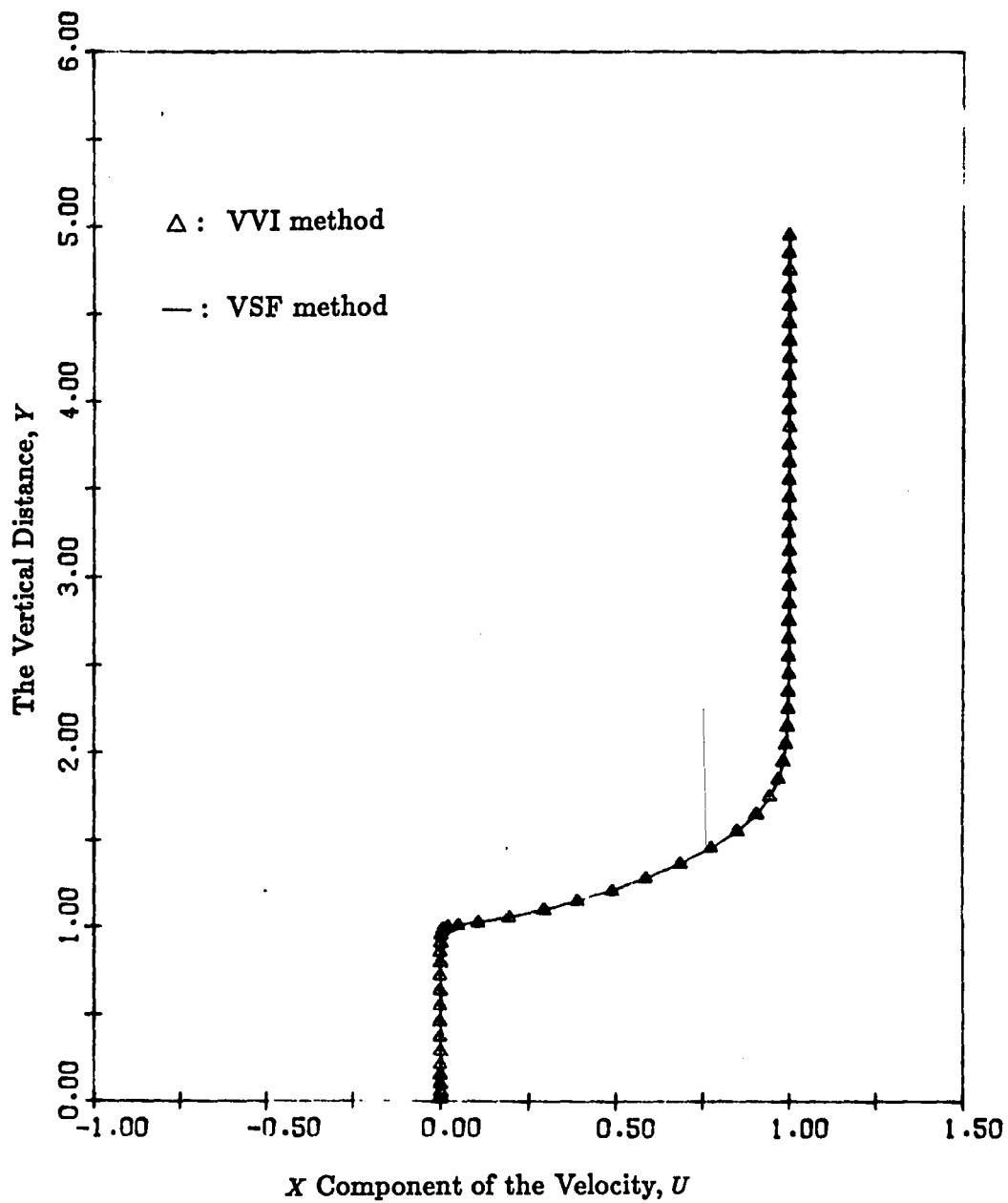


Figure 4.30 Plots of the X component of velocities obtained from the VVI and VSF methods as a function of the vertical distance from the bottom wall at $X = 0.9911$ and $t \approx 6.0$.

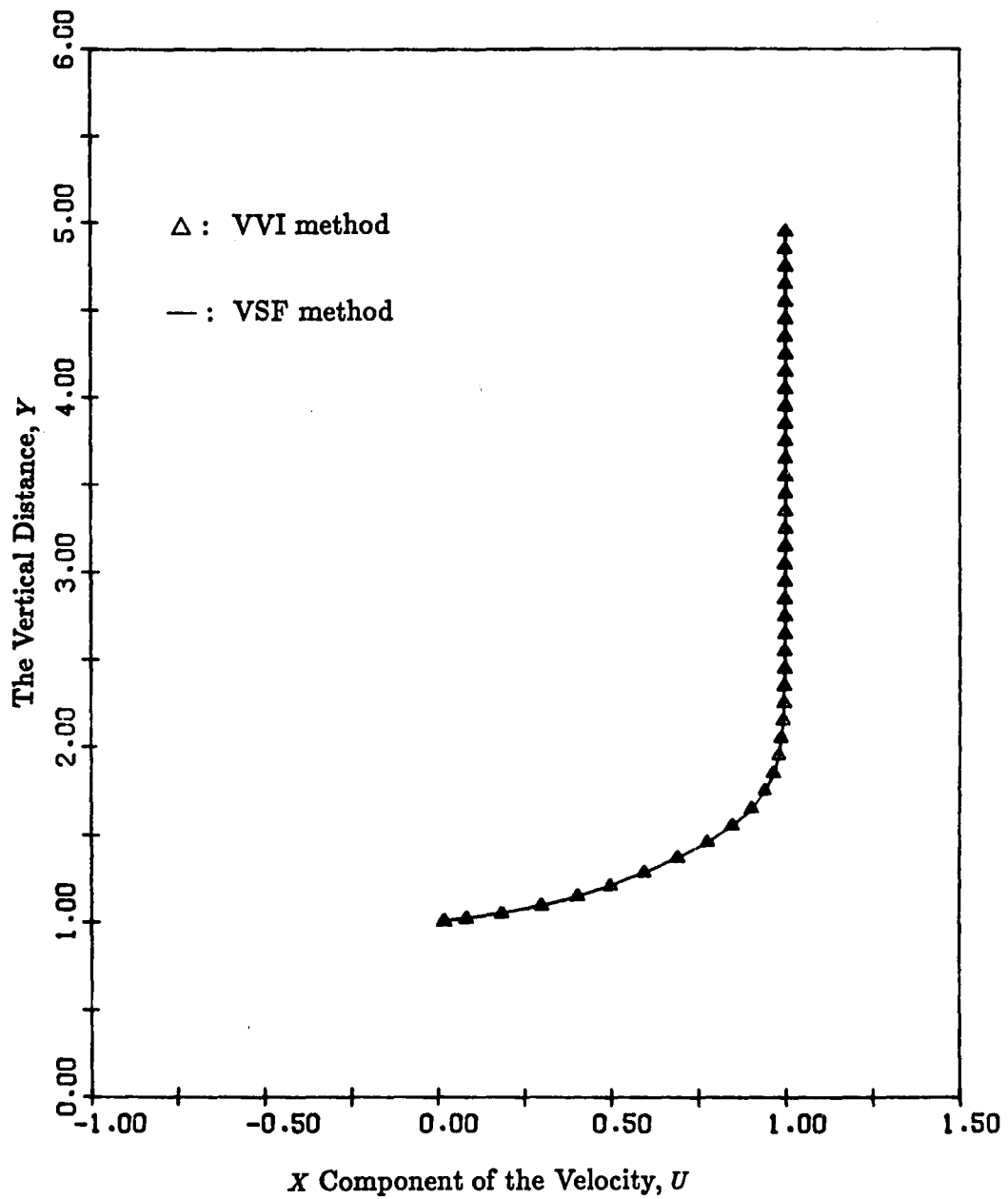
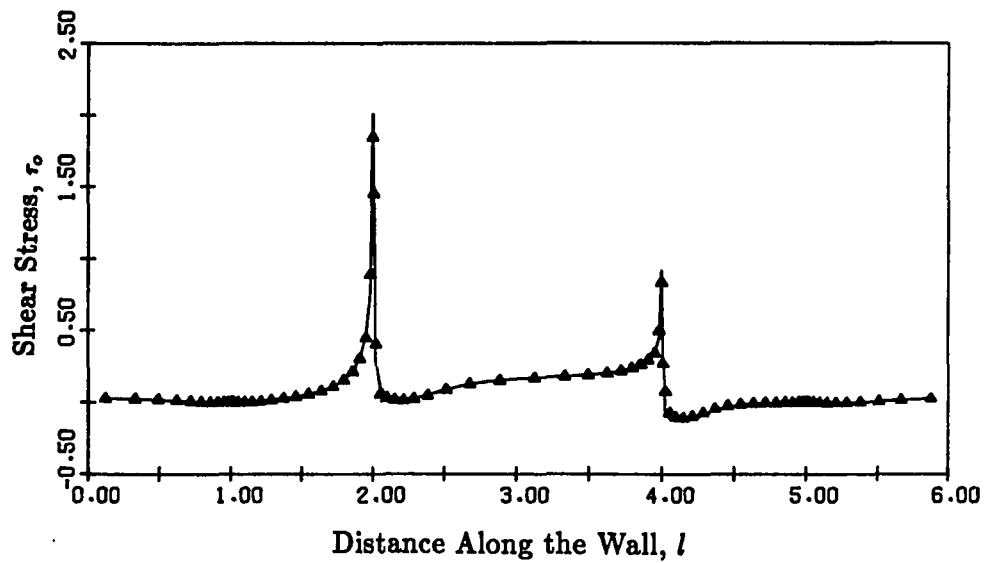
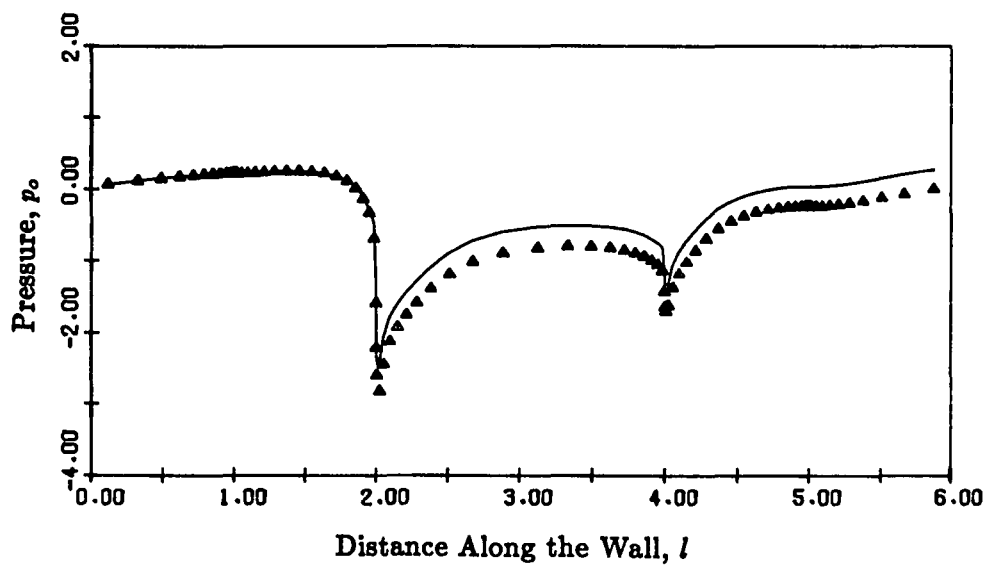


Figure 4.31 Plots of the X component of velocities obtained from the VVI and VSF methods as a function of the vertical distance from the bottom wall at $X = 1.0689$ and $t \cong 6.0$.

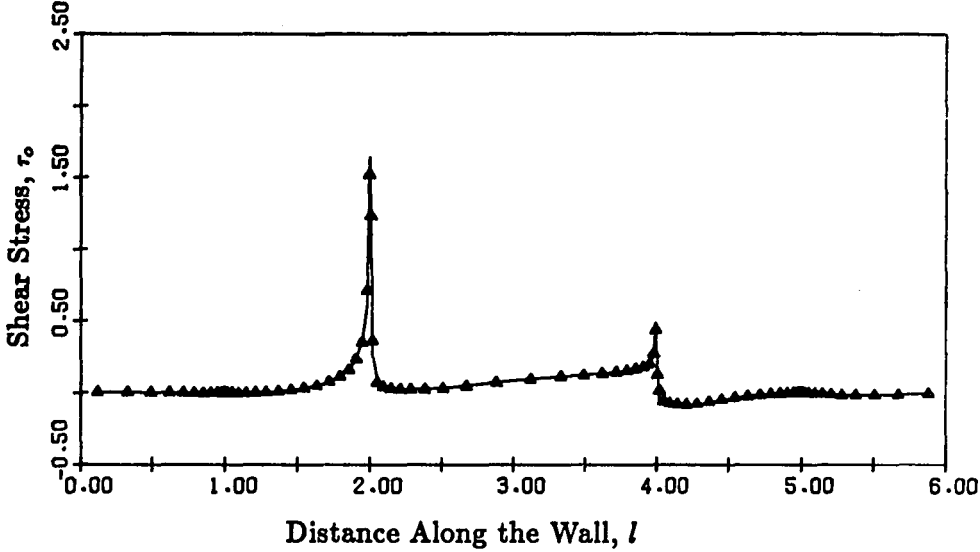


(a)

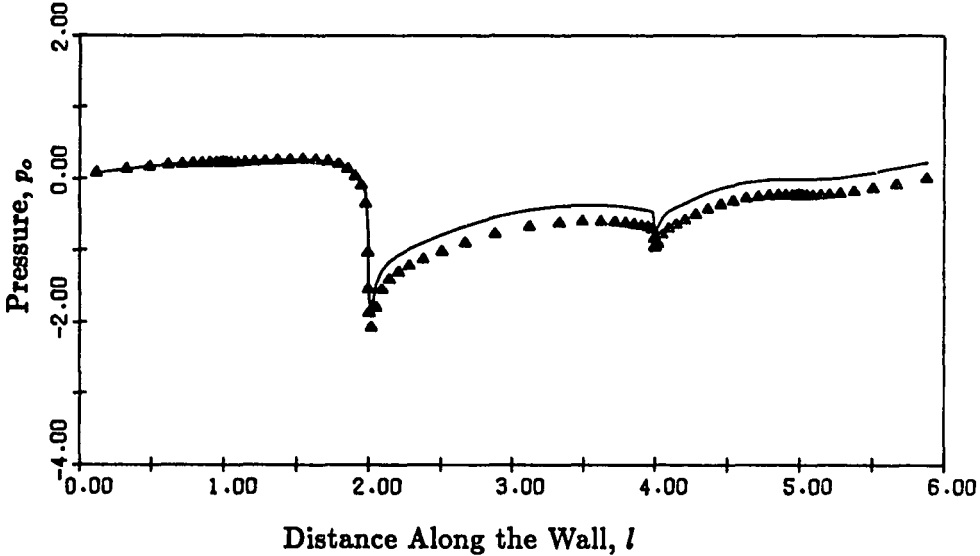


(b)

Figure 4.32 Plots of the distribution of (a) shear stress and (b) pressure along the wall at $t \approx 0.5$ obtained from the VVI (Δ) and VSF (—) methods.

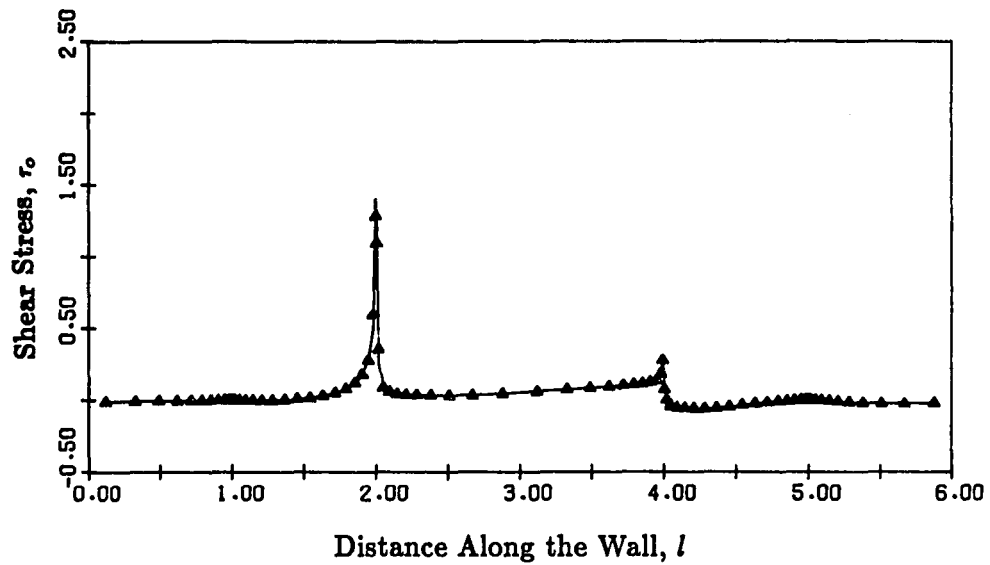


(a)

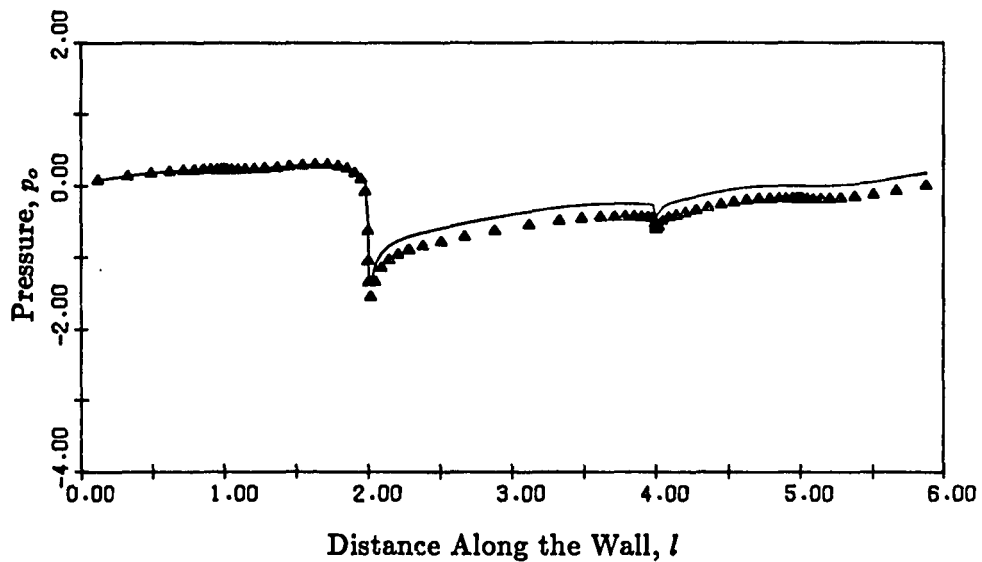


(b)

Figure 4.33 Plots of the distribution of (a) shear stress and (b) pressure along the wall at $t \cong 1.0$ obtained from the VVI (Δ) and VSF (—) methods.

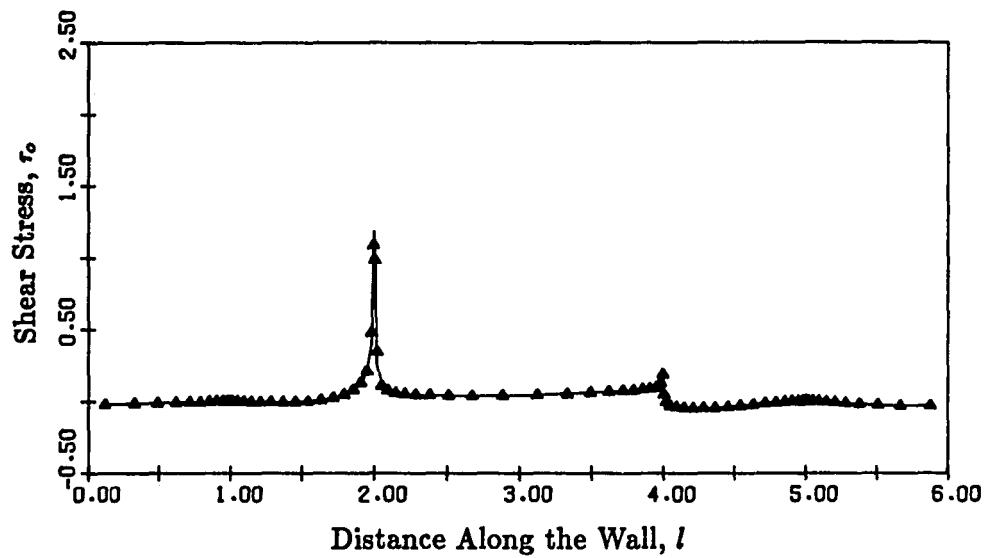


(a)

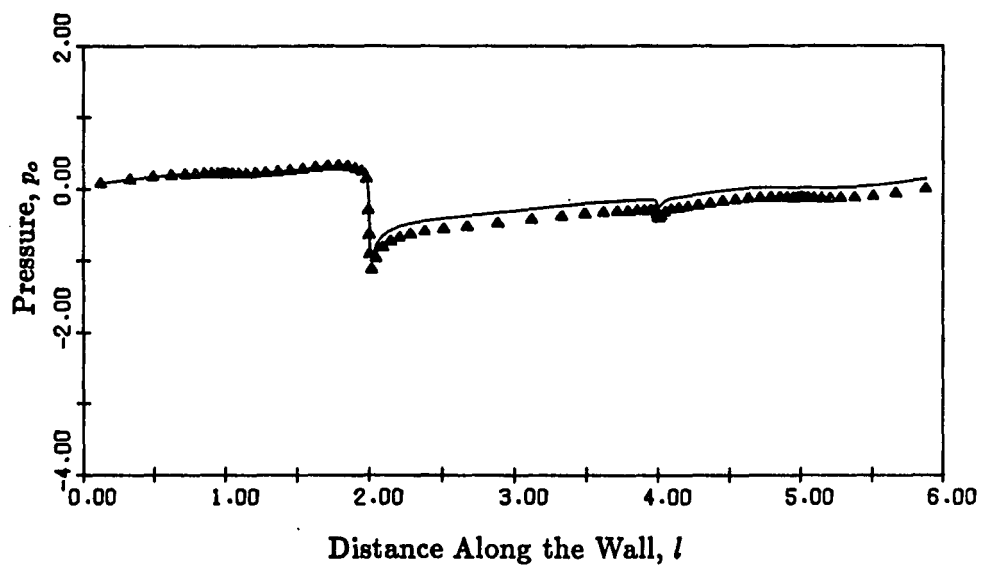


(b)

Figure 4.34 Plots of the distribution of (a) shear stress and (b) pressure along the wall at $t \approx 1.5$ obtained from the VVI (Δ) and VSF (—) methods.

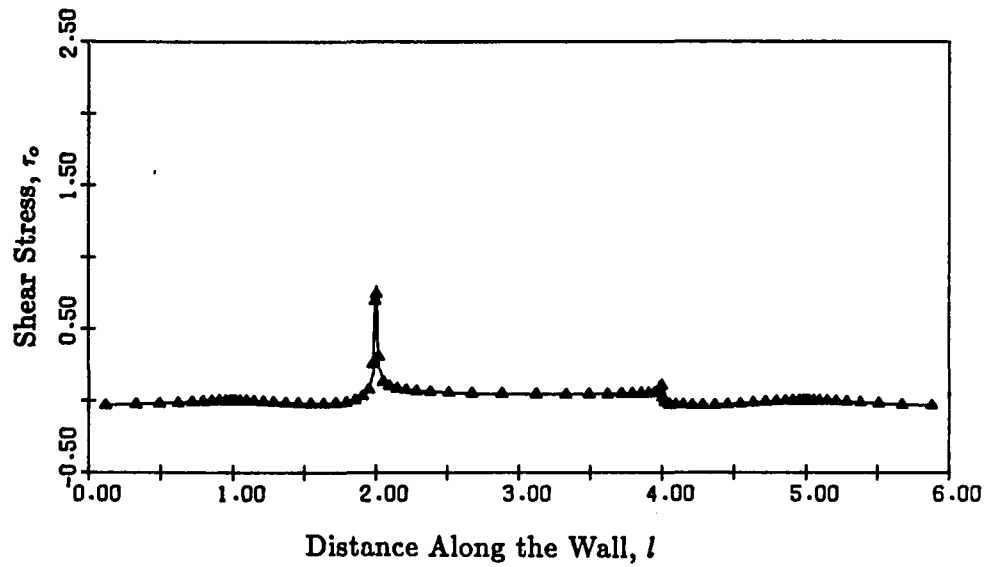


(a)

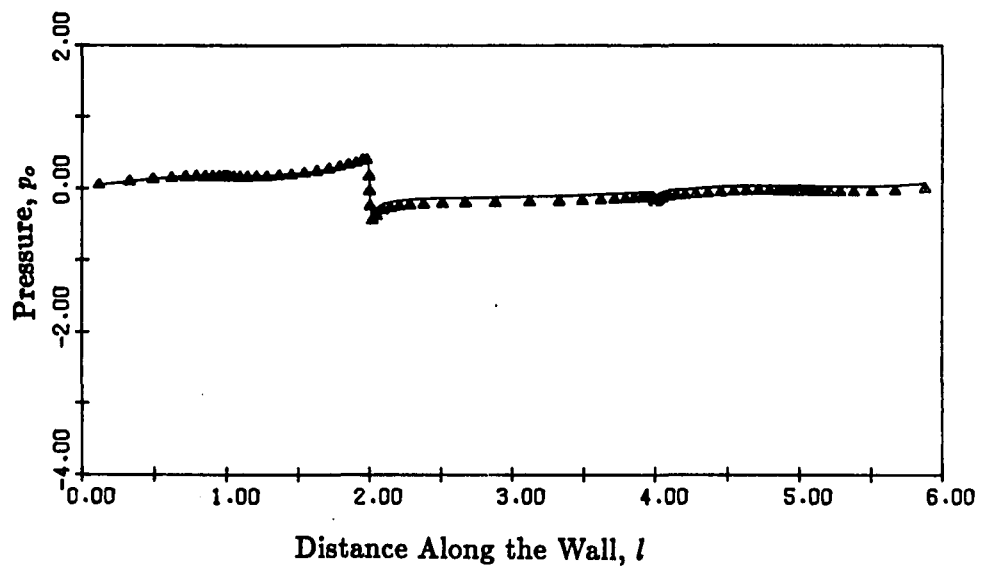


(b)

Figure 4.35 Plots of the distribution of (a) shear stress and (b) pressure along the wall at $t \approx 2.0$ obtained from the VVI (Δ) and VSF (—) methods.

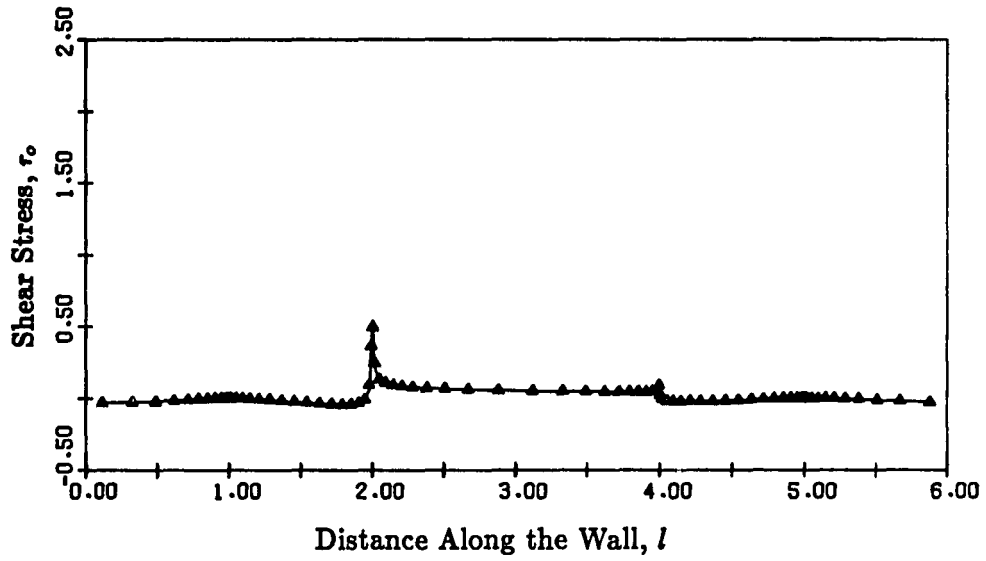


(a)

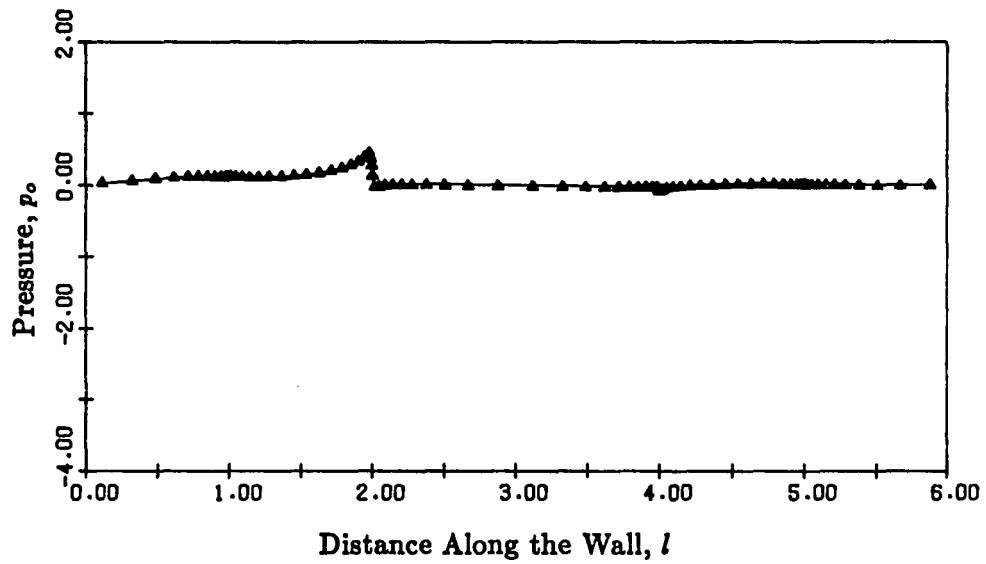


(b)

Figure 4.36 Plots of the distribution of (a) shear stress and (b) pressure along the wall at $t \cong 3.0$ obtained from the VVI (Δ) and VSF (—) methods.

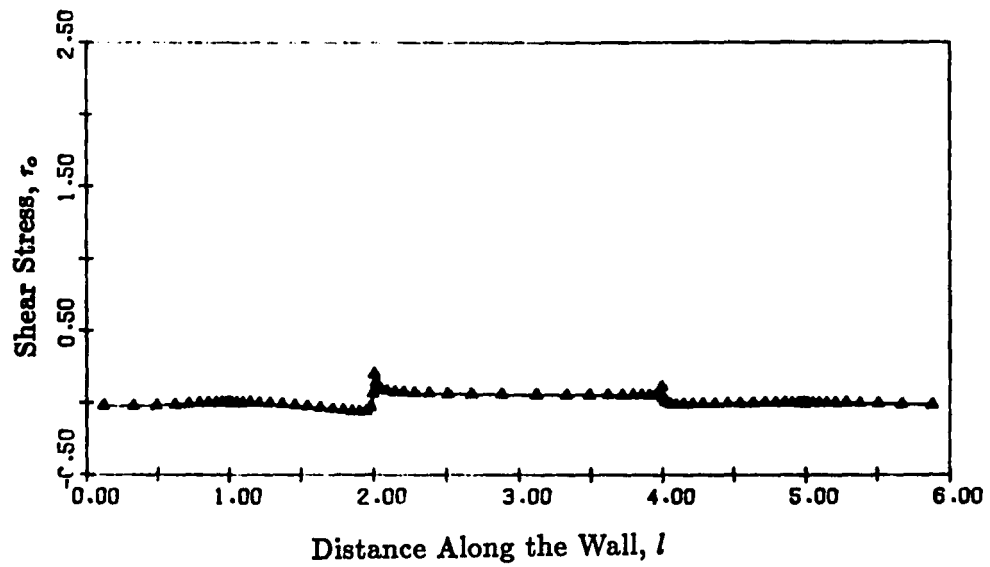


(a)

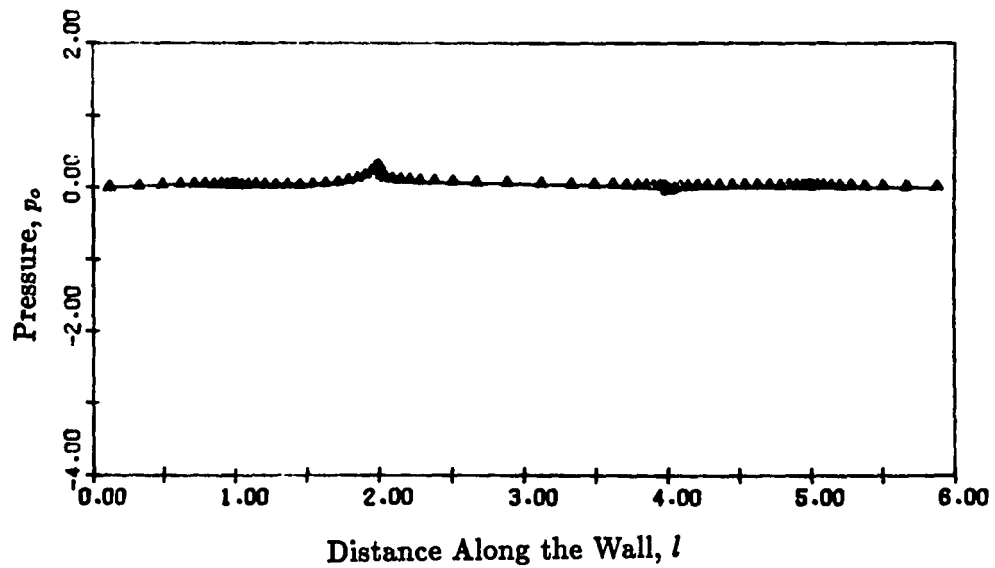


(b)

Figure 4.37 Plots of the distribution of (a) shear stress and (b) pressure along the wall at $t \cong 4.0$ obtained from the VVI (Δ) and VSF (—) methods.



(a)



(b)

Figure 4.38 Plots of the distribution of (a) shear stress and (b) pressure along the wall at $t \cong 6.0$ obtained from the VVI (Δ) and VSF (—) methods.

The peaks occur at $l = 2.0$ and 4.0 in both curves, which correspond to the two upper corners of the groove, respectively. Here, l represents the distance along the surface of the grooved wall starting from the coordinates $(0,0)$ (referring to Figure 3.1). Thus, $l = 1$ corresponds to $(1,0)$; $l = 2$ corresponds to $(1,1)$; $l = 3$ corresponds to $(2,1)$; etc. It is seen that the local minimum is associated with the pressure curve and the local maximum is associated with the shear stress curve. The characteristic low pressure and high shear stress at the sharp corners which normally results in acceleration of fluid particles and large gradient of the velocity, is consistent with physical intuition. At the early time, the shear-stress distributions are nearly identical, the only departure being in the corner regions where the VSF method produces slightly higher values. There is less agreement in the pressure distributions at this time past $l = 2.0$. Indeed, the pressure from the VVI method reaches zero at $l = 6.0$, whereas that from the VSF method has a residual positive value at $l = 6.0$. The pressure should be zero there if the flow field is spatially periodic. However, as the shear layer becomes thicker with increasing time, the strength of the peaks decreases due to the viscous effects, which have smoothed down the velocity gradients near this region. At $t \cong 6.0$, both curves appear to be relative smooth and uniform because, at this instant, the shear layer is fully developed along the wall and occupies the whole groove. The pressure discrepancy at $l = 6.0$ still persists at $t = 3.0$, but it is nearly absent at $t = 6.0$.

In figure 4.39, the time development of the total drag coefficient due to the effect of the pressure and shear forces obtained from the VVI and VSF methods is presented. The pressure drag is dominant, and it is seen that in the earlier time, the VVI method predicts a higher drag coefficient than does the VSF method. This is consistent with the pressure distributions shown in

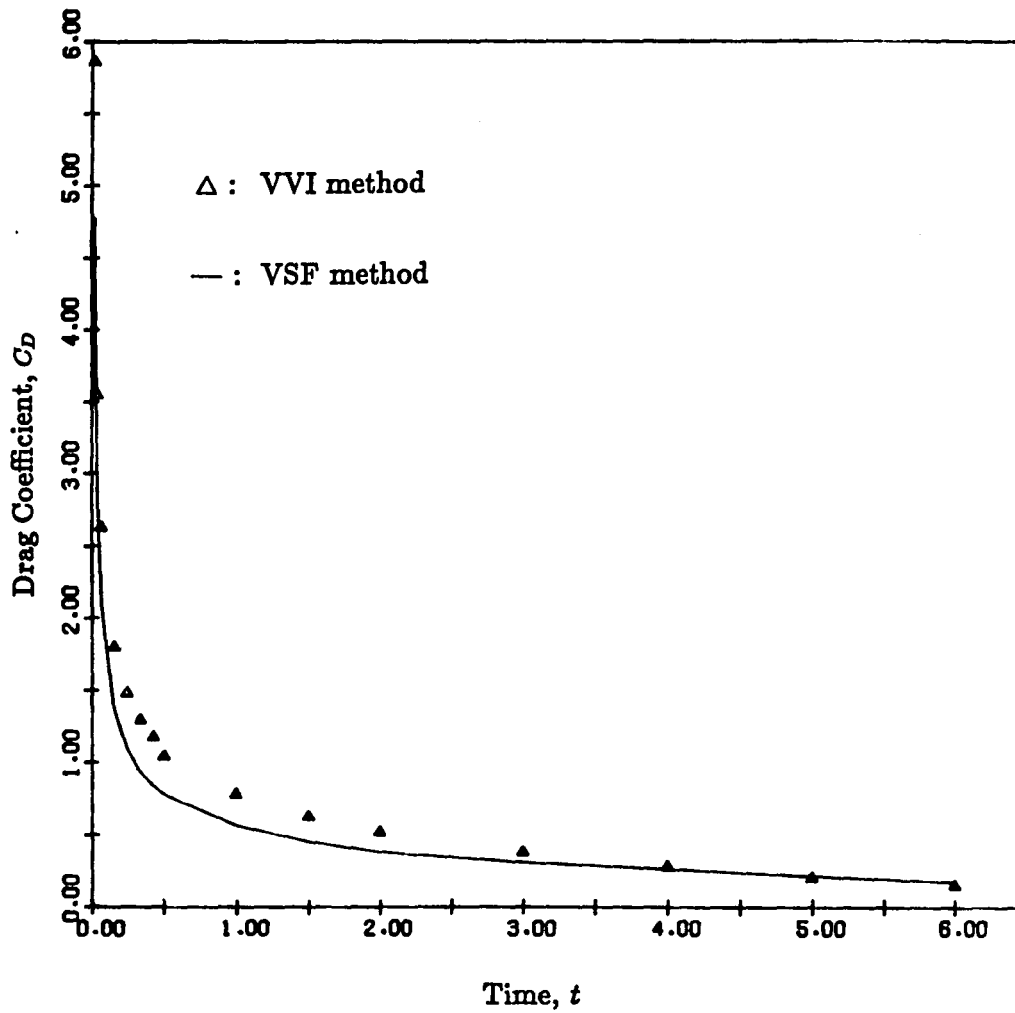


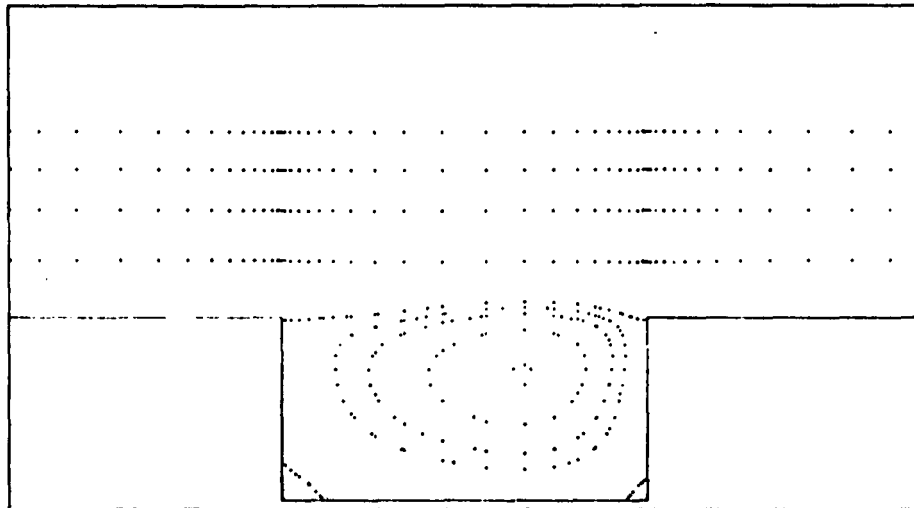
Figure 4.39 Plots of the time development of the drag coefficient from the VVI and VSF methods.

Figure 4.32 through 4.38. However, it is seen that both curves cross at $t \cong 4.0$, and then the value of the drag coefficient from the VVI method is found to be slightly smaller. In view of the fact that the pressure from the VSF calculation does not return exactly to zero at the mid-point of the groove (i.e., at $t = 6.0$), more confidence must be placed on the drag predictions from the VVI method than from the VSF method.

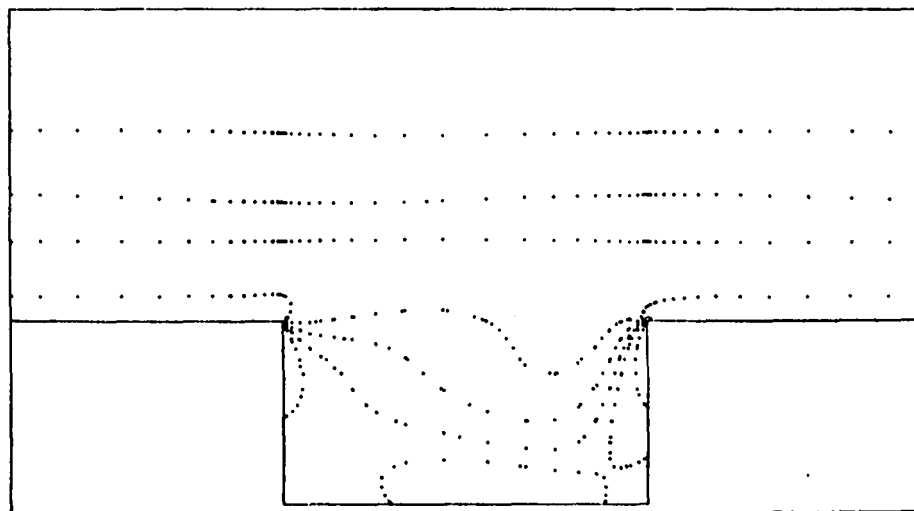
The general features of the flow observed in the above results were found to be nearly the same for both the methods from the initial instant up to $t \cong 6.0$. It was, therefore, decided to run the calculations further in time by using only one method. Since the VSF method is relatively inexpensive in computational cost, the remaining results have been obtained using this method.

Figures 4.40 through 4.44 show the time history of the stream function and vorticity development beginning at $t \cong 8.0$ and spaced at two units of time apart. The overall pattern of the flow follows that at the earlier times. It is worth remarking that at the final instant (i.e., $t = 16.0$), our pictures showing the contours of the stream function and vorticity are qualitatively the same as those from the investigation of the steady flow in grooved channels recently reported by Chaddar, Korczak, Mikic and Patera (1986). The time development of the X component of the velocity profiles from the initial instant to $t \cong 16.0$ is shown in Figures 4.45 through 4.49 at $X = -0.7571, 0, 0.7571, 0.9911$ and 1.0689 . In each picture, there are 8 profiles corresponding to $t \cong 0, 0.5, 1.0, 1.5, 2.0, 4.0, 8.0$ and 16.0 , respectively.

Figure 4.50 shows the time development of the drag coefficient. From the figure, it is seen that the drag coefficient at $t \cong 16.0$ is approximately 0.1, which is a large reduction from its value of approximately 5.0 at $t \cong 0.02$. Note

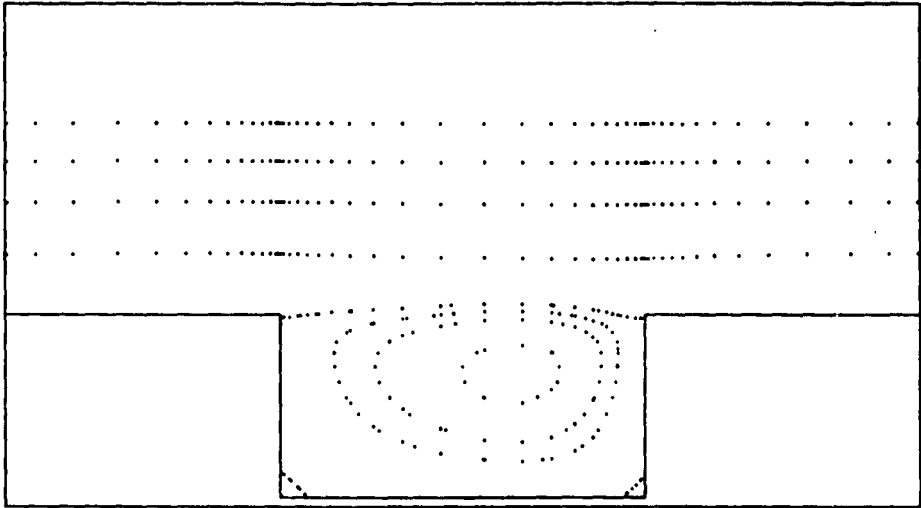


(a)

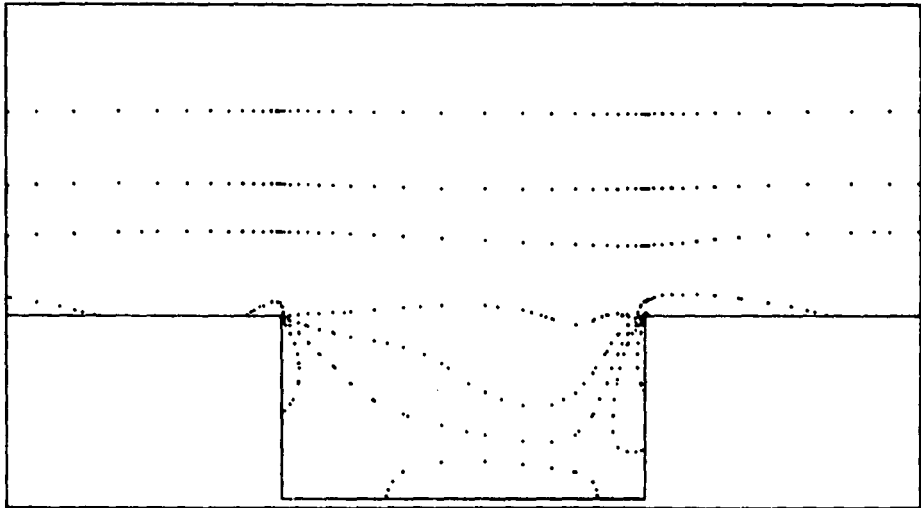


(b)

Figure 4.40 Plots of the (a) stream function and (b) vorticity contours for unsteady flow over the grooved wall at $t=8.00074$ using the VSF method.

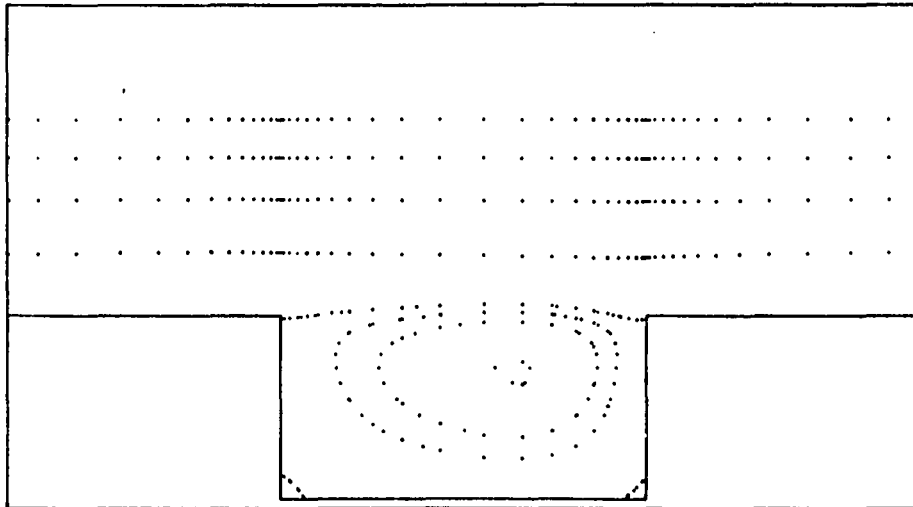


(a)

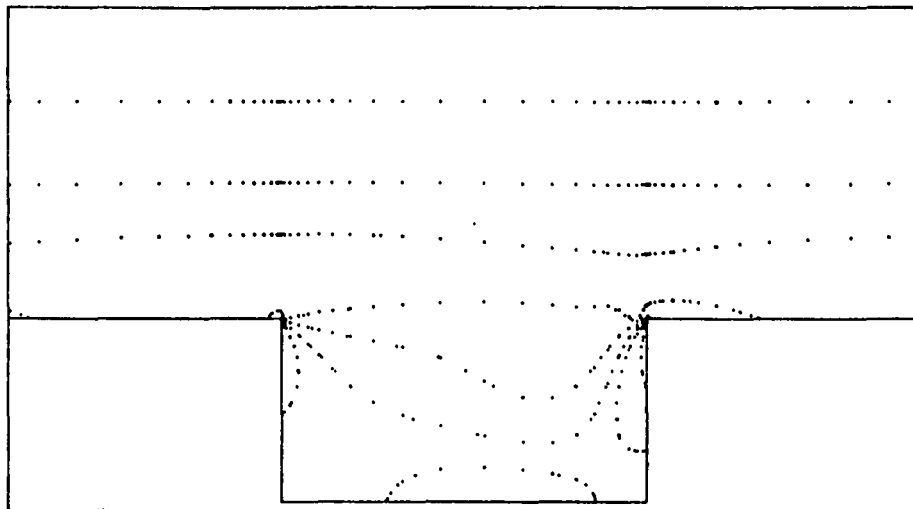


(b)

Figure 4.41 Plots of the (a) stream function and (b) vorticity contours for unsteady flow over the grooved wall at $t=10.0005$ using the VSF method.

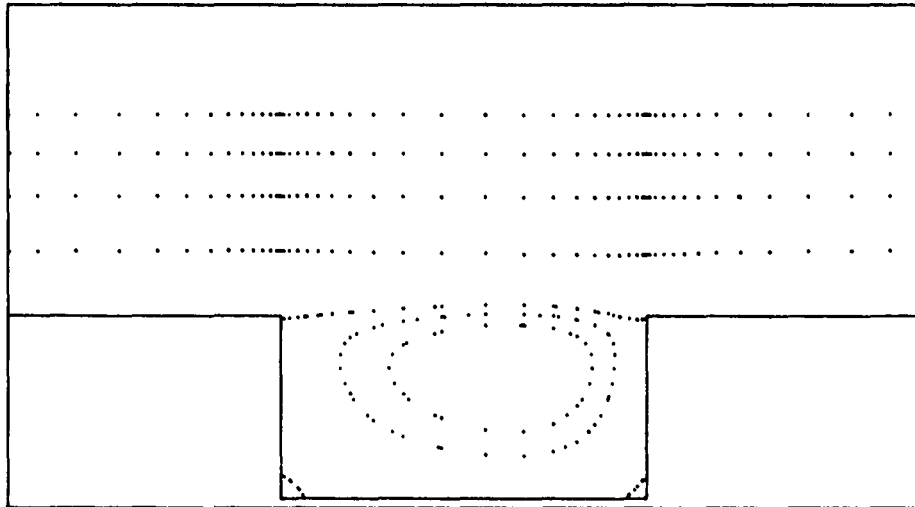


(a)

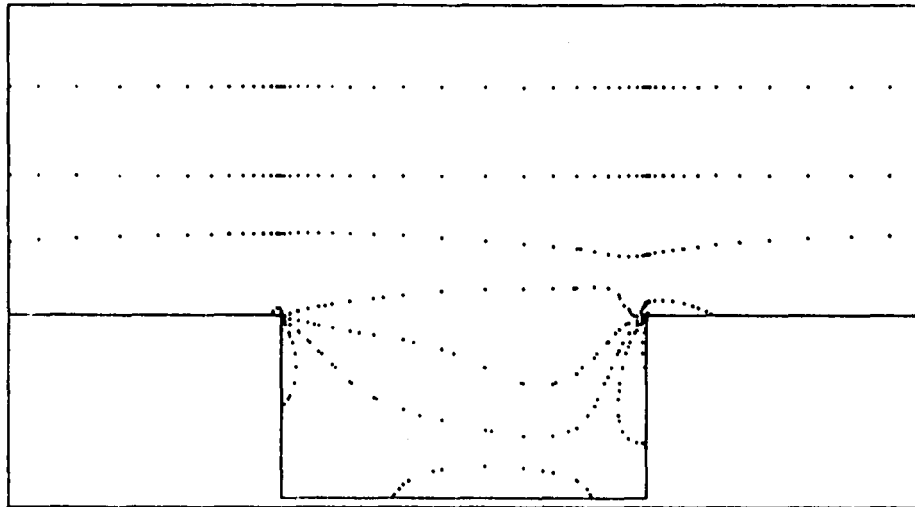


(b)

Figure 4.42 Plots of the (a) stream function and (b) vorticity contours for unsteady flow over the grooved wall at $t=12.0002$ using the VSF method.

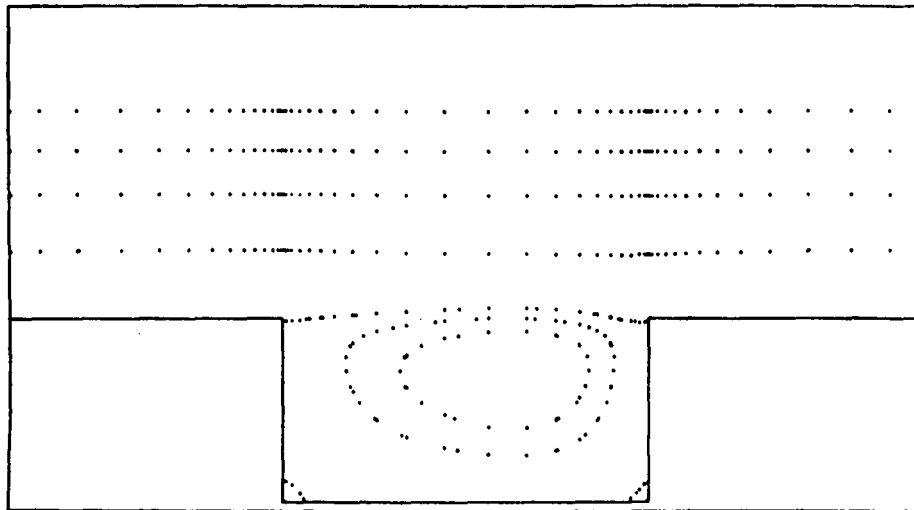


(a)

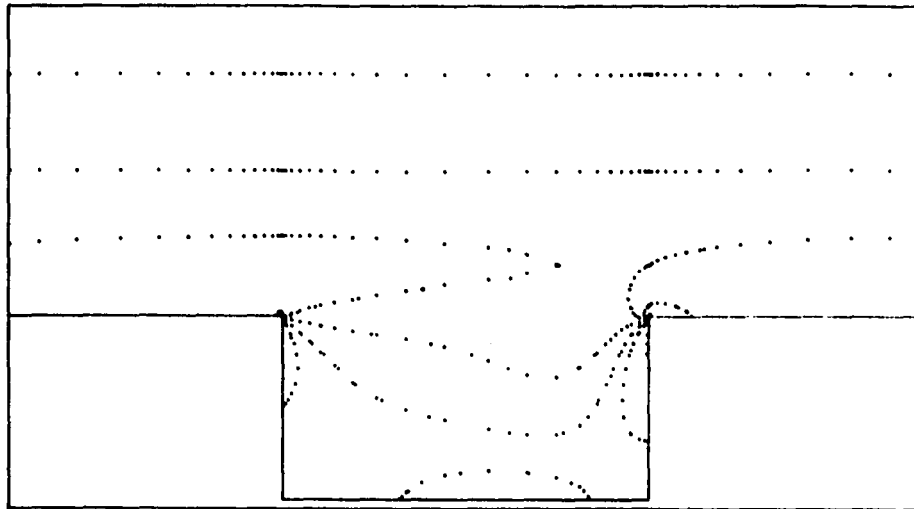


(b)

Figure 4.43 Plots of the (a) stream function and (b) vorticity contours for unsteady flow over the grooved wall at $t=13.9999$ using the VSF method.



(a)



(b)

Figure 4.44 Plots of the (a) stream function and (b) vorticity contours for unsteady flow over the grooved wall at $t=15.9996$ using the VSF method.

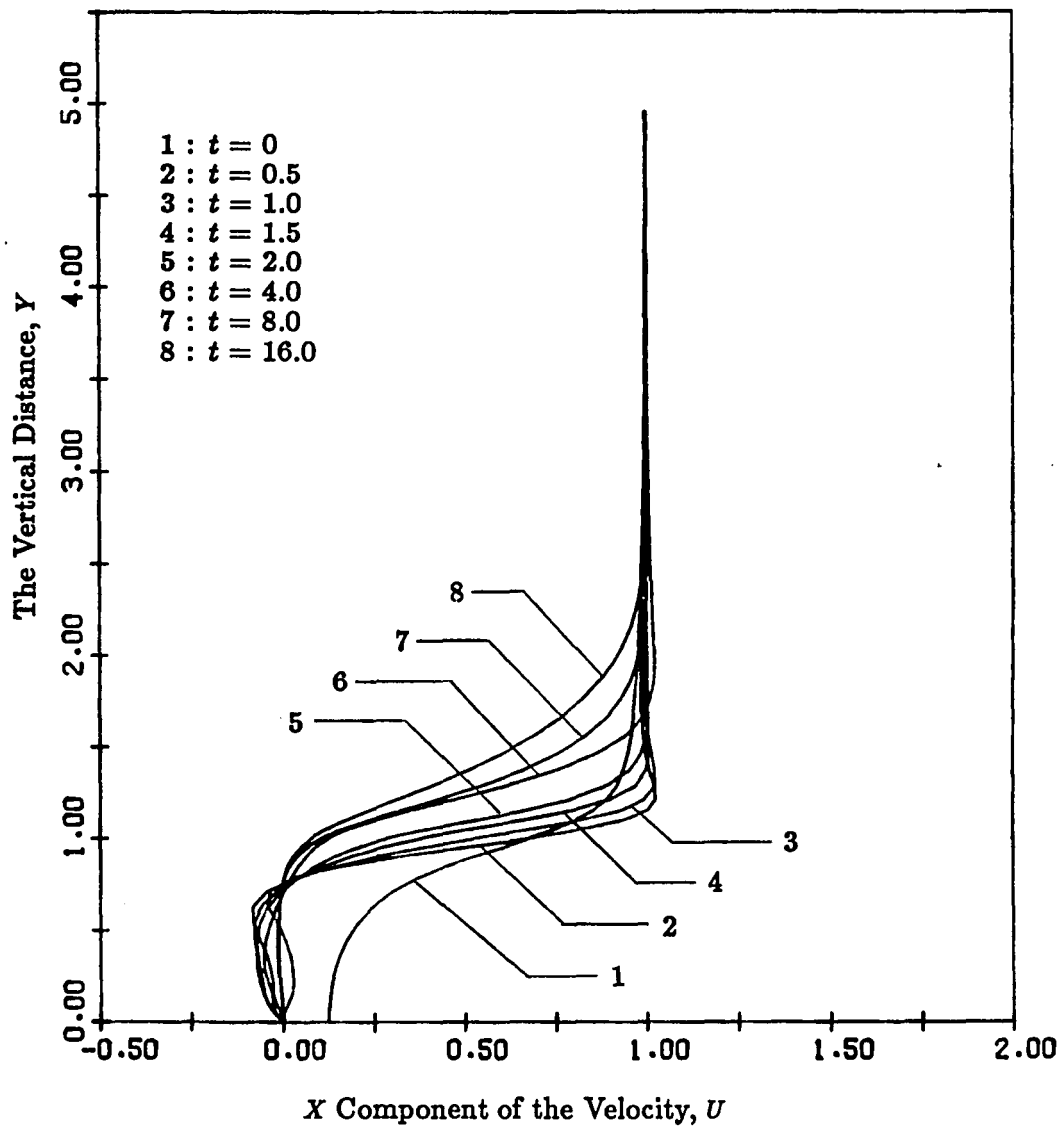


Figure 4.45 Plots of the time development of the X component of velocities from the VSF methods as a function of the vertical distance from the bottom wall at $X = -0.7571$.

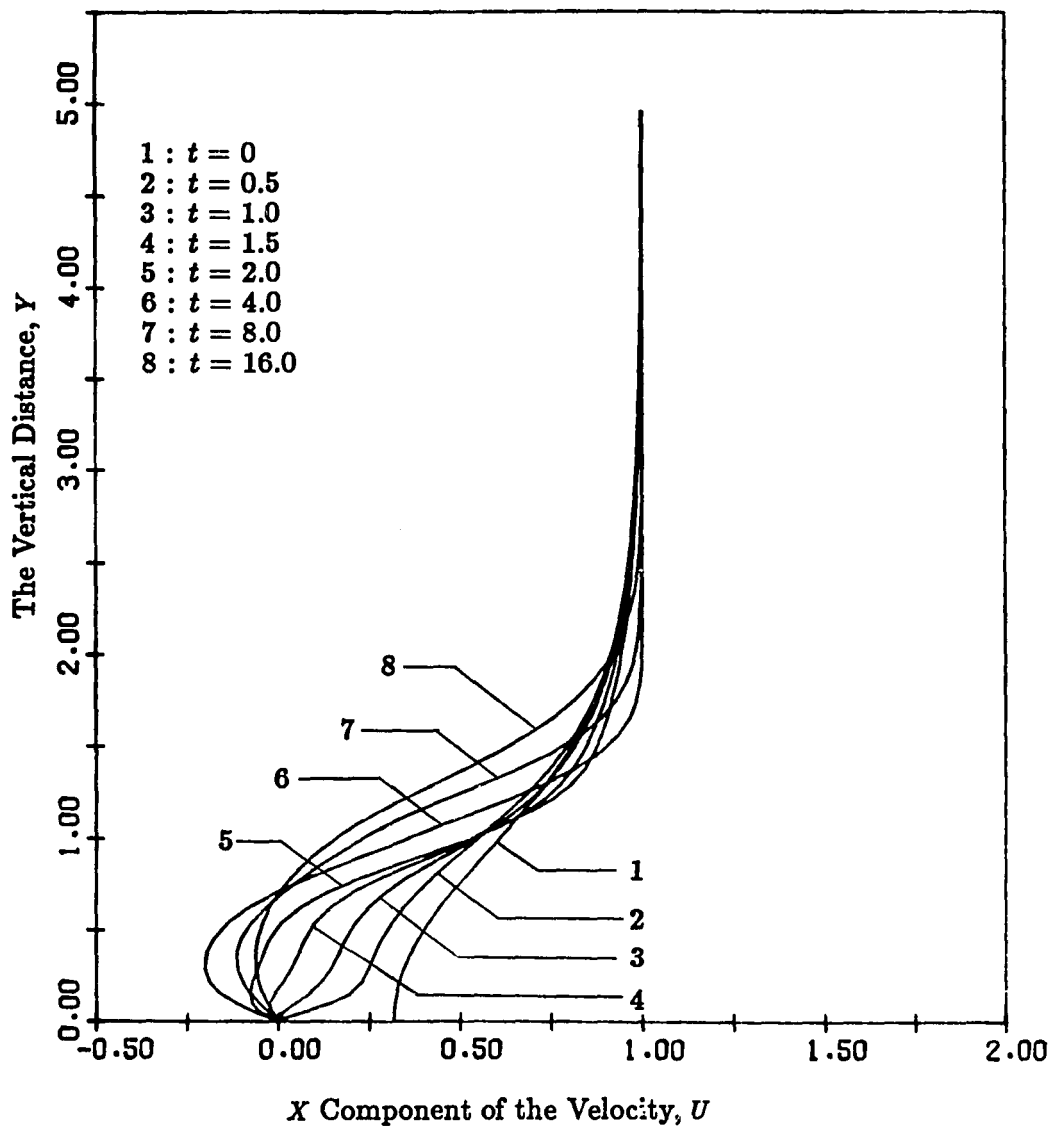


Figure 4.46 Plots of the time development of the X component of velocities from the VSF methods as a function of the vertical distance from the bottom wall at $X = 0$.

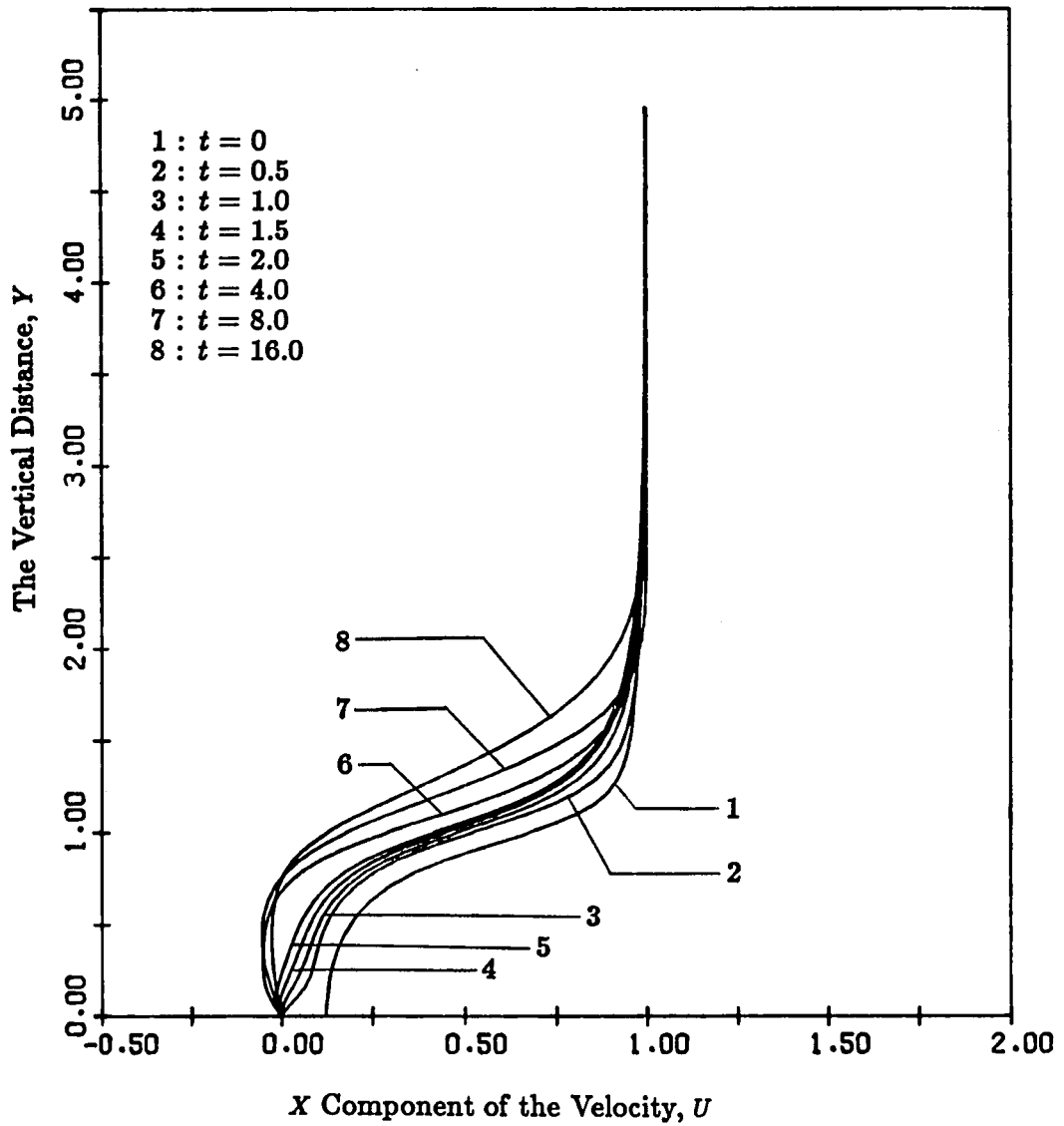


Figure 4.47 Plots of the time development of the X component of velocities from the VSF methods as a function of the vertical distance from the bottom wall at $X = 0.7571$.

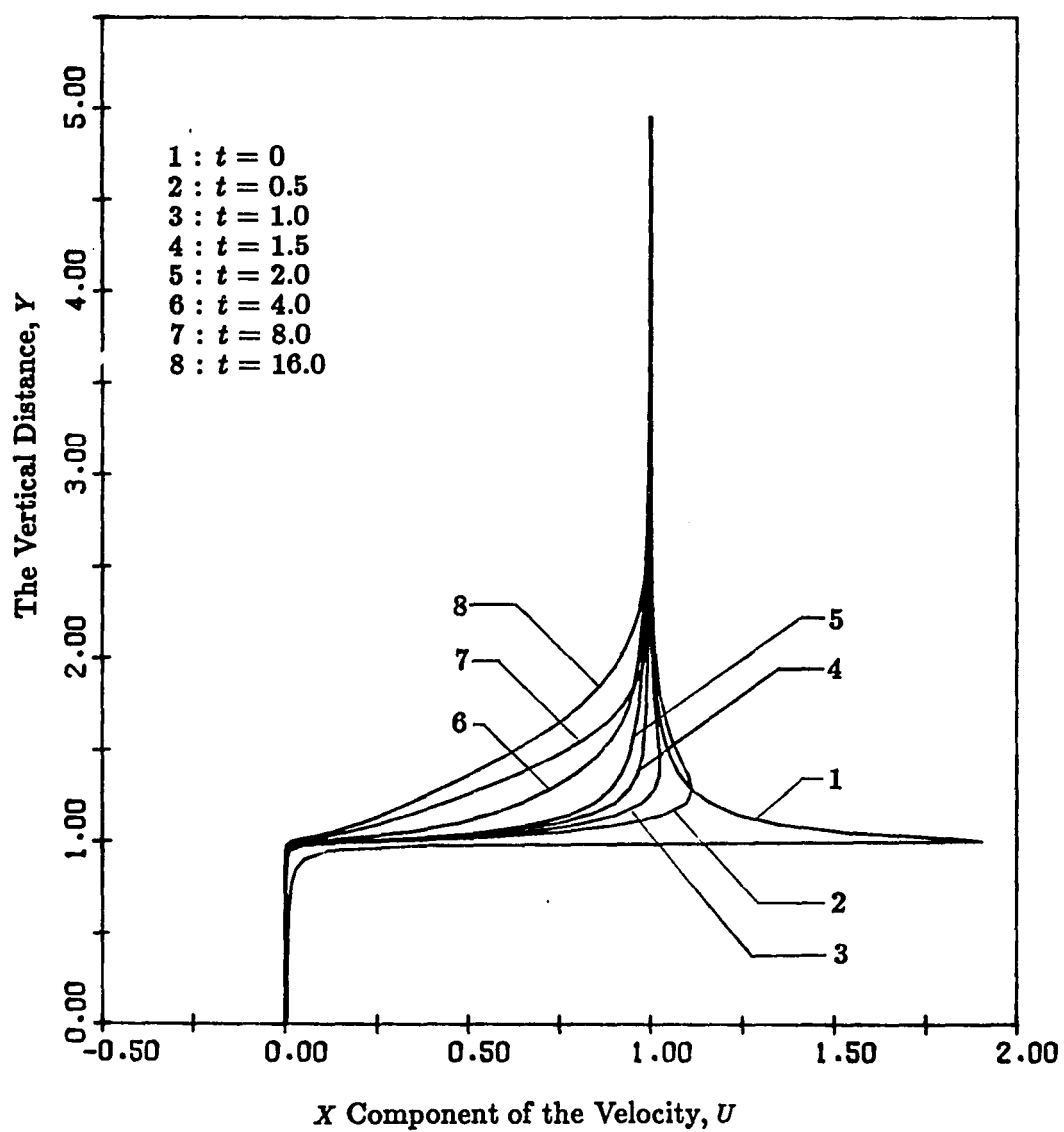


Figure 4.48 Plots of the time development of the X component of velocities from the VSF methods as a function of the vertical distance from the bottom wall at $X = 0.9911$.

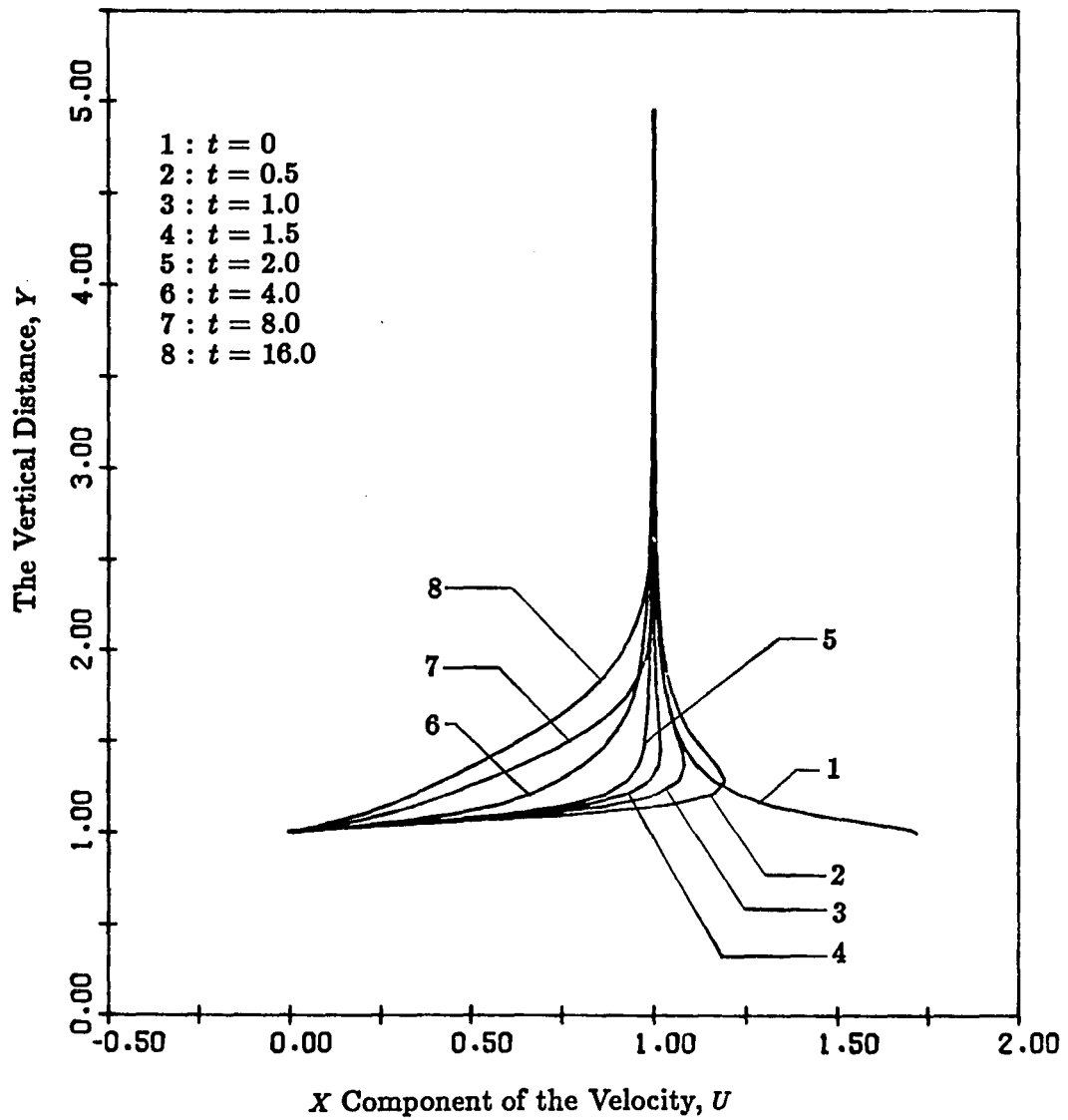


Figure 4.49 Plots of the time development of the X component of velocities from the VSF methods as a function of the vertical distance from the bottom wall at $X = 1.0689$.

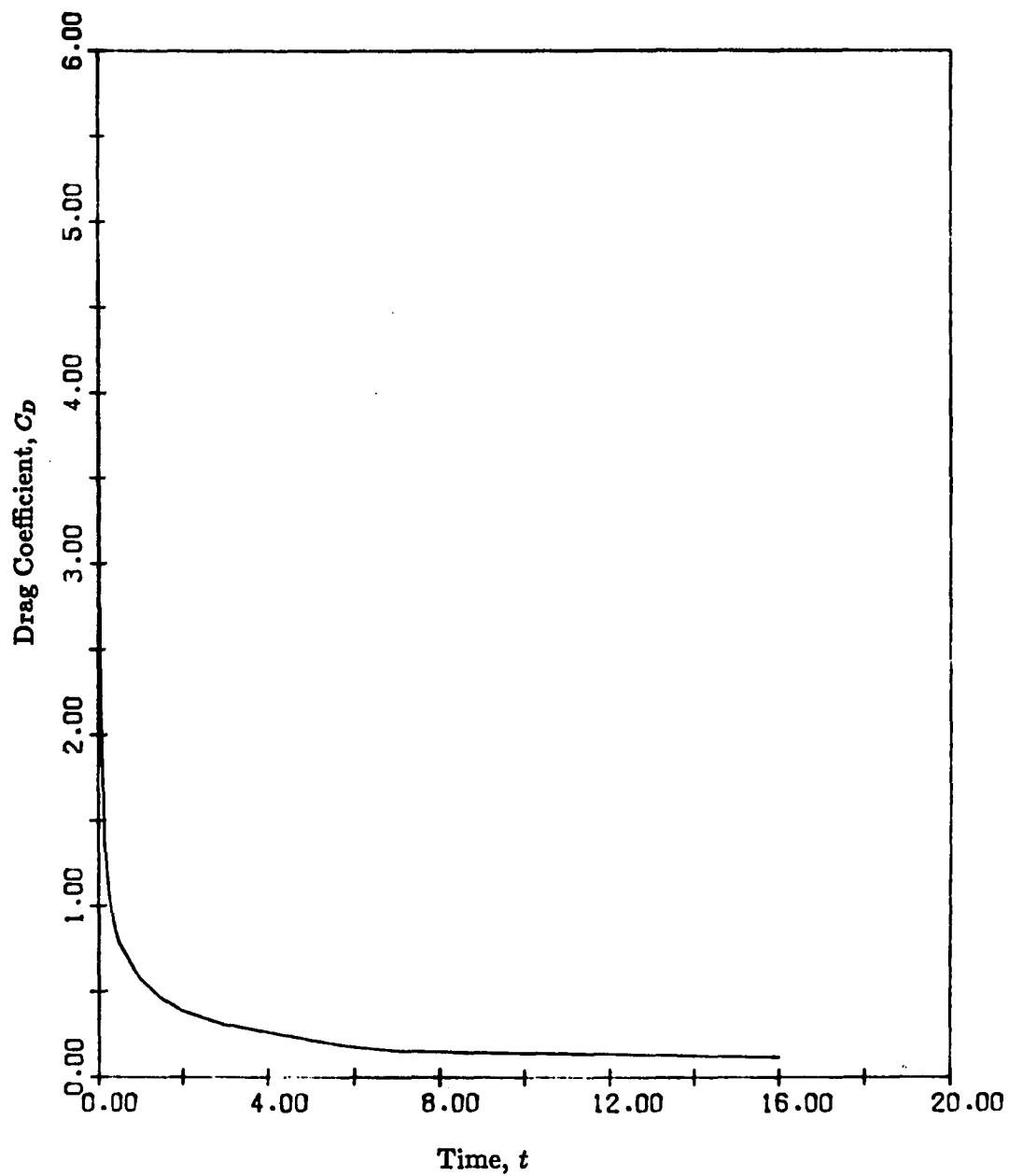


Figure 4.50 Plots of the time development of the drag coefficient from the VSF method.

that the magnitude of the drag coefficient, as also shown in Figure 4.39, seems to be decreasing continuously and appears to be asymptotically approaching zero. It is possible to determine the drag coefficient at the steady state through application of the momentum principle. This states that the sum of all forces acting on a nonaccelerating control volume is equal to the sum of the rate of change of momentum inside the control volume and the net rate of efflux of momentum through the control surface. The results from such an analysis serve to verify the general features seen in the time development of the drag coefficient obtained through integration of the shear and pressure forces along the surface of the grooved wall. This is explained below.

Due to the spatial periodicity in the horizontal direction of the flow field, the influx and outflux of momentum across the left and right boundaries of the computational domain must cancel out. The same conclusion may be drawn for the pressure forces. This leads to the conclusion that the drag on the grooved wall is then determined solely by the change of momentum in the control volume and the flux of the X -component of momentum across the upper and lower boundaries of the domain. Since there is no flow across the lower solid boundary, and the flow at the upper boundary is considered to be undisturbed (that is, the velocity is U_∞ and in the X direction only), therefore, no X -component of momentum crosses the upper and lower boundaries. As a result, the net drag on the grooved wall is only due to the time rate of change of momentum inside the control volume. At steady state, this must vanish. Based upon this analysis, we conclude that the drag coefficient tends to approach zero asymptotically, as shown in Figures 4.39 and 4.50.

CHAPTER 5

SUMMARY AND CONCLUDING REMARKS

A numerical simulation of the unsteady viscous flow over a spatially periodically grooved wall has been studied using the VVI and VSF methods. The flow field has been treated as two dimensional and incompressible. A single aspect ratio for the geometry of the grooved wall and a Reynolds number based on the step height and the onset velocity in the laminar range were chosen for the entire calculation.

The velocity formulations, including the velocity boundary condition, for both methods are basically different, as is the treatment of the vorticity production at the solid surface. The results showing the general features for the time development of the shear layer, free shear layer and recirculating vortex flow are in good agreement. However, a significant deviation exists at early times between the results obtained by the two methods for the distribution of surface pressure along the wall. This deviation occurs at and persists beyond the left-upper corner of the step. This has a noticeable effect on the drag coefficient during the early instants of time, but the gap between the distributions of surface pressure and drag coefficients dies out gradually as time progresses. In view of the fact that the surface pressure from the VSF method does not return to its starting value at the end of one spatial period during the early times, consequently, more confidence should be placed on the drag predictions from the VVI method than from the VSF method. This behavior is believed to be caused by the different procedures for enforcing the no-slip condition at the solid surface. The present

numerical simulation leaves unanswered the question of whether or not the above-mentioned discrepancy would persist in time for the flows with higher Reynolds number and/or with different aspect ratios for the geometry.

Since the current problem does not have the known analytical solution, the direct verification of whether or not the numerical schemes are accurate in simulating the time development of the flow field cannot be made. However, certain features of the flow can be expected to occur, and therefore the following observations and comparisons can be made.

First, the velocity field for an irrotational flow over a single forward-facing step, which has a known analytical solution, was studied using the Biot-Savart law of induced velocities. The comparison between the results for all the selected velocity profiles obtained by the numerical and exact solutions was made and observed to be exceptionally good, as shown in Appendix C. Secondly, the results representing the features of the flow development for the current flow geometry obtained by applying the two independent numerical methods were shown to be consistent in the general aspects. Thirdly, the pictures in the form of stream-function and vorticity contours at the steady state obtained from the VSF method are qualitatively the same as those from the investigation of the steady flow in grooved channels recently reported by Chaddar, et al. (1986). Finally, the results show that the drag coefficient predicted by both methods tends to approach zero asymptotically as time progresses. The zero value at steady state can be verified by applying the momentum principle to the whole primary computational domain.

To conclude this chapter, the following remarks on the advantages and disadvantages of the VVI and VSF methods are made. It is clear from the current

study that the VSF method has a relatively simple formulation, and it is also found that the VSF method is computationally inexpensive. The computational time is in the ratio of about 1:8 for the VSF and VVI methods, respectively. However, some difficulties are associated with the VSF method. First, since the solution of the velocity field involves solving an equation of Poisson's type for the stream function, this requires that the computation to be performed in the whole disturbed flow field which includes rotational and irrotational zones. In the VVI method, on the other hand, the computation needs to be carried out only in the region of non-zero vorticity, which includes only those portions of fluid that have passed near the body surface.

A second difficulty in the VSF method is that velocity components which are obtained directly are tangential to the face of cell elements. Components normal to the face of cell elements must then be found by interpolating the stream function, followed by differentiation. As a result, a lack of spatial smoothness in the stream function could be amplified by the numerical differentiation used in the evaluation of the fluid velocity. The effect can thus propagate throughout the flow. On the other hand, a numerical integration over the vorticity field is carried out in the VVI method which, on the contrary, would smooth out the spatial irregularities. Furthermore, the desired normal velocity components can be found directly.

The third difficulty is that the stream function is not defined in the three-dimensional flow. Therefore, the VSF method is not applicable for this type of flow, whereas the VVI method is applicable, albeit with considerable added complexity.

APPENDIX A

VELOCITY INDUCED BY BOUND AND FREE VORTICITY

The velocity at the point p using the VVI method is given by Eqn.(2.7)

as

$$\bar{V}(r_p, t) = \bar{i} + \frac{1}{2\pi} \iint_A \frac{\bar{\omega}_o \times \bar{r}_{op}}{|\bar{r}_{op}|^2} dA + \frac{1}{2\pi} \int_{\Gamma} \frac{\bar{\gamma}_q \times \bar{r}_{qp}}{|\bar{r}_{qp}|^2} dl \quad (A.1)$$

On the right hand side of Eqn.(A.1), the first term is the velocity due to the onset flow, $U_{\infty}\bar{i}$, which has been used to non-dimensionalize the flow variables. The second term is the velocity due to the free vorticity field, and the third term is the velocity due to the distribution of bound vorticity.

For convenience, we make the following definition:

$$\bar{V}_b(r_p, t) \equiv \frac{1}{2\pi} \int_{\Gamma} \frac{\bar{\gamma}_q \times \bar{r}_{qp}}{|\bar{r}_{qp}|^2} dl \quad (A.2a)$$

$$\bar{V}_f(r_p, t) \equiv \frac{1}{2\pi} \iint_A \frac{\bar{\omega}_o \times \bar{r}_{op}}{|\bar{r}_{op}|^2} dx dy \quad (A.2b)$$

in which the subscripts “ b ” and “ f ” denote the contribution due to the distribution of bound vorticity and the free vorticity field, respectively. Note that in two dimensions, \bar{V}_b and \bar{V}_f can be expressed in the Cartesian coordinates as

$$\bar{V}_b(r_p, t) = u_b \bar{i} + v_b \bar{j} \quad (A.3a)$$

$$\bar{V}_f(r_p, t) = u_f \bar{i} + v_f \bar{j} \quad (A.3b)$$

Using the notation as defined by Eqns.(A.2a,b) and (A.3a,b), Eqn.(A.1) can be expressed as

$$\begin{aligned} \bar{V}(r_p, t) &= \bar{i} + \bar{V}_b(r_p, t) + \bar{V}_f(r_p, t) \\ &= (1 + u_b + u_f) \bar{i} + (v_b + v_f) \bar{j} \end{aligned} \quad (A.4)$$

Velocity due to a Single Bound Vorticity Element

As shown in Eqn.(A.2a), the velocity at the point p due to the distribution of bound vorticity is

$$\bar{V}_b(r_p, t) = \frac{1}{2\pi} \int_{\Gamma} \frac{\bar{\gamma}_q \times \bar{r}_{qp}}{|\bar{r}_{qp}|^2} dl$$

Note that

$$\begin{aligned} \bar{r}_{qp} &= (x_p - x_q)\bar{i} + (y_p - y_q)\bar{j} \\ |\bar{r}_{qp}|^2 &= (x_p - x_q)^2 + (y_p - y_q)^2 \\ \bar{\gamma}_q &= \gamma_q \bar{k} \end{aligned}$$

Thus, \bar{V}_b can be written in the Cartesian coordinates as

$$\begin{aligned} \bar{V}_b(r_p, t) &= \frac{1}{2\pi} \int_{\Gamma} \frac{\gamma_q \bar{k} \times [(x_p - x_q)\bar{i} + (y_p - y_q)\bar{j}]}{(x_p - x_q)^2 + (y_p - y_q)^2} dl \\ &= \frac{1}{2\pi} \int_{\Gamma} \gamma_q \left[\frac{-(y_p - y_q)}{(x_p - x_q)^2 + (y_p - y_q)^2} \bar{i} + \frac{(x_p - x_q)}{(x_p - x_q)^2 + (y_p - y_q)^2} \bar{j} \right] dl \quad (A.5) \end{aligned}$$

According to Eqn.(A.3a) and the above equation, it follows that

$$u_b(x_p, y_p, t) = -\frac{1}{2\pi} \int_{\Gamma} \frac{(y_p - y_q)\gamma_q}{(x_p - x_q)^2 + (y_p - y_q)^2} dl \quad (A.6a)$$

$$v_b(x_p, y_p, t) = \frac{1}{2\pi} \int_{\Gamma} \frac{(x_p - x_q)\gamma_q}{(x_p - x_q)^2 + (y_p - y_q)^2} dl. \quad (A.6b)$$

First, we consider the X component of the velocity at the point p induced by a bound vorticity element, Δx_i , at the horizontal surface of the step. This component of the velocity will be denoted as $\Delta u_{b,i}$. By replacing the range of integration, Γ , with the value from $x_i - \Delta x_i/2$ to $x_i + \Delta x_i/2$ and dl with dx_q in Eqn.(A.6a), we obtain

$$\Delta u_{b,i}(x_p, y_p, t) = -\frac{1}{2\pi} \int_{x_i - \frac{\Delta x_i}{2}}^{x_i + \frac{\Delta x_i}{2}} \frac{(y_p - y_q)\gamma_q}{(x_p - x_q)^2 + (y_p - y_q)^2} dx_q. \quad (A.7)$$

Recall that γ_q at the horizontal surface of the step was given by Eqn.(3.31), which is restated as below.

$$\gamma_q(x_q, t) = \begin{cases} \frac{2(\gamma_i - \gamma_{i-1})}{\Delta x_{i-1} + \Delta x_i} (x_q - x_i) + \gamma_i & \text{if } x_i - \frac{\Delta x_i}{2} \leq x_q \leq x_i; \\ \frac{2(\gamma_{i+1} - \gamma_i)}{\Delta x_i + \Delta x_{i+1}} (x_q - x_i) + \gamma_i & \text{if } x_i \leq x_q \leq x_i + \frac{\Delta x_i}{2}. \end{cases}$$

Substitution of γ_q into Eqn.(A.7), $\Delta u_{b,i}$ is expressed in terms of γ_i , γ_{i-1} and γ_{i+1} as follows:

$$\begin{aligned} \Delta u_{b,i}(x_p, y_p, t) = & -\frac{1}{2\pi} \int_{x_i - \frac{\Delta x_i}{2}}^{x_i} \frac{y_p - y_q}{(x_p - x_q)^2 + (y_p - y_q)^2} \left[\frac{2(\gamma_i - \gamma_{i-1})}{\Delta x_{i-1} + \Delta x_i} (x_q - x_i) + \gamma_i \right] dx_q \\ & + \frac{1}{2\pi} \int_{x_i}^{x_i + \frac{\Delta x_i}{2}} \frac{y_p - y_q}{(x_p - x_q)^2 + (y_p - y_q)^2} \left[\frac{2(\gamma_{i+1} - \gamma_i)}{\Delta x_i + \Delta x_{i+1}} (x_q - x_i) + \gamma_i \right] dx_q \quad (A.8) \end{aligned}$$

For convenience, we define the following variables:

$$x = x_q - x_i, \quad y = y_q - y_j, \quad x_{pi} = x_p - x_i \quad \text{and} \quad y_{pj} = y_p - y_j \quad (A.9)$$

from which it follows that

$$\begin{aligned} x_p - x_q &= (x_p - x_i) - (x_q - x_i) \\ &= x_{pi} - x \\ y_p - y_q &= (y_p - y_j) - (y_q - y_j) \\ &= y_{pj} \\ dx_q &= dx. \end{aligned}$$

By a change of new variables and upon rearrangement, Eqn.(A.8) becomes

$$\Delta u_{b,i}(x_{pi}, y_{pj}, t) = (I_1 + I_2 + I_3)\gamma_i - I_1\gamma_{i-1} - I_2\gamma_{i+1} \quad (A.10)$$

where

$$I_1 = \frac{-y_{pj}}{\pi(\Delta x_{i-1} + \Delta x_i)} \int_{-\frac{\Delta x_i}{2}}^0 \frac{x dx}{(x_{pi} - x)^2 + y_{pj}^2} \quad (\text{A.10a})$$

$$I_2 = \frac{y_{pj}}{\pi(\Delta x_i + \Delta x_{i+1})} \int_0^{\frac{\Delta x_i}{2}} \frac{x dx}{(x_{pi} - x)^2 + y_{pj}^2} \quad (\text{A.10b})$$

$$I_3 = -\frac{y_{pj}}{2\pi} \int_{-\frac{\Delta x_i}{2}}^{\frac{\Delta x_i}{2}} \frac{dx}{(x_{pi} - x)^2 + y_{pj}^2} \quad (\text{A.10c})$$

Note that the integrals in Eqns.(A.10a, b, c) can be carried out exactly. The result is

$$I_1 = \frac{-y_{pj}}{\pi(\Delta x_{i-1} + \Delta x_i)} \left\{ \frac{1}{2} \ln \left[\frac{x_{pi}^2 + y_{pj}^2}{(x_{pi} + \frac{\Delta x_i}{2})^2 + y_{pj}^2} \right] - \frac{x_{pi}}{y_{pj}} \left(\arctan \frac{x_{pi}}{y_{pj}} - \arctan \frac{x_{pi} + \frac{\Delta x_i}{2}}{y_{pj}} \right) \right\} \quad (\text{A.11a})$$

$$I_2 = \frac{y_{pj}}{\pi(\Delta x_i + \Delta x_{i+1})} \left\{ \frac{1}{2} \ln \left[\frac{(x_{pi} - \frac{\Delta x_i}{2})^2 + y_{pj}^2}{x_{pi}^2 + y_{pj}^2} \right] - \frac{x_{pi}}{y_{pj}} \left(\arctan \frac{x_{pi} - \frac{\Delta x_i}{2}}{y_{pj}} - \arctan \frac{x_{pi}}{y_{pj}} \right) \right\} \quad (\text{A.11b})$$

$$I_3 = \frac{1}{2\pi} \left[\arctan \frac{x_{pi} - \frac{\Delta x_i}{2}}{y_{pj}} - \arctan \frac{x_{pi} + \frac{\Delta x_i}{2}}{y_{pj}} \right] \quad (\text{A.11c})$$

Following the same procedure as in evaluating $\Delta u_{b,i}$, the Y component of the velocity, $\Delta v_{b,i}$, induced by the bound vorticity element Δx_i is obtained as below

$$\Delta v_{b,i}(x_{pi}, y_{pj}, t) = (I'_1 + I'_2 + I'_3) \gamma_i - I'_1 \gamma_{i-1} - I'_2 \gamma_{i+1} \quad (\text{A.12})$$

where

$$I_1' = \frac{1}{\pi(\Delta x_{i-1} + \Delta x_i)} \int_{-\frac{\Delta x_i}{2}}^0 \frac{x(x_{pi} - x) dx}{(x_{pi} - x)^2 + y_{pj}^2} \quad (\text{A.12a})$$

$$I_2' = \frac{-1}{\pi(\Delta x_i + \Delta x_{i+1})} \int_0^{\frac{\Delta x_i}{2}} \frac{x(x_{pi} - x) dx}{(x_{pi} - x)^2 + y_{pj}^2} \quad (\text{A.12b})$$

$$I_3' = \frac{1}{2\pi} \int_{-\frac{\Delta x_i}{2}}^{\frac{\Delta x_i}{2}} \frac{(x_{pi} - x) dx}{(x_{pi} - x)^2 + y_{pj}^2} \quad (\text{A.12c})$$

The integrals in the above equations also have the closed form given by

$$I_1' = \frac{-1}{\pi(\Delta x_i + \Delta x_{i-1})} \left\{ \frac{\Delta x_i}{2} + \frac{x_{pi}}{2} \ln \left[\frac{x_{pi}^2 + y_{pj}^2}{(x_{pi} + \frac{\Delta x_i}{2})^2 + y_{pj}^2} \right] \right. \\ \left. + y_{pj} \left(\arctan \frac{x_{pi}}{y_{pj}} - \arctan \frac{x_{pi} + \frac{\Delta x_i}{2}}{y_{pj}} \right) \right\} \quad (\text{A.13a})$$

$$I_2' = \frac{1}{\pi(\Delta x_i + \Delta x_{i+1})} \left\{ \frac{\Delta x_i}{2} + \frac{x_{pi}}{2} \ln \left[\frac{(x_{pi} - \frac{\Delta x_i}{2})^2 + y_{pj}^2}{x_{pi}^2 + y_{pj}^2} \right] \right. \\ \left. + y_{pj} \left(\arctan \frac{x_{pi} - \frac{\Delta x_i}{2}}{y_{pj}} - \arctan \frac{x_{pi}}{y_{pj}} \right) \right\} \quad (\text{A.13b})$$

$$I_3' = -\frac{1}{4\pi} \ln \left[\frac{(x_{pi} - \frac{\Delta x_i}{2})^2 + y_{pj}^2}{(x_{pi} + \frac{\Delta x_i}{2})^2 + y_{pj}^2} \right] \quad (\text{A.13c})$$

In like manner, a set of expressions may be obtained for the velocity at the point p due to the bound vorticity element Δy_j located at the left and right vertical surfaces of the step. The result is

$$\Delta u_{b,j}(x_{pi}, y_{pj}, t) = (I_1 + I_2 + I_3)\gamma_j - I_1\gamma_{j-1} - I_2\gamma_{j+1} \quad (\text{A.14})$$

where

$$\begin{aligned}
 I_1 &= \frac{-1}{\pi(\Delta y_{j-1} + \Delta y_j)} \int_{-\frac{\Delta y_j}{2}}^0 \frac{y(y_{pj} - y) dy}{(y_{pj} - y)^2 + x_{pi}^2} \\
 &= \frac{1}{\pi(\Delta y_j + \Delta y_{j-1})} \left\{ \frac{\Delta y_j}{2} + \frac{y_{pj}}{2} \ln \left[\frac{y_{pj}^2 + x_{pi}^2}{(y_{pj} + \frac{\Delta y_j}{2})^2 + x_{pi}^2} \right] \right. \\
 &\quad \left. + x_{pi} \left(\arctan \frac{y_{pj}}{x_{pi}} - \arctan \frac{y_{pj} + \frac{\Delta y_j}{2}}{x_{pi}} \right) \right\} \tag{A.14a}
 \end{aligned}$$

$$\begin{aligned}
 I_2 &= \frac{1}{\pi(\Delta y_j + \Delta y_{j+1})} \int_0^{\frac{\Delta y_j}{2}} \frac{y(y_{pj} - y) dy}{(y_{pj} - y)^2 + x_{pi}^2} \\
 &= \frac{-1}{\pi(\Delta y_j + \Delta y_{j+1})} \left\{ \frac{\Delta y_j}{2} + \frac{y_{pj}}{2} \ln \left[\frac{(y_{pj} - \frac{\Delta y_j}{2})^2 + x_{pi}^2}{y_{pj}^2 + x_{pi}^2} \right] \right. \\
 &\quad \left. + x_{pi} \left(\arctan \frac{y_{pj} - \frac{\Delta y_j}{2}}{x_{pi}} - \arctan \frac{y_{pj}}{x_{pi}} \right) \right\} \tag{A.14b}
 \end{aligned}$$

$$\begin{aligned}
 I_3 &= -\frac{1}{2\pi} \int_{-\frac{\Delta y_j}{2}}^{\frac{\Delta y_j}{2}} \frac{(y_{pj} - y) dy}{(y_{pj} - y)^2 + x_{pi}^2} \\
 &= \frac{1}{4\pi} \ln \left[\frac{(y_{pj} - \frac{\Delta y_j}{2})^2 + x_{pi}^2}{(y_{pj} + \frac{\Delta y_j}{2})^2 + x_{pi}^2} \right] \tag{A.14c}
 \end{aligned}$$

and

$$\Delta u_{b,j}(x_{pi}, y_{pj}, t) = (I'_1 + I'_2 + I'_3) \gamma_j - I'_1 \gamma_{j-1} - I'_2 \gamma_{j+1} \tag{A.15}$$

where

$$\begin{aligned}
 I'_1 &= \frac{x_{pi}}{\pi(\Delta y_{j-1} + \Delta y_j)} \int_{-\frac{\Delta y_j}{2}}^0 \frac{y dy}{(y_{pj} - y)^2 + x_{pi}^2} \\
 &= \frac{x_{pi}}{\pi(\Delta y_{j-1} + \Delta y_j)} \left\{ \frac{1}{2} \ln \left[\frac{y_{pj}^2 + x_{pi}^2}{(y_{pj} + \frac{\Delta y_j}{2})^2 + x_{pi}^2} \right] \right. \\
 &\quad \left. - \frac{y_{pj}}{x_{pi}} \left(\arctan \frac{y_{pj}}{x_{pi}} - \arctan \frac{y_{pj} + \frac{\Delta y_j}{2}}{x_{pi}} \right) \right\} \tag{A.15a}
 \end{aligned}$$

$$\begin{aligned}
I'_2 &= \frac{-x_{pi}}{\pi(\Delta y_j + \Delta y_{j+1})} \int_0^{\frac{\Delta y_j}{2}} \frac{y dy}{(y_{pj} - x)^2 + x_{pi}^2} \\
&= \frac{-x_{pi}}{\pi(\Delta y_j + \Delta y_{j+1})} \left\{ \frac{1}{2} \ln \left[\frac{(y_{pj} - \frac{\Delta y_j}{2})^2 + x_{pi}^2}{y_{pj}^2 + x_{pi}^2} \right] \right. \\
&\quad \left. - \frac{y_{pj}}{x_{pi}} \left(\arctan \frac{y_{pj} - \frac{\Delta y_j}{2}}{x_{pi}} - \arctan \frac{y_{pj}}{x_{pi}} \right) \right\} \quad (A.15b)
\end{aligned}$$

$$\begin{aligned}
I'_3 &= \frac{x_{pi}}{2\pi} \int_{-\frac{\Delta y_j}{2}}^{\frac{\Delta y_j}{2}} \frac{dy}{(y_{pj} - y)^2 + x_{pi}^2} \\
&= -\frac{1}{2\pi} \left[\arctan \frac{y_{pj} - \frac{\Delta y_j}{2}}{x_{pi}} - \arctan \frac{y_{pj} + \frac{\Delta y_j}{2}}{x_{pi}} \right] \quad (A.15c)
\end{aligned}$$

The results given by Eqns.(A.14) and (A.15) correspond to $CEU_{b,k}$ and $CEV_{b,k}$. They are analogous to those used in Eqns.(3.28a) and (3.28b). To obtain the total velocity at the point p due to the distribution of bound vorticity, the contribution from γ distributed along the surfaces of an infinite number of steps and their corresponding images in the lower half plane must be summed up as given by Eqn.(3.30a, b).

Velocity due to a Single Free Vorticity Element

Recalling from Eqn.(A.2b), the velocity at the point p due to the free vorticity field is

$$\bar{V}_f(r_p, t) = \frac{1}{2\pi} \iint_A \frac{\bar{\omega}_o \times \bar{r}_{op}}{|\bar{r}_{op}|^2} dA. \quad (A.16)$$

Since

$$\begin{aligned}
\bar{r}_{op} &= (x_p - x_o) \bar{i} + (y_p - y_o) \bar{j} \\
|\bar{r}_{op}|^2 &= (x_p - x_o)^2 + (y_p - y_o)^2 \\
dA &= dx_o dy_o \\
\bar{\omega}_o &= \omega_o \bar{k}
\end{aligned}$$

Equation (A.16) becomes

$$\begin{aligned} \vec{V}_f(r_p, t) = \frac{1}{2\pi} \iint_A \omega_o \left[\frac{-(y_p - y_o)}{(x_p - x_o)^2 + (y_p - y_o)^2} \vec{i} \right. \\ \left. + \frac{x_p - x_o}{(x_p - x_o)^2 + (y_p - y_o)^2} \vec{j} \right] dx_o dy_o. \end{aligned} \quad (A.17)$$

According to Eqns.(A.3b) and (A.17), it follows that

$$u_f(x_p, y_p, t) = -\frac{1}{2\pi} \iint_A \frac{y_p - y_o}{(x_p - x_o)^2 + (y_p - y_o)^2} \omega_o dx_o dy_o \quad (A.18a)$$

$$v_f(x_p, y_p, t) = \frac{1}{2\pi} \iint_A \frac{x_p - x_o}{(x_p - x_o)^2 + (y_p - y_o)^2} \omega_o dx_o dy_o. \quad (A.18b)$$

Now, we consider the X and Y components of the velocity, denoted as $\Delta u_{f,ij}$ and $\Delta v_{f,ij}$ respectively, at the point p due to the free vorticity element $\Delta A_{i,j}$ in the fluid. In the calculation, ω_o is assumed to be constant and uniformly distributed over $\Delta A_{i,j}$. Thus, ω_o is equal to $\omega_{i,j}$, which is the vorticity at the node point (i, j) . Using the similar coordinate transformation as described in the derivation of $\Delta u_{b,i}$, we obtain

$$\Delta u_{f,ij}(x_{pi}, y_{pj}, t) = -\frac{\omega_{i,j}}{2\pi} \int_{-\frac{\Delta y_j}{2}}^{\frac{\Delta y_j}{2}} \int_{-\frac{\Delta x_i}{2}}^{\frac{\Delta x_i}{2}} \frac{y_{pj} - y}{(x_{pi} - x)^2 + (y_{pj} - y)^2} dx dy \quad (A.19a)$$

$$\Delta v_{f,ij}(x_{pi}, y_{pj}, t) = \frac{\omega_{i,j}}{2\pi} \int_{-\frac{\Delta y_j}{2}}^{\frac{\Delta y_j}{2}} \int_{-\frac{\Delta x_i}{2}}^{\frac{\Delta x_i}{2}} \frac{x_{pi} - x}{(x_{pi} - x)^2 + (y_{pj} - y)^2} dx dy \quad (A.19b)$$

where

$$x = x_o - x_i, \quad y = y_o - y_j, \quad x_{pi} = x_p - x_i \quad \text{and} \quad y_{pj} = y_p - y_j, \quad (A.20)$$

and the ranges of x and y are $-\Delta x_i/2 \leq x \leq \Delta x_i/2$ and $-\Delta y_j/2 \leq y \leq \Delta y_j/2$.

The two integrals in Eqns.(A.19a, b) can be integrated analytically. The result is

$$\begin{aligned} \Delta u_{f,ij}(x_{pi}, y_{pj}, t) = \frac{\omega_{i,j}}{4\pi} \left\{ (x_{pi} - \frac{\Delta x_i}{2}) \ln \frac{(y_{pj} + \frac{\Delta y_j}{2})^2 + (x_{pi} - \frac{\Delta x_i}{2})^2}{(y_{pj} - \frac{\Delta y_j}{2})^2 + (x_{pi} - \frac{\Delta x_i}{2})^2} \right. \\ - (x_{pi} + \frac{\Delta x_i}{2}) \ln \frac{(y_{pj} + \frac{\Delta y_j}{2})^2 + (x_{pi} + \frac{\Delta x_i}{2})^2}{(y_{pj} - \frac{\Delta y_j}{2})^2 + (x_{pi} + \frac{\Delta x_i}{2})^2} \\ + 2(y_{pj} + \frac{\Delta y_j}{2}) \left[\arctan \frac{x_{pi} - \frac{\Delta x_i}{2}}{y_{pj} + \frac{\Delta y_j}{2}} - \arctan \frac{x_{pi} + \frac{\Delta x_i}{2}}{y_{pj} + \frac{\Delta y_j}{2}} \right] \\ \left. - 2(y_{pj} - \frac{\Delta y_j}{2}) \left[\arctan \frac{x_{pi} - \frac{\Delta x_i}{2}}{y_{pj} - \frac{\Delta y_j}{2}} - \arctan \frac{x_{pi} + \frac{\Delta x_i}{2}}{y_{pj} - \frac{\Delta y_j}{2}} \right] \right\} \quad (A.21a) \end{aligned}$$

$$\begin{aligned} \Delta v_{f,ij}(x_{pi}, y_{pj}, t) = \frac{\omega_{i,j}}{4\pi} \left\{ (y_{pj} - \frac{\Delta y_j}{2}) \ln \frac{(x_{pi} - \frac{\Delta x_i}{2})^2 + (y_{pj} - \frac{\Delta y_j}{2})^2}{(x_{pi} - \frac{\Delta x_i}{2})^2 + (y_{pj} - \frac{\Delta y_j}{2})^2} \right. \\ - (y_{pj} + \frac{\Delta y_j}{2}) \ln \frac{(y_{pj} + \frac{\Delta y_j}{2})^2 + (x_{pi} - \frac{\Delta x_i}{2})^2}{(y_{pj} + \frac{\Delta y_j}{2})^2 + (x_{pi} + \frac{\Delta x_i}{2})^2} \\ + 2(x_{pi} - \frac{\Delta x_i}{2}) \left[\arctan \frac{y_{pj} - \frac{\Delta y_j}{2}}{x_{pi} - \frac{\Delta x_i}{2}} - \arctan \frac{y_{pj} + \frac{\Delta y_j}{2}}{x_{pi} - \frac{\Delta x_i}{2}} \right] \\ \left. - 2(x_{pi} - \frac{\Delta x_i}{2}) \left[\arctan \frac{y_{pj} - \frac{\Delta y_j}{2}}{x_{pi} + \frac{\Delta x_i}{2}} - \arctan \frac{y_{pj} + \frac{\Delta y_j}{2}}{x_{pi} + \frac{\Delta x_i}{2}} \right] \right\} \quad (A.21b) \end{aligned}$$

The results in curly brackets in Eqns.(A.21a, b) correspond to $CEU_{f,ij}$ and $CEV_{f,ij}$ in Eqns.(3.28a, b), respectively. Finally, the total velocity at the point p due to the entire free vorticity field is then obtained by summing the contribution from all cell elements with non-zero free vorticity as specified by Eqn.(3.29a, b).

APPENDIX B

INTERPOLATION METHOD FOR STREAM FUNCTION

The interpolation procedure involves a nine-point formula. To proceed, we assume a biquadratic formula of the following type:

$$\psi = A + Bx + Cy + Dxy + Ex^2 + Fy^2 + Gx^2y + Hxy^2 + Ix^2y^2 \quad (B.1)$$

Here, x and y denote local coordinates, with origin at point 1, as shown in Figure 3.6.

In principle, one can find the nine unknown constants A through I from known values of ψ at nine points in the field. However, the solution of the nine simultaneous equations would be tedious, and we do want a closed form solution. Instead, we utilize a procedure used in finite-element analysis.

We note that the X - and Y -spacing is variable and construct polynomials in X as follows:

$$N_1(x) = \frac{(x - h_1)(x - h_1 - h_2)}{h_1(h_1 + h_2)} \quad (B.2)$$

$$N_2(x) = \frac{-x(x - h_1 - h_2)}{h_1 h_2} \quad (B.3)$$

$$N_3(x) = \frac{x(x - h_1)}{h_2(h_1 + h_2)} \quad (B.4)$$

These expressions have the following properties:

$$N_1(0) = 1, \quad N_1(h_1) = N_1(h_1 + h_2) = 0$$

$$N_2(h_1) = 1, \quad N_2(0) = N_2(h_1 + h_2) = 0$$

$$N_3(h_1 + h_2) = 1, \quad N_3(0) = N_3(h_1) = 0$$

In like manner, we form identical polynomials in Y , but with h_i replaced by k_i , where $i=1, 2$ and 3 . The final expression for ψ becomes

$$\begin{aligned}\psi = & \left[\psi_1 N_1(x) + \psi_2 N_2(x) + \psi_3 N_3(x) \right] N_1(y) \\ & + \left[\psi_4 N_1(x) + \psi_5 N_2(x) + \psi_6 N_3(x) \right] N_2(y) \\ & + \left[\psi_7 N_1(x) + \psi_8 N_2(x) + \psi_9 N_3(x) \right] N_3(y)\end{aligned}\quad (B.5)$$

Next, Eqn.(B.5) is expanded, and terms are collected. After extensive algebra, one can obtain the coefficients A through I by inspection. The results are:

$$A = \psi_1 \quad (B.6)$$

$$B = -\frac{2h_1 + h_2}{h_1(h_1 + h_2)}\psi_1 + \frac{h_1 + h_2}{h_1 h_2}\psi_2 - \frac{h_1}{h_2(h_1 + h_2)}\psi_3 \quad (B.7)$$

$$C = -\frac{2k_1 + k_2}{k_1(k_1 + k_2)}\psi_1 + \frac{k_1 + k_2}{k_1 k_2}\psi_4 - \frac{k_1}{k_2(k_1 + k_2)}\psi_7 \quad (B.8)$$

$$\begin{aligned}D = & \frac{(2h_1 + h_2)(2k_1 + k_2)}{h_1 k_1 (h_1 + h_2)(k_1 + k_2)}\psi_1 - \frac{(h_1 + h_2)(2k_1 + k_2)}{h_1 h_2 k_1 (k_1 + k_2)}\psi_2 \\ & + \frac{h_1(2k_1 + k_2)}{k_1 h_2 (h_1 + h_2)(k_1 + k_2)}\psi_3 - \frac{(2h_1 + h_2)(k_1 + k_2)}{h_1 k_1 k_2 (h_1 + h_2)}\psi_4 \\ & + \frac{(h_1 + h_2)(k_1 + k_2)}{h_1 h_2 k_1 k_2}\psi_5 - \frac{h_1(k_1 + k_2)}{h_2 k_1 k_2 (h_1 + h_2)}\psi_6 \\ & + \frac{k_1(2h_1 + h_2)}{h_1 k_2 (h_1 + h_2)(k_1 + k_2)}\psi_7 - \frac{k_1(h_1 + h_2)}{h_1 h_2 k_2 (k_1 + k_2)}\psi_8 \\ & + \frac{h_1 k_1}{h_2 k_2 (h_1 + h_2)(k_1 + k_2)}\psi_9\end{aligned}\quad (B.9)$$

$$E = \frac{1}{h_1(h_1 + h_2)}\psi_1 - \frac{1}{h_1 h_2}\psi_2 + \frac{1}{h_2(h_1 + h_2 - 2)}\psi_3 \quad (B.10)$$

$$F = \frac{1}{k_1(k_1 + k_2)}\psi_1 - \frac{1}{k_1 k_2}\psi_4 + \frac{1}{k_2(k_1 + k_2 - 2)}\psi_7 \quad (B.11)$$

$$\begin{aligned}
G = & \frac{-(2k_1 + k_2)}{h_1 k_1 (h_1 + h_2)(k_1 + k_2)} \psi_1 + \frac{2k_1 + k_2}{h_1 h_2 k_1 (k_1 + k_2)} \psi_2 \\
& - \frac{2k_1 + k_2}{k_1 h_2 (h_1 + h_2)(k_1 + k_2)} \psi_3 + \frac{k_1 + k_2}{h_1 k_1 k_2 (h_1 + h_2)} \psi_4 \\
& - \frac{k_1 + k_2}{h_1 h_2 k_1 k_2} \psi_5 + \frac{k_1 + k_2}{h_2 k_1 k_2 (h_1 + h_2)} \psi_6 \\
& - \frac{k_1}{h_1 k_2 (h_1 + h_2)(k_1 + k_2)} \psi_7 + \frac{k_1}{h_1 h_2 k_2 (k_1 + k_2)} \psi_8 \\
& - \frac{k_1}{h_2 k_2 (h_1 + h_2)(k_1 + k_2)} \psi_9
\end{aligned} \tag{B.12}$$

$$\begin{aligned}
H = & \frac{-(2h_1 + h_2)}{h_1 k_1 (h_1 + h_2)(k_1 + k_2)} \psi_1 + \frac{h_1 + h_2}{h_1 h_2 k_1 (k_1 + k_2)} \psi_2 \\
& - \frac{h_1}{k_1 h_2 (h_1 + h_2)(k_1 + k_2)} \psi_3 + \frac{2h_1 + h_2}{h_1 k_1 k_2 (h_1 + h_2)} \psi_4 \\
& - \frac{h_1 + h_2}{h_1 h_2 k_1 k_2} \psi_5 + \frac{h_1}{h_2 k_1 k_2 (h_1 + h_2)} \psi_6 \\
& - \frac{2h_1 + h_2}{h_1 k_2 (h_1 + h_2)(k_1 + k_2)} \psi_7 + \frac{h_1 + h_2}{h_1 h_2 k_2 (k_1 + k_2)} \psi_8 \\
& - \frac{h_1}{h_2 k_2 (h_1 + h_2)(k_1 + k_2)} \psi_9
\end{aligned} \tag{B.13}$$

$$\begin{aligned}
I = & \frac{1}{h_1 k_1 (h_1 + h_2)(k_1 + k_2)} \psi_1 - \frac{1}{h_1 h_2 k_1 (k_1 + k_2)} \psi_2 \\
& + \frac{1}{k_1 h_2 (h_1 + h_2)(k_1 + k_2)} \psi_3 - \frac{1}{h_1 k_1 k_2 (h_1 + h_2)} \psi_4 \\
& + \frac{1}{h_1 h_2 k_1 k_2} \psi_5 - \frac{1}{h_2 k_1 k_2 (h_1 + h_2)} \psi_6 \\
& + \frac{1}{h_1 k_2 (h_1 + h_2)(k_1 + k_2)} \psi_7 - \frac{1}{h_1 h_2 k_2 (k_1 + k_2)} \psi_8 \\
& + \frac{1}{h_2 k_2 (h_1 + h_2)(k_1 + k_2)} \psi_9
\end{aligned} \tag{B.14}$$

The spacings h_1, k_1, h_2, \dots , etc. are obtained from the nodal arrangement shown in Figures 3.2 and 3.6; that is, $h_1 = .5(\Delta x_{i-1} + \Delta x_i)$ etc.

APPENDIX C

INVISCID FLOW OVER A FORWARD-FACING STEP

To illustrate the accuracy of the numerical scheme for computing the velocity field from the Biot-Savart law of induced velocities, we consider a case of irrotational flow subject to the uniform onset velocity, \bar{V}_∞ , over a forward-facing step, as shown in Figure C.1. This flow may be calculated by classical means using the Schwarz-Christoffel theorem (Churchill and Drown, 1984; Batchelor, 1967). Therefore, exact solutions can be derived. For purposes of comparison, numerical solutions of the same flow are also obtained.

Exact Solutions

According to the Schwarz-Christoffel theorem, the physical boundary, shown in Figure C.1, is transformed into a straight line of infinite extent along the X -axis, and the corresponding region of flow in the Z -plane (i.e., transformed plane) is the upper half-plane in Figure C.2. For purposes of the calculation, we have chosen a value of h_0 to be 0.999. Consequently, the channel flow in Figure C.1 can now be well approximated as an unconfined external flow. Note that the velocity in the far upstream region is constant, and its value is given by $U_\infty \bar{i}$.

The derivation of the classical solution of the velocity field is given in many elementary textbooks on the theory and applications of functions of a complex variable (Churchill and Drown, 1984) The derivation is reproduced here for completeness.

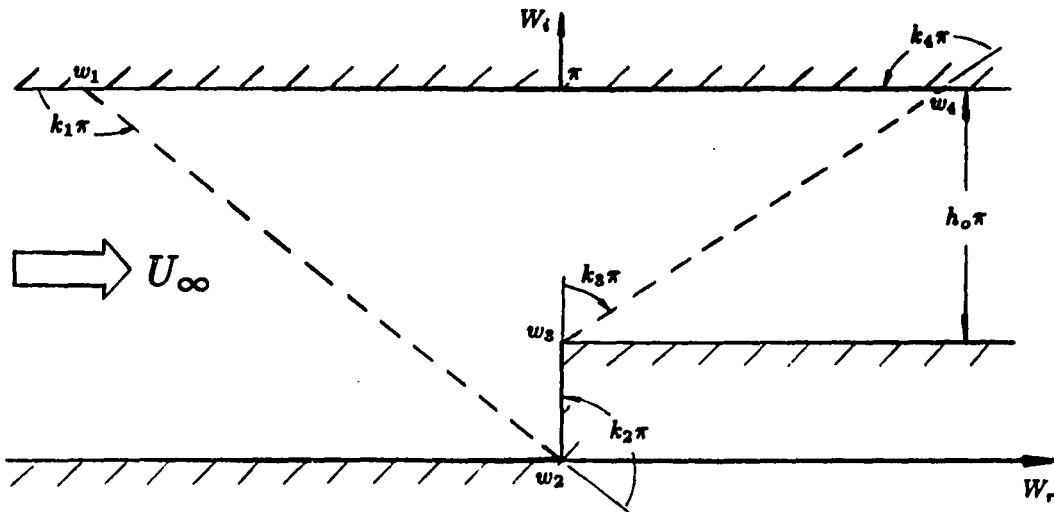


Figure C.1. Irrotational flow over a forward-facing step in the Physical W plane.

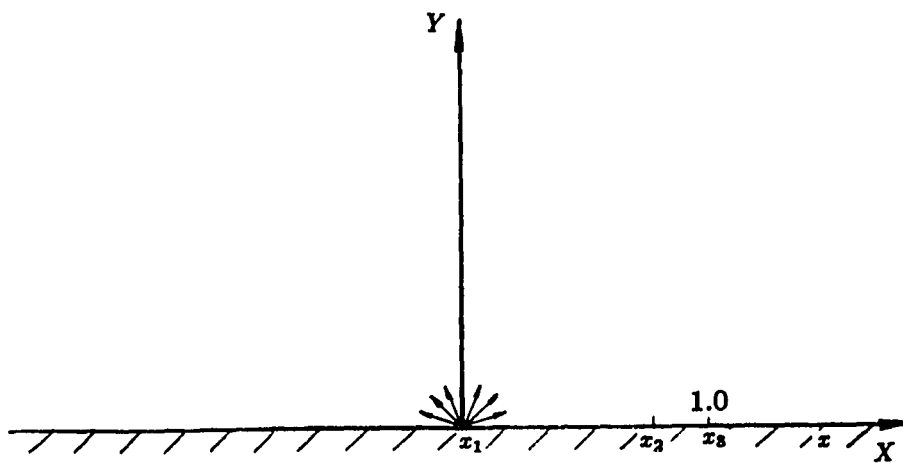


Figure C.2. Irrotational flow due to a source at the origin in the transformed Z plane.

The derivative of the mapping function of the Schwarz-Christoffel theorem for the quadrilateral with the vertices of w_1 , w_2 , w_3 and w_4 shown in Figure C.1 is given as

$$\frac{dw}{dz} = \frac{A'}{(z-x_1)^{k_1}(z-x_2)^{k_2}(z-x_3)^{k_3}(z-x_4)^{k_4}} \quad (C.1)$$

where A' is a complex constant, x_j is the image of w_j , and k_j is a real constant, with $k_j\pi$ being defined as the exterior angle of the polygon at its corresponding vertex. The value of the exterior angles is limited to the range $-\pi$ to π , and it is considered to be positive if the direction of the change in angle is counterclockwise, and negative if the direction of the change in angle is clockwise. In view of this transformation, the geometry in Figure C.1 can be treated as the limiting case of the quadrilateral with its two vertices, w_1 and w_4 , moved infinitely far to the left and to the right, respectively. The corresponding value of the exterior angles are

$$k_1\pi = \pi, \quad k_2\pi = \frac{\pi}{2}, \quad k_3\pi = -\frac{\pi}{2} \quad \text{and} \quad k_4\pi = \pi.$$

According to the theorem, three of the numbers x_j in Eqn.(C.1) can be chosen arbitrarily, and it is convenient to let $x_1 = 0$, $x_3 = 1$, $x_4 = \infty$. This leaves x_2 to be determined, where $0 < x_2 < 1$. Since x_4 is taken to be at infinity, the factor $(z-x_4)^{-k_4}$ in Eqn.(C.1) is then effectively constant and may be regarded as being absorbed into a new constant A . This is done by putting $[(z-x_4)/x_4]^{-k_4} = (-1)^{-k_4}$ and $(-1)^{-k_4}A'x_4^{-k_4} = A$. The values of k_j , x_j and A' are then substituted into Eqn.(C.1), the final expression for the derivative of the mapping function becomes

$$\frac{dw}{dz} = \frac{A(z-1)^{1/2}}{z(z-x_2)^{1/2}}. \quad (C.2)$$

The flow over the step shown in Figure C.1 is produced by a source located infinitely far to the left and a sink located infinitely far to the right. It can be shown that under the Schwarz-Christoffel transformation, a source or a sink at a given point transforms to a source or sink of equal strength at the image of that point (Churchill and Drown, 1984). Since the image of infinity to the left in Figure C.1 is the origin of the Z -plane in Figure C.2, there is an equal source at $z = 0$. By the same argument, there is a corresponding equal sink at infinity in the Z -plane.

The complex velocity potential for a source in the Z -plane is given by

$$F(z) = \frac{Q'}{2\pi} \ln z$$

with strength, Q' , equal to $2\pi U_\infty$. Hence,

$$F(z) = U_\infty \ln z.$$

The complex conjugate of the velocity $\tilde{V}(w)$ in the W -plane can be expressed as

$$\tilde{V}(w) = \frac{dF}{dz} \frac{dz}{dw} \quad (C.3)$$

By referring to Eqns.(C.2) and (C.3), we can write

$$\tilde{V}(w) = \frac{U_\infty}{A} \left(\frac{z - x_2}{z - 1} \right)^{1/2} \quad (C.4)$$

where values of A and x_2 can be determined by considering the limiting position of the point w_1 , corresponding to $z = 0$, where the velocity is U_∞ , and the limiting position of w_4 , corresponding to $z = \infty$, where the velocity is U_∞/h_0 . This is obtained by applying the mass conservation law to this steady incompressible inviscid flow. The values of A and x_2 are found to be

$$A = h_0 \quad \text{and} \quad x_2 = h_0^2.$$

Substitution of values of A and x_2 into Eqn.(C.2) gives

$$\frac{dw}{dz} = \frac{h_0}{z} \left(\frac{z-1}{z-h_0^2} \right)^{1/2} \quad (C.5)$$

To find out the relationship between w and z , we can simply carry out the integration in Eqn.(C.5). For convenience, we introduce a new variable S defined as

$$S = \left(\frac{z-h_0^2}{z-1} \right)^{1/2}$$

It is easy to show that Eqn.(C.5) reduces to

$$\frac{dw}{dS} = 2h_0 \left(\frac{1}{1-S^2} - \frac{1}{h_0^2-S^2} \right)$$

Hence, after integration, we have

$$w = h_0 \ln \frac{1+S}{1-S} - \ln \frac{h_0+S}{h_0-S}. \quad (C.6)$$

The constant of integration is zero because when $z = x_2$, S is zero, and so therefore is w .

By substituting values of A and x_2 into Eqn.(C.4), the complex conjugate of the velocity in the W -plane becomes

$$\tilde{V}(w) = \frac{U_\infty}{h_0} \left(\frac{z-h_0^2}{z-1} \right)^{1/2} \quad (C.7)$$

From Eqn.(C.7), we can see that the magnitude of the velocity becomes infinite at the corner w_3 of the step since it is the image of the point $z = 1$. Also, the corner w_2 is a stagnation point. That is, the velocity is zero there because it is the image of the point $z = h_0^2$.

To obtain the relationship between $\tilde{V}(w)$ and w , we first express $\tilde{V}(w)$ of Eqn.(C.7) in terms of S . The equation becomes

$$\tilde{V}(w) = \frac{U_\infty}{h_0} S$$

consequently,

$$S = \frac{\tilde{V}(w) h_0}{U_\infty} \quad (C.8)$$

By substituting S from this equation into Eqn.(C.6), we get an implicit relation which defines the complex conjugate of the velocity, $\tilde{V}(w)$, as a function of w . Since this equation cannot be solved explicitly for $\tilde{V}(w)$, a method of successive approximation is employed.

First, since S is a complex number, we then substitute $S = S_r + iS_i$ into Eqn.(C.6). After some manipulation and rearrangement, we obtain

$$w_r = \frac{h_0}{2} \ln \left[\frac{(1 + S_r)^2 + S_i^2}{(1 - S_r)^2 + S_i^2} \right] - \frac{1}{2} \ln \left[\frac{(h_0 + S_r)^2 + S_i^2}{(h_0 - S_r)^2 + S_i^2} \right] \quad (C.9a)$$

$$w_i = h_0(\theta_1 - \theta_2) - (\theta_3 - \theta_4) \quad (C.9b)$$

where w_r and w_i are the real and imaginary parts of w , respectively, and

$$\theta_1 = \arctan\left(\frac{S_i}{1 + S_r}\right) \quad \theta_2 = \arctan\left(\frac{-S_i}{1 - S_r}\right)$$

$$\theta_3 = \arctan\left(\frac{-S_i}{h_0 + S_r}\right) \quad \theta_4 = \arctan\left(\frac{-S_i}{h_0 - S_r}\right)$$

By expressing the complex conjugate velocity, $\tilde{V}(z)$, in terms of the real and imaginary parts,

$$\tilde{V}(z) = u - iv$$

and with the aid of Eqn.(C.8), we obtain

$$u = \frac{S_r}{h_0} U_\infty \quad (C.10a)$$

$$v = -\frac{S_i}{h_0} U_\infty. \quad (C.10b)$$

Using the dimensionless variables defined in Chapter 2 and noting that the step height, h , is equal to $(1-h_0)\pi$, Eqns.(C.9a, b) and (C.10a, b) are then written in the dimensionless form as follows:

$$\begin{aligned} w_r^* &= \frac{w_r}{(1-h_0)\pi} \\ &= \frac{h_0}{2\pi(1-h_0)} \ln\left[\frac{(1+S_r)^2 + S_i^2}{(1-S_r)^2 + S_i^2}\right] - \frac{1}{2\pi(1-h_0)} \ln\left[\frac{(h_0+S_r)^2 + S_i^2}{(h_0-S_r)^2 + S_i^2}\right] \end{aligned} \quad (C.11a)$$

$$\begin{aligned} w_i^* &= \frac{w_i}{(1-h_0)\pi} \\ &= \frac{h_0}{(1-h_0)\pi}(\theta_1 - \theta_2) - \frac{1}{(1-h_0)\pi}(\theta_3 - \theta_4) \end{aligned} \quad (C.11b)$$

$$u^* = \frac{u}{U_\infty} = \frac{S_r}{h_0} \quad (C.12a)$$

$$v^* = \frac{v}{U_\infty} = -\frac{S_i}{h_0}. \quad (C.12b)$$

For purposes of comparison between the velocity profiles from both exact and numerical solutions, we need to calculate the non-dimensional velocity components (i.e., u^* and v^*) as a function of w_i^* at specified values of w_r^* in the physical plane. Hence, the following procedure for the calculation of the exact solution is established.

We first specify desired values of u^* and w_r^* . The value of S_r can thus be calculated from Eqn.(C.12a). Next, two trial values of S_i are selected, and two corresponding values of w_i^* are calculated from Eqn.(C.11a). These calculated values of w_i^* are then compared with the specified value of w_r^* . A new approximation to the value of S_i is made, using the local gradient method, and the process is repeated until the calculated value of w_i^* closely approximates the specified value of w_r^* . The iterative process was stopped when the relative change between two successive values of S_i was less than 10^{-5} . With a knowledge of S_i plus the aid of Eqn.(C.12b), the value of v^* was finally obtained.

The values of u^* and v^* found by this procedure are referred to as "exact" values at the point of (w_r^*, w_i^*) in the W -plane. In like manner, a set of exact values for u^* and v^* as function of w_i^* , all with the same value of w_r^* , can be obtained. Following the same procedure, we can derive as many sets of exact values for u^* and v^* as function of w_i^* with the specified values of w_r^* as we want.

Numerical Solutions

The fundamental principles underlying the formulation of the velocity field and the distribution of bound vorticity were described in Chapter 2. The following remarks on the distribution of bound vorticity are made for completeness.

In the flow over a forward-facing step as shown in Figure C.1, the horizontal surface of the step extends infinitely far down stream. Thus, the bound vorticity should be distributed along the step surface accordingly. However, for purposes of the numerical computation, the bound vorticity was distributed only over a finite length of the step surface. Fortunately, the magnitude of the velocity induced by a vortex element decays as $|\bar{r}|^{-2}$, where \bar{r} is the position vector relative to the vortex element. Thus, the bound vorticity far removed from the corner of the step has a negligible effect in the region of the flow where the velocity profiles are to be evaluated.

It is reasonable to assume that the velocity profiles near the singular corner point are the most important in determining the accuracy of the numerical solution. Therefore, we confine our comparisons of the velocity profiles from both the numerical and the exact solution to some selected node points in the region near the singular corner.

In the numerical calculations, we have distributed bound vorticity on the horizontal surface of the step for a distance of 600 step heights from the corner. Consequently, the contribution from the bound vorticity beyond this distance was neglected. Trial calculations showed that this length was sufficient.

For purposes of this numerical calculation, a flow network is chosen to be 242 by 67 nodes in the horizontal and vertical direction, respectively. A portion of the grid network near the step corner is shown in Figure C.3. These grid points are chosen so that the network near the step is identical to that used for the artificially roughened wall. The grid serves no purpose other than to provide a network on which the potential velocity can be evaluated.

The evaluation of the distribution of bound vorticity is discussed in Chapter 2, in which the governing equation is derived and given by Eqn.(2.9). Since irrotational flow is considered in the present problem, the second term on the right-hand side of the equation which is the contribution due to the free vorticity field, is equal to zero. The equation is then reduced to

$$\frac{1}{2\pi} \int_{\Gamma} \left[\frac{\bar{\gamma}_q \times \bar{r}_{qp}}{|\bar{r}_{qp}|^2} dl \right] \cdot \bar{e}_i = -\bar{i} \cdot \bar{e}_i,$$

where Γ consists of the vertical and horizontal surfaces of the step, plus their reflections in the image plane. The above equation is solved numerically by following the procedure described in Chapter 3 to obtain the distribution of bound vorticity, $\bar{\gamma}$. The slip velocity, i.e., the tangential component of the velocity along the surface of the step, is then obtained by putting the value equal to $-\bar{\gamma}$.

In irrotational flow, Eqn.(2.7), the velocity at point p, becomes

$$\mathbf{V}(r_p) = \bar{i} + \frac{1}{2\pi} \int_{\Gamma} \frac{\bar{\gamma}_q \times \bar{r}_{qp}}{|\bar{r}_{qp}|^2} dl.$$

The numerical evaluation of the integral in the above equation is discussed in Chapter 3.

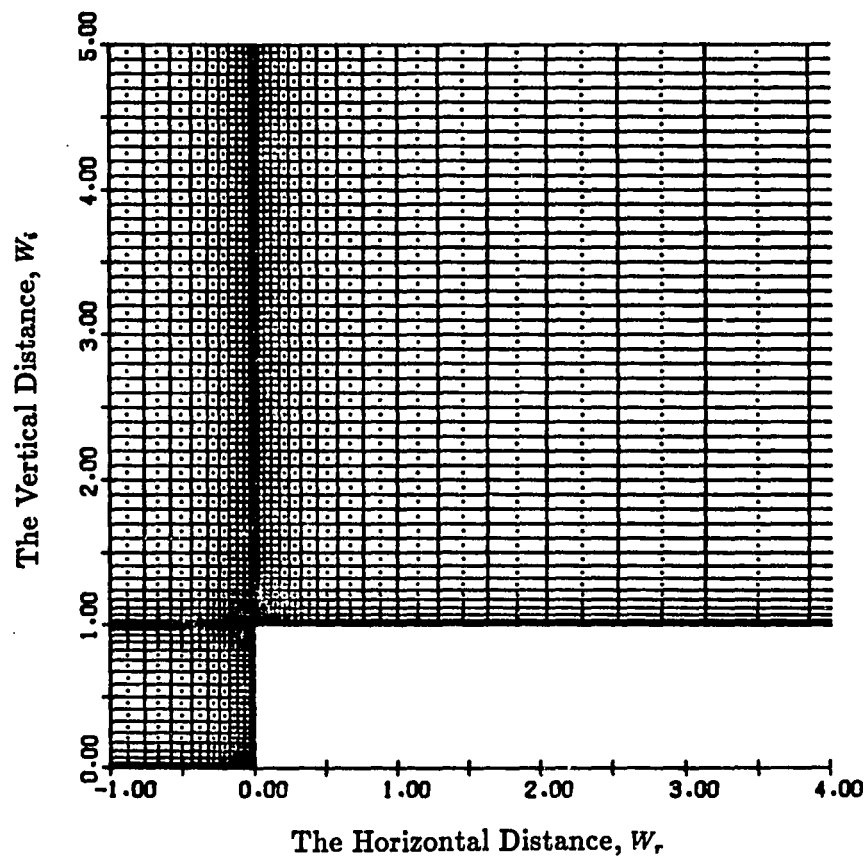


Figure C.3. Layout of the flow network near the corner of the step.

Results

For purposes of comparison, five velocity profiles corresponding to five values of w_2^* on W_r -axis of the physical plane have been calculated. Point values for each velocity have been calculated at the center of each cell boundary for the 67 cells in the vertical direction. The values of w_2^* chosen are -0.0689468 , -0.00893428 , 0 , 0.00893428 and 0.0689468 .

The velocity profiles are plotted in Figures C.4 through C.9, in which the solid lines represent the exact solution, and the points as shown in small triangles represent the numerical solution. In Figure C.4, the slip velocity along the vertical surface of the step is plotted from $l = 0$ to $l = 1.0$, and the slip velocity along the horizontal portion is plotted from $l = 1.0$ to $l = 1.6$. Note that $l = 0$ corresponds to the stagnation point, w_2 in Figure C.1, and $l = 1.0$ corresponds to the corner of the step, w_3 in Figure C.1. Figures C.5 through C.9 are plots of the horizontal component of velocity, u^* , as a function of w_2^* for several values of w_2^* . It is observed that the numerical solutions shown in these figures are in good agreement with the corresponding exact solutions which confirms the accuracy of our numerical formulation.

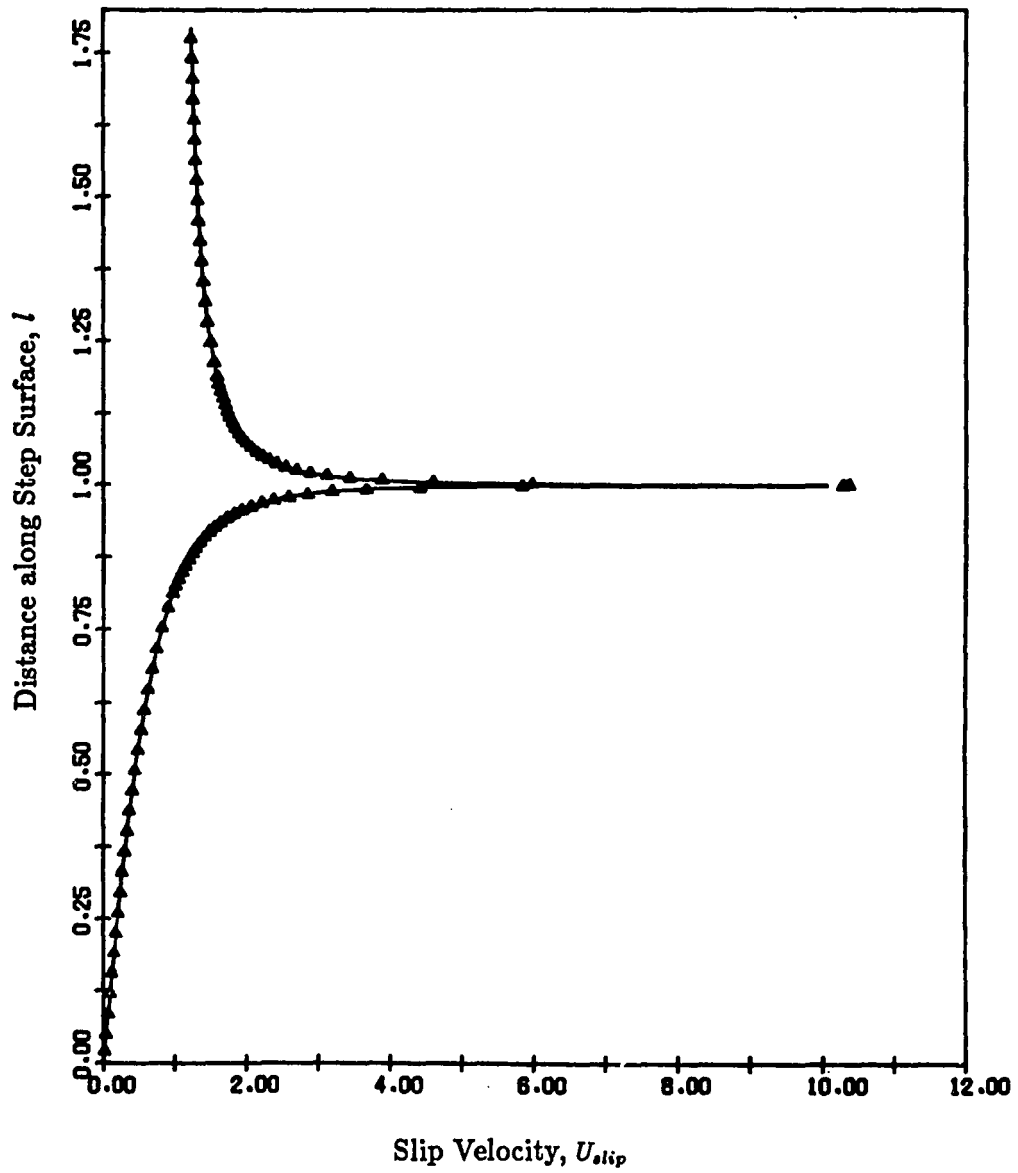


Figure C.4. Comparison between the exact (—) and numerical (Δ) solutions for the slip velocity along the surface of the step.

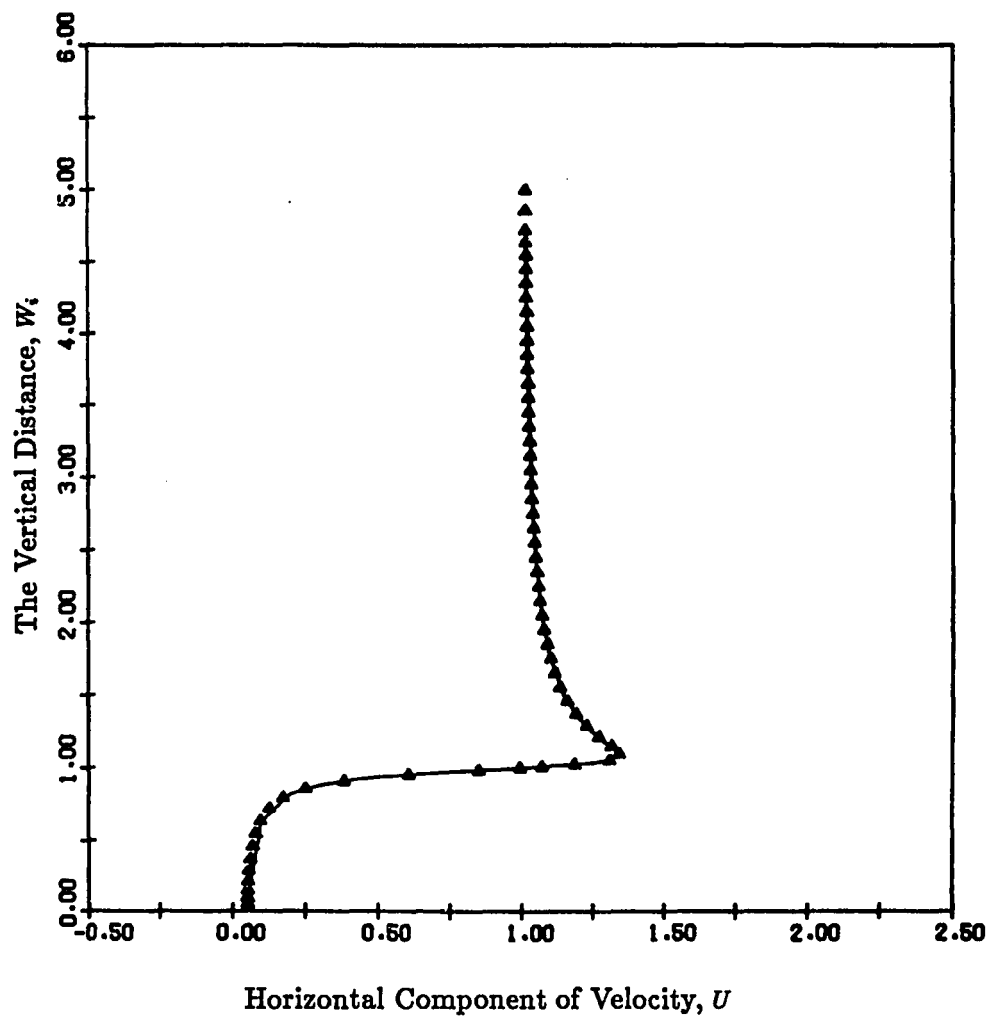


Figure C.5. Comparison between the exact (—) and numerical (Δ) solutions for the horizontal component of velocity at $w_r^* = -0.0689468$.

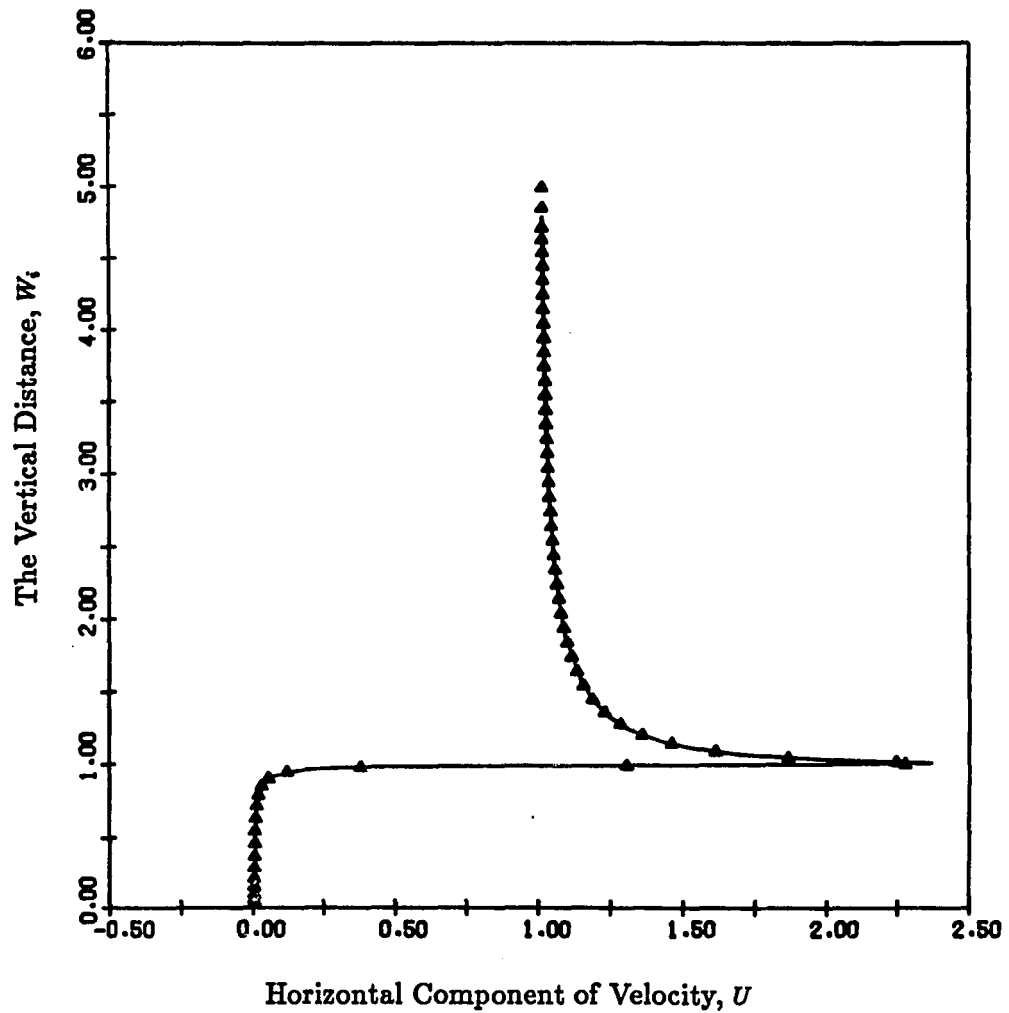


Figure C.6. Comparison between the exact (—) and numerical (Δ) solutions for the horizontal component of velocity at $w_r^* = -0.00893428$.

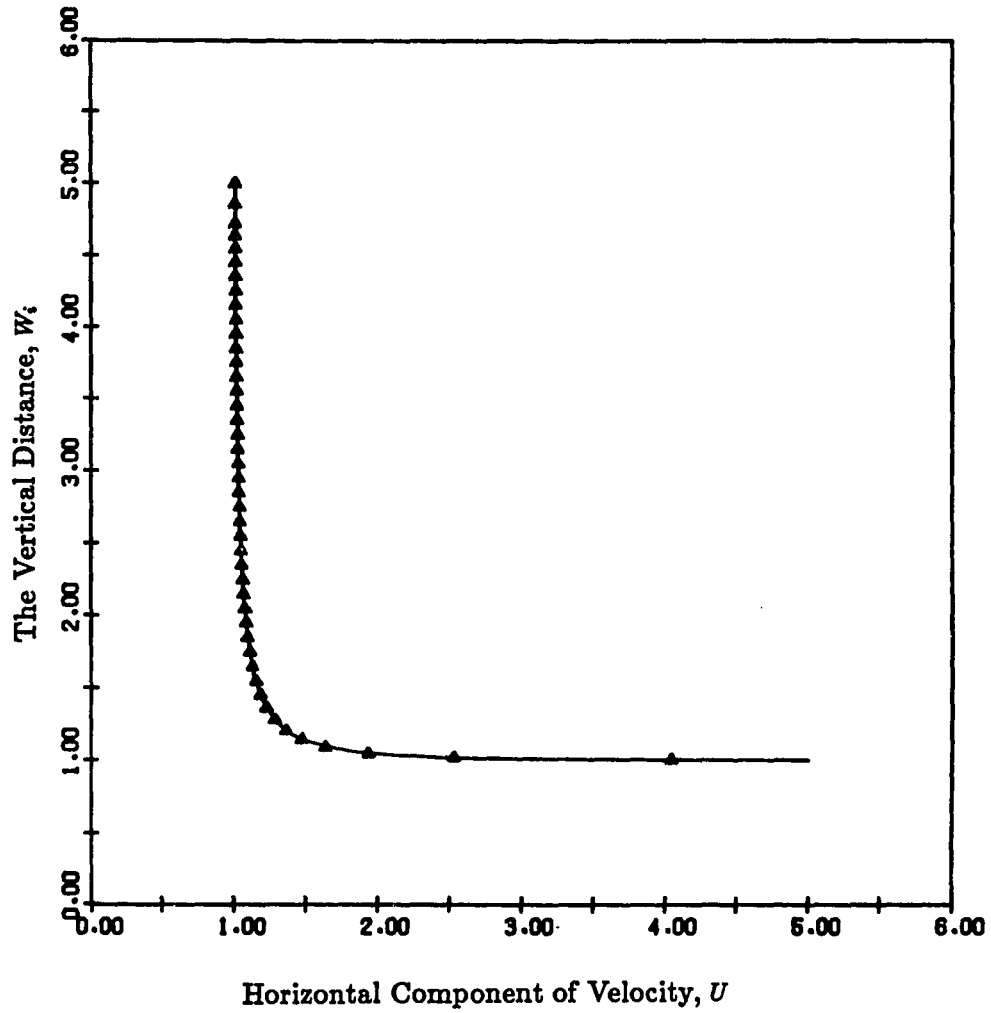


Figure C.7. Comparison between the exact (—) and numerical (Δ) solutions for the horizontal component of velocity at $w_r^* = 0$.

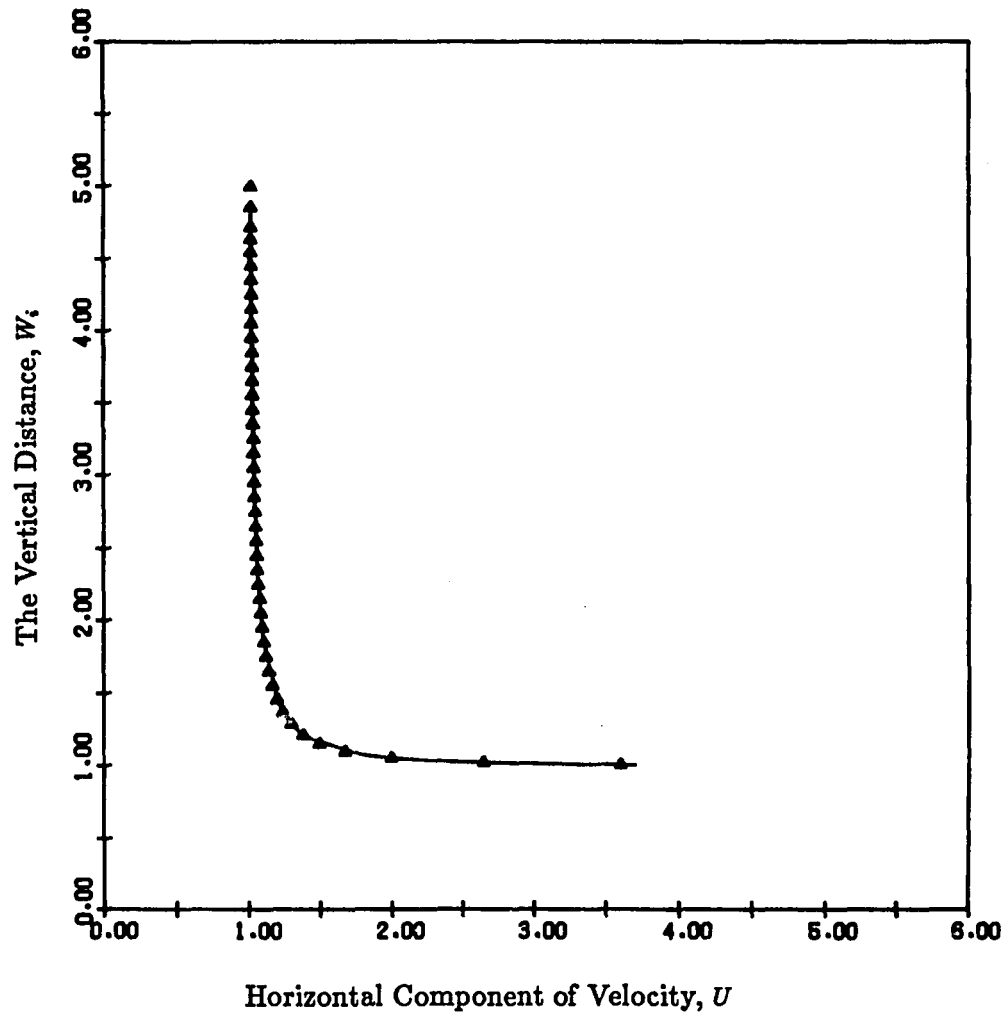


Figure C.8. Comparison between the exact (—) and numerical (Δ) solutions for the horizontal component of velocity at $w_r^* = 0.00893428$.

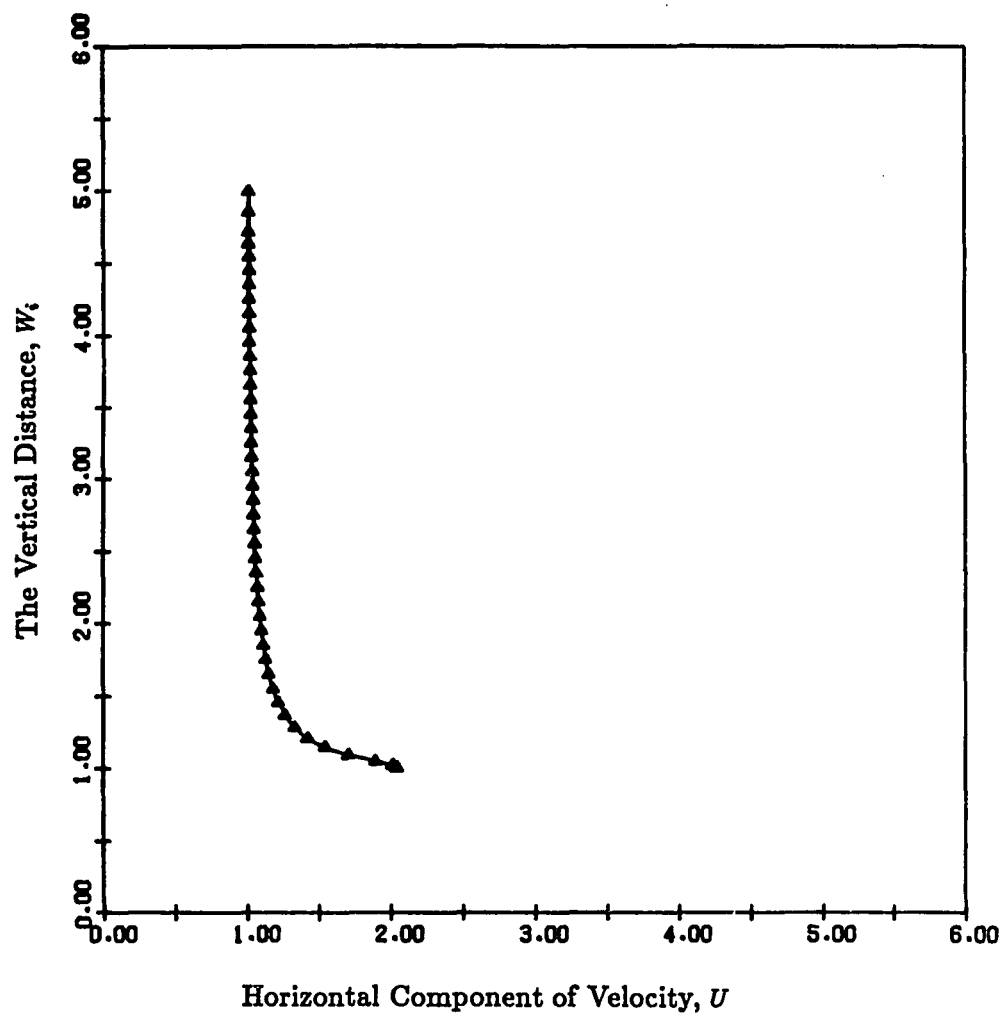


Figure C.9. Comparison between the exact (—) and numerical (Δ) solutions for the horizontal component of velocity at $w_r^* = 0.0689468$.

REFERENCES

- [1] Alkins, D.J., S.J. Maskell and M.A. Patrick: "Numerical Prediction of Separated Flows," Int. Journal for Numerical Methods in Engineering, Vol. 15, pp. 129-144, 1980.
- [2] Batchelor, G.K. : An Introduction to Fluid Dynamics, Cambridge University Press, Cambridge, 1967.
- [3] Cerutti, E.A., R.B. Kinney and M.A. Paolino : "Numerical Predictions for Unsteady Viscous Flow Past an Array of Cylinders," Int. Journal for Numerical Methods in Fluids, Vol. 6, pp. 715-731, October, 1986.
- [4] Cerutti, E.A. : "Numerical Predictions for Unsteady Viscous Flow Past an Array of Cylinders," Ph. D. Dissertation, The University of Arizona, Tucson, Arizona, 1984.
- [5] Churchill, R.V. and J.W. Drown : "The Schwarz-Christoffel Transformation," Chapter 10, Complex Variables and Applications, 4th Edition, McGraw-Hill Book Company, New York, 1984.
- [6] Cielak, Z.M. and R.B. Kinney: "Analysis of Unsteady Viscous Flow Past an Airfoil: Part II — Numerical Formulation and Results," AIAA Journal, Vol. 16, No. 2, pp. 105-110, February, 1978.
- [7] Ghaddar, N.K., K.Z. Korczak, B.B. Mikic and A.T. Patera: "Numerical Investigation of Incompressible Flow in Grooved Channels: Part I. Stability and Self-Sustained Oscillations," J. Fluid Mech., Vol. 163, pp. 99-127, 1986.
- [8] Giaquinta, A.R. : "Numerical Modeling of Unsteady, Separated Viscous Flow," Journal of Fluids Engineering, pp. 657-665, December, 1977.
- [9] Greenberg, Michael D. : Foundations of Applied Mathematics, Prentice-Hall, Inc., 1978.
- [10] Hess, J.L. and A.M.O. Smith: "Calculation of Potential Flow About Arbitrary Bodies," Progress in Aeronautical Sciences, Vol. 8, D. Küchemann, Editor, Pergamon Press, New York, 1967.
- [11] Hobson, E.W. : Treatise on Plane Trigonometry, 4th Edition, Cambridge University Press, 1918.
- [12] Hung, S.C. : "Numerical Predictions for the Unsteady Two-Dimensional Flow in a Rectangular Reservoir," M.S. Research Report, The University of Arizona, Tucson, Arizona, 1982.

- [13] Kanwal, Ram P. : Linear Integral Equations, Academic Press, 1971.
- [14] Karamcheti, K. : Principles of Ideal Fluid Aerodynamics, John Wiley and Sons, Inc., New York, 1966.
- [15] Kinney, R.B. and Z.M. Cielak: "Analysis of Unsteady Viscous Flow past an Airfoil: Part 1 — Theoretical Development," AIAA Journal, Vol. 15, pp. 1712-1717, December 1977.
- [16] Kinney, R.B. and M.A. Paolino: "Flow Transient Near the Leading Edge of a Flat Plate Moving Through a Viscous Fluid," ASME J. Appl. Mech., Vol. 41, pp. 919-924, 1974.
- [17] Kinney, R.B., M.E. Taslim and S.C. Hung: "Numerical Study of Large-Eddy Breakup and Its Effect on the Drag Characteristics of Boundary Layers," NASA CR-3884, March 1985.
- [18] Lamb, H. : Hydrodynamics, Cambridge University Press, Cambridge, 1932.
- [19] Lewis, M.J. : "Optimising the Thermohydraulic Performance of Rough Surfaces," Int. Journal Heat Mass Transfer, Vol. 18, pp. 1243-1248, 1975.
- [20] Paolino, M.A., R.B. Kinney, and E.A. Cerutti: "Numerical Analysis of the Unsteady Flow and Heat Transfer to a Cylinder in Crossflow," J. Heat Transfer, November, 1986.
- [21] Rosenhead L. : Laminar Boundary Layers, Oxford University Press, Oxford, pp. 46-61, 1963.
- [22] Lovitt, William Vernon: Linear Integral Equations, Dover Printed Edition, McGraw-Hill Book Company, Inc., 1950.
- [23] Madala, R.V. and B.E. McDonald: "Solution of Elliptic Equations," Chapter 7, Finite-Difference Techniques for Vectorized Fluid Dynamics Calculations, David L. Bool, Editor, Spring-Verlag, New York, 1981.
- [24] Milne-Thomson, L.M. : "Vortex Motion", Chapter xix, Theoretical Hydrodynamics, 5th Edition, MacMillan, London, 1968.
- [25] Panniker, P.K. and Z. Lavan: "Flow Past Impulsively Started Bodies Using Green's Functions," J. Computational Physics, Vol. 18, pp. 46-65, 1975.
- [26] Payne, R.B. : "Calculations of Unsteady Viscous Flow Past a Circular Cylinder," J. Fluid Mech., Vol. 4, pp. 81-86, 1958.
- [27] Roach P.J. : Computational Fluid Dynamics, Hermosa Publishers, Albuquerque, New Mexico, 1972.
- [28] Roache, P.J. and T.J. Mueller: "Numerical Solutions of Laminar Separated Flows," AIAA Journal, Vol. 8, No. 3, pp. 530-538, 1970.

- [29] Schlichting, H.A. : Boundary Layer Theory, 7th Edition, McGraw-Hill Book Company, New York, 1979.
- [30] Schmall, R.A. and R.B. Kinney: "Numerical Study of Unsteady Viscous Flow Past a Lifting Plate," AIAA Journal, Vol. 12, pp. 1566-1573, November 1974.
- [31] Taslim, M.E., R.B. Kinney and M.A. Paolino: "Analysis of Two-Dimensional Viscous Flow over Cylinders in Unsteady Motion," AIAA Journal, Vol. 22, pp. 586-594, May 1984.
- [32] Torrance, K.E. and J.A. Rockett: "Numerical Study of Natural Convection in an Enclosure with Localized Heating from Below," J. Fluid Mech., Vol. 36, pp. 33-54, 1969.
- [33] Webb, R.L. and E.R.G. Eckert: "Application of Rough Surfaces to Heat Exchanger Design," Int. Journal Heat Mass Transfer, Vol. 15, pp. 1647-58, 1972.
- [34] Wu, J.C. : "Numerical Boundary Conditions for Viscous Flow Problems," AIAA Journal, Vol. 14, No. 8, pp. 1042-1049, August 1976.
- [35] Wu, J.C. and T.F. Thompson: "Numerical Solutions of Unsteady Three-Dimensional Navier-Stokes Equations," Fluid Dynamics of Three-Dimensional and Separated Flows, F.J. Marshall, Editor, Purdue University, pp. 253-284, 1971.
- [36] Wu, J.C. and T.F. Thompson: "Numerical Solution of the Time-Dependent Navier-Stokes Equations Using an Integro-Differential Formulation," Computers and Fluids, Vol. 1, pp. 197-215, 1973.